

---

# Characterization of ictal/non-ictal EEG patterns and Neuronal Networks in Childhood Absence Epilepsy

---

## **Dissertation**

In fulfilment of the requirements for the degree of Dr. rer. nat.  
of the Faculty of Mathematics and Natural Sciences  
at Kiel University

Submitted by

**Ami Kumar**

Kiel, 2020

**First Supervisor:** Prof. Dr. Anand Srivastav

**Second Supervisor:** Prof. Dr. Ulrich Stephani

**Date of oral examination:** 06.10.2020

*This dissertation is dedicated to the cherished memory  
of my father, Prof. Satish Kumar  
and my grandfather, Mr. Prem Kumar*



# Acknowledgements

---

The inspiration to undertake higher studies and research in Neuroscience came from my late father Prof. Satish Kumar. I could not thank him enough for all the support, the encouragement and guidance he gave me through all times.

I would like to express my deep gratitude to my supervisors, Prof. Anand Srivastav and Prof. Ulrich Stephani, for their sustained support, guidance, and encouragement throughout this study. I thank them for making this study an unforgettable experience.

I also express my gratitude to Dr. Natia Japaridze from the department of Neuropediatrics at the University Clinic Schleswig-Holstein (UKSH), Campus Kiel, who was always there as a mentor and guide throughout this study.

I would like to sincerely thank Ms. Ekaterina Lyzhko and Dr. Laith Hamid for their help and support throughout this project, and their assistance regarding the sensor and source level analysis. Special thanks to Jan Geest and Dr. Volkmar Sauerland for their help and useful insight regarding chapter 3.

I thank the research training group, GRK 2154-*Materials for Brain* of the German Research Foundation (DFG) at Kiel University, for giving me the opportunity to be part of the program as an associated doctoral student and for supporting me throughout. I am also grateful for the support of all the members of the Discrete Optimization group at Kiel University.

A special thanks to Iona and Michael with whom I have stayed in Kiel for nearly four years, and who have supported me in every way and helped me all along.

The completion of this task would have been difficult without the cheering and encouraging presence of all my friends who were always there to cheer me up and who never let me lose faith in myself.

Finally, I have my family to thank. They have been my pillars of strength, standing by me through the best and the worst of times, always being there for me. I would like to express my gratitude for all their support and encouragement. I thank my Aunts and Uncles, and both my Grandmother's, for everything that they have done for me. I especially thank my Grandfather, who encouraged and supported me throughout and guided me when the project began. I could not have come this far without them all. Last but not least, to my Mom and little sister Daya, who gave me the strength to chase my dreams, and without whom none of this would be possible.

However, no task big or small can be successfully completed without Supreme Grace which can crown humble efforts. I would like to humbly thank Most Revered Prof. Prem Saran Satsangi Sahab for his immense grace and guidance throughout this project.



# Contents

---

<b>1. Introduction.....</b>	<b>15</b>
1.1 Epilepsy.....	15
1.2 Childhood Absence Epilepsy .....	16
1.3 Previous studies.....	16
1.4 Aim.....	18
1.5 Results of the Thesis .....	18
<b>2. Medical and Methodological Background.....</b>	<b>22</b>
2.1 Childhood Absence Epilepsy (CAE) .....	22
2.1.1 History .....	22
2.1.2 Epidemiology.....	22
2.1.3 Clinical Features .....	23
2.1.4 Electroencephalogram Features.....	24
2.1.5 Pathophysiology .....	24
2.1.6 Neuroimaging .....	25
2.1.7 Treatment.....	26
2.1.8 Prognosis .....	27
2.2 Sensor-space Analysis.....	27
2.2.1 Time Frequency (TF) Analysis.....	27
2.2.2 Frequency Analysis .....	28
2.2.3 Fourier Transform.....	29
2.2.4 Windowing .....	30
2.3 Source Analysis.....	31
2.4 Connectivity Analysis .....	32
<b>3. Forward and Inverse problem for EEG .....</b>	<b>35</b>
3.1 The Maxwell equations .....	36
3.2 The forward problem.....	38
3.3 The discrete form of the forward problem .....	40
3.4 Lead field matrix and corresponding forward problem .....	41
3.5 Noise by the reference electrode .....	42
3.6 The Moore-Penrose Pseudoinverse.....	44
3.7 Regularized inverse solutions .....	48
3.8 The eLORETA algorithm .....	52
3.9 Scalp potential from a point source.....	58
<b>4. Materials and EEG pre-processing .....</b>	<b>63</b>
4.1 Subjects .....	63
4.2 EEG Recordings.....	64
4.3 EEG preprocessing.....	65

4.3.1 Selection of the Time intervals .....	65
4.3.2 Selection of ictal GSWDs.....	66
4.3.3 Selection of non-ictal GSWDs .....	66
<b>5. Sensor-level time frequency analysis.....</b>	<b>69</b>
5.1 Methods.....	69
5.1.1 Selection of ictal and non-ictal GSWDs > 3 seconds.....	69
5.1.2 Time intervals of interest.....	70
5.1.3 Pre-processing .....	70
5.1.4 Artifact Removal .....	71
5.1.5 Normalization .....	72
5.1.6 Time Frequency (TF) Analysis.....	72
5.1.8 Statistical analysis.....	73
5.2 Results .....	75
5.2.1 During-ictal GSWDs .....	75
5.2.2 Pre-ictal GSWDs .....	77
5.2.3 Post-ictal GSWDs.....	79
5.2.4 During-non-ictal GSWDs>3s .....	81
5.2.5 Pre-non-ictal GSWDs>3s .....	83
5.2.6 Post-non-ictal GSWDs>3s.....	85
<b>6. Sensor-level Spectral analysis and Functional connectivity .....</b>	<b>88</b>
6.1 Methods.....	88
6.1.1 Subjects.....	88
6.1.2 Pre-processing .....	88
6.1.3 Frequency analysis .....	89
6.1.4 Functional Connectivity (FC).....	89
6.1.5 Statistical analysis.....	89
6.2 Results .....	91
6.2.1 Spectral Analysis results.....	91
6.2.2 Functional Connectivity results .....	96
<b>7. Source Localization.....</b>	<b>100</b>
7.1 Methods.....	100
7.1.1 Forward calculation .....	100
7.1.2 Inverse calculation.....	100
7.1.3 Statistics.....	101
7.1.3 Visualization.....	101
7.2 Results .....	102
7.2.1 Delta band.....	102
7.2.2 Theta Band.....	104
7.2.3 Alpha band.....	105
7.2.4 Beta band .....	107
<b>8. Source-level Functional Connectivity .....</b>	<b>110</b>
8.1 Methods.....	110
8.1.1 Selecting the seed .....	110
8.1.2 Calculation of the imaginary part of coherency (iCOH) .....	111



8.1.3 Statistics.....	112
8.1.4 Visualization.....	112
8.2 Results.....	112
8.2.1 Seed as source maximum.....	112
8.2.2 Seed as Thalamus.....	117
8.2.3 Comparison of coherence.....	123
<b>9. Discussion for experimental results.....</b>	<b>126</b>
9.1 Sensor level.....	126
9.2 Source level.....	128
<b>10. Conclusion.....</b>	<b>131</b>
10.1 Sensor Level.....	131
10.2 Source Level.....	131
<b>References.....</b>	<b>133</b>
<b>List of Figures.....</b>	<b>141</b>
<b>List of Tables.....</b>	<b>143</b>
<b>Appendix A.....</b>	<b>145</b>
A.1 Source analysis for non-normalized data.....	145
A.1.1 Seed selection.....	145
A.1.2 Source localization results.....	145
A.1.3 Comparison of source analysis for normalized data vs. non-normalized data.....	152
<b>Appendix B.....</b>	<b>154</b>
B.1 Functional connectivity for non-normalized data.....	154
B.1.1 Seed as source maximum.....	154
B.1.2 Seed as Thalamus.....	158
B.1.3 Comparison of normalized and non-normalized datasets.....	163
<b>Appendix C.....</b>	<b>165</b>
C.1 Time frequency topographical plots for ictal GSWDs.....	165
C.2 Time frequency topographical plots for pre-ictal GSWDs.....	169
C.3 Time frequency topographical plots for post-ictal GSWDs.....	173
C.4 Time frequency topographical plots for non-ictal GSWDs.....	177
C.5 Time frequency topographical plots for pre-non-ictal GSWDs.....	179
C.6 Time frequency topographical plots for post non-ictal GSWDs.....	180
<b>Declaration.....</b>	<b>182</b>



# Zusammenfassung

---

Die Absence-Epilepsie des Kindesalters (CAE) ist eines der am häufigsten diagnostizierten Krankheitsbilder in der pädiatrischen Epilepsie. Das Syndrom ist mit einer deutlichen Symptomatologie zu Krampfanfällen und mit klaren elektroenzephalografischen (EEG) Merkmalen verbunden. Allerdings erweist es sich bei CAE-Patienten als schwierig, *ictal* und *non-ictal* generalisierte Spike-Wave-Entladungen (GSWDs) zu unterscheiden, da beide identisch aussehen. Die Unterscheidung dieser beiden Ereignisse ist aber wichtig, weil sie sich direkt auf Diagnose und Behandlungsstrategien im klinischen Umfeld auswirkt. Der Fokus unserer Studie liegt deshalb auf einer Unterscheidung dieser Ereignisse mittels des EEG, sowohl bezüglich der Sensorenmessung (*Sensor-level*) als auch bezüglich der Identifikation der Aktivitätsquelle im Gehirn (*Source-level*). Dabei haben wir uns für das Oberflächen-EEG entschieden, weil dieses in der klinischen Praxis, verglichen mit MEG, MRI und fMRI, das am weitesten verbreitete und kostengünstigste Verfahren ist.

Für unsere retrospektive Studie verwenden wir die Daten von zwölf Patienten, die sowohl *ictal* als auch *non-ictal* Entladungen aufweisen. Für alle Analysen wurde ein Frequenzbereich von 1-30 Hz benutzt, in dem die vier wichtigen Frequenzbänder (Delta-, Theta-, Alpha- und Beta-Band) enthalten sind. Auf dem *Sensor-level* wurden die *ictal* und *non-ictal* GSWDs zunächst einer Spektralanalyse unterzogen und danach die funktionelle Konnektivität (FC) basierend auf dem Imaginärteil der komplexen Kohärenzfunktion untersucht, um die spektralen Veränderungen bzw. die Änderungen im Frequenzspektrum als auch die Konnektivität der Kanäle besser zu verstehen. Auf *Source-level* konnte die Ursprungszone für beide Ereignisse zusammen mit den neuronalen Netzen zwischen den Hirnregionen rekonstruiert werden. Die Quellenrekonstruktion für *ictal* und *non-ictal* Entladungen wurde dabei mit dem eLORETA-Algorithmus durchgeführt. Wir stellen den detaillierten mathematischen Hintergrund der Quellenrekonstruktion im Gehirn mittels des EEG dar, erklären das zugehörige Vorwärts- und Rückwärtsproblem und präsentieren die mathematischen Grundlagen, auf denen der eLORETA-Algorithmus basiert. Wir zeigen, dass das Regularisierungsproblem von Pascual-Marqui et al. (2011) falsch aufgestellt ist, und geben hierzu eine korrekte Formulierung. Ferner liefern wir erstmals einen Korrektheitsbeweis für den eLORETA-Algorithmus, der auf unserer korrekten Formulierung des Regularisierungsproblems basiert.

Die neuronalen Netze wurden für beide Ereignisse mittels FC, basierend auf dem Imaginäranteil der komplexen Kohärenzfunktion auf dem *Source-level* rekonstruiert, um diese Ereignisse besser unterscheiden und verstehen zu können. Interessanterweise haben wir auf dem *Sensor-level* signifikante Unterschiede im elektrischen Leistungsspektrum beobachtet, die belegen, dass *ictal* Entladungen eine höhere Leistungsdichte haben als *non-ictal* Entladungen. Bedeutender noch ist, dass FC eine Desynchronisation von Kanalverbindungen (schwächere Konnektivität) für *ictal* Entladungen im Vergleich zu *non-*

*ictal* Entladungen zeigte. Eine faszinierende Beobachtung auf *Source-level* ist, dass *ictal* und *non-ictal* Entladungen dieselbe Quelle bzw. Ursprungszone im Gehirn aufweisen. Dabei haben *ictal* Entladungen aber eine höhere elektrische Leistung als *non-ictal* Entladungen. FC auf *Source-level* zeigte, dass die Konnektivität zwischen bestimmten Hirnregionen und dem Quellenmaximum und Thalamus stärker war für *ictal* Entladungen als für *non-ictal* Entladungen.

Konnektivitätsmuster für das Delta-Frequenzband zeigen, dass Hirnregionen, die wichtig für Bewusstsein, Sprachverarbeitung, Zahlenverarbeitung, räumliche Orientierung, Erinnerungsvermögen und Visualisierung sind, eine signifikante Kohärenz mit dem Thalamus aufweisen.

Mit dieser Studie zeigen wir signifikante Unterschiede zwischen *ictal* und *non-ictal* Entladungen sowohl auf dem *Sensor-level* als auch dem *Source-level* mittels EEG klar auf. Wir hoffen, dass unsere Ergebnisse in die klinische Praxis einfließen, da sie als potentielle Grundlage künftiger Diagnostikforschung für CAE-Patienten dienen können.

Die Methodik bedarf jedoch noch weiterer Auswertungen hinsichtlich ihrer Sensitivität und Spezifität. Für zukünftige Forschung könnte die von uns gezeigte Korrektheit des von uns verallgemeinerten eLORETA-Algorithmus in experimentellen Anwendungen weiter getestet werden. Ferner könnten bestimmte Algorithmen des maschinellen Lernens zur Klassifizierung entwickelt werden, die beim EEG-Monitoring von Patienten mit CAE helfen würden.

# Summary

---

Childhood absence epilepsy (CAE) is one of the most common pediatric epilepsy syndromes found in children. It is associated with distinct seizure semiology and clear electroencephalographic (EEG) features. However, in these patients, differentiating EEG ictal and non-ictal generalised spikes and waves discharges (GSWDs) is difficult since these events have an identical appearance. The differentiation of these two events is very important since it has a direct effect on diagnosis and management strategies in a clinical setting. Therefore, in this study we focused on differentiating these two events at sensor level and source level using only surface EEG. We chose to use only surface EEG, since it is the most common and inexpensive tool used in clinical practice in comparison to MEG, MRI and fMRI techniques.

In this retrospective study, the data from 12 patients having both ictal and non-ictal discharges was selected. For all levels of analysis, a frequency range of 1-30 Hz containing four important frequency bands (delta, theta, alpha and beta) was used. At sensor level, ictal and non-ictal GSWDs were subjected to power spectral analysis, followed by functional connectivity (FC) based on imaginary part of coherency, to better understand the spectral changes and channel connectivity at the surface respectively. At source level, the onset zone for both these events was reconstructed along with the neuronal networks between brain regions. The source reconstruction of ictal and non-ictal discharges was done using the eLORETA method. We have first given a detailed mathematical background of the EEG, forward and inverse problem, along with the mathematical foundation for the eLORETA algorithm. We showed that the regularization problem posed by Pascual-Marqui et al. (2011) is wrong, and we gave a correct formulation. Additionally, for the first time we prove the correctness of the eLORETA algorithm based on the correct regularization problem. The neuronal networks for both these events were constructed using FC based on imaginary part of coherency at source level, to differentiate and understand these events better.

Interestingly at sensor level, we found significant spectral power differences, demonstrating that ictal discharges have higher power compared to non-ictal discharges. More importantly FC depicted a desynchronization of channel connections (weaker connectivity) for ictal discharges compared to non-ictal discharges. At source level, a fascinating observation was that ictal and non-ictal discharges have the same source or onset zone in the brain. However, ictal discharges had a stronger source power compared to non-ictal discharges. FC at source level revealed that the connectivity between certain brain regions and the seeds of interest (source maximum and thalamus) was stronger for ictal discharges, compared to non-ictal discharges. Connectivity patterns for delta band revealed, brain regions important for consciousness, language processing, number processing, spatial cognition, memory retrieval and visualization to be significantly coherent with the thalamus.

With this study we clearly show that there are significant differences between ictal and non-ictal discharges at sensor and source level using EEG. This study would be a great interest to clinicians, since it could be the potential foundation for future diagnostics research for CAE patients. However, this methodology further requires evaluation regarding sensitivity and specificity. For future aspects, the correctness of the eLORETA algorithm proved by us could further be tested regarding experimental use. Further, certain machine learning algorithms could be developed for classification purposes, which would help in EEG monitoring of patients with CAE.

# Chapter 1

## Introduction

---

### 1.1 Epilepsy

Epilepsy is one of the most common neurological disorders, found to affect people of all ages. It is a disorder characterized by recurring unprovoked seizures. A seizure is a sudden surge of electrical activity caused by hyper synchronous firing activity of nerve cells in the brain [1]. Epileptic episodes can vary in time periods ranging from being brief and undetectable to long periods of vigorous shaking. These episodes may lead to physical injuries in severe cases as well as varying degrees of social confinements.

Around the world, 50 million people suffer from this disorder [2]. Most of the cases have an unknown cause with the remaining resulting from brain injury, stroke, brain tumors, infections in the brain and birth defects. Some cases have also been linked with known genetic mutations. Diagnosis is usually done by using electroencephalogram (EEG), and brain imaging, to look for abnormal brain waves and structural abnormality respectively [3].

Seizures are generally classified into two categories, Focal and Generalized, based on where the abnormal activity in the brain begins. Focal seizures occur only in one part of the brain, while generalized seizures involve all areas of the brain. In 2017 the International League Against Epilepsy (ILAE) updated the classification for seizures [4].

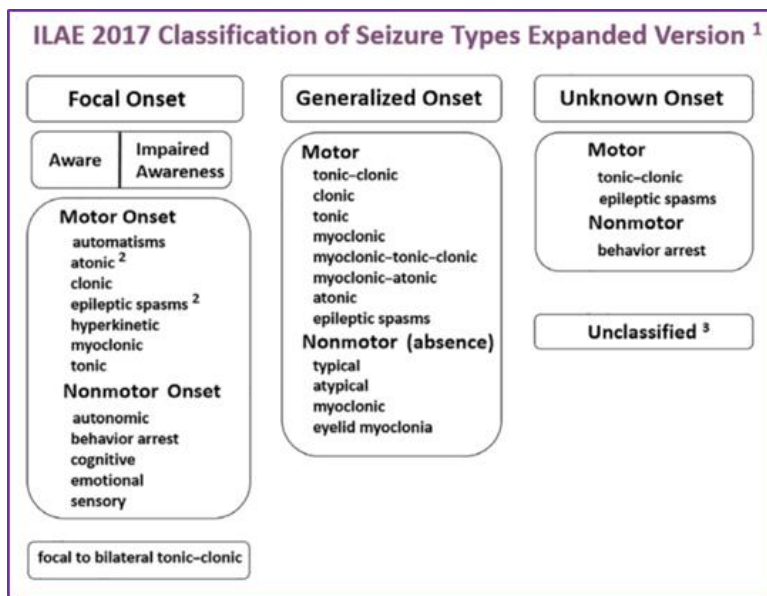


**Figure 1.1 ILAE classification of seizures.** Taken from Fisher et al, *Epilepsia*, 2017, depicting the new classification of various seizure types involved in epilepsy.

## 1.2 Childhood Absence Epilepsy

In this study we focused on a specific syndrome called, childhood absence epilepsy (CAE), which falls under the classification of generalized onset, and non-motor, typical absences.

CAE is one of the most common forms of epilepsy, accounting for 2-10% of all childhood epilepsies. It is an idiopathic form of epilepsy associated with staring spells (absences) as well as impaired consciousness. The seizures in this syndrome are characterized by multiple typical absences having generalized spike and wave discharges (GSWDs) of 3 Hz on the EEG. These GSWDs are bilateral, synchronous and symmetrical and are known to have an abrupt onset as well as an abrupt termination. Absences generally last for 4-10 seconds but in some cases may persist for a longer period. They may occur frequently per day and if treated properly, respond well to antiepileptic drugs. The age of onset is found to be 4-10 years with a peak at 5-7 years [5, 6].

EEG is the best diagnostic test for this syndrome. Electrographically these seizure events are termed as ‘ictal’ discharges while the time period between ictal events is termed as ‘interictal’ region [7]. The interictal EEG of patients with CAE, frequently show GSWDs without impairments of consciousness, behavioural alteration, or subjective symptoms. These GSWDs are identical to ictal EEG patterns seen during the absence seizures. Currently there are no objective tools available to differentiate these two events in the EEG, and only a thorough direct testing of the patient during the occurrence of discharges can distinguish ictal vs. non ictal or rather subclinical events. Direct testing can however be very challenging, since these discharges and absences can be very short and subtle. Additional challenges can be posed by the poor compliance of young children as it requires an active participation of the patients. A careful differentiation of these two events is however very important in clinical practice, as it helps to evaluate the treatment strategies and outcomes.

## 1.3 Previous studies

Various studies have demonstrated the involvement of the thalamo-cortical circuit playing an important role in the pathophysiology of CAE [8–10]. Previous functional magnetic resonance imaging (fMRI) studies revealed that a common network of structures, including the anterior and posterior cortices, thalamus, caudate nuclei, cerebellum, reticular structures of the pons and the default mode network (DMN), play an important role in the generation and propagation of absences [11, 12]. In addition, EEG-fMRI studies show the activation of the thalamus and inactivation in the medial frontal, medial parietal, anterior and posterior cingulate, which are important components of the DMN. It is understood that the DMN is selectively impaired during absences and certain components of the DMN have an overlap with the consciousness system. Studies demonstrate an initial increase in DMN cortical regions, followed by long lasting decreases in the network. BOLD signal decreases have also been reported in the parietal cortex precuneus, caudate nucleus, cingulate gyrus, basal ganglia and posterior temporal cortices, suggesting that cortical-subcortical interactions may play a



role in the decreases of DMN [13]. Further approaches are required to better understand the neuronal networks associated with ictal GSWDs and impairment of consciousness, in contrast with non-ictal GSWDs.

Since brain imaging techniques such as Positron-emission tomography (PET), Single-photon emission computed tomography (SPECT) and fMRI have low temporal resolution, it becomes difficult to use these techniques to demonstrate the dynamics of networks involved within absences. But, EEG and MEG methods are better-suited for the evaluation of connectivity, since they have excellent temporal resolution.

Signal processing techniques involving spectral power analysis on EEG data have proven to give valuable information on the dynamics of a seizure at sensor level. This includes using specific frequency-based techniques such as wavelet and Fourier transforms (FT) [14, 15]. But to better understand the dynamics of seizure onset at a deeper level source analysis is required. However, localizing the area from where the electrical activity originates becomes difficult, because of the uncertainty underlying the static electromagnetic inverse problem. Nonetheless recent developments regarding EEG inverse solutions have significantly improved source localization, leading to the usage of EEG data for investigating neuronal networks even involving deep brain structures.

A new approach to tackle the inverse problem is the exact low-resolution brain electromagnetic tomography (eLORETA) [16, 17]. This method is a non-invasive discrete, three-dimensional (3D) distributed, linear, weighted minimum norm inverse solution. It can be applied to low resolution data such as EEG data, to investigate the current source density in the brain. eLORETA is an improvement over the previously used methods LORETA [18] and the standardized version sLORETA [19]. This technique has been implemented within many toolboxes, and one such toolbox used for this study was the MEG and EEG Toolbox of Hamburg (METH). This toolbox is a collection of MATLAB functions, which can be used for data analysis on MEG and EEG data. This technique has been used for source analysis in various studies. Besides the practical use of the eLORETA algorithm, there are serious mathematical issues which are of concern.

Further, to get an overview of the brain interactions, functional connectivity (FC) can be computed from surface EEG. FC identifies brain regions that have synchronous activity, but it does not give the specific direction of information flow in the brain [20]. The FC can be computed using coherence and phase synchrony methods in the frequency domain. Focusing on the coherence method, this technique quantifies the synchronicity of neuronal patterns in the brain. This method has been widely used in various cognitive and clinical neurological studies in sensor space and source space using EEG [21, 22]. It has also been used in the field of Epileptology to study seizure onset zones [23–25].

As EEG is a non-invasive technique, the problem of volume conduction (VC) arises. This can be described as a spatial spread of the electromagnetic fields, leading to the fact that multiple

electrodes or sensors may pick up the activity of a single brain source. This causes spurious connections to occur in coherence distorting functional connectivity. A robust approach to sensor-level and source-level connectivity estimation is achieved by using the imaginary part of coherency [26], which is an important technique that overcomes volume conduction effects of FC.

These various techniques mentioned here were implemented in our study, focusing solely on using EEG data.

## 1.4 Aim

In this study we focus on identifying significant differences between ictal and non-ictal GSWDs in CAE patients using surface EEG. The data will be analyzed in sensor-space and source space, and further FC based on imaginary part of coherency will be used to understand the neuronal networks. This will be done using pre-ictal/non-ictal, during-ictal/non-ictal, and post-ictal/non-ictal time intervals, in order to better understand the dynamics of these GSWDs. The aims of this study are:

- Spectral analysis and FC based on imaginary part of coherency, at sensor-space level to identify significant frequency bands and significant neuronal networks respectively.
- Source analysis and FC based on imaginary part of coherency, to better understand the ictal/non-ictal GSWDs onset zone alongside the neuronal networks associated with impairment of consciousness.
- Sound mathematical foundation of the forward and inverse problem for EEG source analysis, and proofs for the correctness of the eLORETA algorithm.

## 1.5 Results of the Thesis

In **chapter 1** we give a brief introduction for this study. This is followed by an overview on the medical background regarding the CAE syndrome as well as a methodological background described in **chapter 2**.

We continue with **chapter 3**. Here we give a concise mathematical formulation for the forward and inverse problem of EEG along with its solution, which is required for source reconstruction. We also give a detailed description of the eLORETA algorithm used for source analysis. To begin with, we have described the forward problem using the Maxwell's equations alongside the discrete form of the forward problem. We have defined and calculated the lead field matrix, and also given a proof for a reference independent forward equation. We have also given a brief description of pseudo inverses and have proved certain properties which would further be required for the inverse problem.

Since, the inverse problem is an ill posed problem; it is approached using the so called regularisation approximation. Pascual-Marqui (2007) [17], who formulated the algorithm eLORETA for source reconstruction, described the inverse problem and the solution in his

publications unfortunately in a rudimentary way. The inverse problem in these publications was posed by the weighted minimum norm problem using the Tikhonov regularization parameter, alongside a general solution. We show that the Tikhonov regularization problem alongside the solution given by Pascual-Marqui et al. (2011) is false. Therefore, we formulate a new general Tikhonov regularization problem in detail and give solutions which are mathematically correct. However, for further applications we used the eLORETA algorithm based on the solution described by Pascual-Marqui, since in medical practice it has given meaningful results.

Though, for source localization we used the eLORETA algorithm, we have also given a detailed mathematical foundation for this algorithm which was missing in the papers of Pascual Marqui (2007) [17], and Pascual Marqui et al. (2011) [16]. We have taken into account two critical points within the algorithm, which have not been addressed in the publications of Pascual-Marqui. Firstly, the positivity of the weights, and secondly, the termination criterion of the algorithm. Regarding the positivity of the weights being used in the algorithm, we have given the proof for the first time using linear algebra and the Moore-Penrose inverse.

The general idea of the algorithm is to compute a weight matrix in an iterative way, which at the beginning is the identity matrix as used in the former LORETA algorithm. Thereafter, the weight matrix is updated step by step so that the new weight matrix is always a diagonal matrix. The crucial and critical point is that in the iterations of the algorithm the new weight matrix is computed by inverting the old weight matrix and it is claimed that the diagonal entries of the matrix are all non-negative and implicitly assumed to be non-zero. In all the publications of Pascual-Marqui in more than 20 years (1999, 2007, 2011) [16, 17, 27] and cited also by others, these unproven statements prevail. Thus the correctness of the eLORETA is in doubt. Based on our correct formulation of the Tikhonov regularization problem and its matrix solutions we show for the first time that the diagonal weight matrix has all strictly positive diagonal entries, which establishes the correctness of the eLORETA approach. The proof is heavily based on linear algebra of the Moore-Penrose inverse and the physical fact that the columns of the lead field matrix cannot be zero, which is an important and meaningful assumption in the physics of EEG.

In **chapter 4**, we have described the demographic data of the subjects selected for this study and have given an overview of the selection process for ictal and non-ictal discharges.

Initially for this study we analysed ictal and non-ictal discharges longer than 3 seconds, using time frequency analysis and descriptive statistics. A frequency range of 1-35 Hz was analysed. It was observed that all frequency bands (delta, theta, alpha, beta and gamma) demonstrated significant spectral power ( $p < 0.05$ ) differences, independently for both the groups of interest. This has been described in detail in **chapter 5**. However, since not all patients had non-ictal discharges longer than 3 seconds a comparative analysis of the two groups of interest could not be done. Therefore for the next steps of this study non-ictal

discharges, less than 3 seconds were also included, so that the dataset of all patients could be completed and a comparative analysis could be possible.

**Chapter 6** describes sensor level analysis using spectral analysis and functional connectivity to differentiate between ictal and non-ictal discharges, and also to analyse the network connectivity between the EEG channels. Frequency bands delta, theta, alpha and beta (1-30 Hz) demonstrated significant spectral power difference ( $p < 0.05$ ) between ictal and non-ictal discharges. In all frequency bands it was seen that ictal discharges have a significantly higher power compared to non-ictal discharges. It was also seen that the time interval during-ictal/non-ictal had higher power compare to pre- and post- time intervals.

Functional connectivity at sensor level revealed, that all frequency bands (1-30 Hz) had significant ( $p < 0.05$ ) difference regarding channel connections. Most importantly it was observed that ictal discharges have a weaker connectivity between channels compared to non-ictal discharges. A desynchronization of channel connections was seen for ictal discharges in delta band involving areas of the DMN.

Following sensor level analysis, **chapter 7** describes the source reconstruction of ictal and non-ictal discharges. Using the eLORETA method, interestingly it was seen that ictal and non-ictal discharges have the same source or onset zone in the brain. However, ictal discharges had a stronger source power compared to non-ictal discharges. Frequency bands delta, alpha and beta showed significant differences ( $p < 0.05$ ). Delta band (1-3 Hz) revealed two sources, a deep source in the subcortical regions of caudate and putamen right regions. The second source was a cortical source seen in the supplementary motor right region. The spread of source power was observed in the thalamus, parietal and temporal regions.

Further, functional connectivity was done at source level to better understand the neuronal networks underlying ictal and non-ictal discharges. This has been described in **chapter 8**. The results showed that the coherence was stronger between the brain regions and the seeds of interest (source maximum and thalamus) for ictal discharges, compared to non-ictal discharges. With the thalamus as the seed of interest promising results were seen. For delta band, brain regions important for consciousness, language processing, number processing, spatial cognition, memory retrieval and visualization were seen to be significantly coherent with the thalamus. These regions of the brain were occipital mid (left), parietal inferior and superior (right and left), angular gyrus (left), posterior cingulum (left) and precuneus (left). Many of the significant regions seen also had regions of the DMN in common.

Additionally in **chapter 9** we have discussed the experimental results for sensor and source level. This is finally followed by **chapter 10**, which is the conclusion of this study.

Our findings clearly show that there are significant differences between ictal and non-ictal discharges at sensor and source level, although these discharges have similar appearance on an EEG. Using only EEG surface data significant deep sources in the brain were observed as well as significant connectivity patterns. This indicates that EEG itself is a powerful tool for

analysing ictal and non-ictal discharges. This methodology could be implemented in the future for classification purposes in EEG diagnostics of patients with CAE as well as to develop machine learning algorithms which would assist clinicians in EEG monitoring. This would help in better management of patients with CAE. However, this methodology further requires evaluation regarding sensitivity and specificity.

# Chapter 2

## Medical and Methodological Background

---

### 2.1 Childhood Absence Epilepsy (CAE)

#### 2.1.1 History

Absence seizures were first described by Poupart in 1705 and by Tissot in 1770. Following which in 1824 Calmeil introduced the term ‘absences’ for the first time. In 1838 French psychiatrist Jean-Etienne Dominique Esquirol was the first to use the term “petit mal” to describe absence seizures, which gets its name from the French, meaning “little illness”. The inventor of electroencephalogram (EEG) Hans Berger also made the first EEG recording for an atypical absence but his results were only published in 1933 [28].

The spike and wave complexes of absence seizures were first acknowledged by Gibbs in 1935 [29]. While a more detailed description of the generalized spike and waves in absence seizures were described by Weir in 1965 [30]. In the year 1981 absence seizures were classified as generalized seizures by the commission on classification and terminology of the international league against epilepsy (ILAE) [31]. Generalized seizures indicate events involving both halves of the brain. Further, absence seizures were also differentiated into typical and atypical absences. In 1989 idiopathic epilepsies were clustered according to the onset age, and so typical absence seizures were further classified into childhood absence epilepsy, juvenile absence epilepsy and juvenile myoclonic epilepsy [32]. Recently in 2017 the ILAE published new guidelines for the classification of seizure types and typical absence seizures were listed among the generalized onset, non-motor seizures [4].

#### 2.1.2 Epidemiology

In children with epilepsy 10% of the seizures are typical absence seizures. The estimated annual incidence of CAE is reported to be in the range of 2–8 per 100,000 children under the age of 15–16 years. In the general population the prevalence of this syndrome is 5 to 50/100,000 people. It is seen that girls are at a higher risk compared to boys but it has also been reported that there is an equal incidence in boys and girls [33, 34]. In a community based study done by Callenbach et al. (1998), [35] the prevalence of CAE was found to be 10 % for children younger than 16 years. Similarly, in a community based study done by Berg et al. (2000) on 613 children with epilepsy aged 0 to 16 years, 12% accounted for CAE diagnosis [36]. Based on EEG findings, a retrospective study done on Swedish children aged 0 to 15 found the annual prevalence of absence epilepsy to be 6.3 per 100,000. In a survey

done in southwest France the annual incidence of CAE was estimated to be 8 per 100,000 [37].

### 2.1.3 Clinical Features

CAE is characterized by multiple typical absences accompanied with 3Hz GSWDs in EEG. Absence seizures may occur many times a day, and have an abrupt onset and termination. The most important feature of CAE is the severe impairment of consciousness, where there is a loss of awareness, with behavioural arrest and unresponsiveness. But the level of impairment of consciousness may differ from one seizure to another within and between patients. Patients are unable to recollect the seizure events taking place. Most children completely stop any on-going activity while others may continue the activity in an altered way. They may stare straight ahead with a vacant look or with a gaze drifting upwards [6, 38]. An inclusion and exclusion criteria for CAE patients has been described below according to Panaytopoulos CP., (2006).

<b>Inclusion criteria:</b>	
(1)	Age at onset between 4 and 10 years and a peak at 5 to 7 years.
(2)	Normal neurologic state and development.
(3)	Brief (4 to 20 seconds, exceptionally longer) and frequent (tens per day) absence seizures with abrupt and severe impairment (loss) of consciousness. Automatisms are frequent but have no significance in the diagnosis.
(4)	EEG ictal discharges of generalized high-amplitude spike and double (maximum occasional 3 spikes are allowed) spike-and-slow wave complexes. They are rhythmic at around 3 Hz with a gradual and regular slowdown from the initial to the terminal phase of the discharge. Their duration varies from 4 to 20 seconds.
<b>Exclusion criteria:</b>	
(1)	Early onset before the age of 3 years or late onset after 10 years.
(2)	Other than typical absence seizures such as GTCS, or myoclonic jerks prior to or during the active stage of absences.
(3)	Eyelid myoclonia, perioral myoclonia, rhythmic massive limb jerking, and single or arrhythmic myoclonic jerks of the head, trunk, or limbs. However, mild myoclonic elements of the eyes, eyebrows, and eyelids may be featured, particularly in the first 3 seconds of the absence seizure.
(4)	Mild or no impairment of consciousness during the 3 to 4 Hz discharges.
(5)	Brief EEG 3 to 4 Hz spike-wave paroxysms of less than 4 seconds, multiple spikes (more than 3) or ictal discharge fragmentations.
(6)	Visual (photic) and other sensory precipitation of clinical seizures.

**Table 2.1 Inclusion and exclusion criteria for CAE.**

*This has been adapted from Panaytopoulos 2006 [40].*

In many patients automatisms may be present, with severe impairment of consciousness [39]. They are usually observed in longer seizures or during hyperventilation. Often mild tonic or clonic symptoms may occur during the first second of the seizure but if marked eyelid, perioral, limb or trunk myoclonic jerks persist through the course of the absence seizures then this may lead to exclusion criteria.

Even though absence seizures occur spontaneously, they are influenced by numerous factors such as anger, sorrow, surprise, embarrassment, lack of interest, release of attention, hypoglycaemia and hyperventilation. Hyperventilation is the most important factor for inducing absence seizures. This is often used for diagnostic purposes. In an untreated child if hyperventilation does not provoke a seizure, then the diagnosis should be questioned. In a study done by Hirsch et al. (1994) Hyperventilation provoked typical absence seizures in 100% of CAE patients. Absence seizures provoked consistently by means of photic stimulation do not belong to CAE.

### **2.1.4 Electroencephalogram Features**

**Ictal EEG:** EEG is the best diagnostic test for absence seizures. Ictal EEG refers to the event when the seizure takes place. The characteristic pattern seen on any EEG is the 3 Hz GSWDs which begin and end abruptly. These discharges are bilaterally synchronous and symmetrical [6]. 3 Hz GSWDs less than 4 seconds are not considered typical of CAE. In a study done by Sadlier et al. on 339 absence seizures from 47 patients, defining the many electro clinical features of CAE, it was seen that the average seizure duration was 9.4 seconds [41] as compared to 12.4 seconds [39] which was previously reported. It was observed that GSWDs were of regular 3 Hz with one or two spikes per wave and three or more spikes per wave was rare. Also hyperventilation induced absence seizures in 83% of the cases while intermittent photic stimulation induced 21% of the seizures.

**Interictal EEG:** The interictal EEG refers to the period between seizures in epileptic patients. During this time course brief GSWDs can be observed. They occur most commonly during sleep. These paroxysms may also include non ictal GSWDs which do not have any clinical symptoms and impairment of consciousness [42]. The EEG background is normal.

### **2.1.5 Pathophysiology**

Over several decades the GSWDs in absence seizures have been analysed to study the mechanisms underlying them. Animal models and various neuroimaging studies have provided useful information regarding this.

In 1946 studies done by Jasper and Droogleever-Fortuyn showed that on electrical stimulation of thalamic nuclei in cats at 3 Hz produce synchronous bilateral spike and wave discharges on EEG [43]. Similarly in 1953 spike-and-wave discharges were recorded by using depth electrodes in a child with absence seizure by placing the electrodes in the



thalamus [44]. Interestingly studies done using the feline generalized epilepsy penicillin model of absence seizures and the genetic absence epilepsy rats from Strasbourg revealed that in order to generate synchronous bilateral spike and wave discharges the cortex and thalamus are required [45, 46]. This led to the concept of corticoreticular theory of generalized seizures. Evidently absence seizures involve bilateral cortical and subcortical networks which involve parts of the default mode network (DMN) [13]. There are many genetic animal studies as well as neuroimaging studies done that support this as well as give useful insight regarding the pathophysiology of absence seizures [6].

In an EEG-fMRI study done on ictal and interictal GSWDs in patients with CAE identified, blood-oxygen-level-dependent (BOLD) signal changes in the basal ganglia-thalamocortical loop [47]. Ictal GSWDs were predominantly associated with thalamic activation, and a widespread deactivation in the cortex. Similarly, in a single photon emission tomography (SPECT) study with relation to the pathophysiology of absence seizures, it was seen that the concept of subcortical origin was supported [48].

CAE is genetically determined, but the precise mode of inheritance remains unknown. It has been observed that a positive family history of epilepsy can be found in 15-44% of the cases and with regard to epilepsy in parents the occurrence is 42.6% while in siblings it is found to be 20.7%. In 84% of monozygotic twins, typical spike wave discharges were detected out of which 75% developed absence seizures [49, 50].

Till now only two gene mutations with relation to CAE have been identified and most of the molecular genetic studies have failed to identify the precise genetic factors. Firstly, the gene mutation involved with the generation of spike and wave discharges is the g-aminobutyric acid (GABA) A and B receptors (GABRG2, GABRA1, GABRB3, GABA(B1), GABA(B2)) [51, 52]. And secondly, mutations in genes encoding calcium channels (CACNA1 A, CACNA1 H, CACNA1 G, CACNA1I, and CACNG3) may play an important role in the pathophysiology of CAE [33, 51]. In the Chinese Han population CACNA1 H gene seems to be the most susceptible while it is insufficient to cause epilepsy on its own in Caucasians [53]. In a subset of patients with CAE, CACNG3 as well as gene mutations in the chloride channels CLCN2 may have a susceptible locus [53, 54]. In some cases it has been reported that SLC2A1 mutations have been associated with early onset absence epilepsy. Additionally it has been observed that GLUT1 gene mutations are related to worse prognosis [55, 56].

### **2.1.6 Neuroimaging**

For idiopathic epilepsies the neuroimaging findings are normal and therefore, if typical clinical patterns are present then neuroimaging is not necessary. However to rule out structural abnormalities often neuroimaging tests are done for better diagnosis. Magnetic resonance imaging (MRI) is preferred over computed tomography (CT) scanning since it is more sensitive for detecting anatomical abnormalities.

Patients with CAE seem to develop cognitive difficulties alongside clinical symptoms. These cognitive difficulties mainly involve attention and executive functions [57]. Many neuroimaging studies have been done in this domain to better understand the cognitive functions. Studies show that there is a decreased activation of anterior insula of the medial frontal cortex leading to significant altered attention networks [6]. Also a functional magnetic resonance imaging (fMRI) study done on a CAE patient while doing a continuous attention task revealed that there was impairment in the attention network which involved the anterior insula/frontal operculum and medial frontal cortex [58].

### 2.1.7 Treatment

CAE treatment characteristically involves antiepileptic drugs (AEDs) [59]. Since absence seizures can occur many times a day and can severely impair quality of life, specific prophylactic anticonvulsants are recommended. Depending on the severity of the seizures children with absence seizures may have to undergo treatment for many years, and in some cases even for life. The start of antiepileptic medication is done with extreme care since these drugs could also have severe side effects. The treatment is usually tailored according to patient conditions since certain clinical symptoms may vary from patient to patient.

<b>Drug</b>	<b>Mechanism of Action</b>	<b>Efficacy</b>	<b>Reported Side Effects</b>
Ethosuximide	Diminishes low-threshold (T-type) calcium current in thalamic cells	Complete control in 70% of patients	Nausea, headache, drowsiness
Valproate	Different mechanisms not completely known (raises brain level of g-aminobutyric acid and also affects sodium and calcium channels)	Seizure-free from 88% to 95% of patients	Weight gain, hair loss, hepatitis, polycystic ovaries
Lamotrigine	Blockage of use-dependent voltage sensitive sodium channels	Seizure free in 50% to 56% of patients	Skin rash, drowsiness, dizziness, headache
Levetiracetam	Modulation of a synaptic vesicle protein	Reduction of seizure in 50% of patients	Dizziness, fatigue, irritability

**Table 2.2 Drugs used for CAE patients.**

*This table describes the drugs most commonly used for patients with CAE. The table has been adapted from Matricardi et al. 2014.*

For absence seizures there are two first line drugs approved, which are: ethosuximide (ESM) and valproic acid (VPA) [60]. ESM is specifically effective against absence seizures. It is observed that in 70% of treated patients, this drug allows complete control of the seizures [61]. Alternatively VPA is considered as a broad spectrum antiepileptic drug, since it targets absence seizures as well as generalized tonic-clonic seizures, myoclonic seizures and partial seizures. Studies show VPA having seizure free rates from 88% to 95% [62]. Other than these drugs second line AEDs such as clobazam, clonazepam and acetazolamide may also be used. In the past few years new broad spectrum AEDs have been introduced which include lamotrigine (LTG), levetiracetam (LEV), topiramate (TPM), and zonisamide (ZSM) [6]. In treatment of patients with this syndrome, ESM and VPA are considered to be more effective drugs than LTG [63].

### **2.1.8 Prognosis**

Studies about prognosis and evolution of CAE still remain quite inconclusive since there is always a difference in diagnostics, inclusion exclusion criteria and follow up periods. Nevertheless CAE has a very good prognosis if proper strict diagnostic criteria are used. It has effective AED withdrawal with remission rates ranging from 56% to 84% [6, 40].

## **2.2 Sensor-space Analysis**

Neural activity in the brain has been widely studied over the past years. Neural oscillations or brain rhythms are rhythmic fluctuations of the brain cells. This oscillatory activity may arise through various mechanisms in the brain associated with a single neuron or interaction of neurons. EEG is one of the devices used often to study the rhythmic activity in the brain. These neural oscillations are described using frequency, power and phase. Frequency basically measures the speed of the oscillations, while power measures the amount of energy in a particular frequency band or it can be referred to as the squared amplitude of the oscillation. The phase whereas marks the position along a sine wave at any given time point. These characteristics can be extracted from neural oscillations using various techniques [64].

The first step of differentiating ictal and non-ictal GSWDs required analysis at sensor level. Time-frequency representations of power and power spectral density were computed to analyze ictal and non-ictal GSWDs at sensor level. This would give a better insight into which frequency bands are involved during ictal and non-ictal GSWDs.

### **2.2.1 Time Frequency (TF) Analysis**

TF analysis is a popular technique used to draw inferences regarding brain rhythms. It is a method by which a signal can be analysed in both time and frequency domain simultaneously using numerous time frequency representations (TFRs). It analyses a two dimensional signal. The computation of TFRs of power is essential to understand event related changes taking

place [64, 65]. This will be computed using the Fourier transform alongside a sliding window.

TF analysis has been used as a measure in various fields of science to study oscillations. It has also been widely used in epilepsy research for seizure detection as well as for studying the dynamics of a seizure.

In a study done by Cuspinada-Bravo et al. (2013) [66] on refractory frontal lobe epilepsy patients, TF analysis was used as a measure, to understand whether EEG source localization of the epileptic zone can be improved. By using TF analysis certain features could be identified. Their study included using the Bayesian model averaging (BMA) to compare brain electromagnetic tomographic (BET) images constructed in the TF domain with BET images constructed from only the time domain. Their study showed that TF analysis based on EEG data improves source localization. Tzallus et al. 2007 [67] used TF analysis and Artificial Neural Networks for automatic seizure detection. They applied TF analysis on EEG data and extracted several features for each segment of interest. These features were further used as an input in an artificial neural network, for classification of EEG segments containing seizures or not. Sitnikova et al. (2013) [68] studied the time frequency EEG characteristics and dynamics of sleep spindles in absence epilepsy WAG/Rij rat models. In another study done by Colominas et al. (2018) [69] resting state EEG data of epileptic patients was analyzed using time varying time frequency complexity measures. Their study aimed to evaluate the improvement of patients after medication using existing and a proposed new time frequency entropy measures. They found that these measures could be used to monitor the treatment of epileptic patients. Sun et al. (2016) [70] studied the intracranial EEG in patients with myoclonic seizures using time frequency analysis. Other time frequency analysis studies have been described in various articles such as: Tenny et al (2014) [71], Celka et al. (2001) [72], Williams et al. (1995) [73], Blanco et al. (1997) [74]. Thus, TF analysis has been used in various ways to better understand the dynamics of seizures in epilepsy.

TF analysis was implemented with an aim to investigate the power changes within frequency bands for ictal and non-ictal GSWDs  $> 3$  seconds. In our work this will be done for 3 time intervals of interest: pre-ictal/non-ictal, during- ictal/non-ictal and post ictal/non-ictal, to better understand the changing dynamics of the various frequency bands. This has been described in chapter 5.

### **2.2.2 Frequency Analysis**

Frequency domain analysis, as the name suggests deals with processes that can be localized in the frequency domain. These processes have advantages since they are computationally fast and they can give important insight regarding the dynamics of a signal. In chapter 6, a Fast Fourier Transform (FFT) with a sliding window will be used to analyse the dynamics of a seizure in CAE syndrome. The FFT is basically an algorithm that calculates the discrete

Fourier transform (DFT) or its inverse [64]. The DFT is computed by breaking down a sequence of values into various frequency components.

FFT is widely used in various applications, in the fields of Engineering, Music, Science and Mathematics. It is also a common method used in Epilepsy research to understand the changing dynamics of ictal events in EEG recordings. For example, Drinkenburg et al. (1993) [75], analyzed the EEG of epileptic rats using spectral analysis to study aberrant transients. Spectral analysis was done using a fast Fourier transform. Nuwer (1987) [76], studied EEGs and evoked potentials of patients with complex partial seizures using frequency analysis and topographic mapping, to understand whether this could help in localization of the epileptic focus. Sitnikova et al. (2009) [77], analyzed genetic rat models of absence epilepsy to investigate the EEG precursors of spike and wave discharges using power spectral analysis and coherence as a measure.

At sensor level, frequency analysis was used to find the significant frequency bands and further to know the significant clusters of electrodes between the two groups of interest, ictal and non-ictal GSWDs.

### 2.2.3 Fourier Transform

The Fourier transform is the backbone for TF analysis and frequency analysis. It is an essential signal processing technique used for time series data analysis. A Fourier transform basically deconstructs a signal in the time domain into its constituent frequencies. This in return gives the spectrum or the power spectral density as an output [64].

In chapter 5 and 6, time-frequency representations of power and power spectral density will be computed using the software Fieldtrip [65], which runs via MATLAB. The Fourier transform is the basis of computing the spectrum.

Before calculating the Fourier transform, the data was normalized using a Z-score normalization.

Let  $k = 1, \dots, 31$  be the number of EEG channels being used. For each channel  $k$ , we have  $N$  time points  $t_1, \dots, t_N$  and  $x_{k,1}, \dots, x_{k,N}$  ictal/non-ictal EEG signals ( $\mu\text{V}$ ). For  $\mathbf{X}_k := (x_{k,1}, \dots, x_{k,N})$ , the normalization can be obtained as follows:

$$\mathbf{Z}_k = \frac{\mathbf{X}_k - \mu_k}{\sigma_k} \quad (2.1)$$

Here,  $\mu_k$  is the mean of ictal/non-ictal data, and  $\sigma_k$  is the standard deviation obtained from the interictal EEG data.

Using the normalized EEG data, the complex discrete Fourier transform is calculated.

For data  $\mathbf{Z}_k$ , let  $\mathbf{Z}_k = (z_{k,1}, \dots, z_{k,N})$

Then the complex Fourier Transform per channel, per frequency can be given by the following equation:

$$\begin{aligned} X_{kj} : \\ = \sum_{n=1}^N z_{k,n} \exp(-2\pi i f_j t_n), \end{aligned} \quad (2.2)$$

where,  $\sum_{n=1}^N z_{k,n}$  represents a sum over data  $Z_k$ ,  $i$  is the imaginary unit, the frequencies are  $f_j = j/T$ , where  $j = 1, \dots, 30$ , and the time points are  $t_n$ ,  $n=1, \dots, N$

Using Euler's formula, (2.2) can be rewritten as:

$$X_{kj} = (\sum_{n=1}^N z_{k,n} \cos(-2\pi i f_j t_n)) + i(\sum_{n=1}^N z_{k,n} \sin(2\pi i f_j t_n)) \quad (2.3)$$

Here, the data  $z_{k,n}$  is multiplied by a cosine and sin function at frequency  $j$  at each point in time, which is further summed over time. Therefore, Fourier transform can be understood as the data  $z$  being compared to sinusoids oscillating at frequency  $j$ .

The output of the Fourier transform is the power spectrum (P), defined as:

$$P_{kj} := X_{kj} \cdot X_{kj}^* \quad (2.4)$$

Where,  $P_{kj}$  represents the auto-spectrum of channel  $k$  at a particular frequency  $j$ , and the  $*$  is the complex conjugation.

The spectrum produced using Fourier transform provides a powerful method to assess ictal and non-ictal GSWDs or rhythmic activity in time series data.

## 2.2.4 Windowing

The windowing or tapering function is a mathematical function that is used to reduce spectral leakage. A sliding time window can be applied to calculate the TFRs of power. For using a sliding window two principles can be applied:

- 1) The window has a fixed length and it is independent of frequency changes
- 2) The time window decreases with increase in frequency.

The power is calculated for each time window. In this study a fixed window length is used.

Before calculating the power spectrum the data is multiplied by one or more tapers. We use tapers for time and frequency smoothing, so that spectral leakage is prevented. Spectral estimates are usually contaminated with considerable endpoint discontinuities, when windowing data that has significant low frequency variability. To remove these discontinuities one possible method is to multiply each window of the time series by a weight

function or a taper that goes to zero at the end points smoothly [78]. Here, the Hanning taper [79] is used. The Hanning taper or Hann function is named after the Austrian meteorologist Julius von Hann.

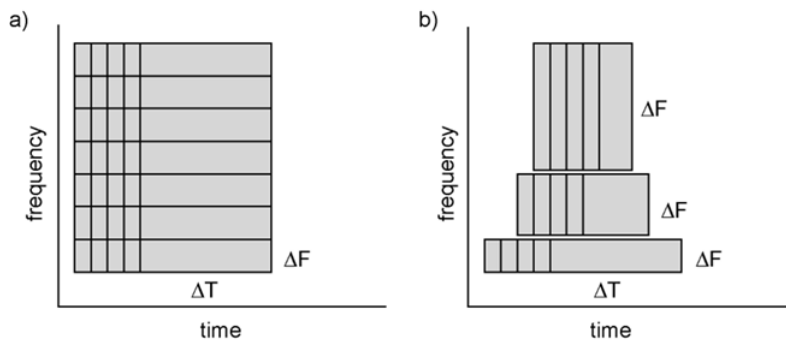


**Figure 2.1 Time and frequency smoothing.**

*Adapted from Fieldtrip software tutorials. a) For a time window having a fixed length, the time and frequency smoothing remains fixed. b) With a decrease in frequency the time window decreases, leading to temporal smoothing decreases and the frequency smoothing increases.*

## 2.3 Source Analysis

Over the past decades, electroencephalogram (EEG) is one of the most widely used techniques to measure neuronal oscillations in the brain. It has been widely used for clinical diagnosis in the field of Epileptology. Earlier, EEG was used for visual inspection of brain activity only, but with technological advancement now various characteristics of the brain oscillations can be investigated.

Presently many functional brain imaging techniques have been developed in order to identify the seizure onset zone as well as the neuronal networks. These techniques mainly involve Positron Emission Tomography (PET), Single Photon Emission Computer Tomography (SPECT) and functional Magnetic Resonance Imaging (fMRI) with or without simultaneous EEG recordings. Unfortunately because of low temporal resolution and limited sample sizes it becomes difficult to use these techniques to demonstrate the temporal follow up between structures involved with absence seizures. But higher temporal resolution EEG allows a better option for analysis. However, because of the uncertainty underlying the static electromagnetic inverse problem, it is a problem to localize the area from where the electrical activity originates. This brings about a challenge to perform deep brain source imaging. Nonetheless recent developments regarding EEG inverse solutions have significantly improved source localization, making it easier to trace the source of the neuronal activity using surface EEG recordings.

The measure of source analysis depicts analyzing the neuronal data at a deeper level, as in some form of intracranial activity, and to study the origin of the observed neuronal activity. Source analysis specifies moving from sensor space to source space, compensating for the spatial resolution problem consisting within EEG. Various state of the art source localization methods have been established over the years [80]. The methods to solve the inverse problem have been categorized in two groups: parametric and nonparametric methods. Some of the state-of-the-art nonparametric methods are: Low resolution brain electromagnetic tomography (LORETA), standardized low resolution brain electromagnetic tomography (sLORETA), exact low resolution brain electromagnetic tomography (eLORETA), Variable Resolution Electromagnetic Tomography (VARETA), S-MAP, ST-MAP, local autoregressive average (LAURA), and adaptive standardized LORETA/FOCUSS (ALF) etc. Among the modern parametric methods are: Multiple signal classification (MUSIC), and FINES.

In this study the eLORETA method was used for source localization, since it is one of the most robust techniques for EEG source localization.

For source localization two major steps are required. This involves 1) computing the forward model, and 2) computing the inverse model. Forward modeling deals with the estimation of the potential for a source that is known, and also for a known head model. While the inverse problem deals with estimating sources that are unknown from the measured EEG. This has further been described in detail in chapter 3.

## **2.4 Connectivity Analysis**

To better understand the brain regions correlated with each other, during ictal and non-ictal GSWDs, functional connectivity (FC) was determined. FC identifies correlated brain regions based on similar signal content. It does not identify the direction of information flow. FC was determined at sensor and source level for this study, and the imaginary part of coherency (iCOH) was used as a method. As mentioned earlier, with EEG the problem of volume conduction arises, which further cause's misinterpretation of brain interactions. When using EEG channels there is a tendency of multiple channels picking up activity of a particular source in the brain leading to the volume conduction problem. A method proposed by Nolte et al. (2004) [26], used iCOH to interpret brain interactions. They described using the iCOH as a superior method to overcome the volume conduction effect since the iCOH is not affected by it, and is not generated as an artifact of volume conduction. The assumption that is used is that, any potential observed at the scalp has no time lag, to the underlying source activity. However, the iCOH is only responsive to synchronizations of events that are time lagged to each other. If volume conduction does not create any time lag then, the iCOH becomes unaffected to any kind of artifactual self-interaction.

To better understand iCOH, the equation of coherency is necessary. At a given frequency, coherency between two EEG channels is the linear relationship between the two. The



coherency can be estimated using the cross spectral density function. If  $X_{kj}$  and  $X_{k'j}$  are the complex Fourier transforms of channels  $k$  and  $k'$  respectively, then the cross-spectrum can be given as:

$$S_{kk'j} = X_{kj} \cdot X_{k'j}^* \quad (2.5)$$

Where,  $*$  is the complex conjugation

The cross spectral density of signal  $k$  and  $k'$  are estimated using individual auto-spectral density functions. Further, using the cross-spectral density equation the coherency can be defined as:

$$C_{kk'j} = \frac{S_{kk'j}}{(S_{kk} \cdot S_{k'k'})^{1/2}}, \quad (2.6)$$

while the coherence is defined as the magnitude of coherency:

$$Coh_{kk'j} = |C_{kk'j}| \quad (2.7)$$

Coherence and coherency are bivariate measures that simultaneously analyse only two signals. Apart from the magnitude and phase of coherency, the real and imaginary part of coherency can also be investigated:

$$C_{kk'} = \Re C_{kk'} + \Im C_{kk'} \quad (2.8)$$

Here,  $\Re$  denotes the real-part of coherency while,  $\Im$  depicts the imaginary-part of coherency. From the complex coherence equation iCOH can be directly obtained.

Studying the brain connectivity using iCOH is useful since it is inconsistent with non-interacting sources and it reveals a dynamical interaction. In other words, this method aims of eliminating any irrelevant source coherence caused by instantaneous activity, and has a capability to capture true source interactions at a given time lag.

The iCOH has been used as a measure for connectivity in various fields to better understand the brain interactions. Sander et al. (2010) [81], studied the interactions between muscle control and cortical, subcortical regions in patients with movement disorders alongside healthy subjects. They used coherence and iCOH as a combination to study the MEG and electromyographic (EMG) data. The iCOH was used on a control dataset where interactions were known to verify the robustness of iCOH. Then the combination of coherence and iCOH was used to identify cortico-muscular and cortico-thalamic coupling. Dominguez et al. (2013) [82], used iCOH as a measure in preschool children with autism to assess cortical functional connectivity. Their study also presents evidence that iCOH is a good measure that provides features that could be used in making a classifier for autism, which can be used as a biomarker. In another study done by Elshahabi et al. (2015) [83], on patients with idiopathic/genetic generalized epilepsy using MEG data, functional network connectivity was

analysed. The connectivity networks were constructed using coherence and only the iCOH was used to represent the couplings in the brain regions. Since Nolte et al. described this method in 2004 [26], it has been widely used to study brain interactions.

In chapter 8 connectivity analysis has been done at sensor and source level to better understand the functional connectivity between ictal and non-ictal GSWDs.

# Chapter 3

## Forward and Inverse problem for EEG

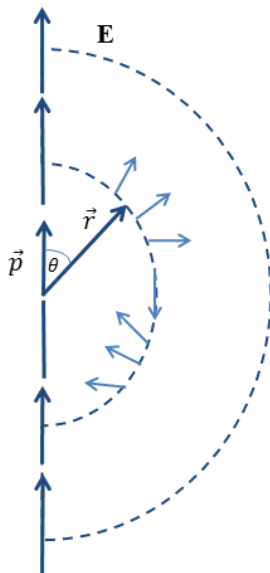
---

In this chapter we give the mathematical modelling for source analysis and describe the algorithms used in exact low resolution electromagnetic tomography (eLORETA). We aim for a mathematical concise formulation, which unfortunately in some state-of-the-art literature (e.g. Pascual-Marqui (1999, 2007,2011)) [16, 17, 27] is given only in a rudimentary way or is even wrong. We will give proofs if possible and clearly state when experimental algorithms without a performance or correctness proofs are used in practice.

We start with the presentation of the forward problem for EEG based on the work of Wolters, Grasedyck, Hackbusch (2004) [84] and Wolters, Köstler, Möller, Härdtlein, Grasedyck and Hackbusch (2007) [85].

Our ultimate goal is to reconstruct current sources in the human brain on the basis of EEG measurements at the scalp. Currents caused in the brain are results of the movement of ions within activated regions of the cortex sheet and such currents are called primary currents. The primary current in the brain is modelled as a current dipole [86, 87].

Here is a geometric illustration of an electric dipole.



$$\mathbf{E} = -\text{grad } u = \frac{3\vec{e}_r(\vec{p} \cdot \vec{e}_r) - \vec{p}}{r^3}$$

$$u = \frac{\vec{p} \cdot \vec{e}_r}{r^2} = \frac{p \cos \theta}{r^2}$$

**Figure 3.1 Geometric illustration of an electric dipole.** dipole  $\vec{p}$ , electric field  $\mathbf{E}$ , potential  $u$ ,  $\vec{e}_r$  unit vector in  $\vec{r}$  direction.

The current dipole causes an Ohmic return current which flows through the brain. The EEG measures the potential difference from the return currents.

The reconstruction of the dipole sources in the brain is called the **inverse problem** of EEG. For this purpose the computation of the field potential in the head induced by dipoles is necessary. This is the **forward problem**. The forward problem is derived from the Maxwell equations. We first briefly state the Maxwell equations in this context.

### 3.1 The Maxwell equations

For the convenience of readers with less mathematical background we introduce the differential operators *div*, *curl* and *grad*.

Since we are working in  $\mathbb{R}^3$ , let  $D \subseteq \mathbb{R}^3$  be the domain of a function  $f$ ,

$f: D \rightarrow \mathbb{R}$ , and we assume that the partial derivatives of  $f$  exists. Let  $x = (x_1, x_2, x_3) \in \mathbb{R}^3$

The gradient of  $f$  is the vector

$$\text{grad } f(x) := \nabla f(x) := \left( \frac{\partial f(x)}{\partial x_1}, \frac{\partial f(x)}{\partial x_2}, \frac{\partial f(x)}{\partial x_3} \right) \quad (3.1)$$

$\nabla$  is the Nabla-operator and  $\nabla$  is just another notion of the gradient.

Let  $g: \mathbb{R}^3 \rightarrow \mathbb{R}^3$  be a vector field with  $g = (g_1, g_2, g_3)$ , where  $g_i = \mathbb{R}^3 \rightarrow \mathbb{R}$  are partially differentiable functions,  $i=1, 2, 3$ .

The divergence *div* of  $g$  is the vector field,

$$\text{div } g(x) := \frac{\partial g_1(x)}{\partial x_1} + \frac{\partial g_2(x)}{\partial x_2} + \frac{\partial g_3(x)}{\partial x_3}, \quad x \in \mathbb{R}^3. \quad (3.2)$$

Let  $h: \mathbb{R}^3 \rightarrow \mathbb{R}^3$  be a vector field with  $h = (h_1, h_2, h_3)$  and partially differentiable functions

$h_i: \mathbb{R}^3 \rightarrow \mathbb{R}$ ,  $i=1, 2, 3$ . For  $x \in \mathbb{R}^3$  the curl operator is defined by

$$\text{curl } h(x) := \left( \frac{\partial h_3(x)}{\partial x_2} - \frac{\partial h_2(x)}{\partial x_3}, \frac{\partial h_1(x)}{\partial x_3} - \frac{\partial h_3(x)}{\partial x_1}, \frac{\partial h_2(x)}{\partial x_1} - \frac{\partial h_1(x)}{\partial x_2} \right), \quad (3.3)$$

so  $\text{curl } h(x)$  is a vector field in  $\mathbb{R}^3$ .

Finally, for a function  $k: \mathbb{R}^3 \rightarrow \mathbb{R}$ , the Laplace operator  $\Delta$  of  $k$  is defined by

$$\Delta f(x) = \frac{\partial^2 f(x)}{\partial x_1^2} + \frac{\partial^2 f(x)}{\partial x_2^2} + \frac{\partial^2 f(x)}{\partial x_3^2},$$

where  $x \in \mathbb{R}^3$  and  $f$  is supposed to be 2-times partially differentiable.

A suggestive way to understand div and curl is the notion of vector analysis. For  $x, y \in \mathbb{R}^3$ , the standard inner product is

$$\langle x, y \rangle := x \cdot y := x_1 y_1 + x_2 y_2 + x_3 y_3, \quad (3.4)$$

where  $x = (x_1, x_2, x_3)$  and  $y = (y_1, y_2, y_3)$ .

We will use both forms  $\cdot$  and  $\langle \cdot, \cdot \rangle$  of the inner product notation.

We may write

$$\nabla = \left( \frac{\partial}{\partial x_1}, \frac{\partial}{\partial x_2}, \frac{\partial}{\partial x_3} \right) \quad (3.5)$$

So, “abusing” the inner product notation (3.4), for the above mentioned function  $g = \mathbb{R}^3 \rightarrow \mathbb{R}^3$  we get

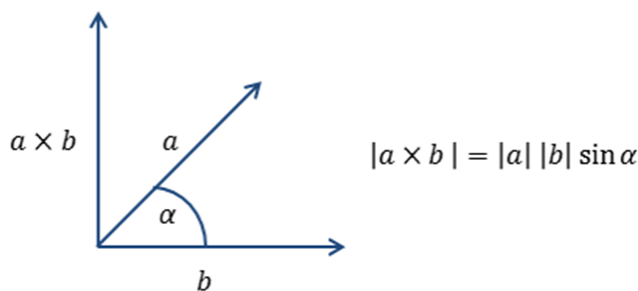
$$\operatorname{div} g = \nabla \cdot g = \frac{\partial g_1}{\partial x_1} + \frac{\partial g_2}{\partial x_2} + \frac{\partial g_3}{\partial x_3} \quad (3.6)$$

Further, for two vectors  $a, b \in \mathbb{R}^3$ ,  $a = (a_1, a_2, a_3)$ ,  $b = (b_1, b_2, b_3)$ , the cross product is defined as

$$a \times b := (a_2 b_3 - a_3 b_2, a_3 b_1 - a_1 b_3, a_1 b_2 - a_2 b_1) \quad (3.7)$$

so

$$a \times b \in \mathbb{R}^3$$



With (3.5) and (3.7) we can write curl in compact form as

$$\operatorname{curl} h = \nabla \times h \quad (3.8)$$

With the notion of grad and curl in vector analysis, it is straightforward to verify

$$\operatorname{curl} \operatorname{grad} = \nabla \times \nabla = 0 \quad (3.9)$$

We are now ready to state the Maxwell equations for the human brain under the global assumption that the sources of electric activity in the brain are electric dipoles.

Let  $\mathbf{E}$  be the electric field in the brain,  $\mathbf{D}$  the electric displacement,  $\rho$  the electric free charge density,  $\varepsilon$  the electric permeability and  $\mathbf{j}$  the electric current density. Let  $\mu$  be the magnetic permeability,  $\mathbf{H}$  the magnetic field and  $\mathbf{B}$  the magnetic induction. We assume that  $\mu$  is constant over the brain volume and equal to the permeability of vacuum. The essential modelling step for the brain is the assumption that the brain tissue behaves as an electrolyte.

This gives the (brain) material couplings

$$\mathbf{D} = \varepsilon \mathbf{E} \text{ and } \mathbf{B} = \mu \mathbf{H} \quad (3.10)$$

The Maxwell equations are

$$\operatorname{div} \mathbf{D} = \rho \quad (3.11)$$

$$\operatorname{curl} \mathbf{E} = 0 \quad (3.12)$$

$$\operatorname{curl} \mathbf{B} = \mu \mathbf{j} \quad (3.13)$$

$$\operatorname{div} \mathbf{B} = 0 \quad (3.14)$$

Since we assume that the electric field is caused by a dipole, it is induced by a scalar potential  $u : \mathbb{R}^3 \rightarrow \mathbb{R}$ , and we have

$$\mathbf{E} = -\operatorname{grad} u \quad (3.15)$$

## 3.2 The forward problem

As said, the current has two components, the primary current, say  $\mathbf{j}^p$  and the return currents  $\mathbf{j}^r$ . The return currents are dependent in a non-linear way on the conductivity  $\sigma$  of the material, which is a  $3 \times 3$  tensor and the electric field  $\mathbf{E}$ , coupled by

$$\mathbf{j}^r = \sigma \mathbf{E} \quad (\in \mathbb{R}^3) \quad (3.16)$$

(in our context  $\sigma$  is just a  $3 \times 3$  matrix).

$\mathbf{j}^p$  is the current caused by movements of ions in the activated region of the brain.

By Plonsy and Heppner (1967) [88],  $\mathbf{j}$  decomposes as a sum

$$\mathbf{j} = \mathbf{j}^p + \sigma \mathbf{E} \quad (3.17)$$

We seek an equation coupling  $\mathbf{j}$  and the potential  $u$ . Let us assume that  $\Omega \subseteq \mathbb{R}^3$  is the head domain.

**Proposition 3.1:**  $-\operatorname{div}(\sigma \operatorname{grad} u) = -\operatorname{div}(\mathbf{j}^p)$  in  $\Omega$  (3.18)

**Proof:** Since  $\operatorname{div} \operatorname{curl} = 0$  (by straightforward calculation or taking this as a well-known fact from vector analysis), we have

$$\begin{aligned}
 0 &= \operatorname{div} \operatorname{curl}(\mathbf{B}) \\
 &= \operatorname{div}(\mu \mathbf{j}) && \text{by (3.13)} \\
 &= \operatorname{div}(\mu \mathbf{j}^p + \mu \sigma \mathbf{E}) && \text{by (3.17)} \\
 &= \mu (\operatorname{div}(\mathbf{j}^p) + \operatorname{div}(\sigma \mathbf{E})) && \text{(div is linear)} \\
 &= \mu (\operatorname{div}(\mathbf{j}^p) - \operatorname{div}(\sigma \operatorname{grad} u)) && \text{by (3.15)}
 \end{aligned}$$

Hence, since  $\mu \neq 0$ ,

$$-\operatorname{div}(\sigma \operatorname{grad} u) = -\operatorname{div}(\mathbf{j}^p) \quad \text{in } \Omega. \quad \blacksquare$$

The boundary conditions are:

- a) we have a reference electrode with a given potential

$$u_{ref} = 0 \quad (3.19)$$

and

- b) the homogeneous von Neumann condition

$$\sigma \operatorname{grad} u \cdot \mathbf{n} = 0 \text{ on the domain boundary } \Gamma = \partial\Omega, \quad (3.20)$$

holds, where  $\mathbf{n}$  is the unit surface normal vector.

Summarising, the boundary problem is

$  \begin{aligned}  -\operatorname{div}(\sigma \operatorname{grad} u) &= -\operatorname{div}(\mathbf{j}^p) \quad \text{in } \Omega \\  \sigma \operatorname{grad} u \cdot \mathbf{n} &= 0 \quad \text{on } \Gamma = \partial\Omega \\  u_{ref} &= 0  \end{aligned}  $	(3.21)
---	--------

**Definition 3.2:** The forward problem of EEG is given by (3.21), where the primary current  $\mathbf{j}^p$  and the conductivity matrix  $\sigma$  is known, and we are looking for the unknown potential  $u$ .

If  $\sigma$  is the identity matrix,  $\sigma = \begin{pmatrix} 1 & 0 & 0 \\ 0 & 1 & 0 \\ 0 & 0 & 1 \end{pmatrix}$ , and using the fact  $\text{div grad} = \Delta$ , (3.21) becomes

the Poisson problem

$$\begin{aligned} \Delta u &= -\text{div}(\mathbf{j}^p) && \text{in } \Omega \\ \text{grad } u \cdot \mathbf{n} &= 0 && \text{on } \Gamma = \partial\Omega \\ u_{ref} &= 0 \end{aligned} \tag{3.22}$$

Such a modelling is used by Gulrajani (1998) [89].

### 3.3 The discrete form of the forward problem

The forward problem (3.21) is solved in literature in a numerical way [84]. We link the forward problem (3.21) with the geometry of the EEG data measured. Let  $N$  be the number of electrodes at the scalp, and let  $n$  be the number of voxel positions with the primary source. In our applications  $N = 31$  and  $n = 5003$ .

Let  $V$  be a  $M$ -dimensional vector space,  $M$  an integer, with standard finite element basis  $\psi_1, \dots, \psi_M$ .

Finite element (FE) techniques applied to (3.21) with basis  $\psi_1, \dots, \psi_M$  lead to a system of linear equations.

$$\mathbf{G}u = \mathbf{j} \tag{3.22}$$

where  $u \in \mathbb{R}^M$  is the unknown potential vector,  $\mathbf{j} \in \mathbb{R}^M$  is the current density vector, and most importantly,  $\mathbf{G} \in \mathbb{R}^{M \times M}$  is the stiffness or geometry matrix, where

$$\mathbf{G}_{ij} = \int_{\Omega} \nabla \psi_j(\mathbf{y}) \cdot \sigma(\mathbf{y}) \nabla \psi_i(\mathbf{y}) d\mathbf{y} \tag{3.23}$$

for all  $1 \leq i, j \leq M$ .

By the ellipticity of the bilinear form in the integral (3.23),  $\mathbf{G}$  is symmetric and positive definite (Wolters et al. 2004) [84], so  $\mathbf{G}^{-1}$  exists.

Equation (3.22) gives

$$u = \mathbf{G}^{-1}\mathbf{j} \tag{3.24}$$

Different algorithms, boundary element method (BEM) or FE have been used to solve (3.22).



The problem is the efficient computation of the inverse  $\mathbf{G}^{-1}$  of  $\mathbf{G}$ , which is a notorious hard problem in numerical linear algebra.

Wolters et al. (2004) [84] gave, to the best of our knowledge the most efficient algorithms for solving (3.22) and the inverse problem. We will come to this point in the next sections.

Since the EEG setup we are using is associated best with the different LORETA solvers [18], we will describe the underlying approach being aware that it might not be computationally the fastest. Our purpose to distinguish between ictal and non-ictal events, both at sensor as well as source level, and to draw medical relevant consequences, the eLORETA algorithm is sufficient. Of course, in further work the algorithms of Wolters et. al.(2004) [84] should be involved and studied in practical applications, too.

Let us proceed to the definition and calculation of the lead field matrix.

### 3.4 Lead field matrix and corresponding forward problem

Let  $N$  be the number of EEG electrodes with one of them as the reference electrode. Let  $\nu$  be the number of sources, each modelled as a dipole in  $\mathbb{R}^3$ . This is understood as three orthogonal unit dipoles of a specific source. Since each of these dipoles at a specific source influences the electric field and the potential, we consider all of them and say that  $n=3\nu$  voxels are influencing the electric field.

In Wolters et al. (2004) [84] it is shown that a matrix  $\mathbf{R} \in \mathbb{R}^{N \times M}$ , the so called restriction matrix, can be computed so that

$$\mathbf{R}u = \Phi, \tag{3.25}$$

where  $u$  is the potential and  $\Phi$  is the potential vector with components of  $u$  at the  $N$  electrodes.  $\Phi$  is the so called scalp potential. Since,  $u_{ref} = 0$  in (3.21), we demand the property that the index  $i \in 1, \dots, N$  representing the reference electrode fulfils  $(\mathbf{R}u)_i = 0$ .

The lead field basis  $\mathbf{B}_{eeg}$  is according to Wolters et al. (2004) [84] defined as the product of  $\mathbf{R}$  and the inverse of the geometry matrix  $\mathbf{G}$ , so

$$\mathbf{B}_{eeg} := \mathbf{R}\mathbf{G}^{-1} \in \mathbb{R}^{N \times M} \tag{3.26}$$

Using  $\mathbf{B}_{eeg}$  and the solution of the forward problem  $u$ , Wolters et. al (2004) [84] compute a matrix  $\mathbf{T} \in \mathbb{R}^{M \times n}$  and a vector  $\mathbf{j} \in \mathbb{R}^n$  such that

$$\mathbf{T}\mathbf{j} = u \tag{3.27}$$

The matrix

$$\mathbf{K} := \mathbf{B}_{\text{eeg}} \mathbf{T} \in \mathbb{R}^{N \times n} \quad (3.28)$$

is the lead field matrix for the EEG problem.

$\mathbf{K}$  satisfies the equation

$$\mathbf{KJ} = \Phi \quad (3.29)$$

which is often referenced as the forward problem (Pascual-Marqui 1999) [27].

The equation (3.29) holds, because

$$\begin{aligned} \mathbf{KJ} &\stackrel{(3.28)}{=} \mathbf{B}_{\text{eeg}} \mathbf{TJ} \stackrel{(3.27)}{=} \mathbf{B}_{\text{eeg}} \mathbf{j} \stackrel{(3.26)}{=} \mathbf{R} \mathbf{G}^{-1} \mathbf{j} \\ &\stackrel{(3.24)}{=} \mathbf{R} \mathbf{u} \stackrel{(3.25)}{=} \Phi \end{aligned}$$

With the solution of the forward problem the lead field matrix  $\mathbf{K}$  is computed. On this basis we will later consider the inverse problem.

### 3.5 Noise by the reference electrode

Noise at the reference electrode induces noise at the non-reference electrodes. According to Yao et al. (2019) [90], the potential  $\Phi$  is disturbed by a noise vector  $\varepsilon \in \mathbb{R}^N$ , so we have

$$\Phi + \varepsilon \text{ instead of } \Phi. \quad (3.30)$$

In Yao et.al (2019) a method for noise correction is explained with a non-stochastic matrix, the so called centering matrix. Its effect is in averaging out the noise and in this way to calibrate a noise-free forward problem.

The solution of the forward problem under noise is called the **reference electrode problem**. In the special case  $\varepsilon = c\mathbf{1}$ ,  $c > 0$  a constant and  $\mathbf{1} \in \mathbb{R}^N$  the constant 1 vector, the centring matrix has a simple form and a noise-free reformation of the forward problem can be achieved.

According to (3.29) and (3.30) the forward problem with noise is

$$\Phi = \mathbf{KJ} + c\mathbf{1} \quad (3.31)$$

Let,  $\mathbf{H} := \mathbf{I} - \frac{\mathbf{1}\mathbf{1}^T}{\mathbf{1}^T\mathbf{1}}$ .  $\mathbf{H}$  is the average reference operator, better known in statistics as the centering matrix.

We give a proof that the forward solution is independent of the reference electrode.

**Proposition 3.3:** Let  $\mathbf{I} \in \mathbb{R}^{N \times N}$  be the identity matrix and  $\mathbf{H} = \mathbf{I} - \frac{\mathbf{1}\mathbf{1}^T}{\mathbf{1}^T\mathbf{1}}$ , as above. Then

- (i)  $\mathbf{H}\mathbf{1} = 0$
- (ii)  $\mathbf{H}\Phi = \mathbf{H}\mathbf{K}\mathbf{J}$

**Proof:** (i) By definition of  $\mathbf{H}$ ,

$$\mathbf{H} = \begin{pmatrix} 1 - \frac{1}{N} & & * \\ & \ddots & \\ * & & 1 - \frac{1}{N} \end{pmatrix},$$

where all non-diagonal entries are  $-\frac{1}{N}$ . Hence

$$\mathbf{H}\mathbf{1} = \begin{pmatrix} 1 - \frac{1}{N} - \frac{N-1}{N} \\ \vdots \\ 1 - \frac{1}{N} - \frac{N-1}{N} \end{pmatrix} = 0$$

(ii) The identity in (i) leads immediately to (ii), when we let  $\mathbf{H}$  act on equation (3.31). ■

This justifies the assumption that if the lead field as well as the EEG measurements is average reference transformed, by (ii) the additive constant  $c$  vanishes.

Thus, by setting

$$\Phi = (\mathbf{H}\Phi) \tag{3.32}$$

and

$$\mathbf{K} = (\mathbf{H}\mathbf{K}) \tag{3.33}$$

the reference independent forward equation (2.4) can be rewritten as

$$\Phi = \mathbf{K}\mathbf{J} \tag{3.34}$$

This equation is later used to compute the unknown current density  $\mathbf{J}$ , and since (3.34) holds for any  $c$ , and  $\mathbf{J}$  is independent of  $c$ , (3.34) indeed leads to the correct  $\mathbf{J}$ .

### 3.6 The Moore-Penrose Pseudoinverse

If we consider the forward problem w.r.t the  $N$  electrodes and  $n$  voxels, (3.29) has the form

$$\mathbf{K}\mathbf{J} = \Phi,$$

with  $\mathbf{K} \in \mathbb{R}^{N \times n}$  the lead field matrix,  $\mathbf{J} \in \mathbb{R}^n$  the current density vector at the  $n$  voxels and  $\Phi \in \mathbb{R}^N$  the electrode potential. Algorithms implemented in the eLORETA software (Pascual-Marqui, (2007, 2011)) [16, 17] seek for a solution of the inverse problem in this particular form. Since  $\mathbf{K}$  is neither symmetric, nor non-singular in general, the Moore-Penrose pseudoinverse matrix involving products of  $\mathbf{K}$  is used. Thus, we give a brief introduction to such pseudoinverses and prove properties needed later. We start with basics in linear algebra.

Let  $\mathbf{A} \in \mathbb{R}^{m \times n}$  be a matrix  $= (a_{ij})_{\substack{1 \leq i \leq m \\ 1 \leq j \leq n}}$ .

Its transpose  $\mathbf{A}^T$  is the matrix  $\mathbf{A}^T = (a_{ji})_{\substack{1 \leq j \leq n \\ 1 \leq i \leq m}}$ .

Thus the rows of  $\mathbf{A}$  are the columns of  $\mathbf{A}^T$ .

$\mathbf{A} \in \mathbb{R}^{n \times n}$  is called symmetric, if  $\mathbf{A}^T = \mathbf{A}$ .

Let  $\langle \cdot, \cdot \rangle$  be the standard inner product in  $\mathbb{R}^n$ . Note that for any matrix  $\mathbf{A} \in \mathbb{R}^{n \times n}$  for all  $x, y \in \mathbb{R}^n$  it holds that  $\langle \mathbf{A}x, y \rangle = \langle x, \mathbf{A}^T y \rangle$ . (3.35)

A symmetric matrix is called positive definite resp. positive semidefinite, if

$$\langle x, \mathbf{A}x \rangle > 0 \text{ for all } x \in \mathbb{R}^n \setminus \{0\},$$

$$\text{resp. } \langle x, \mathbf{A}x \rangle \geq 0 \text{ for all } x \in \mathbb{R}^n,$$

A positive definite matrix is non-singular, while a positive semidefinite matrix is not necessarily. All eigenvalues of a positive definite matrix respectively positive semidefinite matrix are positive resp. non-negative and the converse is true, too.

For a positive semidefinite matrix  $\mathbf{A}$ , the spectral theorem shows the existence of a square root  $\mathbf{A}^{1/2}$  of  $\mathbf{A}$  in the following way. A matrix  $\mathbf{B} \in \mathbb{R}^{n \times n}$  is said to be orthogonal, if

$$\mathbf{B}\mathbf{B}^T = \mathbf{B}^T\mathbf{B} = \mathbf{I}, \tag{3.36}$$

$\mathbf{I} \in \mathbb{R}^{n \times n}$  the identity matrix. For a positive semidefinite matrix  $\mathbf{A}$  its  $n$  orthogonal eigenvectors  $v_1, \dots, v_n$  form the orthogonal matrix  $\mathbf{Q} = (v_1, \dots, v_n) \in \mathbb{R}^{n \times n}$  and with the  $n$  eigenvalues  $\lambda_1, \dots, \lambda_n$  of  $\mathbf{A}$  the diagonal matrix  $\mathbf{D}$  is defined as

$$\mathbf{D} = \begin{pmatrix} \lambda_1 & & 0 \\ & \ddots & \\ 0 & & \lambda_n \end{pmatrix}.$$

This allows the decomposition

$$\mathbf{A} = \mathbf{Q}\mathbf{D}\mathbf{Q}^T \quad (3.37)$$

The square root  $\mathbf{A}^{1/2}$  of  $\mathbf{A}$  then is

$$\mathbf{A}^{1/2} = \mathbf{Q}\mathbf{D}^{1/2}\mathbf{Q}^T \quad (3.38)$$

where

$$\mathbf{D}^{1/2} = \begin{pmatrix} \sqrt{\lambda_1} & & 0 \\ & \ddots & \\ 0 & & \sqrt{\lambda_n} \end{pmatrix}.$$

since  $\mathbf{Q}\mathbf{Q}^T = \mathbf{Q}^T\mathbf{Q} = \mathbf{I}$ , (3.37) implies

$$\mathbf{A}^{1/2}\mathbf{A}^{1/2} = \mathbf{Q}\mathbf{D}^{1/2}\mathbf{Q}^T\mathbf{Q}\mathbf{D}^{1/2}\mathbf{Q}^T = \mathbf{Q}\mathbf{D}^{1/2}\mathbf{D}^{1/2}\mathbf{Q}^T = \mathbf{Q}\mathbf{D}\mathbf{Q}^T = \mathbf{A}, \text{ so}$$

$$\mathbf{A} = \mathbf{A}^{1/2}\mathbf{A}^{1/2}, \quad (3.39)$$

which is also viewed as a defining property of the square root of  $\mathbf{A}$ .

One can check the positive (semi-) definiteness of a matrix by calculating its eigenvalues. But there is a much simpler criterion, which takes recourse only to the entries of the matrix.

**Lemma 3.4:** Let  $\mathbf{A} \in \mathbb{R}^{n \times n}$ ,  $\mathbf{A} = (a_{ij})_{1 \leq i, j \leq n}$  be a symmetric matrix.  $\mathbf{A}$  is positive (semi)definite, if  $\mathbf{A}$  is (weak) diagonal dominant, that is

$$\sum_{\substack{i=1, \\ i \neq j}}^n |a_{ij}| \leq a_{jj} \text{ for all } j \in 1, \dots, n.$$

Further, we have some simple properties of sums and products of positive (semi-) definite vertices.

**Proposition 3.5:** Let  $\mathbf{A}, \mathbf{B} \in \mathbb{R}^{n \times n}$  symmetric matrices.

- (i) Let  $\mathbf{A}$  and  $\mathbf{B}$  be positive semidefinite. Then the sum  $\mathbf{A} + \mathbf{B}$  is positive semidefinite and if at least one of  $\mathbf{A}$  and  $\mathbf{B}$  is positive definite the sum is also positive semidefinite.
- (ii)  $\mathbf{AB}$  is symmetric, if and only if  $\mathbf{A}$  and  $\mathbf{B}$  commutes i.e.  $\mathbf{AB} = \mathbf{BA}$ .

**Proof:** (i) Let  $x \in \mathbb{R}^n \setminus \{0\}$ . Then

$$\langle x, (\mathbf{A} + \mathbf{B})x \rangle = \underbrace{\langle x, \mathbf{A}x \rangle}_{\substack{\geq 0 \\ \text{resp } > 0}} + \underbrace{\langle x, \mathbf{B}x \rangle}_{\substack{\geq 0 \\ > 0}},$$

And all statements follow from this decomposition by case distinctions.

(ii)  $(\mathbf{AB})^T = \mathbf{B}^T \mathbf{A}^T = \mathbf{BA}$ , so

$(\mathbf{AB})^T = \mathbf{AB}$  if and only if  $\mathbf{AB} = \mathbf{BA}$ .

■

We are ready to define the Moore-Penrose pseudoinverse, briefly called MP inverse, see (Magnus and Neudecker (1988), chapter 3, section 5) [91].

**Definition 3.6** (Moore-Penrose inverse) Let  $\mathbf{A} \in \mathbb{R}^{m \times n}$ . A matrix  $\mathbf{X} \in \mathbb{R}^{n \times m}$  is the Moore-Penrose inverse of  $\mathbf{A}$ , if

$$\mathbf{AXA} = \mathbf{A} \tag{3.40}$$

$$\mathbf{XAX} = \mathbf{X} \tag{3.41}$$

$$(\mathbf{AX})^T = \mathbf{AX} \tag{3.42}$$

$$(\mathbf{XA})^T = \mathbf{XA} \tag{3.43}$$

$\mathbf{X}$  is denoted by  $\mathbf{A}^+$ .

**Theorem 3.7** (Magnus and Neudecker (1988),chapter 2, section 5, Theorem 4 and 5) [91].

- (i) For each  $\mathbf{A}$ ,  $\mathbf{A}^+$  exists and is unique.
- (ii) If  $\mathbf{A} \in \mathbb{R}^{m \times n}$  has rank  $r$ , there are semi-orthogonal matrices  $\mathbf{S}$ ,  $\mathbf{T}$  and a positive definite matrix  $\mathbf{C} \in \mathbb{R}^{r \times r}$ , such that  $\mathbf{A}^+ = \mathbf{TC}^{-1/2}\mathbf{S}^T$  and  $\mathbf{A} = \mathbf{SC}^{-1/2}\mathbf{T}^T$  (3.44)
- (iii) If  $\mathbf{A}$  is non-singular, then  $\mathbf{A}^+ = \mathbf{A}^{-1}$
- (iv)  $(\mathbf{A}^+)^+ = \mathbf{A}$  (3.45)
- (v)  $(\mathbf{A}^+)^T = (\mathbf{A}^T)^+$  (3.46)
- (vi)  $\mathbf{A}^T \mathbf{A} \mathbf{A}^+ = \mathbf{A}^T = \mathbf{A}^+ \mathbf{A} \mathbf{A}^T$  (3.47)
- (vii)  $\mathbf{A}^T \mathbf{A}^+ \mathbf{A}^T \mathbf{A}^+ = \mathbf{A}^+ = \mathbf{A}^+ \mathbf{A}^+ \mathbf{A}^T \mathbf{A}^T$  (3.48)
- (viii)  $(\mathbf{A}^+ \mathbf{A})^+ = \mathbf{A}^+ \mathbf{A}^{+T}, (\mathbf{A} \mathbf{A}^T)^+ = \mathbf{A}^{+T} \mathbf{A}^+$  (3.49)

We will use the following facts. Statement (iii) in Proposition 3.8 is new, while the others are easily delivered from Theorem 3.7.

**Proposition 3.8** Let  $\mathbf{A} \in \mathbb{R}^{n \times n}$  be a symmetric matrix. Then

- (i)  $\mathbf{A}^+$  is symmetric.
- (ii) If  $\mathbf{A}$  is positive semidefinite, then  $\mathbf{A}^+$  is also positive semidefinite.
- (iii) If  $\mathbf{A}^+x = 0$ , then  $\mathbf{A}x = 0$ , so  $\text{Ker } \mathbf{A}^+ \subseteq \text{Ker } \mathbf{A}$ .

**Proof:**

(i)  $(\mathbf{A}^+)^T = (\mathbf{A}^T)^+ = \mathbf{A}^+$ .

(ii) Let  $x \in \mathbb{R}^n$ . Then

$$\begin{aligned} \langle x, \mathbf{A}^+x \rangle &\stackrel{(3.41)}{=} \langle x, \mathbf{A}^+ \mathbf{A} \mathbf{A}^+x \rangle = \langle (\mathbf{A}^+)^T x, \mathbf{A} \mathbf{A}^+x \rangle \\ &= \langle \mathbf{A}^+x, \mathbf{A} \mathbf{A}^+x \rangle && \text{by (i) } \mathbf{A}^+ \text{ is symmetric.} \\ &= \langle y, \mathbf{A}y \rangle && \text{with } y := \mathbf{A}^+x \\ &\geq 0 && \text{because } \mathbf{A} \text{ is positive semidefinite.} \end{aligned}$$

(iii) Let  $x \in \mathbb{R}^n$  such that  $\mathbf{A}^+x = 0$ , so  $x \in \text{Ker } \mathbf{A}^+$ .

Then, by (3.44)  $\mathbf{A}^+ = \mathbf{T} \mathbf{C}^{-1/2} \mathbf{S}^T$   
 so  $\mathbf{T}^T \mathbf{A}^+ = \mathbf{T}^T \mathbf{T} \mathbf{C}^{-1/2} \mathbf{S}^T = \mathbf{C}^{-1/2} \mathbf{S}^T$ ,  
 hence  
 $0 = \mathbf{A}^+x = \mathbf{T}^T \mathbf{A}^+x = \mathbf{C}^{-1/2} \mathbf{S}^T x$ ,  
 and by multiplying with  $\mathbf{C}^{1/2}$  we get  $\mathbf{S}^T x = 0$ .  
 Again with (3.44)

$$\mathbf{A}^T x = \left( \mathbf{S} \mathbf{C}^{-\frac{1}{2}} \mathbf{T}^T \right)^T x = \mathbf{T} \mathbf{C}^{-\frac{1}{2}} \mathbf{S}^T x = 0$$

But  $\mathbf{A}$  is symmetric, so  $\mathbf{A}x = \mathbf{A}^T x = 0$ , hence  $x \in \text{Ker } \mathbf{A}$ . ■

An important fact used later for matrices appearing in the discrete inverse problem for EEG is positive definiteness of the MP inverse:

**Theorem 3.9** Let  $\mathbf{A} \in \mathbb{R}^{n \times n}$  be a positive definite matrix. Then  $\mathbf{A}^+$  is positive definite.

**Proof:** A short proof using eigenvalues is the following.  $\mathbf{A}^{-1}$  is positive definite, because the eigenvalues of  $\mathbf{A}^{-1}$  are  $1/\lambda$ ,  $\lambda$  an eigenvalue of  $\mathbf{A}$ . But  $\mathbf{A}^+ = \mathbf{A}^{-1}$  and we are done.

Another proof using the defining property of positive definiteness is via Proposition 3.6.

By Proposition 3.6,  $\text{Ker } \mathbf{A}^+ \subseteq \text{Ker } \mathbf{A} = \{0\}$ , so

$\text{Ker } \mathbf{A}^+ = \{0\}$ . For any  $x \in \mathbb{R}^n \setminus \{0\}$  we have

$$\begin{aligned}
\langle x, \mathbf{A}^+ x \rangle &\stackrel{\text{3.41}}{=} \langle x, \mathbf{A}^+ \mathbf{A} \mathbf{A}^+ x \rangle = \langle \mathbf{A}^{+\top} x, \mathbf{A} \mathbf{A}^+ x \rangle \\
&\stackrel{\text{3.45}}{=} \langle \mathbf{A}^+ x, \mathbf{A} \mathbf{A}^+ x \rangle \geq 0,
\end{aligned} \tag{3.50}$$

Since  $x \notin \{0\} = \text{Ker } \mathbf{A} = \text{Ker } \mathbf{A}^+$ ,  $\mathbf{A}^+ x \neq 0$  and the last inequality (3.50) is strict by the positive definiteness of  $\mathbf{A}$ . ■

We are now prepared to prove certain properties of matrices appearing in the EEG inverse problem.

### 3.7 Regularized inverse solutions

Consider the inverse problem (3.34)

$$\Phi = \mathbf{KJ},$$

where the noisy solution  $\Phi$  of the forward problem and the lead field matrix  $\mathbf{K}$  are given. The task is to find  $\mathbf{J}$ . Since we are confronted with a noisy solution, (3.34) is an ill-posed problem. Such problems are treated through an approximation by some well-posed problems. This approach is called regularization and is formulated as follows (see Grech, Cassar et al.2008) [80].

We wish to find a best-approximate solution  $z \in \mathbb{R}^n$  of  $\mathbf{Kz} = y$  such that noisy data  $y^\delta \in \mathbb{R}^N$  is approximated by the noise-less data  $y \in \mathbb{R}^N$  with  $\|y^\delta - y\| \leq \delta$ , where  $\delta > 0$ . The minimization problem is

$$\min_z \|\mathbf{Kz} - y^\delta\|^2 + \alpha L(z), \tag{3.51}$$

where  $L: \mathbb{R}^n \rightarrow \mathbb{R}^+$  and  $\alpha > 0$  is a regularization parameter. In Tikhonov regularization,  $L(z) = \|z\|^2$ . The different regularization methods are discussed in (Grech et.al (2008)) [80]. In the general low resolution electric tomography (LORETA) [18], Pascual-Marqui et.al (2011) [16] claim that in (3.51) the functional  $L$  has the following form

$$\min_{\mathbf{J}} \|\mathbf{KJ} - \Phi\|^2 + \alpha \underbrace{\mathbf{J}^T \mathbf{WJ}}_{=:L(\mathbf{J})}, \tag{3.52}$$

where  $\mathbf{W} \in \mathbb{R}^{n \times n}$  is a positive definite matrix, and

a general solution of (3.52) is



$$\mathbf{J} = \mathbf{W}^{-1}\mathbf{K}^T(\mathbf{KW}^{-1}\mathbf{K}^T + \alpha\mathbf{H})^+\Phi, \quad (3.53)$$

where  $\mathbf{H}$  is the centering matrix from section 3.5 and  $\alpha > 0$  is the (Tikhonov) regularization parameter (see Pascual-Marqui et al. (2011)) [16].

We show in the following that the statement (3.53) is false, further, in view of the eLORETA anticipated solution for  $\mathbf{J}$ , already the proposition of the Tikhonov regularization problem (3.52) is false, as well.

Let us start with a general Tikhonov regularization problem, or in the context of linear algebra, the generalized least square minimization problem

$$\min_{x \in \mathbb{R}^n} \|\mathbf{A}x - y\|^2 + \langle x, \mathbf{B}x \rangle, \quad (3.54)$$

where  $\mathbf{A} \in \mathbb{R}^{m \times n}$ ,  $y \in \mathbb{R}^m$ ,  $\mathbf{B} \in \mathbb{R}^{n \times n}$ .

We may assume that  $\mathbf{B}$  is positive semidefinite.

Let

$$f(x) := \|\mathbf{A}x - y\|^2 + \langle x, \mathbf{B}x \rangle \quad (3.55)$$

$$\begin{aligned} &= \langle \mathbf{A}x - y, \mathbf{A}x - y \rangle + \langle x, \mathbf{B}x \rangle \\ &= x^T \mathbf{A}^T \mathbf{A} x - 2x^T \mathbf{A} y - y^T y + x^T \mathbf{B} x \end{aligned} \quad (3.56)$$

The minimum  $x$  in (3.55) must satisfy

$$\nabla f(x) = 0. \quad (3.57)$$

Now

$$\begin{aligned} \nabla f(x) &= 2\mathbf{A}^T \mathbf{A} x - 2\mathbf{A}^T y + 2\mathbf{B}x, \\ &= 2(\mathbf{A}^T \mathbf{A} + \mathbf{B})x - 2\mathbf{A}^T y, \end{aligned} \quad (3.58)$$

So (3.57) and (3.58) give

$$(\mathbf{A}^T \mathbf{A} + \mathbf{B})x = \mathbf{A}^T y \quad (3.59)$$

If  $(\mathbf{A}^T \mathbf{A} + \mathbf{B})^{-1}$  exists,

$$x = (\mathbf{A}^T \mathbf{A} + \mathbf{B})^{-1} \mathbf{A}^T y \quad (3.60)$$

is the unique solution. In general, when  $(\mathbf{A}^T \mathbf{A} + \mathbf{B})^{-1}$  does not exist a theorem of M. James (1978) [92] gives a characterization of the set of all solutions of the least square problem, with generalized inverses, for example the Moore-Penrose inverse.

**Theorem 3.10:**

$x = \mathbf{A}^+ \mathbf{b} + (\mathbf{I} - \mathbf{A}^+ \mathbf{A}) \mathbf{w}$ , where  $\mathbf{w} \in \mathbb{R}^n$  is an arbitrary vector, are all solutions of the problem  $\mathbf{A} \mathbf{x} = \mathbf{b}$ .

We apply Theorem 3.10 to (3.59) and get the following solution:

**Corollary 3.11:**

$$x = (\mathbf{A}^T \mathbf{A} + \mathbf{B})^+ \mathbf{A}^T \mathbf{y} + [\mathbf{I} - (\mathbf{A}^T \mathbf{A} + \mathbf{B})^+ (\mathbf{A}^T \mathbf{A} + \mathbf{B})] \mathbf{w},$$

where  $\mathbf{w} \in \mathbb{R}^n$  is an arbitrary vector represents the entire set of solutions of (3.54).

A special solution for  $\mathbf{w} = 0$  is

$$x = (\mathbf{A}^T \mathbf{A} + \mathbf{B})^+ \mathbf{A}^T \mathbf{y} \tag{3.61}$$

**Corollary 3.12:** A special solution for (3.52) is

$$\mathbf{J} = (\mathbf{K}^T \mathbf{K} + \alpha \mathbf{W})^+ \mathbf{K}^T \Phi \tag{3.62}$$

**Proof:** this follows immediately from Corollary 3.11. ■

We see that the solution (3.53) proposed by Pascual-Marqui (2007, 2011) [16, 17] is not of the form (3.62), in particular, (3.62) has no matrix  $\mathbf{H}$  in it. Therefore, (3.53) is **not** a solution of (3.52).

To achieve a solution of the form (3.53), we must consider the following least square approximation problem with a diagonal positive definite matrix  $\mathbf{W}$ .

$$\min_{\mathbf{J}} \|\mathbf{W}^{-1/2} \mathbf{K} \mathbf{J} - \Phi\|^2 + \alpha \mathbf{J}^T \mathbf{H} \mathbf{J} \tag{3.63}$$

We can consider (3.63) as a weighted inverse problem.

**Corollary 3.13:** A solution of (3.63) is

$$\mathbf{J} = (\mathbf{K}^T \mathbf{W}^{-1} \mathbf{K} + \alpha \mathbf{H})^+ \mathbf{K}^T \mathbf{W}^{-1/2} \Phi \tag{3.64}$$

In fact, for  $\mathbf{W} = \mathbf{I}$  the identity matrix, (3.63) is just the Tikhonov regularization problem, used in the sLORETA algorithm. The matrix  $\mathbf{W}^{-1/2}$  tries to adjust the electric potential associated with  $\mathbf{J}$ , namely  $\mathbf{K} \mathbf{J}$ , even better to the noisy solution  $\Phi$ . This, of course, is a heuristic approach.

If we consider the following minimization problem instead of (3.63)

$$\min_{\mathbf{J}} \|\mathbf{W}^{-1}\mathbf{K}\mathbf{J} - \Phi\|^2 + \alpha \mathbf{J}^T \mathbf{H} \mathbf{J} \quad (3.65)$$

then

**Corollary 3.14:** A solution of (3.65) is

$$\mathbf{J} = (\mathbf{K}^T \mathbf{W}^{-2} \mathbf{K} + \alpha \mathbf{H})^+ \mathbf{K}^T \mathbf{W}^{-1} \Phi \quad (3.66)$$

In fact, (3.66) is close to the claim (3.53).

However, Corollary 3.13 and 3.14 tells us that either we apply the weight matrix  $\mathbf{W}^{-1}$  or  $\mathbf{W}^{-1/2}$ , leading to (3.64) or (3.66), but in no case (3.53) in form of

$$\mathbf{J} = \mathbf{W}^{-1} \mathbf{K} (\mathbf{K} \mathbf{W}^{-1} \mathbf{K}^T + \alpha \mathbf{H})^+ \Phi \quad (3.67)$$

is possible. In order to fully compare (3.64) and (3.66) with (3.53), we must shift  $\mathbf{K}^T \mathbf{W}^{-1}$  from the right in (3.64) resp. (3.66) to the front of the formula. This can be proved as in

Grech et al. (2008), at least if  $\mathbf{W} = \begin{pmatrix} 1 & 0 \\ & \ddots \\ 0 & 1 \end{pmatrix}$ , and  $\mathbf{H}$  is the identity matrix  $\mathbf{I}$  in  $\mathbb{R}^{N \times N}$  and  $(\mathbf{K} \mathbf{K}^T + \alpha \mathbf{I})^{-1}$  exists:

**Theorem 3.15:** (Grech et al. (2008), Appendix, page 30) [80].

$$(\mathbf{K}^T \mathbf{K} + \alpha \mathbf{I})^{-1} \mathbf{K}^T = \mathbf{K}^T (\mathbf{K} \mathbf{K}^T + \alpha \mathbf{I})^{-1}. \quad (3.68)$$

In view of Theorem 3.15, we may take a weight matrix  $\mathbf{W}$ ,  $\mathbf{W}$  being a positive definite diagonal matrix, in the following way. The formulas below are heuristically justified solutions of the different weighted Tikhonov regularization problems for EEG:

$$\mathbf{J} = \mathbf{W}^{-1} \mathbf{K} (\mathbf{K} \mathbf{W}^{-1} \mathbf{K}^T + \alpha \mathbf{H})^+ \Phi \quad (3.69)$$

or

$$\mathbf{J} = \mathbf{W}^{-1/2} \mathbf{K} (\mathbf{K} \mathbf{W}^{-1} \mathbf{K}^T + \alpha \mathbf{H})^+ \Phi \quad (3.70)$$

or

$$\mathbf{J} = \mathbf{W}^{-1} \mathbf{K} (\mathbf{K} \mathbf{W}^{-2} \mathbf{K}^T + \alpha \mathbf{H})^+ \Phi \quad (3.71)$$

(3.70) and (3.71) are mathematically correct, but the Pascual-Marqui formula (3.69) must be considered as an unproved heuristical approach only. Since this approach in practice is giving meaningful results, we take (3.69) for further discussion as a hypothesis being aware that it is certainly not the correct solution of the weighted Tikhonov regularization problem. We proceed to the eLORETA algorithm.

### 3.8 The eLORETA algorithm

Let us present the eLORETA algorithm based on (3.53) along with its serious mathematical issues.

The family of algorithms, where  $\mathbf{W} = \begin{pmatrix} 1 & 0 \\ & \ddots \\ 0 & 1 \end{pmatrix}$  is the identity matrix, is known as the sLORETA method (Pascual-Marqui, 2002) [19]. Pascual-Marqui argues that the “non-weighted minimum norm has very bad localization properties, misplacing deep sources to the surface. The reason is because this solution is a harmonic function that attains its extreme values at the boundary of the solution space” (Pascual-Marqui et. al (2011), page 3771) [16].

He thus devised a new algorithm known as eLORETA, which computes the matrix  $\mathbf{W}$ ,  $\mathbf{W}$  not the identity matrix, in an iterative way. Since we apply the eLORETA algorithm for source localization in our applications, let us review the mathematical foundation in more detail, which is missing in the papers of Pascual-Marqui (2007) [17], and Pascual-Marqui et. al (2011) [16], e.g. the proof of positivity of the weights  $w_1, \dots, w_n$  in order to define  $\mathbf{W}^{-1} = \begin{pmatrix} w_1^{-1} & 0 \\ & \ddots \\ 0 & w_n^{-1} \end{pmatrix}$ . This is a major deficit of the papers of Pascual-Marqui (2007) [17], Pascual-Marqui et. al (2011) [16].

We will prove this in our work for the first time. In fact the proof is non-trivial heavily using linear algebra of MP inverses.

Let  $\mathbf{K}_i$  be the  $i$ -th column of the lead field matrix,  $i = 1, \dots, n$ . The eLORETA algorithm computes the diagonal weighted matrix in an iterative way. We give a generalization, which covers also the correct mathematical form of the inverse solution (3.71).

A central question is how to choose the weight matrix  $\mathbf{W}$ . Let  $\mathbf{C} := (\mathbf{K}\mathbf{W}^{-1}\mathbf{K}^T + \alpha\mathbf{H})^+$ .  $\mathbf{C}$  is a  $N \times N$  matrix. Let  $g(w)$  be the  $n \times n$  matrix defined by

$$g(w) := \mathbf{W}^{-1}\mathbf{K}^T\mathbf{C}\mathbf{K}\mathbf{W}^{-1}.$$

In Bayesian statistics  $g(w)$  is considered as a generalized i.e. weighted covariance matrix. The optimal weight matrix is found by the following matrix minimization problem

$$\min_{\mathbf{W}} \|\mathbf{I} - g(w)\|^2 \tag{3.72}$$

This is the minimization problem as in Pascual-Marqui (2007) [17], section 7.2. A general reference for an overview to the weighted covariance matrix is the paper of Grech et. al.(2008) [80].

Pascual-Marqui (2007) [17] claims that the optimal solution to (3.72) satisfies the non-linear system of equations

$$w_i^2 = \mathbf{K}_i^T \mathbf{C} \mathbf{K}_i, \quad (3.73)$$

$i = 1, \dots, n$ , leading to weights

$$w_i = (\mathbf{K}_i^T \mathbf{C} \mathbf{K}_i)^{1/2} \quad (3.74)$$

A proof has not been given by him.

In view of the correct inverse solutions in (3.70) and (3.71), we will work with weights of the form

$$w_i = [\mathbf{K}_i^T \mathbf{C}(s) \mathbf{K}_i]^{1/s}, \mathbf{C}(s) := (\mathbf{K} \mathbf{W}^{-s} \mathbf{K}^T + \alpha \mathbf{H})^+, \text{ and } s \in \{1, 2\}. \quad (3.75)$$

For  $s = 1$ , this is (3.73). In future work it should be proved that (3.75) indeed solves problem (3.72). For the sake of our work we take this as an heuristical approach justified by experimental evidence.

We are ready to formulate our generalized version of the eLORETA algorithm.

**Algorithm eLORETA** ( $s$ ) weights:

0. Parameter  $s \in \{1, 2\}$  fixed.

1. Initialization:  $\mathbf{W} = \begin{pmatrix} w_1 & 0 \\ & \ddots \\ 0 & w_n \end{pmatrix}$ ,  $w_j = 1$  for all  $j = 1, \dots, n$ .

2. Compute the Moore-Penrose inverse  $\mathbf{C} = (\mathbf{K} \mathbf{W}^{-s} \mathbf{K}^T + \alpha \mathbf{H})^+$

3. Compute for  $i = 1, \dots, n$ .

$$w_i = [\mathbf{K}_i^T \mathbf{C} \mathbf{K}_i]^{1/s}$$

4. Go to step 2 and iterate until a termination criterion is reached. ■

Note that for  $s = 1$  we have the Pascual Marqui matrix (3.69)  $\mathbf{C}(1)$  and the original eLORETA algorithm, and for  $s = 2$  the correct inverse solution matrix (3.71).

We remind the reader about the dimension of the matrices:  $\mathbf{H}$  is a  $N \times N$  matrix,  $\mathbf{K} \mathbf{W}^{-s} \mathbf{K}^T$  is a  $N \times N$  matrix, so  $\mathbf{C}$  is also a  $N \times N$  matrix.

There are two critical points with this algorithm:

a) Is  $w_i > 0$  for all  $i = 1, \dots, n$  in each iteration, because this is needed to build the inverse matrix.

$$\mathbf{W}^{-s} = \begin{pmatrix} w_1^{-s} & 0 \\ & \ddots \\ 0 & w_n^{-s} \end{pmatrix}$$

b) What is a termination criterion?

Problem a) is not addressed in the eLORETA publications of Pascual-Marqui, (2007) [17], and Pascual-Marqui et. al (2011) [16] at all. This is indeed a major drawback and questions the correctness of the algorithm. For problem b) it is stated that “until convergence i.e. stop when the change in weight matrix is sufficiently small” (Pascual-Marqui et.al (2011), page 3774) [16], but no convergence proof is given.

In practice, zero weights have not been produced by the eLORETA software in our applications. In the following, we will give the first proof of this empirically known fact.

However, we must consider the second problem b) as an open problem. In practice eLORETA is producing good source localizations which we found valid by benchmark studies.

Our main theorem is:

**Theorem 3.16:** In any iteration of the algorithm **eLORETA (s)-weights**, the matrix

$\mathbf{W} = \begin{pmatrix} w_1 & & 0 \\ & \ddots & \\ 0 & & w_n \end{pmatrix}$  is a positive definite diagonal matrix, so  $w_i > 0$  for all  $i = 1, \dots, n$ .

**Proof:** By definition,

$$w_i = [\mathbf{K}_i^T \mathbf{C} \mathbf{K}_i]^{1/s} \text{ with } \mathbf{C}(s) := (\mathbf{K} \mathbf{W}^{-s} \mathbf{K}^T + \alpha \mathbf{H})^+, \quad i = 1, \dots, n.$$

Let us first consider the matrix  $\mathbf{H}$ ,  $\mathbf{H} = (h_{ij})_{1 \leq i, j \leq N}$

By Lemma (3.4),  $\mathbf{H}$  is positive semidefinite, if

$$\sum_{\substack{i=1, \\ i \neq j}}^N |h_{ij}| \leq h_{jj} \text{ for all } j = 1, \dots, N.$$

Now  $h_{ij} = -\frac{1}{N}$  for  $i \neq j$  and  $h_{jj} = 1 - \frac{1}{N}$ . So

$$\sum_{\substack{i=1, \\ i \neq j}}^N |h_{ij}| = \frac{N-1}{N} = 1 - \frac{1}{N} = h_{jj} \text{ for all } j = 1, \dots, N,$$

thus  $\mathbf{H}$  is positive semidefinite.

We proceed by induction of the number of iterations. At the start of the induction,  $\mathbf{W}$  is the identity matrix, so

$$\mathbf{W} = \begin{pmatrix} w_1 & 0 \\ & \ddots \\ 0 & w_n \end{pmatrix} = \mathbf{W}^{-s}, \text{ and } w_i^{-s} = 1, \text{ for all } i = 1, \dots, n \text{ is well defined.}$$

Assume that at iteration  $l$ ,  $\mathbf{W}^{-s}$  is a well-defined matrix. This is true at the start as said. To enter the next iteration, we must update the weights  $w_1, \dots, w_n$ , and show  $w_i > 0$  for all  $i = 1, \dots, n$ .

$\mathbf{KW}^{-s}\mathbf{K}^T$  is a positive semidefinite  $N \times N$  matrix, because for any  $x \in \mathbb{R}^n$  we have

$$\langle x, \mathbf{KW}^{-s}\mathbf{K}^T x \rangle = \langle \mathbf{K}^T x, \mathbf{W}^{-s}\mathbf{K}^T x \rangle \geq 0, \quad (3.76)$$

since  $\mathbf{W}$  is positive definite. We cannot show that  $\mathbf{KW}^{-s}\mathbf{K}^T$  is positive definite: if we consider any  $x \in \text{Ker } \mathbf{K}^T$ , so  $\mathbf{K}^T x = 0$ , then (3.76) is true, even if  $x \neq 0$ .

But, since  $\mathbf{KW}^{-s}\mathbf{K}^T$  as observed is positive semidefinite,  $\mathbf{H}$  is positive semidefinite and using  $\alpha > 0$ , by Proposition 3.5,  $\mathbf{KW}^{-s}\mathbf{K}^T + \alpha\mathbf{H}$  is positive semidefinite, by Proposition 3.8,  $\mathbf{C} = (\mathbf{KW}^{-s}\mathbf{K}^T + \alpha\mathbf{H})^+$  is positive semidefinite.

Therefore,

$$\mathbf{K}_i^T \mathbf{C} \mathbf{K}_i = \langle \mathbf{K}_i, \mathbf{C} \mathbf{K}_i \rangle \geq 0, \text{ and}$$

$$w_i = [\mathbf{K}_i^T \mathbf{C} \mathbf{K}_i]^{1/s} \text{ is well defined, for all } i = 1, \dots, n.$$

**Claim 0:**  $w_i > 0$  for all  $i = 1, \dots, n$ .

Assume for a moment that  $w_i = 0$  for some  $i \in \{1, \dots, n\}$ .

$$\text{Then } w_i^s = 0,$$

so,

$$0 = w_i^s = \mathbf{K}_i^T \mathbf{C} \mathbf{K}_i = \langle \mathbf{K}_i, \mathbf{C} \mathbf{K}_i \rangle \quad (3.77)$$

Since  $\mathbf{C}$  is positive semidefinite,  $\mathbf{C}$  has a symmetric square root matrix  $\mathbf{B}$  with  $\mathbf{C} = \mathbf{B}\mathbf{B} = \mathbf{B}^2$ , and (3.77) gives

$$\begin{aligned} 0 &= \langle \mathbf{K}_i, \mathbf{C} \mathbf{K}_i \rangle = \langle \mathbf{K}_i, \mathbf{B}\mathbf{B} \mathbf{K}_i \rangle \\ &= \langle \mathbf{B}^T \mathbf{K}_i, \mathbf{B} \mathbf{K}_i \rangle \stackrel{\substack{= \\ \mathbf{B} \text{ symmetric}}}{=} \langle \mathbf{B} \mathbf{K}_i, \mathbf{B} \mathbf{K}_i \rangle \\ &= \|\mathbf{B} \mathbf{K}_i\|^2, \text{ so } \|\mathbf{B} \mathbf{K}_i\| = 0, \end{aligned}$$

hence  $\mathbf{B} \mathbf{K}_i = 0$ , and  $\mathbf{C} \mathbf{K}_i = \mathbf{B}\mathbf{B} \mathbf{K}_i = 0$ ,

which shows  $\mathbf{K}_i \in \text{Ker } \mathbf{C}$ . By Proposition 3.8,

$$\text{Ker } \mathbf{C} = \text{Ker} (\mathbf{KW}^{-s}\mathbf{K}^T + \alpha\mathbf{H})^+ \subseteq \text{Ker} (\mathbf{KW}^{-s}\mathbf{K}^T + \alpha\mathbf{H}).$$

So,

$$0 = (\mathbf{KW}^{-s}\mathbf{K}^T + \alpha\mathbf{H})\mathbf{K}_i = \mathbf{KW}^{-s}\mathbf{K}^T\mathbf{K}_i + \alpha\mathbf{H}\mathbf{K}_i \quad (3.78)$$

We claim:

$$\mathbf{K}_i \notin \text{Ker } \mathbf{H} \quad (3.79)$$

We give a proof combining mathematical arguments and a fact from the physics of EEG scalp measurements.

Assume that (3.79) is not true:  $\mathbf{K}_i \in \text{Ker } \mathbf{H}$ .

To shorten the notation let's say  $\mathbf{K}_i = (k_1, \dots, k_N)^T$ . Then

$$\begin{aligned} 0 = \mathbf{H}\mathbf{K}_i &= \begin{pmatrix} 1 - \frac{1}{N} & & * \\ & \ddots & \\ * & & 1 - \frac{1}{N} \end{pmatrix} \begin{pmatrix} k_1 \\ \vdots \\ k_N \end{pmatrix} \\ &= \begin{pmatrix} \left(1 - \frac{1}{N}\right)k_1 - \frac{1}{N}k_2 - \dots - \frac{1}{N}k_N \\ -\frac{1}{N}k_1 + \left(1 - \frac{1}{N}\right)k_2 - \dots - \frac{1}{N}k_N \\ \vdots \\ -\frac{1}{N}k_1 - \dots - \frac{1}{N}k_{N-1} + \left(1 - \frac{1}{N}\right)k_N \end{pmatrix} \end{aligned}$$

Therefore,

$$k_i = \frac{1}{N}(k_1 + \dots + k_N)$$

for all  $i = 1, \dots, N$ . This is a system of linear equations, and in fact, it has a very simple solution, namely  $k_i = k_j$  for all  $i, j \in \{1, \dots, N\}$ , so all components of  $\mathbf{K}_i$  are the same! We can see this as follows. Let  $i, j \in \{1, \dots, N\}$  and  $i \neq j$ . Then, as  $k_i = \frac{1}{N}(k_1 + \dots + k_N)$  for all  $i \in \{1, \dots, N\}$ , we have

$$k_i - k_j = \sum_{l \neq i} k_l - \sum_{l \neq j} k_l$$

$$\Leftrightarrow k_i - k_j = k_j - k_i$$

$$\Leftrightarrow 2k_i = 2k_j$$



$$\Leftrightarrow k_i = k_j \text{ for all } i, j.$$

This means, all electrode field components are the same, which is not the case in EEG, and also completely unrealistic from a physics point of view. Thus  $\mathbf{K}_i \notin \text{Ker } \mathbf{H}$ .

From (3.78) we get

$$\begin{aligned} 0 &= \mathbf{K}_i^T \mathbf{K} \mathbf{W}^{-s} \mathbf{K}^T \mathbf{K}_i + \alpha \mathbf{K}_i^T \mathbf{H} \mathbf{K}_i \\ &= \underbrace{\langle \mathbf{K}_i, \mathbf{K} \mathbf{W}^{-s} \mathbf{K}^T \mathbf{K}_i \rangle}_{=:a} + \alpha \underbrace{\langle \mathbf{K}_i, \mathbf{H} \mathbf{K}_i \rangle}_{=:b} \end{aligned} \quad (3.80)$$

We show now that  $a > 0$  and  $b > 0$ , leading to the contradiction

$$0 = a + b > 0, \text{ so } 0 > 0. \quad (3.81)$$

In fact,  $b \geq 0$ , and  $a > 0$  is sufficient for this contradiction.

**Claim 1:**  $b > 0$ .

**Proof of Claim 1:** Since  $\mathbf{H}$  is positive semidefinite, its square root matrix  $\mathbf{A} := \mathbf{H}^{-1/2}$  exists. Thus

$$\begin{aligned} b &= \langle \mathbf{K}_i, \mathbf{H} \mathbf{K}_i \rangle = \langle \mathbf{K}_i, \mathbf{A} \mathbf{A} \mathbf{K}_i \rangle \\ &= \langle \mathbf{A} \mathbf{K}_i, \mathbf{A} \mathbf{K}_i \rangle = \|\mathbf{A} \mathbf{K}_i\|^2. \end{aligned}$$

The assumption  $b = 0$  gives  $\|\mathbf{A} \mathbf{K}_i\|^2 = 0$ , so  $\mathbf{A} \mathbf{K}_i = 0$ .

Thus

$\mathbf{H} \mathbf{K}_i = \mathbf{A} \mathbf{A} \mathbf{K}_i = 0$ , enforcing  $\mathbf{K}_i \in \text{Ker } \mathbf{H}$ , which is a contradiction to (3.79).

**Claim 2:**  $a > 0$ .

**Proof of Claim 2:** Since  $\mathbf{K} \mathbf{W}^{-s} \mathbf{K}^T$  is positive semidefinite, its square root  $\mathbf{B}$  exists,

so  $\mathbf{B} \mathbf{B} = \mathbf{K} \mathbf{W}^{-s} \mathbf{K}^T$ .

Now

$$\begin{aligned} a &= \langle \mathbf{K}_i, \mathbf{B} \mathbf{B} \mathbf{K}_i \rangle = \langle \mathbf{B} \mathbf{K}_i, \mathbf{B} \mathbf{K}_i \rangle \\ &= \|\mathbf{B} \mathbf{K}_i\|^2. \end{aligned}$$

The assumption  $a = 0$  implies  $\|\mathbf{B} \mathbf{K}_i\|^2 = 0$ , so  $\mathbf{B} \mathbf{K}_i = 0$ ,

$\mathbf{K} \mathbf{W}^{-s} \mathbf{K}^T \mathbf{K}_i = \mathbf{B} \mathbf{B} \mathbf{K}_i = 0$ ,

So

$$\mathbf{K}_i \in \text{Ker } \mathbf{K}\mathbf{W}^{-s}\mathbf{K}^T \quad (3.82)$$

By (3.60),  $\mathbf{K}\mathbf{W}^{-s}\mathbf{K}^T\mathbf{K}_i = 0$ , so

$$0 = \langle \mathbf{K}_i, \mathbf{K}\mathbf{W}^{-s}\mathbf{K}^T\mathbf{K}_i \rangle = \langle \mathbf{K}^T\mathbf{K}_i, \mathbf{W}^{-s}\mathbf{K}^T\mathbf{K}_i \rangle. \quad (3.83)$$

Since  $\mathbf{W}^{-s}$  is positive definite, (3.83) can hold if and only if

$$\mathbf{K}^T\mathbf{K}_i = 0 \quad (3.84)$$

Let us compute  $\mathbf{K}^T\mathbf{K}_i$ . The columns of  $\mathbf{K}$  are the rows of  $\mathbf{K}^T$ . So

$$0 \stackrel{(3.84)}{=} \mathbf{K}^T\mathbf{K}_i = \begin{pmatrix} \mathbf{K}_1 \cdot \mathbf{K}_i \\ \vdots \\ \mathbf{K}_i \cdot \mathbf{K}_i \\ \vdots \\ \mathbf{K}_n \cdot \mathbf{K}_i \end{pmatrix} = \begin{pmatrix} \mathbf{K}_1 \cdot \mathbf{K}_i \\ \vdots \\ \|\mathbf{K}_i\|^2 \\ \vdots \\ \mathbf{K}_n \cdot \mathbf{K}_i \end{pmatrix},$$

hence  $\|\mathbf{K}_i\|^2 = 0$ , so  $\mathbf{K}_i = 0$ .

This is absurd, because the  $i$ -th column of the lead field matrix is certainly not the zero vector, since the  $i$ -th source is generating a non-zero electric field, of course.

Therefore,  $a > 0$  and we have produced the contradiction in (3.81), concluding the proof of the theorem. ■

### 3.9 Scalp potential from a point source

In this section we show that under the special assumption of the electrode potential  $\Phi$  being generated by a single source  $j \in \{1, \dots, n\}$ , the current density has a local maximum. Let  $j \in \{1, \dots, n\}$  be arbitrary, but now fixed. The electric activity of source  $j$  is captured by the  $j$ th column  $\mathbf{K}_j$  of the lead field matrix  $\mathbf{K}$ .

We make the following assumption:

$$\Phi = a\mathbf{K}_j \quad (3.85)$$

with some  $a > 0$ . (3.85) says that only the source  $j$  is generating the scalp potential  $\Phi$ .

We shorten the notation by fixing an arbitrary column  $\mathbf{K}_i$  of  $\mathbf{K}$ ,  $i = 1, \dots, n$  and setting

$$x = (x_1, \dots, x_N) = \mathbf{K}_i, \text{ and } y = (y_1, \dots, y_N) = \mathbf{K}_j,$$

where  $\mathbf{K}_j$  is as in (3.85).

Further, we define for  $x \in \mathbb{R}^n$

$$f(x) := a^2 \langle x, \mathbf{C}x \rangle^{-1} \langle x, \mathbf{C}y \rangle^2, \quad (3.86)$$

with  $\mathbf{C} := (\mathbf{K}\mathbf{W}^{-1}\mathbf{K}^T + \alpha\mathbf{H})^+$  as in (3.75) for  $s = 1$ , also reflecting the correct inverse solution (3.70).

We show now that the  $i$ -th current density squared is exactly the function value  $f(x)$ ,

**Lemma 3.17** Then with  $\mathbf{C}$  and  $x$  defined as above,  $f(x) = \mathbf{J}_i^2$ .

**Proof:**

By (3.70)

$$\mathbf{J} = \mathbf{W}^{-\frac{1}{2}}\mathbf{K}(\mathbf{K}\mathbf{W}^{-1}\mathbf{K}^T + \alpha\mathbf{H})^+\Phi$$

Remember, that in the algorithm eLORETA(s),  $w_i$  was defined as

$$w_i = [\mathbf{K}_i^T\mathbf{C}\mathbf{K}_i]^{1/s} = [\mathbf{K}_i^T\mathbf{C}\mathbf{K}_i]$$

So

$$\begin{aligned} \mathbf{J}_i &= w_i^{-\frac{1}{2}}\mathbf{K}_i^T\mathbf{C}\Phi \\ &= [\mathbf{K}_i^T\mathbf{C}\mathbf{K}_i]^{-1/2}\mathbf{K}_i^T\mathbf{C}\Phi \\ &\stackrel{\Phi = a\mathbf{K}_j}{=} a[\mathbf{K}_i^T\mathbf{C}\mathbf{K}_i]^{-1/2}\mathbf{K}_i^T\mathbf{C}\mathbf{K}_j. \end{aligned}$$

Therefore

$$\begin{aligned} \mathbf{J}_i^2 &= a^2 [\mathbf{K}_i^T\mathbf{C}\mathbf{K}_i]^{-1} (\mathbf{K}_i^T\mathbf{C}\mathbf{K}_j)^2 \\ &= a^2 \langle \mathbf{K}_i, \mathbf{C}\mathbf{K}_i \rangle^{-1} \langle \mathbf{K}_i, \mathbf{C}\mathbf{K}_j \rangle^2 \\ &= f(x). \end{aligned}$$

■

Let  $\nabla f(x)$  be the gradient of  $f$  w.r.t.  $x$ . The first lemma states that the gradient of  $f$  vanishes in  $x = y$ .

**Lemma 3.18**  $\nabla f(y) = 0$

**Proof:**

We first compute

$$\nabla f(x) = \left( \frac{\partial f(x)}{\partial x_1}, \dots, \frac{\partial f(x)}{\partial x_N} \right).$$

So, let us choose  $l \in \{1, \dots, N\}$  arbitrary, but now fixed and consider  $\frac{\partial f(x)}{\partial x_l}$ .

Let  $\mathbf{C} = (c_{ij})_{1 \leq i, j \leq N}$ ,  $g(x) := \langle x, \mathbf{C}x \rangle^{-1}$  and  $h(x) := \langle x, \mathbf{C}y \rangle^2$ .  $g$  and  $h$  are quadratic forms in  $x$ .

By product rule

$$\frac{\partial f(x)}{\partial x_l} = a \cdot \left[ \frac{\partial g(x)}{\partial x_l} \cdot h(x) + g(x) \cdot \frac{\partial h(x)}{\partial x_l} \right]. \quad (3.87)$$

Now,

$$\begin{aligned} \frac{\partial g(x)}{\partial x_l} &= \frac{\partial}{\partial x_l} \left[ \left( \sum_{i,j=1}^N c_{ij} x_i x_j \right)^{-1} \right] \\ &= - \frac{\partial}{\partial x_l} \left( \sum_{i,j=1}^N c_{ij} x_i x_j \right) \cdot \left( \sum_{i,j=1}^N c_{ij} x_i x_j \right)^{-2} \\ &= - \left[ \sum_{j=1}^N c_{lj} x_j + \sum_{i=1}^N c_{il} x_i \right] \cdot \langle x, \mathbf{C}x \rangle^{-2} \\ &\stackrel{\substack{\text{C symmetric} \\ \Downarrow}}{=} -2 \sum_{j=1}^N c_{lj} x_j \cdot \langle x, \mathbf{C}x \rangle^{-2} \\ &= -2 \langle c_l, x \rangle \cdot \langle x, \mathbf{C}x \rangle^{-2}, \end{aligned} \quad (3.88)$$

where  $c_l$  is the  $l$ -th row vector of  $\mathbf{C}$ .

Further, as above

$$\begin{aligned} \frac{\partial h(x)}{\partial x_l} &= \frac{\partial}{\partial x_l} \left[ \left( \sum_{i,j=1}^N c_{ij} x_i y_j \right)^2 \right] \\ &= 2 \frac{\partial}{\partial x_l} \left( \sum_{i,j=1}^N c_{ij} x_i y_j \right) \cdot \left( \sum_{i,j=1}^N c_{ij} x_i y_j \right)^{2-1} \end{aligned}$$

$$\begin{aligned}
&= 2 \cdot \left( \sum_{j=1}^N c_{lj} y_j \right) \cdot \langle x, \mathbf{C}y \rangle \\
&= 2 \langle c_l, y \rangle \cdot \langle x, \mathbf{C}y \rangle.
\end{aligned} \tag{3.89}$$

(3.88) and (3.89) substituted in (3.87) give

$$\begin{aligned}
\frac{\partial f(x)}{\partial x_l} &= a[-2\langle c_l, x \rangle \langle x, \mathbf{C}x \rangle^{-2} \langle x, \mathbf{C}y \rangle^2 + 2\langle x, \mathbf{C}x \rangle^{-1} \cdot \langle c_l, y \rangle \langle x, \mathbf{C}y \rangle] \\
&= 2a \left[ -\frac{\langle c_l, x \rangle \langle x, \mathbf{C}y \rangle^2}{\langle x, \mathbf{C}x \rangle^2} + \frac{\langle c_l, y \rangle \langle x, \mathbf{C}y \rangle}{\langle x, \mathbf{C}x \rangle} \right]
\end{aligned} \tag{3.90}$$

Thus

$$\begin{aligned}
\frac{\partial f(y)}{\partial x_l} &= 2a \left[ -\frac{\langle c_l, y \rangle \langle y, \mathbf{C}y \rangle^2}{\langle y, \mathbf{C}y \rangle^2} + \frac{\langle c_l, y \rangle \langle y, \mathbf{C}y \rangle}{\langle y, \mathbf{C}y \rangle} \right] \\
&= 2a \left[ \underbrace{-\langle c_l, y \rangle + \langle c_l, y \rangle}_{=0} \right] \\
&= 0.
\end{aligned}$$

Since  $l$  was arbitrary,  $\frac{\partial f(y)}{\partial x_j} = 0$  for all  $j \in \{1, \dots, N\}$ , hence

$$\nabla f(y) = \left( \frac{\partial f(y)}{\partial x_1}, \dots, \frac{\partial f(y)}{\partial x_N} \right) = 0.$$

■

The next theorem is the main result of this section.

**Theorem 3.19** Let  $\mathbf{C}$  and  $f$  be as in (3.86).

- (i)  $f$  has a global maximum in  $y$ .
- (ii) For a point source  $\Phi = a\mathbf{K}_j$  as in (3.85),  $a > 0$ , the current density in square,  $\mathbf{J}_i^2$ , has a global maximum for  $\mathbf{K}_i = \mathbf{K}_j$ .

**Proof:**

- (i) Since  $\mathbf{C}$  is positive semidefinite, there exists a orthogonal basis (OB)  $e_1, \dots, e_N$  of  $\mathbb{R}^N$  with respect to  $\mathbf{C}$ , i.e.
$$\langle e_i, \mathbf{C}e_j \rangle = 0 \text{ for all } i \neq j. \tag{3.91}$$

We can assume that  $\langle y, \mathbf{C}y \rangle > 0$  and  $e_1 = y$  (after normalizing  $y$ , if required). Let  $U \subseteq \mathbb{R}^N$  an arbitrary neighbourhood of  $y$  and let  $x \in \mathbb{R}^N$ .  $x$  has an expansion w.r.t. the basis  $e_1, \dots, e_N$  as

$$x = \sum_{i=1}^N a_i \cdot e_i,$$

With suitable coefficients  $a_1, \dots, a_N$  in  $\mathbb{R}$ . Now

$$\begin{aligned} f(x) &= a^2 \langle x, \mathbf{C}x \rangle^{-1} \langle x, \mathbf{C}y \rangle^2 \\ &= a^2 \left\langle \sum_{i=1}^N a_i \cdot e_i, \sum_{j=1}^N a_j \cdot \mathbf{C}e_j \right\rangle^{-1} \cdot \left\langle \sum_{i=1}^N a_i \cdot e_i, \mathbf{C}y \right\rangle^2 \\ &= a^2 \left( \sum_{i=1}^N \sum_{j=1}^N a_i \cdot a_j \langle e_i, \mathbf{C}e_j \rangle \right)^{-1} a_1^2 \langle y, \mathbf{C}y \rangle^2 \\ &\stackrel{(e_i) \text{ OB}}{=} a^2 \underbrace{\left( \sum_{i=1}^N a_i^2 \langle e_i, \mathbf{C}e_i \rangle \right)^{-1}}_{\geq a_1^2 \langle y, \mathbf{C}y \rangle} \cdot a_1^2 \langle y, \mathbf{C}y \rangle^2 \\ &\leq a^2 (a_1^2 \langle y, \mathbf{C}y \rangle)^{-1} a_1^2 \langle y, \mathbf{C}y \rangle^2 \\ &= a^2 \frac{a_1^2 \langle y, \mathbf{C}y \rangle^2}{a_1^2 \langle y, \mathbf{C}y \rangle} \\ &= a^2 \langle y, \mathbf{C}y \rangle \\ &= f(y). \end{aligned}$$

So  $f(x) \leq f(y)$  for all  $x \in U$ , thus (i) holds.

- (ii) By Lemma 3.17, for  $\mathbf{C} = (\mathbf{K}\mathbf{W}^{-1}\mathbf{K}^T + \alpha\mathbf{H})^+$ ,  $f(x) = \mathbf{J}_i^2$ . The statement immediately follows from the first part (i). ■

From Lemma 3.18 and Theorem 3.19,

**Corollary 3.20:** The function  $f(x) = \mathbf{J}_i^2$  has exactly 1 global maximum and no other local maxima.

# Chapter 4

## Materials and EEG pre-processing

---

### 4.1 Subjects

All patients for this study were recruited from the North German Epilepsy center for children and adolescents in Schwentinal Ralsdorf, Germany. The patient data was retrospectively collected and analyzed. The data received from the hospital was completely anonymized. This study was approved by the Ethics Committee of the Faculty of Medicine, University of Kiel, Germany (Number D 456/19).

Patients	Gender	Age of onset (years)	Age at EEG (years)	Seizures still $\pm$	Seizures in Family	Normal Cognitive Development	Anti-Epileptic Drugs
P1	M	6	6	-	Febrile, afebrile, GTCs	Yes	ESM
P2	M	9	9	-	-	Yes	LTG
P3	M	5	5	-2012	-	Yes	LTG
P4	M	7	12	-2018	-	Yes	LTG
P5	M	6	6	-2018	-	Yes	ESM, LTG, VPA
P6	F	4	6			Yes	LTG, ESM
P7	M	4	8	-2017	-	Yes	ESM, VPA
P8	F	6	7	-	-	Yes	ESM
P9	M	5	10	-	-	Yes	LTG
P10	F	10	13	-	-	Yes	LTG
P11	F	4	7	-	No data	Mild learning difficulties	ESM, VPA
P12	F	7	9	-	Migraine	Yes	ESM, LTG, VPA

**Table 4.1 Demographic data of all subjects.**

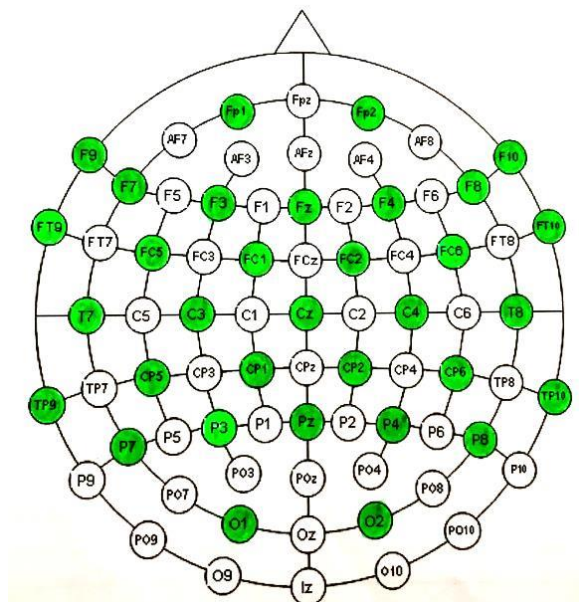
(+ present, - not present), EEG electroencephalography, ESM ethosuximid, VPA valproic acid, LTG lamotrigine,

Since the data was anonymized, the patients were given numbers to identify them. 26 patients with a clear diagnosis of CAE were selected for this study. The diagnosis was made based on the 2017 International League against Epilepsy (ILAE) classification for epilepsies [4]. The selected patients were further checked by viewing their EEG recordings to make sure they fulfill the criteria of our study. Firstly, the ictal and non-ictal discharges were classified based on the timely and reliable testing of patients during EEG recordings by experienced technicians. The level of consciousness during the GSWDs were tested by asking direct short questions (e.g. what is your name? where are you? etc.) during the first few seconds of the event. Also, any disruption in activities such as counting or reading was noted via video recordings. Only those segments were selected for the analyses where the level of consciousness was successfully and reliably evaluated. A second criterion of selection was that the patients should have both ictal and non-ictal GSWDs present. Those patients that did not fulfill these criteria were excluded from the study.

Following this, 205 EEG recordings from these patients were analyzed and 12 patients were selected. For reference the patients were given numbers (P1...P12). These 12 patients had both ictal and non-ictal GSWDs in 111 EEGs. In the cohort of 12 patients, 7 were males and 6 were females with a mean age of  $7.3 \pm 1.5$  years. All patients had a normal cognitive development except P11 who had mild learning difficulties. P1 was the only patient with family history seizures. As of 2019 all the selected patients are seizure free.

## 4.2 EEG Recordings

The EEGs files consisted of sleep and wakeful state recordings of the patients. But for this study only awake state recordings were included.





The recordings were performed using the 10/20 standard system (EEG recording system: Neurofile; IT-med, Bad Homburg, Germany) with additional electrodes which were FC1, FC2, FC5, FC6, CP1, CP2, CP5, CP6, FT9, FT10, TP9, TP10 and ECG.

The reference was located between Fz and Cz. The sampling rate was 512 Hz and the Impedance was kept below 10 kOhms. The EEG was recorded from 31 scalp sites for all patients. In some EEG recordings two additional lateral electrodes F9 and F10 were used in patients P1, P2, P3, P4, P5, P7, P9, P11, P12.

### 4.3 EEG preprocessing

For this study we chose to analyze 3 Hz ictal and non-ictal GSWDs in CAE patients. All the EEG files were converted offline using the software Cartool. The file formats were changed to brain vision format (.eeg) since this format can be read easily by other software's. The data was visually inspected using the software BESA Research 7.0 (<https://www.besa.de/>). BESA is a comprehensive software package for signal processing of EEG and MEG data. It is user friendly, versatile and contains various tools and scripts for preprocessing raw data as well as for source analysis. Using this software, high pass and low pass filters were applied for artifact removal (high pass filter- 0.5 Hz low pass filter- 35 Hz). A total number of 111 EEG recordings from the 12 patients were visually analyzed to mark ictal and non-ictal GSWDs. BESA software was further used to cut the regions of interest for further analysis.

#### 4.3.1 Selection of the Time intervals

For this study ictal and non-ictal GSWDs were analyzed at three time periods: pre- ictal/non-ictal, during- ictal/non-ictal, post- ictal/non-ictal. For pre- and post- ictal/non-ictal, 3 second time periods were taken, while for during- ictal/non-ictal the entire length of the discharge was taken. For a part of the sensor level analysis we also chose to analyze 10 seconds pre- and post- ictal/non-ictal.

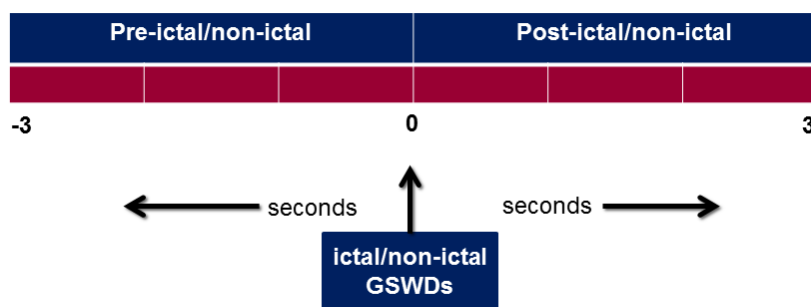


**Figure4. 2 Time intervals of interest**

*The entire duration of ictal/non-ictal discharges were selected. For pre- and post-ictal/non-ictal intervals the duration of 3 seconds was selected.*

### **4.3.2 Selection of ictal GSWDs**

Seizures in CAE are usually 3 Hz, consisting of GSWDs such as that seen in Figure. 3.4. During the course of the seizure the patients have staring spells alongside severe impaired consciousness, which resumes soon after the discharge ends.

For further analysis seizure segments or ictal GSWDs were selected based on the following criteria:

- Clinically defined CAE characteristics
- Tested for impairment of consciousness.
- Ictal discharges longer than 3 seconds and less than 30 seconds
- Spontaneous seizures and provoked seizures by hyperventilation

Following this, 46 ictal GSWDs were selected from the 12 patients. In table 3.2, the number of seizures per patient with the duration of the discharges can be found.

### **4.3.3 Selection of non-ictal GSWDs**

Non-ictal GSWDs in CAE are similar to ictal GSWDs on the EEG with 3 Hz discharges, but they show no clinical symptoms of a seizure and most importantly have no impairment of consciousness. (Fig 3.5)

These non-ictal GSWDs are shorter than ictal GSWDs. These segments were selected based on the following criteria:

- Patients were tested for impairment of consciousness by asking simple questions during the EEG recordings,
- No clinical symptoms of an absence seizure
- Non tested paroxysms excluded
- Length of discharge should be longer than 1 second

Based on the selection criteria 42 non-ictal GSWDs were selected, for which the duration has been depicted in Table 3.2.

For a specific part of the sensor level analysis only those non-ictal GSWDs were taken which were longer than 3 seconds. There were only 23 non-ictal GSWDs longer than 3 seconds and out of 12 patients only 4 (P7, P8, P10, P11) had these.

The mean duration of ictal discharges was 8.4 seconds (SD 3.4) and was significantly ( $p < 0.001$ ) longer than the mean duration (4.1 seconds, SD 2.4) of non-ictal discharges.

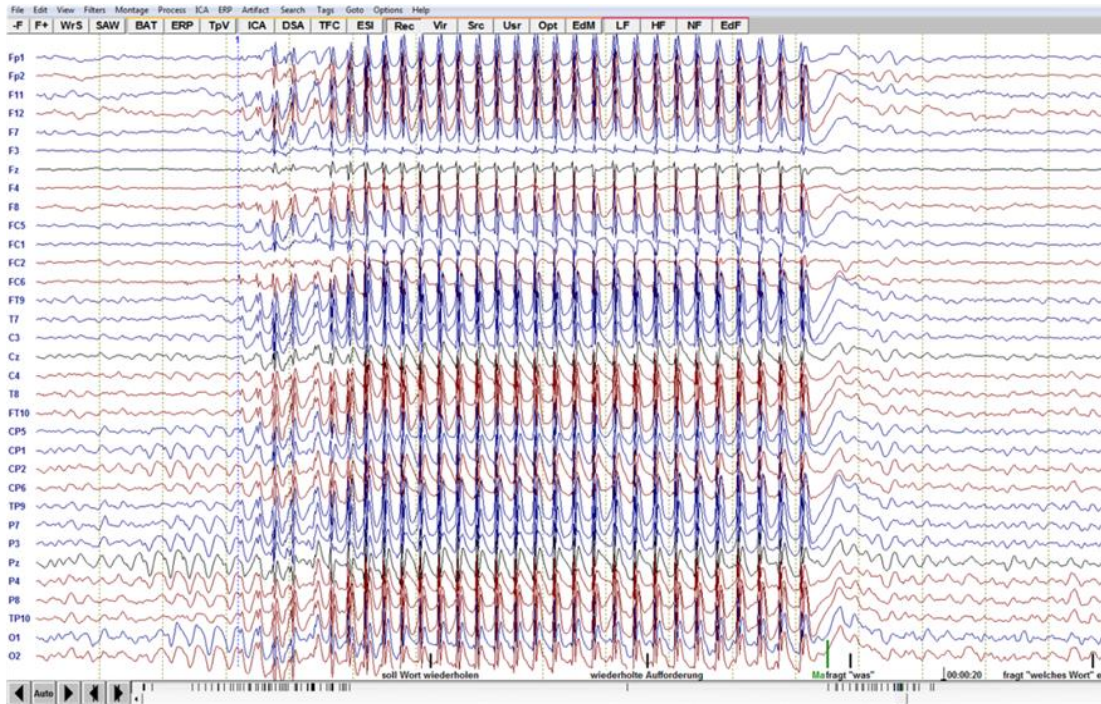


**Figure 4. 3 EEG ictal GSWDs.**

*3 Hz ictal discharges during an EEG recording. Patient has clinical symptoms with severe impairment of consciousness.*

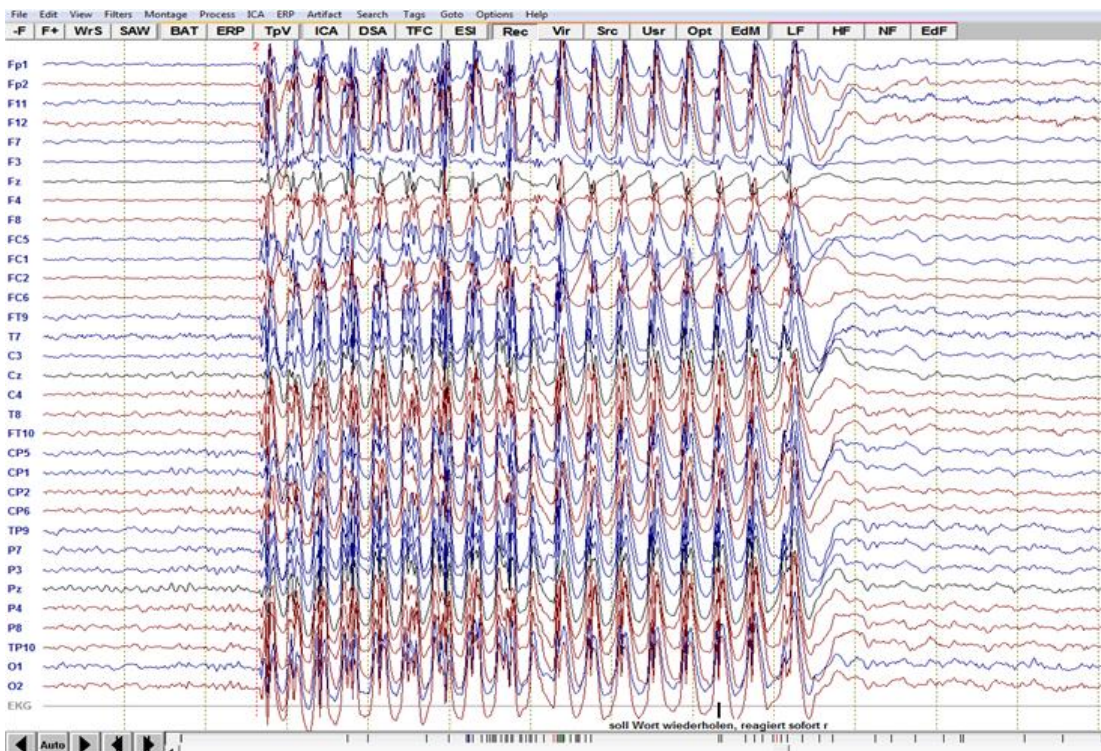


**Figure 4. 4 EEG Non-ictal GSWDs.**

*Non-ictal discharges of 3 Hz during an EEG recording. Patient is aware during the entire paroxysm.*

<b>Patients</b>	<b>Number of ictal GSWDs</b>	<b>ictal GSWDs duration (seconds)</b>	<b>Number of non-ictal GSWDs</b>	<b>Non-ictal GSWDs duration (seconds)</b>
<b>P1</b>	2	9-11.7	2	1-1.3
<b>P2</b>	2	12-13.8	6	1.2-3.3
<b>P3</b>	1	8.9	2	1.2-3.4
<b>P4</b>	2	9-12.8	1	1.3
<b>P5</b>	3	12-18.8	1	5
<b>P6</b>	1	3.5	4	2.2-8.8
<b>P7</b>	1	5.1	3	3.5-8.3
<b>P8</b>	6	5-15.7	1	1.2
<b>P9</b>	1	5.1	14	3-8.6
<b>P10</b>	4	6.5-9	5	2-12.6
<b>P11</b>	11	4-6.8	1	2.3
<b>P12</b>	11	4-10.9	2	2.9-3.4

**Table 4.2 The durations of ictal and non-ictal.**

# Chapter 5

## Sensor-level time frequency analysis

---

In this chapter time frequency analysis was used as a measure to analyse ictal and non-ictal GSWDs > 3 seconds. This was implemented to better understand the spectral power changes within frequency bands ranging from 1-30 Hz. Descriptive statistics was applied to analyse the various frequency bands in ictal and non-ictal GSWDs.

### 5.1 Methods

#### 5.1.1 Selection of ictal and non-ictal GSWDs > 3 seconds

All 12 patients mentioned in the materials section (chapter3) were included in this part of the study. All 12 patients had ictal GSWDs, however only 4 patients had non-ictal GSWDs>3 seconds. Ictal GSWDs were selected based on the criteria mentioned in chapter 3. While non-ictal GSWDs were selected based on the following criteria: 1) patients were tested for impairment of consciousness 2) no clinical symptoms of absence seizures 3) the duration of discharges being 3 or more seconds. Following this 44 ictal GSWDs and 23 non-ictal GSWDs were selected. The TFA was done for the entire duration of ictal and non-ictal GSWDs.

Patients	Number of ictal GSWDs	duration (seconds)	Number of non-ictal GSWDs>3 seconds	duration (seconds)
P1	2	9-11.7	-	-
P2	2	12-13.8	-	-
P3	1	8.9	-	-
P4	2	9-12.8	-	-
P5	3	12-26.3	-	-
P6	1	3.5	3	3-8.8
P7	1	5.1	3	6-8.3
P8	5	5-15.7	-	-
P9	1	5.1	14	3-8.6
P10	4	9	3	6-12.6
P11	11	4-6.8	-	-
P12	11	4-10.9	-	-

**Table 5.1** Depiction of number of ictal and non-ictal GSWDs> 3 seconds.

### 5.1.2 Time intervals of interest

For time frequency analysis the time intervals selected for ictal and non-ictal GSWDs were as follows: pre-ictal/non-ictal (10 seconds), during-ictal/ non-ictal (entire event), and post-ictal/non-ictal (10 seconds).

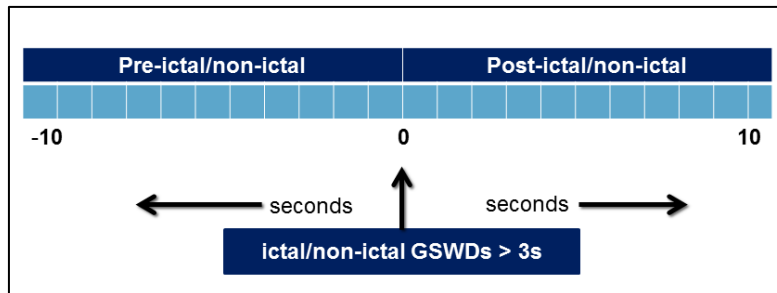


**Figure 5.1** Time intervals.

*Demonstration of the time intervals of interest.*

### 5.1.3 Pre-processing

Pre-processing refers to reading of the data, segmenting the data, temporal filtering and also re-referencing. This was done based on the pipeline implemented in the Fieldtrip toolbox [65] (<http://fieldtriptoolbox.org>). The toolbox carries out a series of calls to specific functions, which analyse the data conceptually. A configuration (*cfg*) is always used as an input for these functions. This contains all information regarding the dataset filenames, trials and pre-processing options. The basic pre-processing step can be achieved by the call to the function *ft\_preprocessing*. The specific segments of interest were firstly imported from the BESA software in the *.edf* format. For the pre-processing function firstly the dataset was loaded. After which the channel number was specified so that all or selected channels can be read. The pre-processing options for the channels selected include various filters, where various specifications can be applied such as: filter type, filter range, filter direction, filter window type etc. Also channel labels were specified based on the labels in the original EEG recording. The specifications for pre-processing used for this data, and run through MATLAB have been given below.

```
%%Pre-processing code as used in Fieldtrip software
cfg = [];
cfg.dataset = 'C:\Analysis\CAE\Patients CAE\P6-M.S\seizure\sz1.edf';
cfg.channel= [1:31];
cfg.bpfiler = 'yes';
cfg.bpfreq = [0.53 70];
cfg.bpfilttype = 'but';
cfg.bpfiltidir = 'twopass';
cfg.bpfiltwintype = 'hann';
cfg.dftfilter = 'yes';
cfg.dftfreq = [50];
data1 = ft_preprocessing(cfg);
data1.label = {'Fp1', 'Fp2', 'F7', 'F3', 'Fz', 'F4', 'F8', 'FC5', 'FC1',
'FC2', 'FC6', 'FT9', 'T7', 'C3', 'Cz', 'C4', 'T8', 'FT10', 'CP5', 'CP1',
'CP2', 'CP6', 'TP9', 'P7', 'P3', 'Pz', 'P4', 'P8', 'TP10', 'O1', 'O2'};
```

### 5.1.4 Artifact Removal

For artifact removal the method of independent component analysis (ICA) was implemented. For this, the software EEGLAB (<https://sccn.ucsd.edu/eeglab/index.php>) was used, which is also a toolbox working on the basis of MATLAB. The EEG data is usually contaminated with signals such as muscle artifacts, ocular artifacts, loose electrode connections and high amplitude events. It is important to correct these artifacts since they may distort results. ICA is a method which allows isolation and subtraction of statistically independent source activity as linear combinations of electrodes. In EEGLAB users can select various ICA algorithms for ICA decompositions. The algorithm *runica* is one of the default algorithms of this toolbox, and was used for this study to remove artifacts. This algorithm selects components which have a super gaussian activity distribution.

In this study the pre-processed data was firstly imported to EEGLAB. Then the layout of the electrodes based on the number was also loaded. The data was then subjected to the ICA algorithm (*runica*), which gave an output of independent components, based on the number of electrodes. Following the EEGLAB guide as well as a practical guide published by Chaumon et al. 2015 [93], certain components containing artifacts were removed. Subsequently the data was saved and exported back to Fieldtrip for further analysis.

The toolbox offers various options for visualizing the results. The independent components (ICs) can be viewed as topographical plots (Figure 4.2). Each of these topographical plots can further be viewed independently, as they include information regarding the activity of the power spectrum (Figure 4.3).

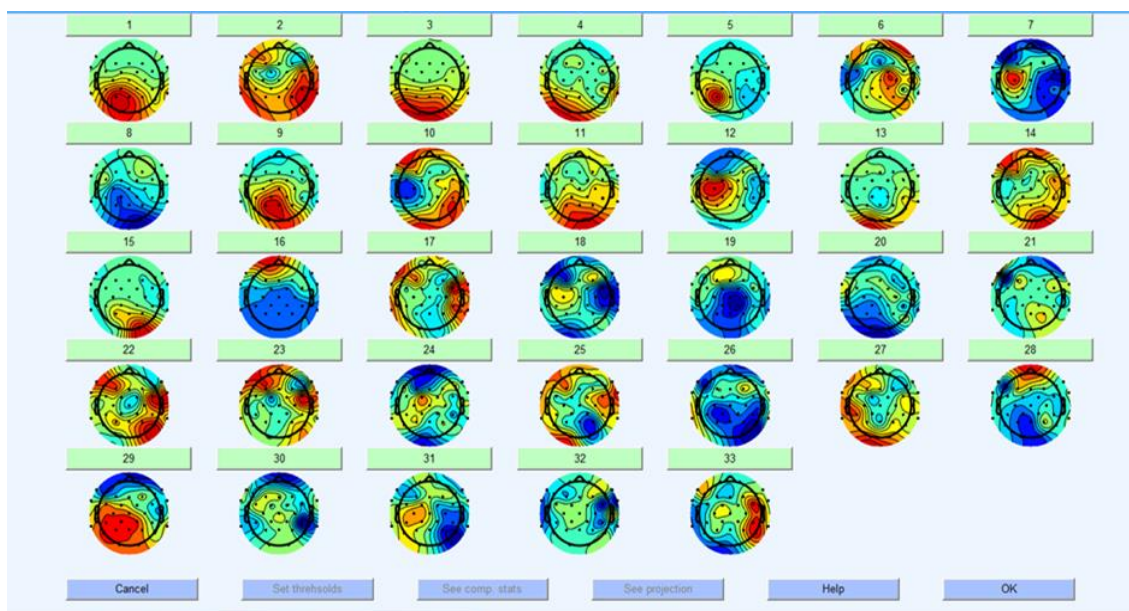


**Figure 5. 2 ICA topographical plots.**  
*Two dimensional topographical plots of the ICs.*

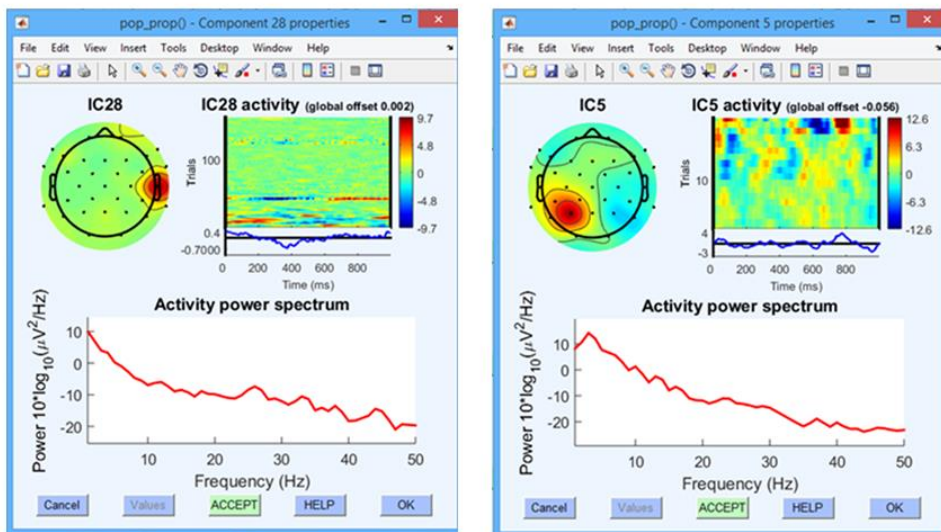


**Figure 5.3 ICA plot properties.**

*Examples of ICs depicting power spectrum activity. IC28 shows the presence of a muscle artifact, which would be removed and IC5 depicts a component without any presence of artifacts.*

### 5.1.5 Normalization

After artifact correction the data was normalized. Normalization is important before further steps of analysis, since the scales of measure for each patient differ drastically. Therefore to bring all the data to a standardized scale it is essential that normalization be done. For this study Z-score normalization was used. Once the data was loaded and read, the mean was subtracted firstly. Then the largest standard deviation was found over all selected segments and further, these segments were then divided by the largest standard deviation value. Once this was done, the datasets were saved.

### 5.1.6 Time Frequency (TF) Analysis

In Fieldtrip (<http://fieldtriptoolbox.org>) the function `ft_freqanalysis` performs frequency and time frequency analysis. This requires the input of various measures. Firstly for the configuration, the method ‘`mtmconvol`’ was chosen, which implements multitaper TF analysis based on multiplication in the frequency domain. Secondly the taper was chosen as the ‘Hanning’ window. For the output ‘`power-spectra`’ was chosen as an option. Following this the frequency of interest was specified as 0.5 to 35 Hz, covering all the ranges up to lower gamma frequency range, so that we can visualize the dominant frequency. Also, the time of interest was specified based on the segment of interest being analysed.

Visualization of the results was done using topographical plots as well as single plots of the channels. The topographical plots depict the changes in power underlying the data. The



function *ft\_topoplotTFR* is used to obtain topographical plots while, *ft\_singleplotTFR* is used for obtaining single plots of various electrodes. TF analysis was done for all time intervals of interest, for both ictal and non-ictal GSWDs>3 seconds.

```

%% Time-frequency analysis code as used in Fieldtrip software
cfg = [];
cfg.output = 'pow';
cfg.method = 'mtmconvol';
cfg.taper = 'hanning';
cfg.foi = 0.5:0.01:35;                                %0.5 to 35
cfg.t_ftimwin = ones (length(cfg.foi),1).*0.05;      %length of
time window is 0.5 sec
cfg.toi = 0:0.01:10;
freq_prel = ft_freqanalysis (cfg, dataprel);

```

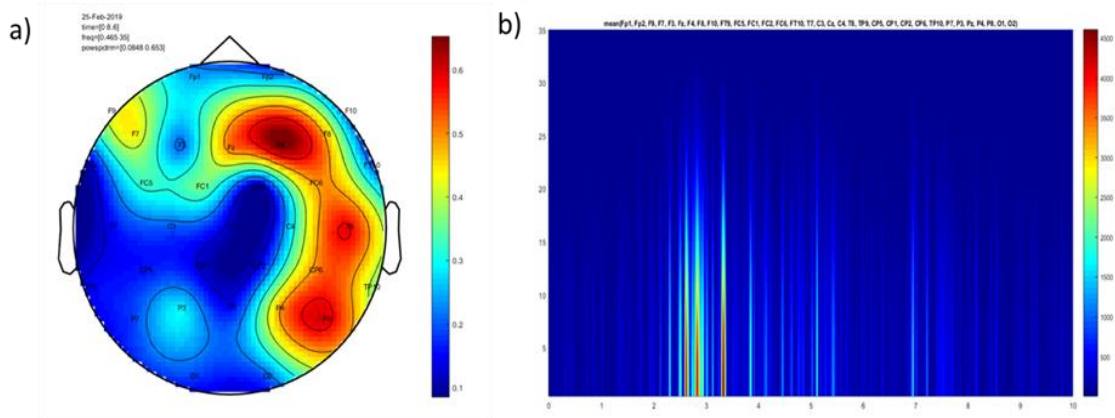


**Figure 5.4 Time frequency analysis.**

*Time frequency representations of power for visualization. a) Topographical plot b) single plot.*

### 5.1.7 Extraction of frequency band power

Following the TFA, per subject the various frequency values per channel were extracted. This involved extracting power spectral values of frequency bands: delta (0.5-4 Hz), theta (4-7 Hz), Alpha (8-13 Hz), Beta (13-30 Hz) and lower gamma (30-35 Hz).

### 5.1.8 Statistical analysis

Statistical analysis was done using the software SPSS (<https://www.ibm.com/id-en/products/spss-statistics>) [94]. This is a software package which includes various statistical tests which can be used easily and interactively. The two groups of interest, ictal and non-

ictal GSWDs > 3s were analysed by statistical tests separately and not compared with each other since not all patients had non-ictal GSWDs.

A repeated measure one way ANOVA [95] including descriptive statistics was applied to measure the 5 frequency bands (delta, theta, alpha, beta, gamma), extracted from TFA results of ictal and non-ictal GSWDs >3s. This test was used since there were and the subjects being tested were same in all. This test is used for related groups or within subject analysis. It measures the mean of three or more groups for comparison, where the subjects are same in each group.

The null hypothesis ( $H_0$ ) for this measure states that the means are equal and this can be shown as follows:

$$H_0: \mu_1 = \mu_2 = \mu_3 = \dots = \mu_k$$

Where,

$\mu$  = population mean

$k$  = number of related groups

Additionally, the alternative hypothesis ( $H_A$ ) would be that the related population means are not equal, i.e.:

$$H_A: \textit{at least two means are significantly different}$$

A repeated measure ANOVA only tells if there is a significant difference between the means, but does not give where the difference lies. For this test certain relevant assumptions are made which have been described below.

Assumptions:

1. Independent observations
2. Multivariate normal distribution: test variables in the population follow this, but if the sample size is  $\geq 25$  then this assumption is not required.
3. Sphericity: the population variances of the differences between all combinations of related groups must be equal. This is usually tested using the Mauchly's test.

Firstly the values extracted per frequency band per subject were averaged. Then, a one way repeated measure ANOVA was run on the five frequency bands. This test was used to analyse the five frequency bands separately in the two groups of interest, to know if there is a significant difference in the means. This was done for all time points of interest.

In SPSS, the repeated measure one way ANOVA, gives an output of descriptive statistics, multivariate tests, Mauchley's test for sphericity, and tests for within subject effects and tests for between subjects effect.

## 5.2 Results

### 5.2.1 During-ictal GSWDs

#### a) Descriptive statistics

On applying the repeated measure one way ANOVA test, descriptive statistics revealed the mean and standard deviation of the averaged power spectral values for all frequency bands. This helps us understand certain patterns in the data.

It was observed that the mean of delta frequency was highest (mean=0.42, SD=0.126) compared to the others. Followed by theta frequency (mean=0.39, SD 0.118), then alpha frequency (mean=0.30, SD=0.094), then beta frequency (mean=0.11, SD= 0.042), and lastly lower gamma frequency (mean=0.01, SD=0.013). These have been depicted in tables 4.

Descriptive Statistics			
	Mean	Std. Deviation	N
Delta	.424395058872265	.126817204169155	44
theta	.393824544407524	.118248228531745	44
alpha	.308819367755157	.094697445668572	44
beta	.117650133168901	.042463951041578	44
gamma	.017592531910557	.013740015848058	44

**Table 5.2 Descriptive statistics for during-ictal GSWDs interval.**

#### b) Mauchly's Test for sphericity

Following this, the Mauchly's test for sphericity was checked to see, if the data meets the assumption. The null hypothesis for this test is that the variances of the differences are equal. Therefore if this test shows statistical significance ( $p < .05$ ) then the null hypothesis can be rejected and the alternative hypothesis that the variances of the differences are not equal gets accepted.

Mauchly's Test of Sphericity							
Measure: MEASURE_ictal							
Within Subjects Effect	Mauchly's W	Approx. Chi-Square	df	Sig.	Epsilon		
					Greenhouse-Geisser	Huynh-Feldt	Lower-bound
Frequency	.000	925.291	9	.000	.252	.253	.250

**Table 5.3 Mauchly's test of sphericity for during-ictal interval.**

*The values marked in green are of importance.*

In this study the assumption of sphericity was not met, as the p-value was less than .05. This can be represented using the values of Chi-Square, degrees of freedom and p-value as given below:

The Mauchley's test of sphericity:  $\chi^2(9) = 925.291, p = .000$

**c) Test of within subject effects**

This test gives the main ANOVA results depicting level of significance. The results for ictal GSWDs are demonstrated in Table 6. Since the test for sphericity was not met, the correction test Greenhouse-Geisser is accepted, which relies on estimating the sphericity. The degree of freedom (df), F-ratio (F), and the significance level (Sig) are important to understand the results.

Tests of Within-Subjects Effects							
Measure: MEASURE_ictal							
Source		Type III Sum of Squares	df	Mean Square	F	Sig.	Partial Eta Squared
Frequency	Sphericity Assumed	5.547	4	1.387	519.467	.000	.924
	Greenhouse-Geisser	5.547	1.010	5.493	519.467	.000	.924
	Huynh-Feldt	5.547	1.010	5.489	519.467	.000	.924
	Lower-bound	5.547	1.000	5.547	519.467	.000	.924
Error(Frequency)	Sphericity Assumed	.459	172	.003			
	Greenhouse-Geisser	.459	43.419	.011			
	Huynh-Feldt	.459	43.449	.011			
	Lower-bound	.459	43.000	.011			

**Table 5.4 Tests for within subject effects for during-ictal interval.**

*Here we focus on the Greenhouse-Geisser test, the values marked in green are of importance.*

Based on the Greenhouse-Geisser correction test, repeated measure ANOVA showed that the p-value is less than 0.05, hence the null hypothesis is rejected. Therefore, there is a **significant difference** between the means of the frequencies measured in ictal GSWDs.

The results show that:  $df=1.010, \text{error } df = 43.419, F\text{-ratio} = 519.467, p = 0.000$

This can be reported as:  $F(1.010, 43.419) = 519.467, p < 0.05$

**d) Plot**

To visualize the data, SPSS gives an output based on estimated marginal means. The frequency is plotted on the X axis while the estimated marginal means are shown on the Y axis.

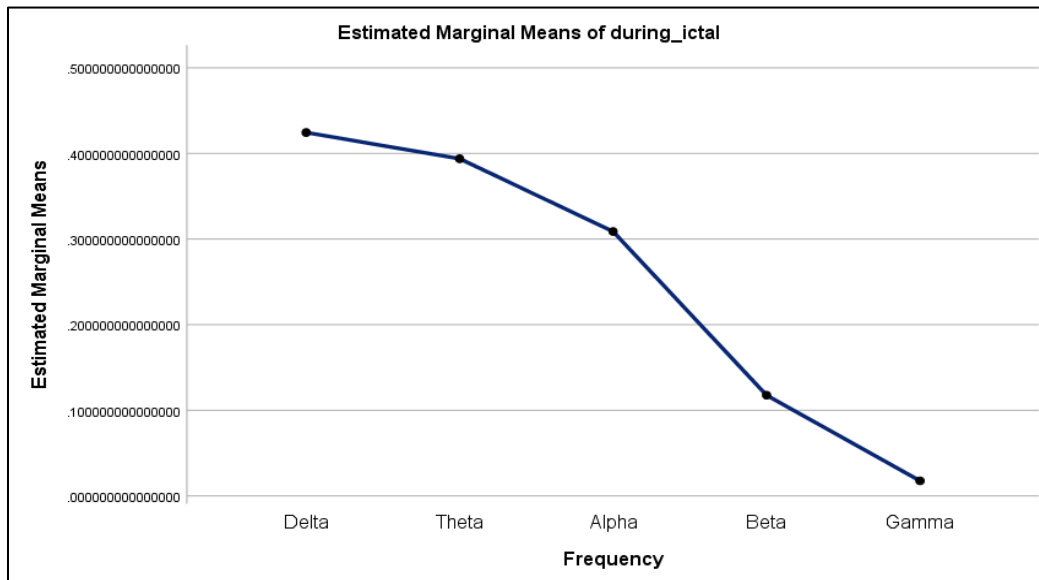


**Figure 5.5 Estimated marginal means for during-ictal interval.**

**4.2.2 Pre-ictal GSWDs**

**a) Descriptive statistics**

Descriptive statistics for the pre-ictal time interval showed that the mean of delta frequency was highest (mean=0.027, SD=0.022) compared to the others. Followed by theta frequency (mean=0.025, SD=0.020), then alpha frequency (mean=0.019, SD=0.015), then beta frequency (mean=0.007, SD=0.005), and lastly lower gamma frequency (mean=0.0008, SD=0.0004).

<b>Descriptive Statistics</b>			
	Mean	Std. Deviation	N
delta	.027368124257318	.022679480045505	44
theta	.025309631411739	.020867270320216	44
alpha	.019608152698974	.015885301881579	44
beta	.007046180914299	.005277879041365	44
gamma	.000803885981625	.000435857907978	44

**Table 5.5 Descriptive statistics for pre-ictal interval.**

**b) Mauchley's test for sphericity**

For the pre-ictal interval the Mauchley's test for sphericity showed that the assumption of sphericity was not met ( $p$ -value < 0.05).

The Mauchley's test of sphericity:  $\chi^2(9) = 1654.958, p = .000$

Mauchly's Test of Sphericity <sup>a</sup>							
Pre-ictal							
Within Subjects Effect	Mauchly's W	Approx. Chi-Square	df	Sig.	Epsilon <sup>b</sup>		
					Greenhouse-Geisser	Huynh-Feldt	Lower-bound
Frequency	.000	1654.958	9	.000	.250	.250	.250

**Table 5.6 Mauchley's test of sphericity for pre-ictal interval.**

**c) Test of within subject effects**

As mentioned before this test gives the main ANOVA results depicting the level of significance. Since the test for sphericity was not met for the pre-ictal interval, the correction test Greenhouse-Geisser was used.

Tests of Within-Subjects Effects							
Measure: Pre-ictal							
Source		Type III Sum of Squares	df	Mean Square	F	Sig.	Partial Eta Squared
Frequency	Sphericity Assumed	.024	4	.006	61.898	.000	.590
	Greenhouse-Geisser	.024	1.000	.024	61.898	.000	.590
	Huynh-Feldt	.024	1.001	.024	61.898	.000	.590
	Lower-bound	.024	1.000	.024	61.898	.000	.590
Error(Frequency)	Sphericity Assumed	.017	172	9.597E-5			
	Greenhouse-Geisser	.017	43.021	.000			
	Huynh-Feldt	.017	43.022	.000			
	Lower-bound	.017	43.000	.000			

**Table 5.7 Tests of within subject effects for pre-ictal interval.**

Repeated measure ANOVA based on the Greenhouse-Geisser correction test, showed that the  $p$ -value is less than 0.05, which in return rejects the null hypothesis. Hence, there is a **significant difference** between the means of the frequencies measured in the pre-ictal GSWDs interval.

For this test:  $df=1.000$ , error  $df = 43.021$ ,  $F$ -ratio =  $61.898$ ,  $p = 0.000$

This can be represented as:  $F(1.000, 43.021) = 61.898, p < 0.05$

**d) Plot**

The estimated marginal means of the pre-ictal interval have been demonstrated in the plot below. On X axis the frequency has been demonstrated while on the Y axis the estimated marginal means are given.

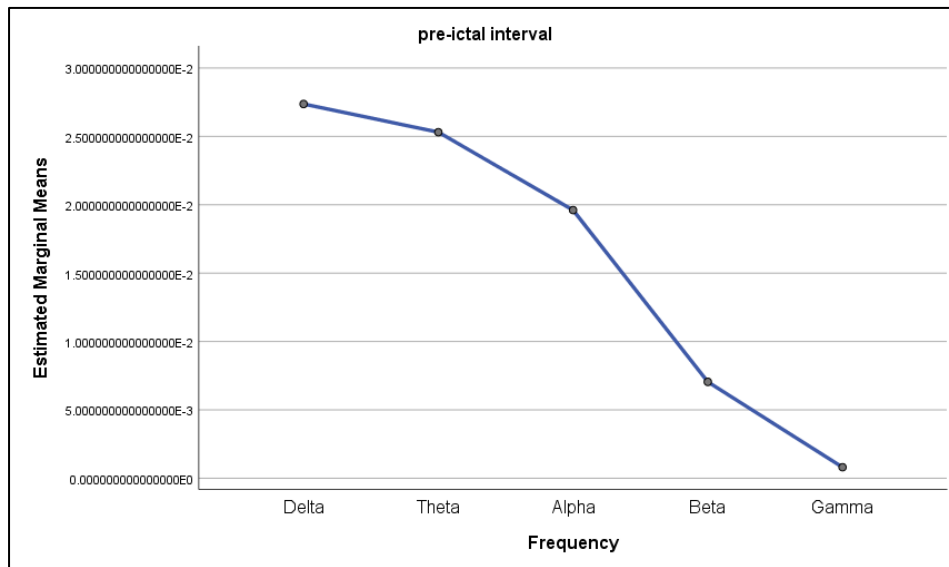


**Figure 5.6 Estimated marginal means for pre-ictal interval.**

**5.2.3 Post-ictal GSWDs**

**a) Descriptive statistics**

Descriptive statistics for the post-ictal time interval also showed a similar trend like during-ictal and pre-ictal intervals. Delta frequency had the highest mean (mean=0.042, SD=0.053), followed by theta frequency (mean=0.039, SD=0.049), then alpha frequency (mean=0.030, SD=0.037), then beta frequency (mean=0.010, SD=0.012), and lastly lower gamma frequency (mean=0.001, SD=0.001).

Descriptive Statistics			
	Mean	Std. Deviation	N
delta	.042735876444539	.053224899355817	44
theta	.039435933314620	.049049577083532	44
alpha	.030325484107798	.037545030459987	44
beta	.010549528523539	.012791412957849	44
gamma	.001024128238538	.001147816118244	44

**Table 5.8 Descriptive statistics for post-ictal interval.**

### b) Mauchly's test for sphericity

For the post-ictal interval the Mauchly's test for sphericity also showed that the assumption of sphericity was not met ( $p$ -value  $< 0.05$ ).

The Mauchly's test of sphericity:  $\chi^2(9) = 1936.451$ ,  $p = .000$

Mauchly's Test of Sphericity <sup>a</sup>							
Measure: Post-ictal							
Within Subjects Effect	Mauchly's W	Approx. Chi-Square	df	Sig.	Epsilon <sup>b</sup>		
					Greenhouse-Geisser	Huynh-Feldt	Lower-bound
Frequency	.000	1936.451	9	.000	.250	.250	.250

**Table 5.9 Mauchly's test of sphericity for post-ictal interval.**

### c) Test of within subject effects

Following the test of sphericity, the test of within subject effects was investigated. Here also the correction test Greenhouse-Geisser was used, because the test of sphericity was not met. The Greenhouse-Geisser correction test showed that the  $p$ -value is less than 0.05, which in return rejects the null hypothesis. Hence, there is a **significant difference** between the means of the frequencies measured in the interval of post-ictal GSWDs.

For this test:  $df=1.000$ , error  $df = 43.014$ ,  $F$ -ratio = 28.064,  $p = 0.000$

This can be represented as:

$F(1.000, 43.014) = 28.064$ ,  $p < 0.05$

Tests of Within-Subjects Effects							
Measure: Post-ictal							
Source		Type III Sum of Squares	df	Mean Square	F	Sig.	Partial Eta Squared
Frequency	Sphericity Assumed	.059	4	.015	28.064	.000	.395
	Greenhouse-Geisser	.059	1.000	.059	28.064	.000	.395
	Huynh-Feldt	.059	1.000	.059	28.064	.000	.395
	Lower-bound	.059	1.000	.059	28.064	.000	.395
Error(Frequency)	Sphericity Assumed	.090	172	.001			
	Greenhouse-Geisser	.090	43.014	.002			
	Huynh-Feldt	.090	43.015	.002			
	Lower-bound	.090	43.000	.002			

**Table 5.10 Tests of within subject effects for post-ictal interval.**



**d) Plot**

For the post-ictal interval, the estimated marginal means have been demonstrated in the plot below. The estimated marginal mean values are low for all frequency bands. Delta band has the highest mean value while gamma band has the lowest.

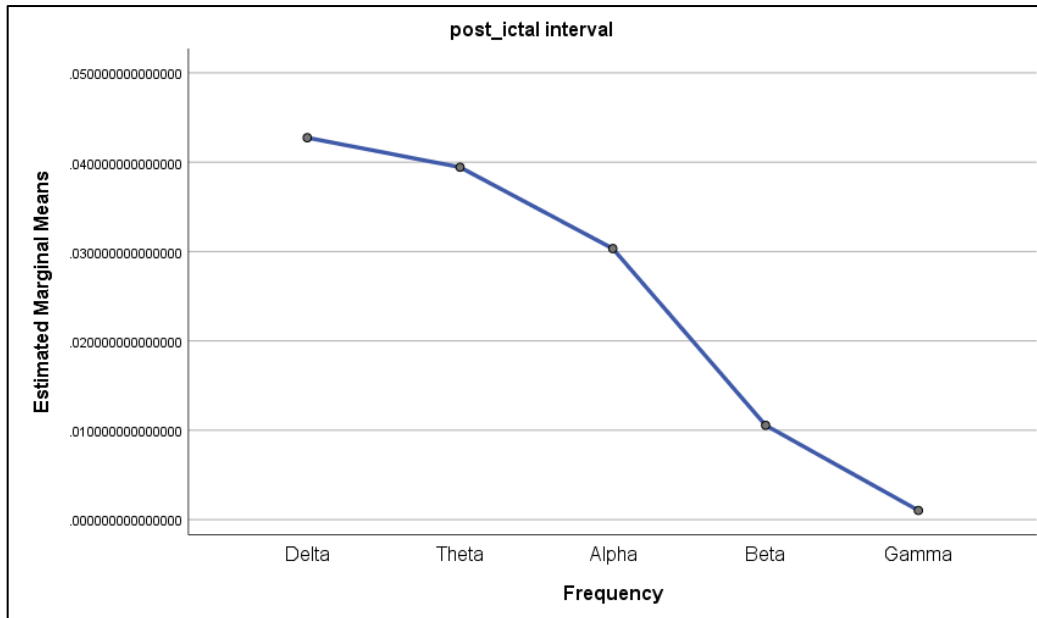


**Figure 5.7 Estimated marginal means for post-ictal interval.**

**5.2.4 During-non-ictal GSWDs>3s**

**a) Descriptive statistics**

Similar to the results of ictal GSWDs, the repeated measure one way ANOVA test gave descriptive statistics with the mean and standard deviation for all frequency bands. The sample size was 23 for all bands.

Descriptive Statistics			
	Mean	Std. Deviation	N
Delta	.388035295226858	.174648550946402	23
theta	.359054111945618	.161788659160174	23
alpha	.278501376682356	.126019777071992	23
beta	.101110224972053	.046898036387950	23
gamma	.012294320992910	.006849599527184	23

**Table 5.11 Descriptive statistics for during-non-ictal GSWDs > 3 seconds.**

It was seen that for non-ictal GSWDs, a similar trend like the ictal GSWDs was seen regarding the mean values. Delta frequency was highest (mean=0.38, SD=0.17), followed by theta frequency (mean=0.35, SD 0.16), then alpha frequency (mean=0.27, SD=0.12), then beta frequency (mean=0.10, SD= 0.04), and lastly lower gamma frequency (mean=0.01, SD=0.006).

### b) Mauchly's Test for sphericity

In the case of non-ictal GSWDs, the Mauchly's test for sphericity demonstrated significance since the p-value was 0.000. Therefore the null hypothesis was rejected and the alternative hypothesis was accepted being, that the variances of the differences are not equal.

Mauchly's Test of Sphericity <sup>a</sup>							
Measure: MEASURE_non-ictal							
Within Subjects Effect	Mauchly's W	Approx. Chi-Square	df	Sig.	Epsilon <sup>b</sup>		
					Greenhouse-Geisser	Huynh-Feldt	Lower-bound
frequency	.000	528.595	9	.000	.250	.250	.250

**Table 5.12 Mauchly's test of sphericity for durin-non-ictal GSWDs > 3 seconds.**

The assumption of sphericity was not met for non-ictal GSWDs, and these results can be reported as follows:  $\chi^2(9) = 528.595, p = .000$

### c) Test of within subject effects

Similar to ictal GSWDs results, since the test for sphericity was not met, the correction test Greenhouse-Geisser is evaluated to understand the main results of the repeated measure one way ANOVA. The degree of freedom (df), F-ratio (F), and the significance level (Sig) are essential to interpret the results.

Tests of Within-Subjects Effects							
Measure: MEASURE_non-ictal							
Source		Type III Sum of Squares	df	Mean Square	F	Sig.	Partial Eta Squared
frequency	Sphericity Assumed	2.483	4	.621	114.696	.000	.839
	Greenhouse-Geisser	2.483	1.001	2.482	114.696	.000	.839
	Huynh-Feldt	2.483	1.001	2.482	114.696	.000	.839
	Lower-bound	2.483	1.000	2.483	114.696	.000	.839
Error(frequency)	Sphericity Assumed	.476	88	.005			
	Greenhouse-Geisser	.476	22.011	.022			
	Huynh-Feldt	.476	22.013	.022			
	Lower-bound	.476	22.000	.022			

**Table 5. 13 Tests for within subject effects for during-non-ictal GSWDs > 3 seconds.**

*Here we focus on the Greenhouse-Geisser test, the values marked in green are of importance.*

As seen above in Table 9, the Greenhouse-Geisser correction test, revealed that the  $p$ -value is .000 i.e.  $p < 0.05$ , therefore the null hypothesis gets rejected. Hence, there is a **significant difference** between the mean values of the five frequency bands measured in non-ictal GSWDs.

The results demonstrate:  $df=1.001$ , error  $df = 22.011$ ,  $F\text{-ratio} = 114.696$ ,  $p = 0.000$

This can be reported as:  $F(1.001, 22.011) = 114.696$ ,  $p < 0.05$

#### d) Plot

For visualization of the dataset, as described before in the case of ictal GSWDs, an output based on estimated marginal means is given by SPSS. The frequency is plotted on the X axis while the estimated marginal means are shown on the Y axis.

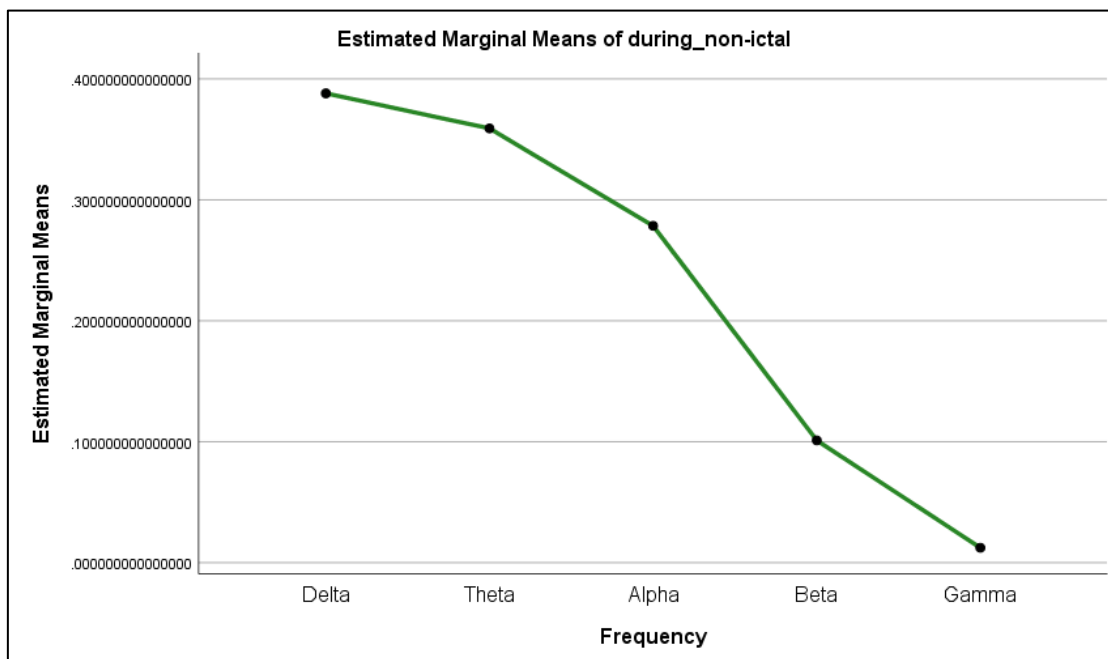


**Figure 5.8 Estimated marginal means for during-non-ictal interval.**

### 5.2.5 Pre-non-ictal GSWDs>3s

#### a) Descriptive statistics

Similar to the results so far, descriptive statistics for the pre interval, in non-ictal GSWDs showed that delta frequency had the highest mean (mean=0.029, SD=0.022), followed by theta frequency (mean=0.027, SD=0.020), then alpha frequency (mean=0.021, SD=0.015), then beta frequency (mean=0.007, SD=0.005), and lastly lower gamma frequency (mean=0.001, SD=0.0006). The sample size for pre-interval for all frequency bands was 19.

Descriptive Statistics			
	Mean	Std. Deviation	N
delta	.029849471515114	.022449263691771	19
theta	.027599595143118	.020635773823953	19
alpha	.021386056657250	.015673957601487	19
beta	.007834142704386	.005301717455837	19
gamma	.001162949010769	.000697773707102	19

**Table 5.14 Descriptive statistics for pre-non-ictal GSWDs > 3 seconds.**

**b) Mauchly's test for sphericity**

For the pre-non-ictal interval the Mauchly's test for sphericity also showed that the assumption of sphericity was not met (p-value < 0.05).

The Mauchly's test of sphericity:  $\chi^2(9) = 628.623$ ,  $p = .000$

Mauchly's Test of Sphericity <sup>a</sup>							
Measure: pre-non-ictal							
Within Subjects Effect	Mauchly's W	Approx. Chi-Square	df	Sig.	Epsilon <sup>b</sup>		
					Greenhouse-Geisser	Huynh-Feldt	Lower-bound
Frequency	.000	628.623	9	.000	.250	.250	.250

**Table 5.15 Mauchly's test of sphericity for pre-non-ictal GSWDs > 3 seconds.**

**c) Test of within subject effects**

Tests of Within-Subjects Effects							
Measure: Pre-non-ictal							
Source		Type III Sum of Squares	df	Mean Square	F	Sig.	Partial Eta Squared
Frequency	Sphericity Assumed	.012	4	.003	32.489	.000	.643
	Greenhouse-Geisser	.012	1.000	.012	32.489	.000	.643
	Huynh-Feldt	.012	1.000	.012	32.489	.000	.643
	Lower-bound	.012	1.000	.012	32.489	.000	.643
Error(Frequency)	Sphericity Assumed	.007	72	9.210E-5			
	Greenhouse-Geisser	.007	18.007	.000			
	Huynh-Feldt	.007	18.008	.000			
	Lower-bound	.007	18.000	.000			

**Table 5.16 Tests of within-subject effects for pre-non-ictal GSWDs > 3 seconds.**

Here we focus on the Greenhouse-Geisser test, the values marked in green are of importance.

Since the test for sphericity was not met in this case the Greenhouse-Geisser correction test was accepted. The Greenhouse-Geisser correction test showed that the  $p$ -value is less than 0.05, which in return rejects the null hypothesis. Hence, there is a **significant difference** between the means of the frequencies measured in the interval of post-ictal GSWDs.

For this test:  $df=1.000$ , error  $df = 18.007$ ,  $F\text{-ratio} = 32.489$ ,  $p = 0.000$

This can be represented as:  $F(1.000, 18.007) = 32.489, p < 0.05$

#### d) Plot

For the pre-non-ictal interval, the estimated marginal means have been demonstrated in the plot below. Delta band has the highest estimated marginal mean while gamma band has the lowest.

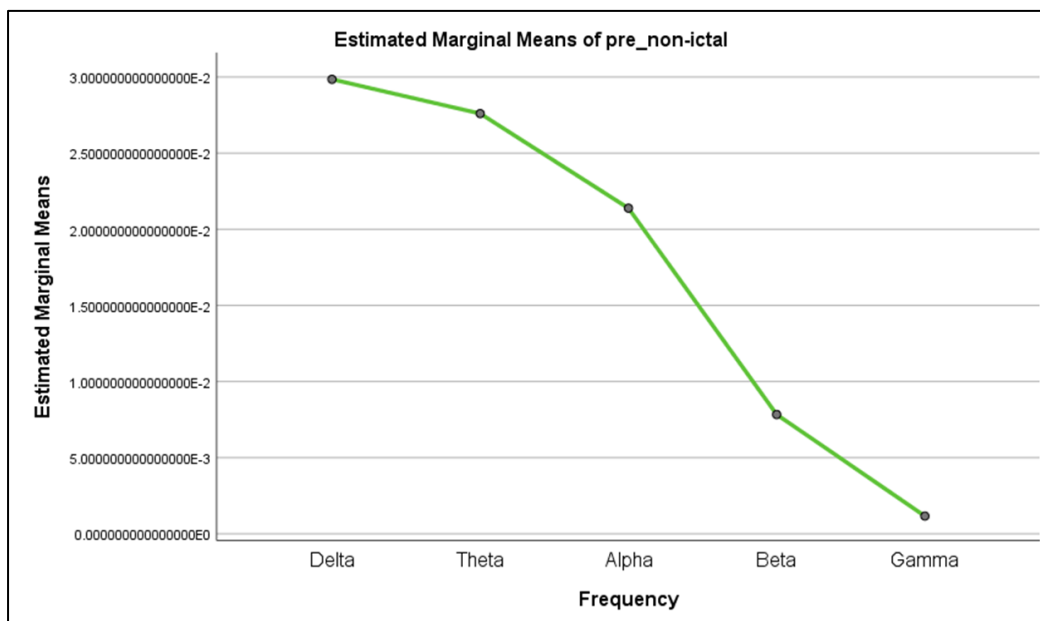


**Figure 5.9 Estimated marginal means for pre-non-ictal interval.**

### 5.2.6 Post-non-ictal GSWDs>3s

#### a) Descriptive statistics

For post-non-ictal interval also delta frequency had the highest mean (mean=0.046, SD=0.040), followed by theta frequency (mean=0.043, SD=0.037), then alpha frequency (mean=0.033, SD=0.028), then beta frequency (mean=0.011, SD=0.010), and lastly lower gamma frequency (mean=0.001, SD=0.001). The sample size for all frequency bands in the post-interval was 21.

Descriptive Statistics			
	Mean	Std. Deviation	N
delta	.046996836959631	.040603931013163	21
theta	.043401420266656	.037449200167816	21
alpha	.033482562542249	.028768884004730	21
beta	.011969258229357	.010140864628450	21
gamma	.001518387030354	.001284712550068	21

**Table 5.17 Descriptive statistics for post-non-ictal GSWDs > 3 seconds.**

**b) Mauchley's test for sphericity**

For the post-non-ictal interval the Mauchley's test for sphericity also showed that the assumption of sphericity was not met (p-value < 0.05).

The Mauchley's test of sphericity:  $\chi^2(9) = 815.277$ ,  $p = .000$

Mauchly's Test of Sphericity							
Measure: post-non-ictal							
Within Subjects Effect	Mauchly's W	Approx. Chi-Square	df	Sig.	Epsilon <sup>b</sup>		
					Greenhouse-Geisser	Huynh-Feldt	Lower-bound
Frequency	.000	815.277	9	.000	.250	.250	.250

**Table 5. 18 Mauchley's test of sphericity for post-non-ictal GSWDs > 3 seconds.**

**c) Test of within subject effects**

Tests of Within-Subjects Effects							
Measure: Post-non-ictal							
Source		Type III Sum of Squares	df	Mean Square	F	Sig.	Partial Eta Squared
Frequency	Sphericity Assumed	.033	4	.008	27.983	.000	.583
	Greenhouse-Geisser	.033	1.000	.033	27.983	.000	.583
	Huynh-Feldt	.033	1.000	.033	27.983	.000	.583
	Lower-bound	.033	1.000	.033	27.983	.000	.583
Error(Frequency)	Sphericity Assumed	.024	80	.000			
	Greenhouse-Geisser	.024	20.004	.001			
	Huynh-Feldt	.024	20.005	.001			
	Lower-bound	.024	20.000	.001			

**Table 5.19 Tests of within-subject effects for post-non-ictal GSWDs > 3 seconds.**

Similar to the above results, the Greenhouse-Geisser correction test showed that the  $p$ -value is less than 0.05, which in return rejects the null hypothesis. Hence, there is a **significant difference** between the means of the frequencies measured in the interval of post-ictal GSWDs. For this test:  $df=1.000$ , error  $df = 20.004$ ,  $F\text{-ratio} = 27.983$ ,  $p = 0.000$

This can be represented as:

$$F(1.000, 20.004) = 27.983, p < 0.05$$

#### d) Plot

For the post-non-ictal interval, the estimated marginal means have been demonstrated in the plot below. The estimated marginal mean values are low for all frequency bands.

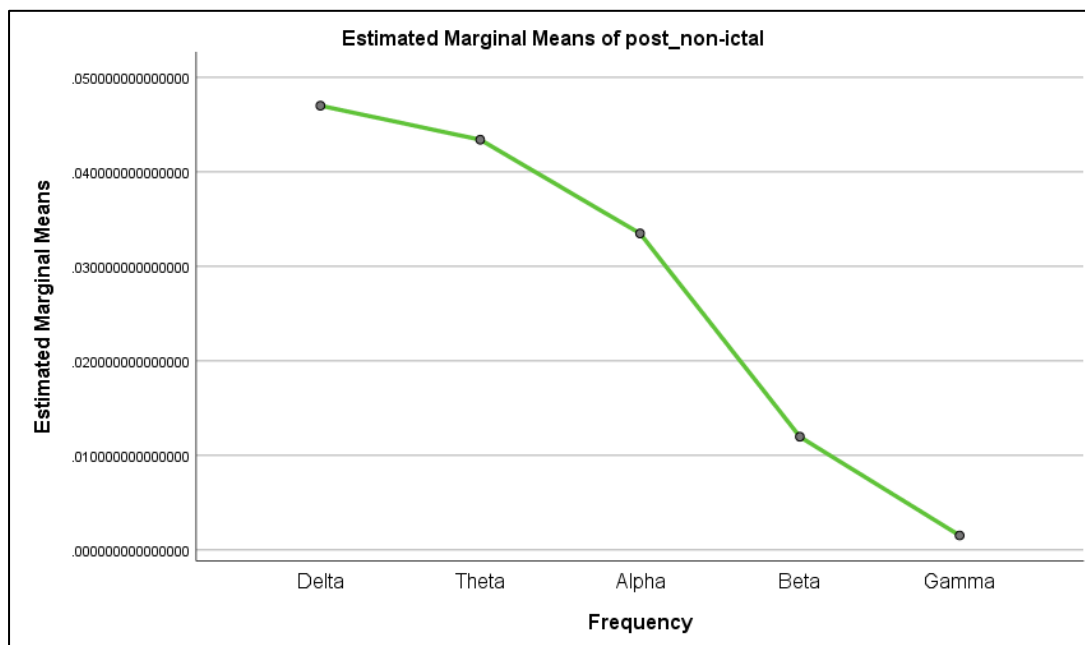


**Figure 5.10 Estimated marginal means of post-non-ictal interval.**

# Chapter 6

## Sensor-level Spectral analysis and Functional connectivity

---

In this chapter spectral analysis and functional connectivity (FC) was done for ictal and non-ictal GSWDs at sensor level. Spectral analysis was done to observe the significant power spectral changes in frequency bands, while FC was computed between the channels to better understand the surface networks between ictal and non-ictal GSWDs. The theoretical background regarding the techniques being used in this chapter has been described in detail in chapter 2. The results of this chapter have been submitted for publication to the journal *Epilepsy Research* [96].

### 6.1 Methods

#### 6.1.1 Subjects

Subjects selected for this part of the sensor level study have been described in detail in chapter 3. The ictal and non-ictal GSWDs were selected from 12 patients and were further subjected to analysis.

#### 6.1.2 Pre-processing

The pre-processing of the data for frequency analysis also involved using the Fieldtrip software (<http://fieldtriptoolbox.org>). The raw EEG data was firstly band-pass filtered between the range of 0.1 Hz and 31 Hz. Band pass filtering helps remove unwanted frequencies from the data. Following this, independent component analysis (ICA) was used to suppress eye-blinks and eye-movement artefacts. The function for ICA in Fieldtrip is *ft\_componentanalysis*. This was computed using the method *'runica'*. This method implements decomposing the EEG data into its components, which can be further visualized as topographical plots. The components containing artifacts can then be removed from the dataset [97].

Once artifact removal was completed, the EEG channels were re-referenced to the common average reference (CAR) [98]. In EEG, the issue of referencing exists. During recordings any activity present in the reference electrode, gets reflected in all other electrodes. Therefore any noise in the reference electrode will show up in all other electrodes. Thus, choosing a reference carefully is important. CAR is a technique that is reference free, and is not affected



by the issue that arises from an actual physical reference. In this method, the potential at every electrode is computed with respect to the average of all electrodes.

Further, the data was normalized to bring the dataset to a standardized measure, as mentioned in chapter 2 in equation (2.1). After normalization, the selected regions of interest were divided into 1 second long segments. This was done so that quantification of oscillations becomes easier.

### 6.1.3 Frequency analysis

Frequency analysis was conducted for the 1 second long segments by using a FFT with a Hanning window. The Fourier transform has been described in chapter 2, equation (2.2). This was done using the software Fieldtrip. This method was applied on the frequency range from 1-30 Hz and the window function was applied in steps of 1 Hz. This in return calculates the power spectrum (equation 2.4). These various specifications can be given as an input in Fieldtrip. The function that computes the frequency analysis is the *ft\_freqanalysis*, and the configuration used for the method was *mtmfft*. Following this the power values were averaged through the segments for every subject for both group's ictal and non-ictal GSWDs.

### 6.1.4 Functional Connectivity (FC)

For FC based on the imaginary part of coherency (iCOH) at sensor level, the Fieldtrip toolbox was used. Firstly, using the function *ft\_freqanalysis*, the complex Fourier spectrum was obtained. This spectrum consists of a matrix having  $N_{\text{channels}} \times \text{frequencies}$  (31x30). Secondly, using the function *ft\_connectivityanalysis* the connectivity between EEG channels was computed. The input for this function consisted of the method, which was based on coherence (*cfg.method = 'coh'*), and the complex configuration which would compute the absolute value of imaginary part of coherency (*cfg.complex = 'absimag'*). The imaginary part of coherency has been described in chapter 2, equation (2.19). The output of this function consists of a three dimensional matrix of  $N_{\text{channels}} \times N_{\text{channels}} \times \text{frequencies}$  (31x31x30). Further, the iCOH value for each frequency band was averaged.

### 6.1.5 Statistical analysis

The EEG data was analysed using a 2-way repeated measurement ANOVA, based on cluster permutation and non-parametric statistics as implemented in the FieldTrip toolbox. To avoid the condition that the data should have a normal distribution, a non-parametric approach via cluster-based Monte Carlo resampling is used to evaluate the ANOVA test [99, 100]. A cluster based approach was used to solve the multiple comparison problems.

Prior to the calculation of the significance probability, a cluster-based test statistic needs to be computed. Firstly a F-value is calculated for each of the sample points. This F-value is combined in a cluster if its value exceeds a threshold value of 0.05. After clusters are created, the within-cluster F-values are added to create a cluster-level statistic for each cluster. Finally

the maximum of the cluster-level statistics is chosen as the cluster-based test-statistic. This procedure was repeated for 2000 permuted data. After that, significance probability was estimated as a proportion between the numbers of cases with a larger test statistic than the observed one to the number of permutations. A p-value below 0.05 was considered significant.

A two-way repeated measurement ANOVA with two within-subjects factors (group x time) was performed for different frequency bands (delta 1-3 Hz, theta 4-7 Hz, alpha 8-12 Hz, beta 13-30 Hz) by averaging the respective power spectra in each frequency band. The "group" factor included two types of abnormal activity, ictal ( $\alpha_1$ ) and non-ictal ( $\alpha_2$ ) GSWDs. The "time" factor was analysed for three different time intervals: pre- ictal/non-ictal ( $\alpha_3$ ), during- ictal/non-ictal ( $\alpha_4$ ) and post- ictal/non-ictal ( $\alpha_5$ ). Firstly the time factor was analysed (Table 6.1), followed by the group effect (Table 6.2). Finally the interaction of the two factors was analysed (Table 6.3).

Groups	Time points		
	Pre ( $\alpha_3$ )	During( $\alpha_4$ )	Post ( $\alpha_5$ )
Ictal ( $\alpha_1$ )	( $\alpha_1$ ) ( $\alpha_3$ )	( $\alpha_1$ ) ( $\alpha_4$ )	( $\alpha_1$ ) ( $\alpha_5$ )
Non-ictal ( $\alpha_2$ )	( $\alpha_2$ ) ( $\alpha_3$ )	( $\alpha_2$ ) ( $\alpha_4$ )	( $\alpha_2$ ) ( $\alpha_5$ )

Time effect

**Table 6.1 Time effect.**

Groups	Time points		
	Pre ( $\alpha_3$ )	During( $\alpha_4$ )	Post ( $\alpha_5$ )
Ictal ( $\alpha_1$ )	( $\alpha_1$ ) ( $\alpha_3$ )	( $\alpha_1$ ) ( $\alpha_4$ )	( $\alpha_1$ ) ( $\alpha_5$ )
Non-ictal ( $\alpha_2$ )	( $\alpha_2$ ) ( $\alpha_3$ )	( $\alpha_2$ ) ( $\alpha_4$ )	( $\alpha_2$ ) ( $\alpha_5$ )

Group effect

**Table 6.2 Group effect.**

Groups	Time points		
	Pre ( $\alpha_3$ )	During( $\alpha_4$ )	Post ( $\alpha_5$ )
Ictal ( $\alpha_1$ )	( $\alpha_1$ ) ( $\alpha_3$ )	( $\alpha_1$ ) ( $\alpha_4$ )	( $\alpha_1$ ) ( $\alpha_5$ )
Non-ictal ( $\alpha_2$ )	( $\alpha_2$ ) ( $\alpha_3$ )	( $\alpha_2$ ) ( $\alpha_4$ )	( $\alpha_2$ ) ( $\alpha_5$ )

Interaction effect

**Table 6.3 Interaction effect (group x time).**

The function *ft\_freqstatistics* was used alongside a configuration implementing the two-way repeated measurement ANOVA (*cfg.statistic = depAnova2way*). The method for calculating

significant probabilities was specified to Monte-Carlo, a non-parametric permutation test (*cfg.method = 'montecarlo'*).

Further, a post-hoc test was performed for significant ANOVA results which have more than one pair of comparisons (time or interaction effects). The statistic function used for this computes a dependent sample T-statistic (*cfg.statistic= ft\_statfun\_depsamplesT*). For FC results, a two-way repeated measurement ANOVA was done per channel (31 times), corresponding to all other channels.

### 6.1.6 Visualization

For visualization Fieldtrip toolbox was used. Visualization of the spectral analysis and functional connectivity results were done using topographical plots. The electrode clusters showing significant activity have been marked by (x) or (\*). The function *ft\_topoplotER* was used to visualize frequency analysis results. The power differences have also been demonstrated graphically in the form of bar plots. For FC the function *ft\_plot\_lay* was used. The connectivity between the channels was depicted using different colours. The colour of the connectivity lines demonstrated the significant difference of iCOH for every condition. The colour red depicted stronger connectivity while blue depicted weaker connectivity between the channels.

## 6.2 Results

### 6.2.1 Spectral Analysis results

On applying a two factor (*group x time*) ANOVA on the dataset, it was revealed that for the main effect of *time*, all frequency bands over all channels showed significance. While for the main effect of *group*, except for theta band all frequency bands showed significance. The interaction between *group* and *time* factors also revealed significance for delta, alpha and beta band but not for theta band.

Post-hoc test for main effect of time revealed that the during-ictal/non-ictal interval has higher power compared to pre- and post- ictal/non-ictal intervals in all frequency bands (Fig.1b). Post- ictal/non-ictal interval showed significant higher power compared to pre-ictal/non-ictal interval for delta and theta bands. The main effect of group for delta, alpha and beta band showed that ictal GSWDs had higher power compared to non-ictal GSWDs. These significant differences were observed in fronto-central, centro-parietal and temporal regions for delta band (electrodes: FC2, Cz, C4, CP1, CP2, Pz, T4, TP10). For alpha band significant differences were widespread in frontal, fronto-central, centro-parietal and temporal regions (electrodes: Fp1, F3, Fz, FC5, FC1, FCz Cz, C4, CP2, Pz FT10, TP9, TP10). For beta band these significant differences were localized mostly in centro-parietal, temporal and occipital regions (electrodes: Cz, CP1, CP5, CPz, CP6, Pz, P4, FT10, T4, TP9, TP10, O2). For interaction effect, post-hoc tests were performed for delta, alpha and beta bands. The power

changes in delta band from pre-ictal state to during-ictal state were higher compared to the corresponding changes in non-ictal states. These differences were localized primarily in the central region (electrodes: FC2, Cz, C4, CP2). For alpha and beta frequency bands also the transition periods of ictal GSWDs had higher power compared to the non-ictal GSWDs. The power changes in alpha band were localized in the frontal, frontal-central, temporal regions (electrodes: F3, Fz, FC5, FC1, FC2, T3, Cz, C4, TP9) and for beta band in the fronto-parietal, centro-parietal, temporal and parietal regions (electrodes: FP1, FP2, F7, FT10, CP1, CP2, CP6, TP10, T4, Pz, P4).

Frequency bands	Factor	<i>p</i> value
Delta (1-3 Hz)	time	0.0009
	group	0.01
	time x group	0.04
Theta (4-7 Hz)	time	0.0009
	group	no clusters
	time x group	no clusters
Alpha (8-12 Hz)	time	0.0009
	group	0.02
	time x group	0.01
Beta (13-30 Hz)	time	0.0009
	group	0.02
	time x group	0.006

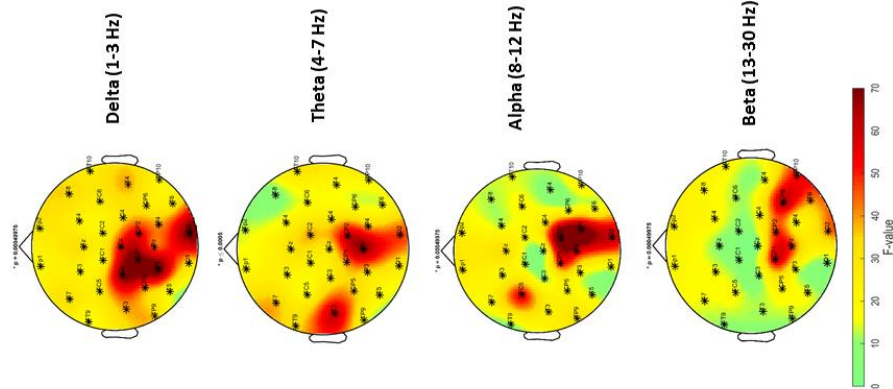
**Table 6.4 Spectral analysis p-values for two way ANOVA test.**

Conditions	Delta (1-3 Hz)	Theta (4-7 Hz)	Alpha (8-12 Hz)	Beta (13-30 Hz)
<b>Effect of Time</b>				
during vs. pre	0.0009	0.0009	0.0009	0.0009
during vs. post	0.0009	0.0009	0.0009	0.0009
post vs. pre	0.008	0.04	-	-
<b>Effect of Group</b>				
ictal vs. nonictal	0.01	-	0.01	0.02
<b>Interaction: time x group</b>				
ictal <sub>during-pre</sub> vs. nonictal <sub>during-pre</sub>	0.01	-	0.01	0.01
ictal <sub>during-post</sub> vs. nonictal <sub>during-post</sub>	-	-	0.01	0.007
ictal <sub>post-pre</sub> vs. non-ictal <sub>post-pre</sub>	-	-	-	-

**Table 6.5 Spectral analysis p-values for Post hoc comparisons. (- no significance)**

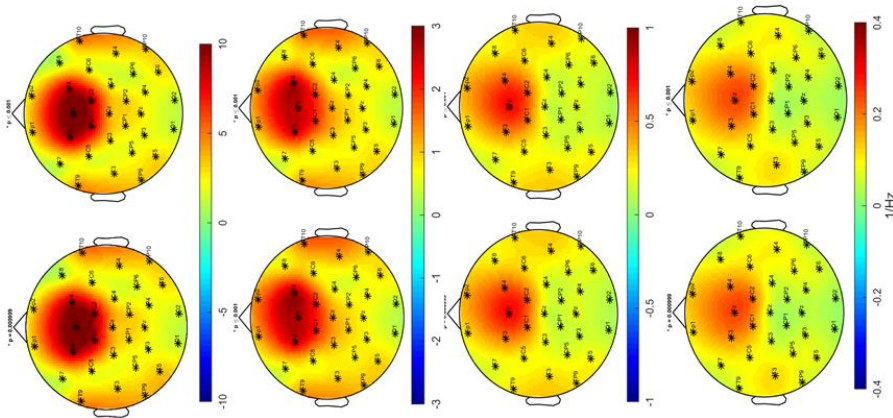
### Sensor level: Time Effect

1a) Two way ANOVA



1b) Post-hoc test

during vs. pre during vs. post



Significance: x  $p < 0.05$  \*  $p < 0.01$

during vs. pre during vs. post

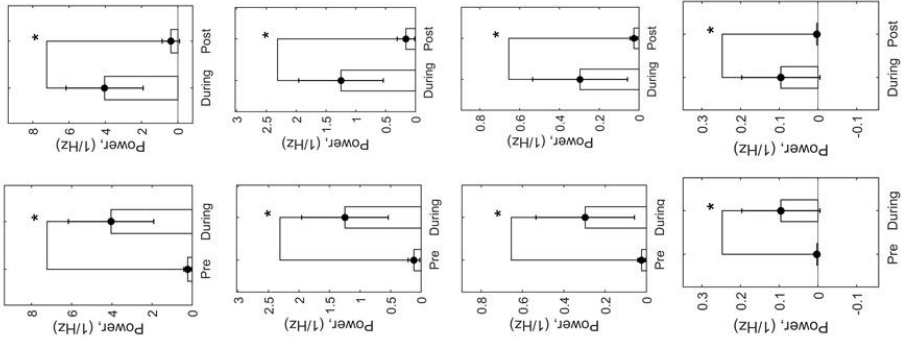


**Figure 6.1 Spectral analysis-time effect.**

1a) Two way ANOVA revealed significant differences for all frequency bands. 1b) Post-hoc test revealed that the during-ictal/ non-ictal interval had higher power in all frequency bands compared to pre- and post- ictal /non-ictal intervals. (x:  $p < 0.05$ , \*:  $p < 0.01$ )

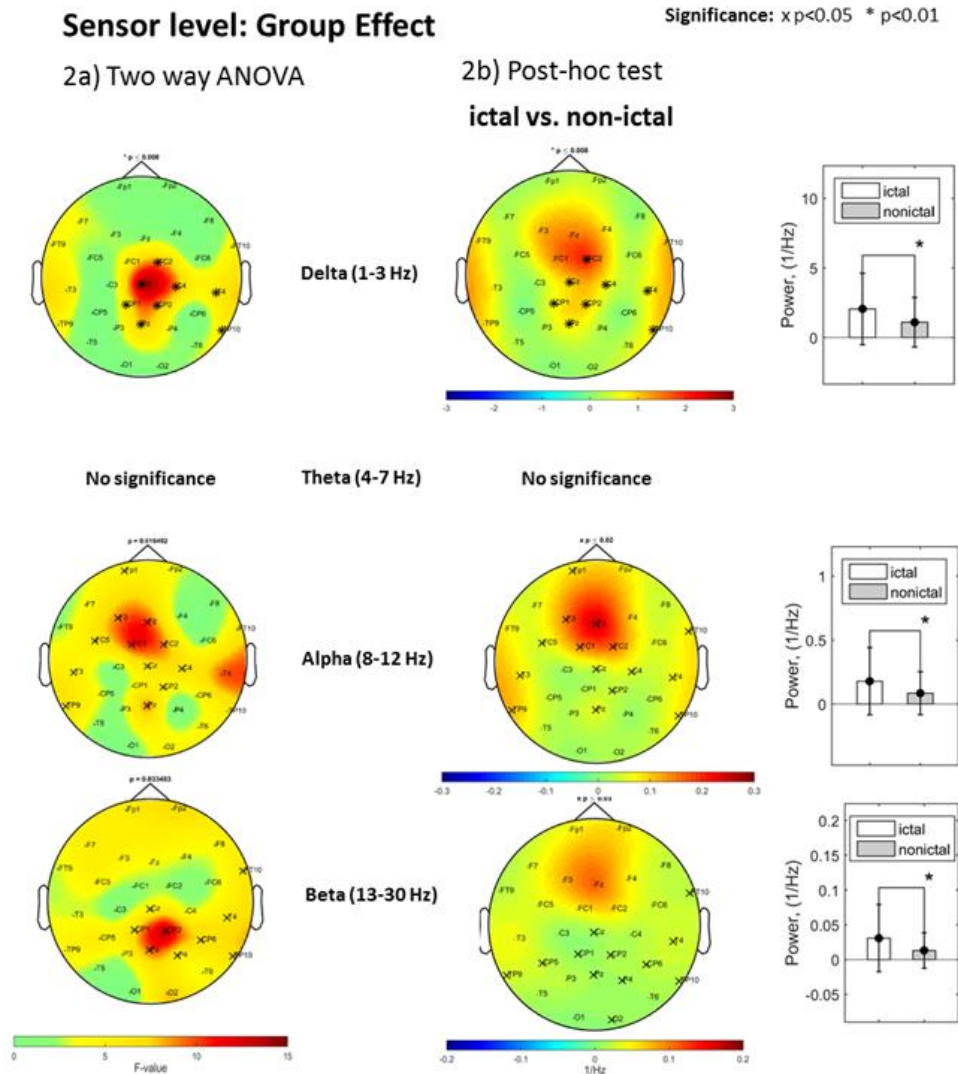


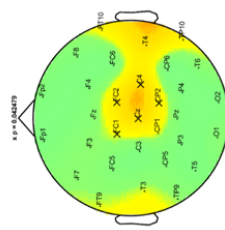
**Figure 6.2 Spectral analysis-group effect**

2a) Two way ANOVA results demonstrated significant differences in delta, alpha and beta bands. 2b) Post-hoc test revealed that for all significant frequency bands, ictal GSWDs had higher power compared to non-ictal GSWDs. The electrodes showing significance have been marked by x in the spectral plots, and in the graphical plots the significant power differences can be seen between ictal and non-ictal GSWDs.

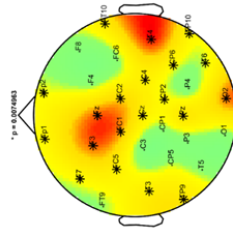
Significance: x p<0.05 \* p<0.01

### Sensor level: Interaction Effect

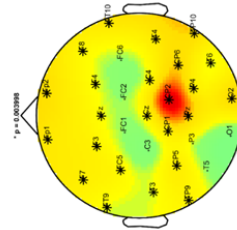
#### 3a) Two way ANOVA



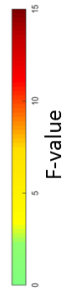
Delta (1-3 Hz)



Alpha (8-12 Hz)

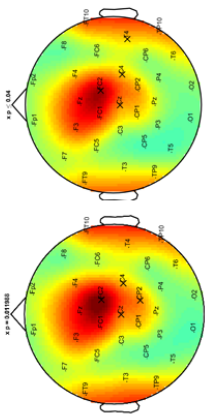


Beta (13-30 Hz)



#### 3b) Post-hoc test

##### ictal vs. non-ictal during-pre



##### ictal vs. non-ictal during-post

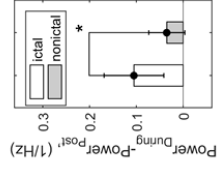
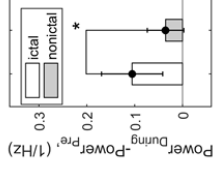
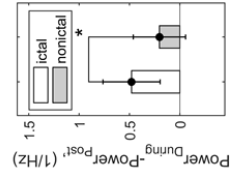
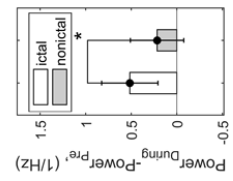
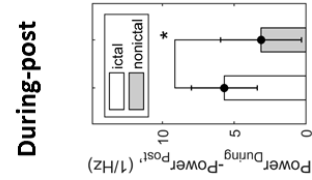
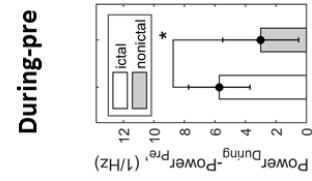
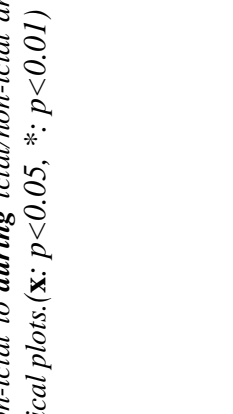
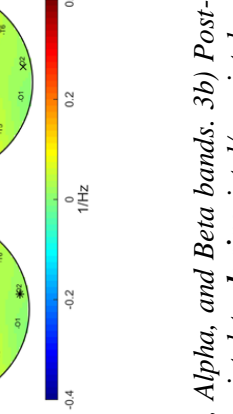
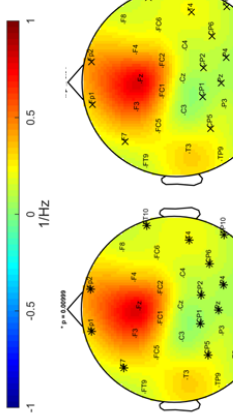
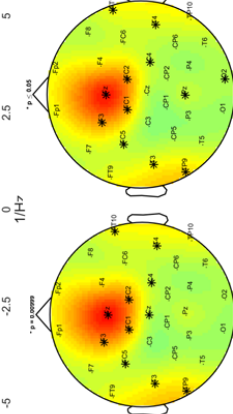
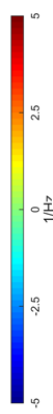
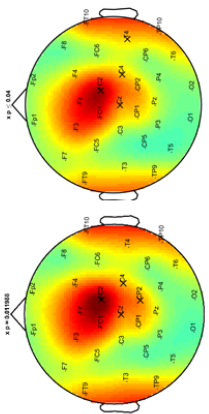


**Figure 6.3 Spectral analysis- interaction effect**

3a) Two way ANOVA, power spectral results for Delta, Alpha, and Beta bands. 3b) Post-hoc test results for significant frequency bands, for ictal and non-ictal GSWDs. The transition from pre-ictal/non-ictal to during ictal/non-ictal and from during ictal/non-ictal to post-ictal/non-ictal are depicted here in topographical spectral plots and graphical plots. (x: p<0.05, \*: p<0.01)

## 6.2.2 Functional Connectivity results

Two way repeated measure ANOVA (group x time) demonstrated a significant difference for the time effect over all frequency bands. It was seen that there was an increase in synchronization between all channels as the frequency oncreased. In other words alpha and beta bands had higher channel synchronization compared to delta and theta bands. Further, there was no main effect of group seen for all frequency bands. Interaction effect showed significant differences for all frequency bands.

Following ANOVA test results post hoc tests revealed for the main effect of time that during-ictal/non-ictal interval has higher iCOH compared to pre- and post- ictal/non-ictal intervals in all frequency bands. Post-ictal/non-ictal intervals didn't show any significant difference of iCOH when compared to the pre- ictal/non-ictal intervals for delta, theta and beta frequency bands. Only alpha band showed weak iCOH, when post- ictal/non-ictal and pre- ictal/non-ictal intervals were compared.

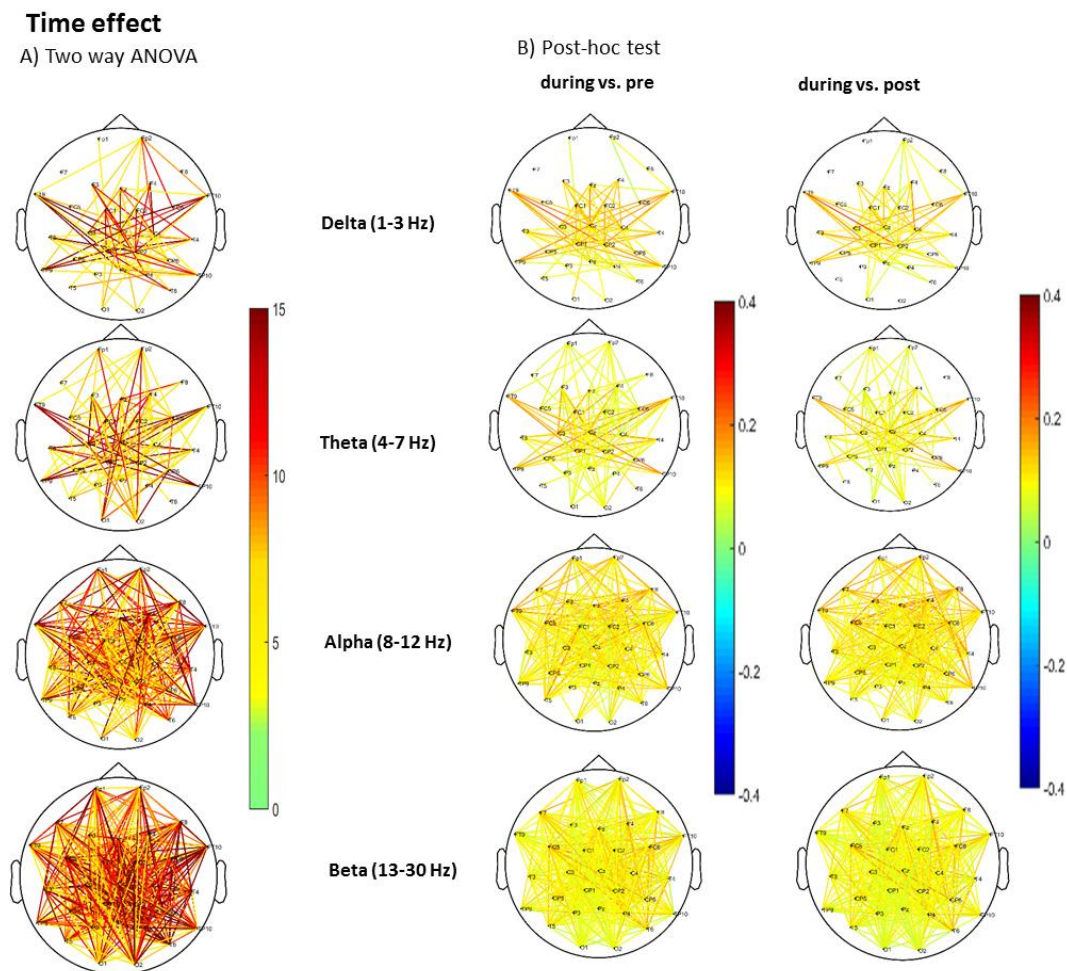


**Figure 6.4 Functional connectivity-time effect.**

*a) Two way ANOVA revealed significant differences for all frequency bands. b) Post-hoc test revealed that the during-ictal/ non-ictal interval had stronger connectivity for all frequency bands compared to pre- and post- ictal /non-ictal intervals.*



For interaction effect, most of the significant results were found for changes in ictal/non-ictal intervals compared to pre- and post-intervals for all bands. Post-hoc test revealed that the transition of connectivity from pre-ictal to during-ictal and from during-ictal to post-ictal was significantly weaker in all bands, compared to the non-ictal transition periods. For delta band (1-3 Hz) connectivity differences were observed in frontal-temporal, frontal-central, and central-parietal regions. There was a desynchronization of channels seen in delta band involving the regions of the default mode network (DMN). While, differences in connectivity for theta, alpha and beta bands were long range, linking the right and left hemispheres of the brain. Only delta band showed a weak connectivity difference for post- and pre-ictal/non-ictal intervals.

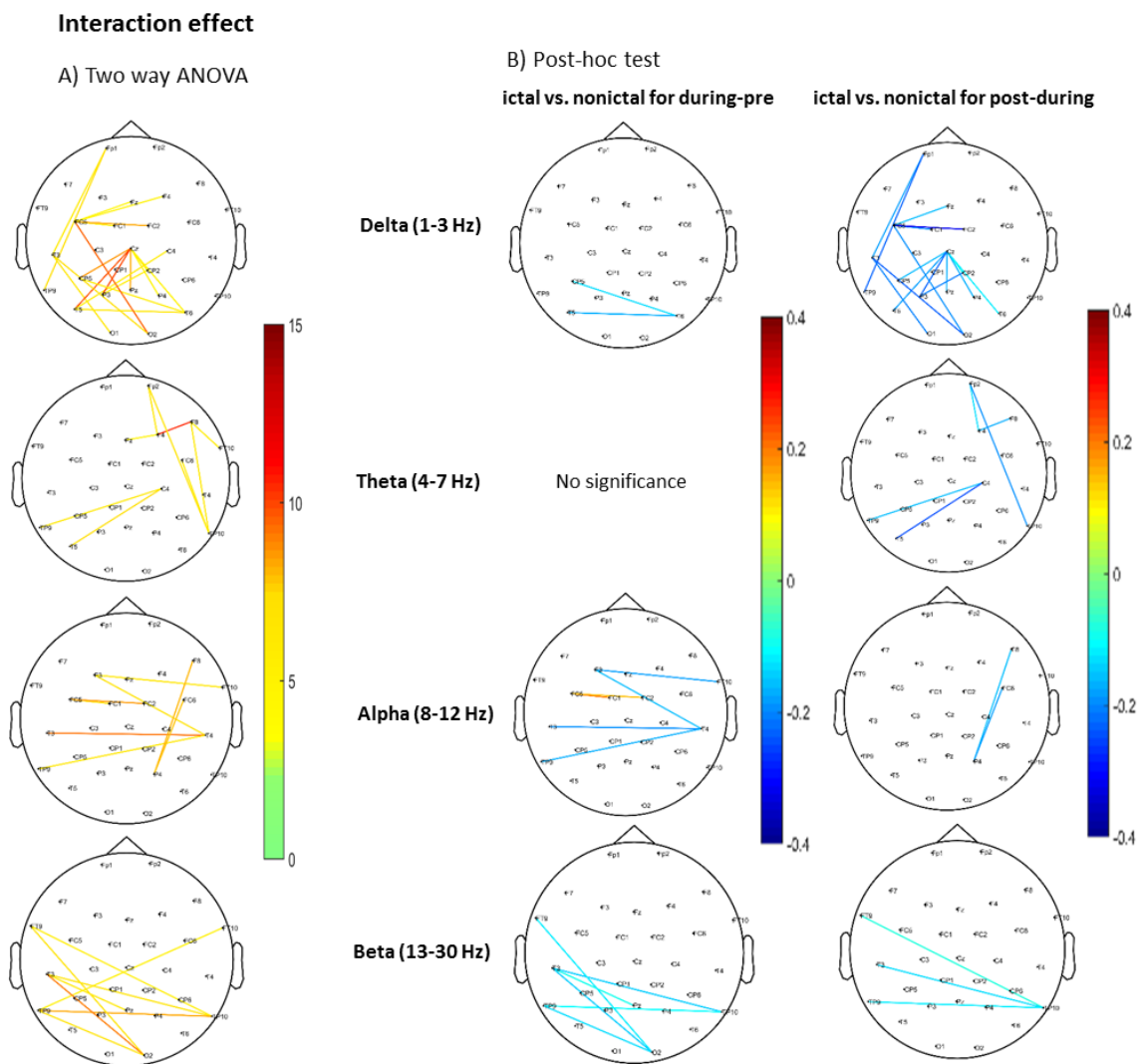


**Figure 6.5 Functional connectivity-interaction effect.**

a) Two way ANOVA showed a significant interaction effect for all frequency bands. b) Post-hoc test results depicting weaker connectivity for ictal transition periods for all frequency bands.

Frequency band	Interaction effect conditions	Functional hubs	Channel connections
Delta band	ictal vs. non-ical (during-pre)	T6	CP5, T5
	ictal vs. non-ical (post-during)	Fp1	T3, TP9
		FC5	Fz, FC1,FC2,O2
		T3	O1,O2
		Cz	CP5,T5, Pz, P4, T6
		P3	Cz, CP2
Theta band	ictal vs. non-ical (during-pre)	No significance	
	ictal vs. non-ical (post-during)	FP2	F4,TP10
		F4	FP2, F8
		C4	TP9, T5
Alpha band	ictal vs. non-ical (during-pre)	T4	F3, T3, TP9
		F3	FT10, T4
		FC5	FC1, FC2
	ictal vs. non-ical (post-during)	P4	F8, FC6
	Beta band	ictal vs. non-ical (during-pre)	T3
		TP9	O2, TP10
		O2	TP9, T3, FT9
		TP10	TP9, T3
ictal vs. non-ical (post-during)		TP9	FT9, T3, TP9

**Table 6.6 Functional hubs and there significant connections for all channels.**

Frequency bands	Factor	<i>p</i> value
Delta (1-3 Hz)	time	p<0.04
	group	-
	time x group	p<0.04
Theta (4-7 Hz)	time	p<0.03
	group	-
	time x group	p<0.05
Alpha (8-12 Hz)	time	p<0.02
	group	-
	time x group	p<0.04
Beta (13-30 Hz)	time	p<0.0005
	group	-
	time x group	p<0.04

**Table 6.7 Functional connectivity *p*-values for two way ANOVA test.**

<b>Post hoc comparisons</b>				
<b>Conditions</b>	<b>Delta <i>P</i> values</b>	<b>Theta <i>P</i> values</b>	<b>Alpha <i>P</i> values</b>	<b>Beta <i>P</i> values</b>
<b>Effect of Time</b>				
during vs. pre	0.02	0.02	0.02	0.004
during vs. post	0.02	0.02	0.02	0.003
post vs. pre	-	-	-	-
<b>Effect of Group</b>				
ictal vs. nonictal	-	-	-	-
<b>Interaction effect</b>				
ictal vs.non-ictal (during-pre)	0.01	-	0.02	0.02
ictal vs non-ictal (during-post)	0.02	0.02	0.02	0.01
ictal vs non-ictal (post-pre)	-	-	-	-

**Table 6.8 Functional connectivity p-values for post-hoc comparisons.**

## Source Localization

---

### 7.1 Methods

For source reconstruction as mentioned before the forward and inverse problems need to be solved. In this study source localization was performed using the algorithms included in the METH toolbox (<https://www.nitrc.org/projects/meth/>) and Fieldtrip software.

#### 7.1.1 Forward calculation

For the head model, or volume conductor, a standard head model associated with a standard MRI was selected from the Fieldtrip toolbox. A standard MRI was selected since the subjects did not have any individual MRI scans. The standard MRI selected that was the *single\_subj\_T.nii*. The standard MRI already contains the segmented MRI consisting of the scalp, skull and brain. This segmentation into 3 compartments is done using the boundary element method (BEM). The lead field matrix (LFM) is calculated in the METH toolbox as a result of the previously mentioned numerical solution of the forward problem in chapter 3. For a detailed description of the forward problem the review article by Hallez et al. (2007) [101] can be referred.

For the forward calculations firstly using the METH toolbox structural calculations were done. This does not include the EEG data but has the information regarding the volume conductor and channel positions. This toolbox combines all the structural information into a particular structure termed as 'sa'. The 'sa' structure contains information regarding three grid options: coarse, medium and fine. The function *mk\_sa\_eeg* was used to calculate the 'sa' structure for EEG data. This only required the input of the sensor positions in the Montreal Neurological Institute (MNI) coordinates. This function was used to calculate the lead field matrix for all grid options. Following this, for the source model *grid\_medium* was selected, since this was the most appropriate grid for the data under consideration. The *grid\_medium* has 5003 points, with 7.5 mm distance of neighboring nodes. Each point or node in the grid acts as a dipole with three directions x, y and z.

#### 7.1.2 Inverse calculation

Firstly, for the inverse calculation, a spatial filter was constructed. The function *mk\_filt\_eloreta* was used to calculate this according to the eLORETA method. Spatial filters are important to increase the signal to noise ratio. This filter was constructed for each voxel as well as for all three orthogonal dipole directions. It can be calculated using the lead field

alone and without the EEG data. The filter for a given voxel is an  $M \times 3$  matrix of  $M$  sensors. The 3-dimensional filter can be constructed using the input  $M \times L \times P$  lead field tensors. Where,  $M$  is the number of sensors (31 sensors),  $L$  is the number of voxels (5003 voxels) and  $P$  is the direction of dipoles (3).

Secondly, the cross-spectrum was calculated for sensor-space using the function *data2cs\_event*. The input data or the raw data is an  $N \times M$  matrix consisting of  $N$  time points and  $M$  channels. This was calculated for 1 second long segments. The cross-spectra were estimated for frequency from 1 to 30 Hz with 1 Hz step. The output is  $M \times M \times$  frequency bins for each segment. The resulting spectra were averaged over segments and frequency ranges (delta, theta, alpha, and beta).

Following this, the 3-dimensional filter alongside the cross-spectral matrix in sensor space was used to determine the source direction for each voxel, based on the one that maximizes the power for the voxel. This was done using the function *getdipdir*. This calculates the dipole orientation that maximizes the power. The output for this function is the power at each voxel, the dipole direction for each voxel and a 1-dimensional filter at each voxel. This gives the source for the sensor-space activity.

### 7.1.3 Statistics

Following inverse calculations the data was converted back to the Fieldtrip software format, as the statistical analysis was done using Fieldtrip. For statistics a two way repeated measure ANOVA based on cluster permutation was implemented. This has been described in detail in chapter 5. The function *ft\_sourcestatistics* was used for this. The configuration for this function included the parameter for the data such as ‘pow’, which is the power spectrum (*cfg.parameter = ‘pow’*), the method ‘Monte-carlo’, which is a non-parametric permutation test (*cfg.method = ‘montecarlo’*), and a cluster correction to overcome the multiple comparison problem (*cfg.correctm = ‘cluster’*). The configuration also included a statistic parameter to implement a two way ANOVA in the code (*cfg.statistic = depAnova2way*). For ANOVA results that depicted significance, and had more than one pair of comparisons such as time and interaction effect, a post-hoc test was done (*cfg.statistic = ft\_statfun\_depsamplesT*). Using this method, the source activity for ictal and non-ictal GSWDs could be statistically differentiated.

### 7.1.3 Visualization

For visualization of two way ANOVA results, the fieldtrip toolbox was used. Before visualization, firstly, the data was interpolated using the function *ft\_sourceinterpolate*. This function interpolates the results of the source activity and statistical maps onto the voxels. Firstly the statistic results alongside the anatomical MRI were interpolated. The method in fieldtrip that was used to run this function was termed as ‘nearest’. Secondly, the source activity alongside the anatomical MRI and a mask from statistics was used for interpolation.

The mask from statistics is the significant p-value that is generated ( $p < 0.05$ ). Since the anatomical MRI data is volumetric in nature, the output is also a volume structure. To further visualize these results the function *ft\_sourceplot* was used. The configuration for this function includes the method, which can be ‘slice’ or ‘ortho’, the mask parameter, which is taken based on the statistics output and an atlas parameter for labeling. For anatomical labeling the Automated Anatomical Labeling (AAL) atlas was used [102]. Using this function the data was visualized in two ways, 1) as 2D axial slices of the brain on which the functional data is plotted and 2) as three slices containing three orthogonal directions (axial, sagittal and coronal).

## 7.2 Results

### 7.2.1 Delta band

For delta band, two-way repeated measure ANOVA (group x time) depicted a significant effect of time, significant effect of group as well as a significant interaction effect.

Post-hoc test for main effect of time revealed that during-ictal/non-ictal interval had a stronger source power compared to pre- and post-ictal/non-ictal intervals. The significant source maximum for during vs. pre interval was observed in the rectus right (R),left (L) region. While for the during vs. post interval also, the source maximum was observed in the rectus R,L, and caudate L region.

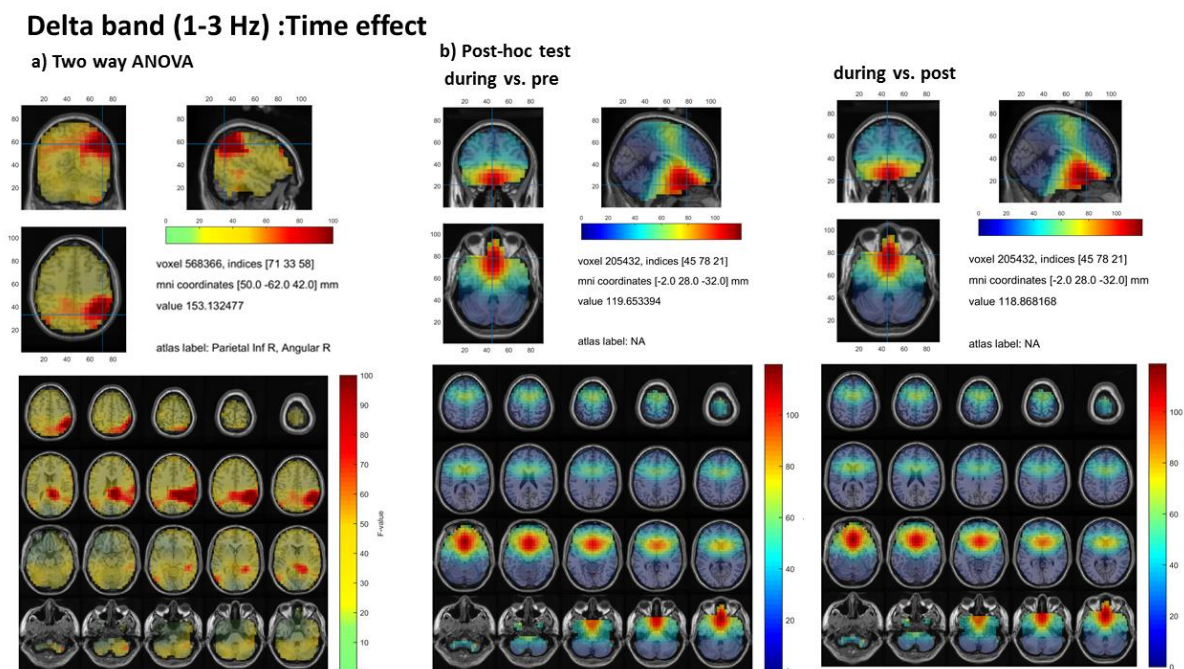
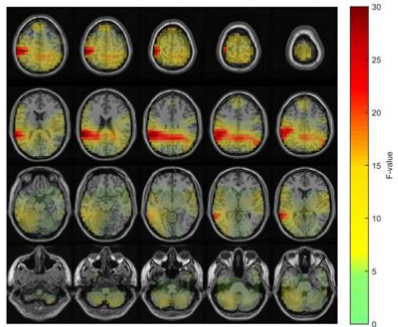
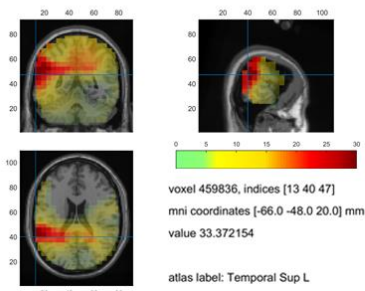


**Figure 7.1 Delta band time effect.**

a) Two way ANOVA results depicting the F-value b) Post-hoc test results for conditions during vs. pre interval and during vs. post interval, indicating the source maximum.

**Delta band (1-3 Hz) :Group effect**

**a) Two way ANOVA**



**b) Post-hoc test  
ictal vs. non-ictal**

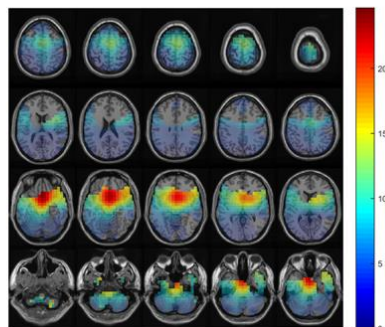
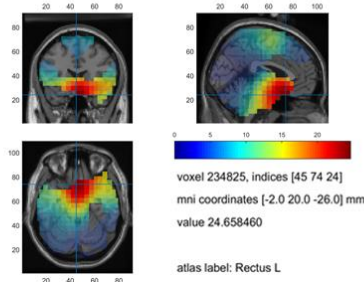
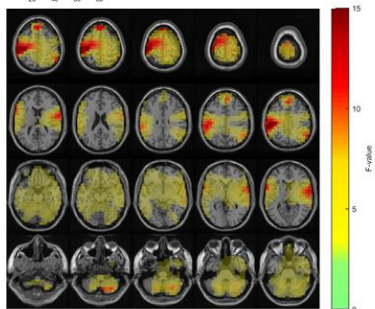
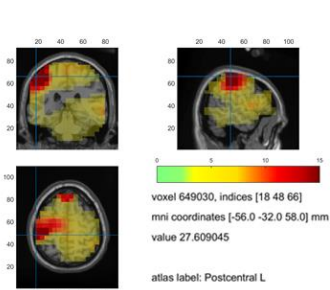


**Figure 7.2 Delta band group effect.**

*a) Two way ANOVA results depicting the F-value b) Post-hoc test results for the condition ictal vs. non-ictal, indicating the source maximum.*

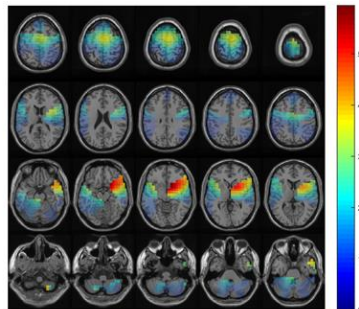
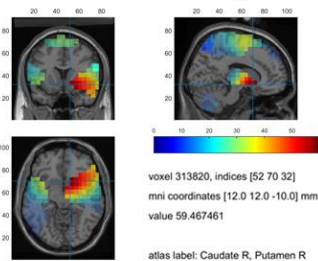
**Delta band (1-3 Hz) :Interaction effect**

**a) Two way ANOVA**



**b) Post-hoc test**

**ictal vs. non-ictal for during-pre**



**ictal vs. non-ictal for during-post**

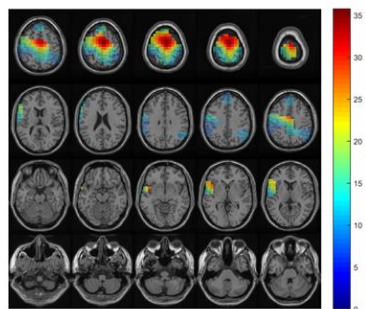
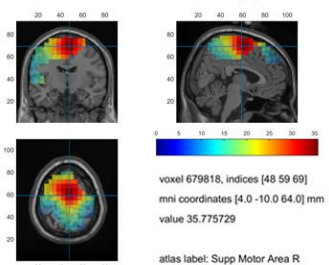


**Figure 7. 3 Delta band interaction effect.**

*a) Two way ANOVA results depicting the F-value b) Post-hoc test results for the conditions ictal vs. non-ictal (during-pre) and ictal vs. non-ictal (during-post), indicating the source maximum.*

For the effect of group it was seen that the source power for ictal GSWDs was stronger compared to non-ictal GSWDs. The source maximum, for the significant difference between ictal vs. non-ictal group was seen in the Rectus R, with neighbouring sources being in the caudate L, frontal medial orbital R, and the cingulum anterior L region.

Further, post hoc tests for interaction effect depicted, that the source power transition from pre interval to during interval and from during interval to post interval is stronger for ictal GSWDs is stronger compared to the transition periods of non-ictal GSWDs. The source maximum for the significant difference of during-pre (ictal/non-ictal) was observed in caudate R, and putamen R region, while, the source maximum for the significant difference of post-during (ictal/non-ictal), was seen in the supplementary motor R, region.

## 7.2.2 Theta Band

For theta band two-way repeated measure ANOVA, only demonstrated a significant effect of time. A significant group effect and interaction effect was not found. Post hoc tests for the main effect of time depicted that during-ictal/non-ictal interval had a stronger source power compared to pre- and post-ictal/non-ictal intervals. The significant source maximum for during vs. pre interval and for during vs. post interval was observed in the rectus R,L region. While neighbouring sources were found in the frontal mid orbital R, frontal inferior triangular part R, and frontal inferior orb R, region.

### Theta band (4-7 Hz) :Time effect

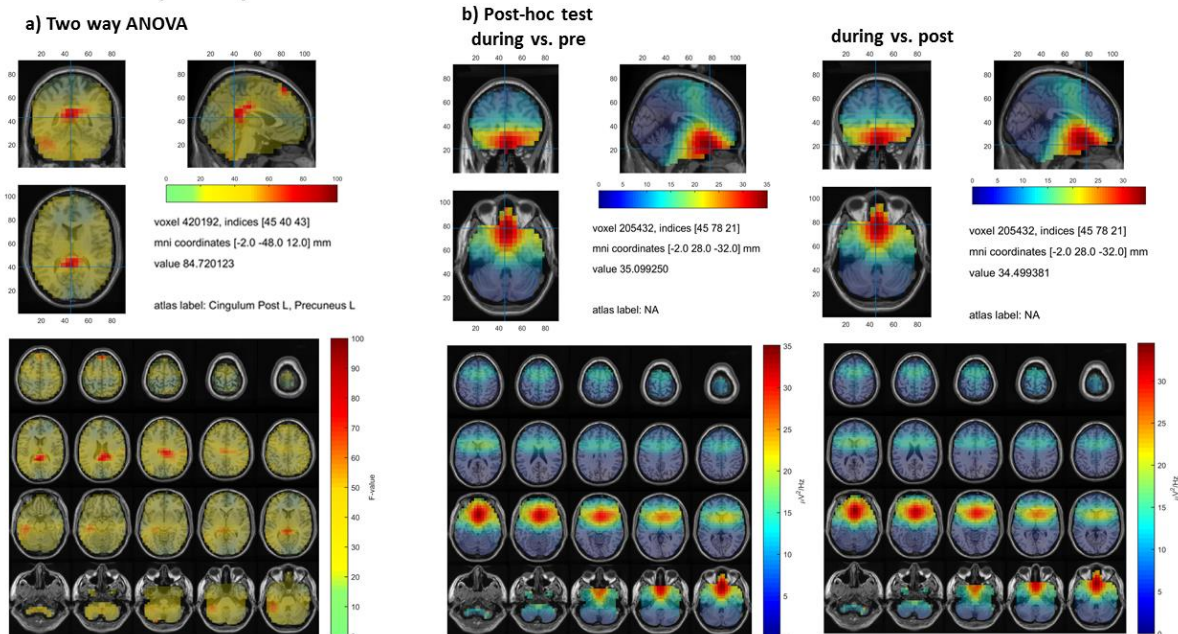


**Figure 7.4 Theta band time effect.**

a) Two way ANOVA results depicting the F-value b) Post-hoc test results for conditions during vs. pre interval and during vs. post interval, indicating the source maximum.



### 7.2.3 Alpha band

Two-way repeated measure ANOVA (group x time) for alpha band, depicted a significant effect of time, significant effect of group and a significant interaction effect.

Post-hoc test for main effect of time revealed that during-ictal/non-ictal interval for alpha band frequency had a stronger source power compared to pre- and post-ictal/non-ictal intervals. The significant source maximum for during vs. pre interval and during vs. post interval was observed in the rectus R,L region. The neighbouring sources were found in the regions of frontal mid orbital R, frontal inferior triangular part R, and frontal inferior orbital R.

#### Alpha band (8 -12 Hz) :Time effect

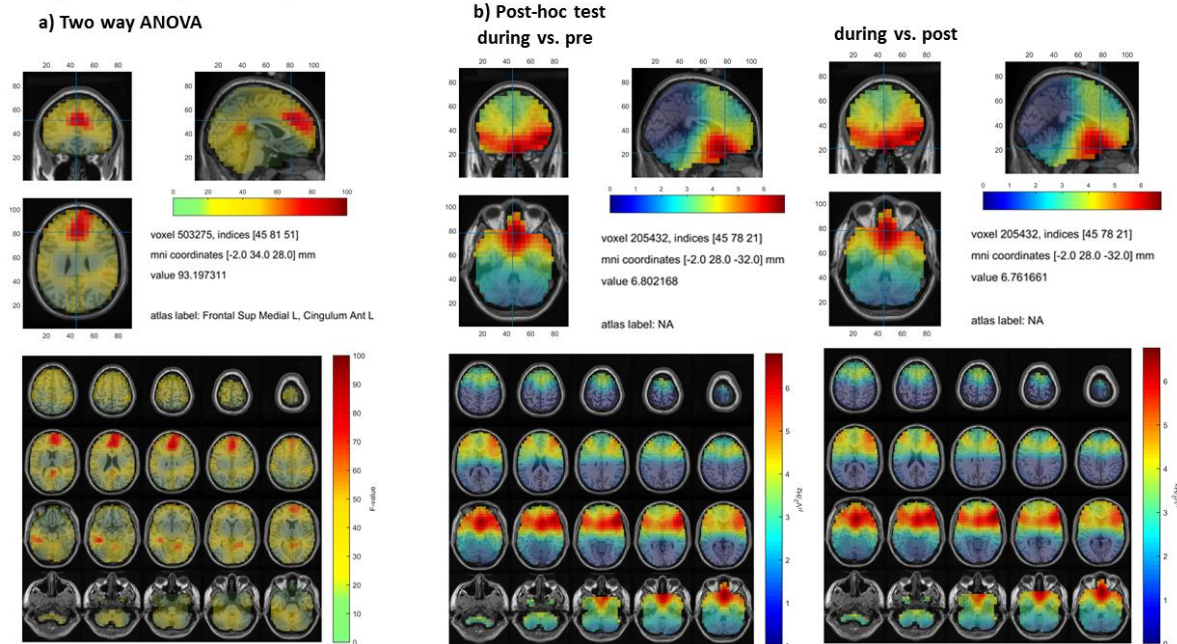


**Figure 7.5 Alpha band time effect.**

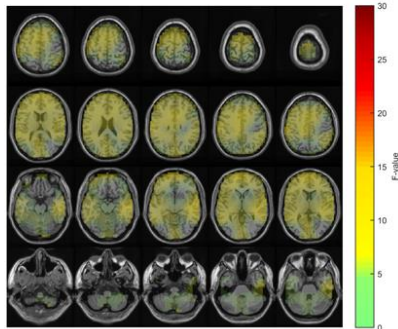
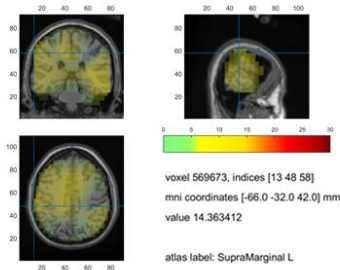
a) Two way ANOVA results depicting the  $F$ -value b) Post-hoc test results for conditions during vs. pre interval and during vs. post interval, indicating the source maximum.

For the effect of group it was seen that the source power for ictal GSWDs was stronger compared to non-ictal GSWDs. The source maximum, for the significant difference between ictal vs. non-ictal group was seen in frontal inferior orbital L region.

Post hoc tests for interaction effect revealed, that the source power transition from pre interval to during interval and from during interval to post interval was stronger for ictal GSWDs is stronger compared to the transition periods of non-ictal GSWDs. The source maximum for the significant difference of during-pre (ictal/non-ictal) and post-during (ictal/non-ictal) was observed in frontal inferior orbital L region.

### Alpha band (8 -12 Hz):Group effect

a) Two way ANOVA



b) Post-hoc test ictal vs. non-ictal

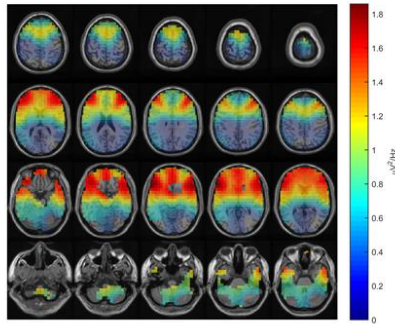
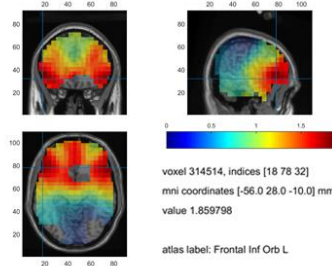
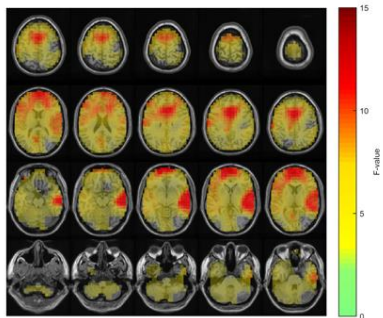
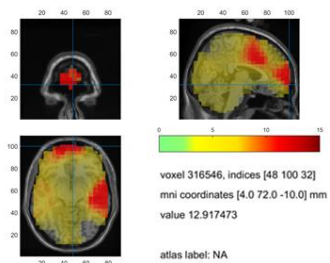


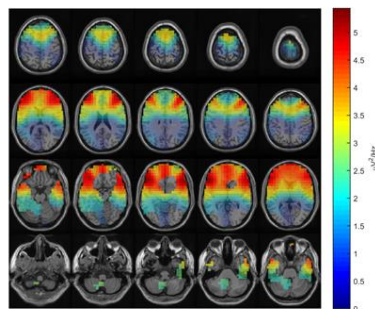
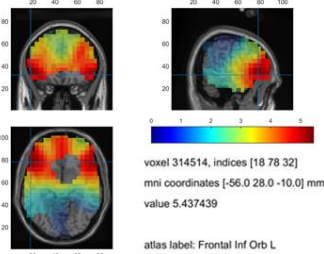
**Figure 7.6 Alpha band group effect.** a) Two way ANOVA results depicting the  $F$ -value b) Post-hoc test results for the condition ictal vs. non-ictal, indicating the source maximum.

### Alpha band (8 -12 Hz) : Interaction effect

a) Two way ANOVA



b) Post-hoc test ictal vs. non-ictal for during-pre



ictal vs. non-ictal for during-post

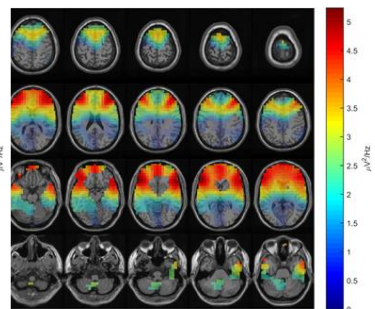
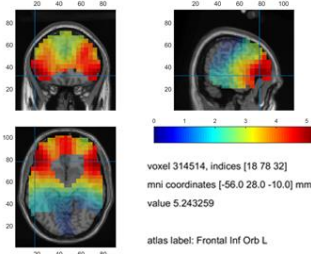


**Figure 7.7 Alpha band interaction effect.**

a) Two way ANOVA results depicting the  $F$ -value b) Post-hoc test results for the conditions ictal vs. non-ictal (during-pre) and ictal vs. non-ictal (during-post), indicating the source maximum.

## 7.2.4 Beta band

Two-way repeated measure ANOVA for beta band depicted a significant effect of time, significant effect of group and a significant interaction effect.

Post-hoc test for main effect of time revealed that during-ictal/non-ictal interval for beta band frequency had a stronger source power compared to pre- and post-ictal/non-ictal intervals. The significant source maximum for during vs. pre interval and during vs. post interval was observed in the frontal orbital R, region.

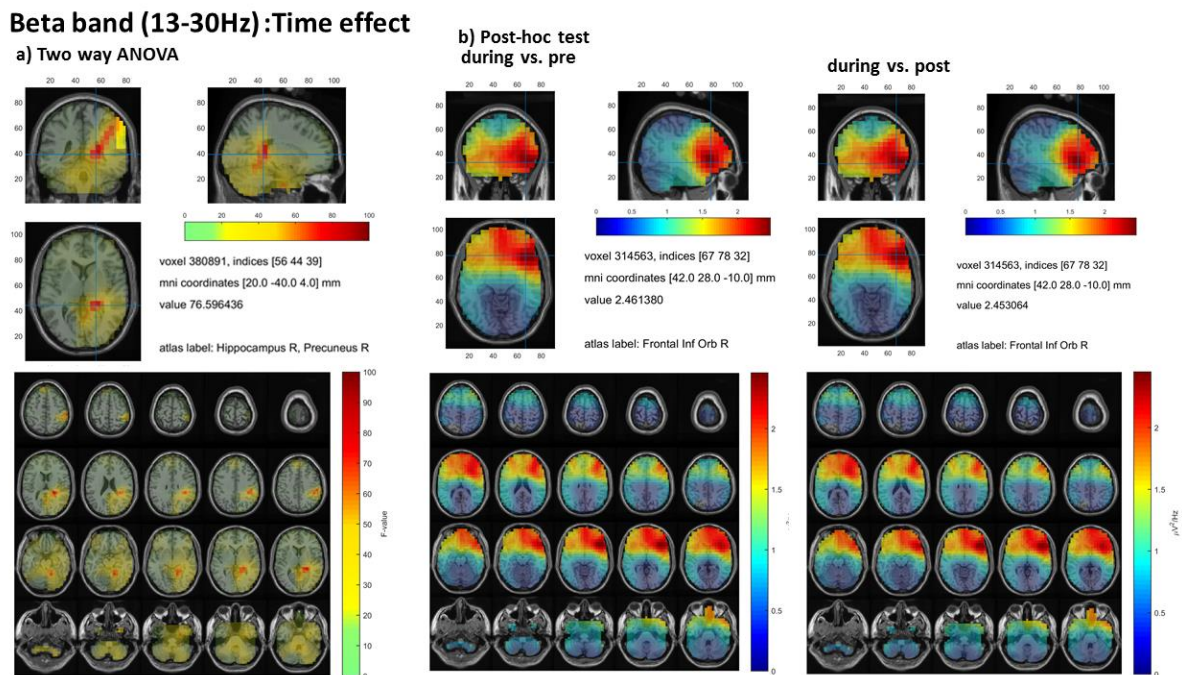


**Figure 7.8 Beta band time effect.**

*a) Two way ANOVA results depicting the F-value b) Post-hoc test results for conditions during vs. pre interval and during vs. post interval, indicating the source maximum.*

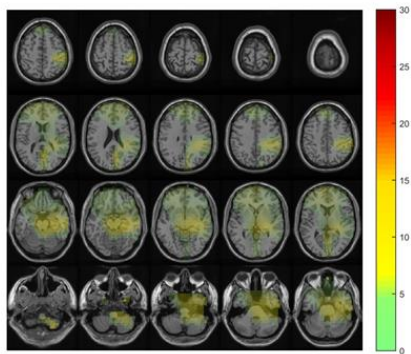
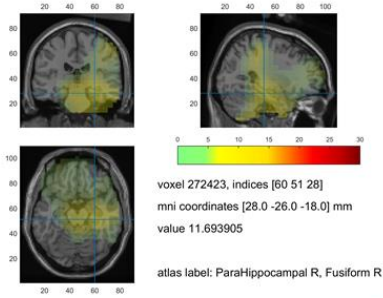
For the effect of group it was seen that the source power for ictal GSWDs was stronger compared to non-ictal GSWDs. The source maximum, for the significant difference between ictal vs. non-ictal group was seen in frontal superior medial R, region.

Post hoc tests for interaction effect revealed, that the source power transition from pre interval to during interval and from during interval to post interval was stronger for ictal GSWDs is stronger compared to the transition periods of non-ictal GSWDs. The source maximum for the significant difference of during-pre (ictal/non-ictal) and post-during (ictal/non-ictal) was again observed in frontal superior medial R region.

In the tables 7.1 and 7.2 the p-values generated for source analysis and the brain regions depicting the source maximum have been described for all frequency bands.

### Beta band (13-30Hz): Group effect

#### a) Two way ANOVA



#### b) Post-hoc test ictal vs. non-ictal

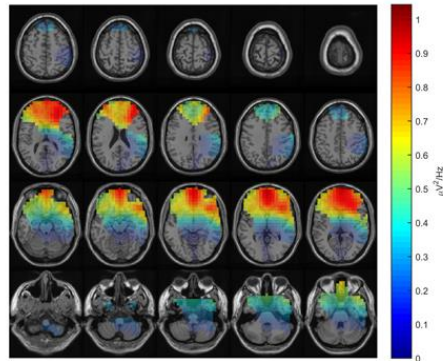
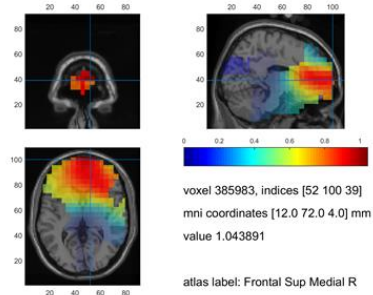
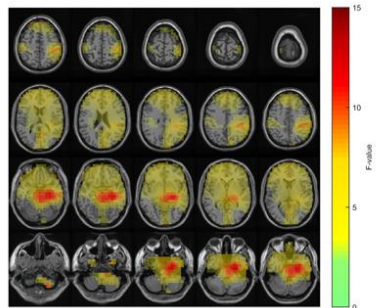
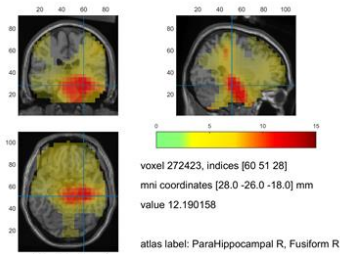


**Figure 7.9 Beta band group effect.**

a) Two way ANOVA results depicting the F-value b) Post-hoc test results for the condition ictal vs. non-ictal, indicating the source maximum.

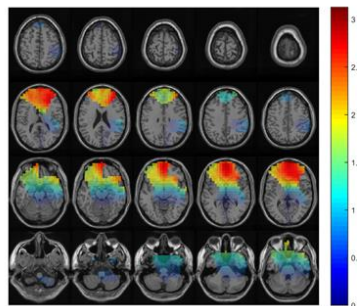
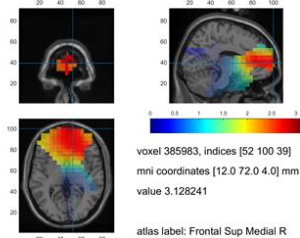
### Beta band (13-30Hz): Interaction effect

#### a) Two way ANOVA



#### b) Post-hoc test

##### ictal vs. non-ictal for during-pre



##### ictal vs. non-ictal for during-post

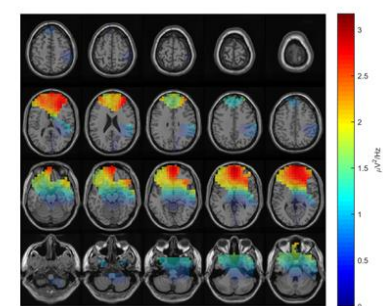
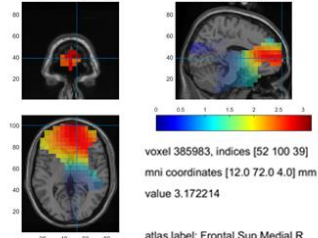


**Figure 7.10 Beta band interaction effect.**

a) Two way ANOVA results depicting the F-value b) Post-hoc test results for the conditions ictal vs. non-ictal (during-pre) and ictal vs. non-ictal (during-post), indicating the source maximum.

Conditions	Frequency Bands			
	Delta	Theta	Alpha	Beta
<b>Effect of time</b>				
during vs. pre	0.001	0.001	0.001	0.001
during vs. post	0.001	0.001	0.001	0.001
<b>Effect of group</b>				
ictal vs. non-ictal	0.002	No significance	0.01	0.04
<b>Interaction effect</b>				
ictal vs. non-ictal (during-pre)	0.01	No significance	0.005	0.01
ictal vs. non-ictal (during-post)	0.04	No significance	0.008	0.01

**Table 7.1 Source analysis p-values for all frequency bands and conditions.**

Frequency bands	Conditions	Source maximum	
<b>Delta Band</b>	<b>Effect of time</b>		
	during vs. pre	Rectus R,L	
	during vs. post	Rectus R,L, Caudate L	
	<b>Effect of group</b>		
	ictal vs. non-ictal	Rectus R	
	<b>Interaction effect</b>		
	ictal vs. non-ictal (during-pre)	Caudate R, Putamen R	
	ictal vs. non-ictal (during-post)	Supplementary Motor area R	
	<b>Theta Band</b>	<b>Effect of time</b>	
		during vs. pre	Rectus R,L
during vs. post		Rectus R,L	
<b>Effect of group</b>		No significance	
<b>Interaction effect</b>		No significance	
<b>Alpha Band</b>		<b>Effect of time</b>	
	during vs. pre	Rectus R,L	
	during vs. post	Rectus R,L	
	<b>Effect of group</b>		
	ictal vs. non-ictal	Frontal inferior orb L	
	<b>Interaction effect</b>		
	ictal vs. non-ictal (during-pre)	Frontal inferior orb L	
	ictal vs. non-ictal (during-post)	Frontal inferior orb L	
<b>Beta Band</b>	<b>Effect of time</b>		
	during vs. pre	Frontal orb R	
	during vs. post	Frontal orb R	
	<b>Effect of group</b>		
	ictal vs. non-ictal	Frontal superior medial R	
	<b>Interaction effect</b>		
	ictal vs. non-ictal (during-pre)	Frontal superior medial R	
	ictal vs. non-ictal (during-post)	Frontal superior medial R	

**Table 7.2 Brain regions showing the source maximum.**

# Chapter 8

## Source-level Functional Connectivity

---

In the current chapter functional connectivity based on imaginary part of coherency (iCOH) was implemented to analyse the neuronal networks in ictal and non-ictal GSWDs. Functional connectivity was mapped out based on the seed or node of interest being the source maximum achieved from source localization in chapter 7 and the thalamus.

### 8.1 Methods

#### 8.1.1 Selecting the seed

The seed or point of interest was selected based on the interaction effect results obtained from source localization (chapter 7). The first seed was based on the source maximum from the interaction effect, as a result of a two way repeated measure ANOVA test (group x time). This was done because the interaction effect is the most important result of source analysis. A second seed of interest was selected as the thalamus, since literature describes it as an important area involved during seizure onset and propagation.

A second seed of interest was also used as it was presumed that the source maximum was shifted due to being a deep source. Therefore, the distance between the source maximum and thalamus were also calculated for all frequency bands (Table 8.1). This distance was calculated based on the following formula:

$$d = \sqrt{(x_2 - x_1)^2 + (y_2 - y_1)^2 + (z_2 - z_1)^2}$$

Where,

$(x_1, y_1, z_1)$  = coordinates of first point

$(x_2, y_2, z_2)$  = coordinates of second point

The source maximum MNI (Montreal Neurological Institute) coordinates for all frequency bands are given in tables 8.1, and for thalamus the MNI coordinate selected was: [0, -0.75, 0.75] cm.

Connectivity analysis was done for Delta, alpha and beta band. Theta band was excluded since this frequency band did not show any interaction effect for source localization. Delta band was the only frequency band that revealed two source maximums. Hence, both source maximum points were selected as a seed for connectivity analysis for this band. For seed selection of the source maximum and thalamus the MNI coordinates were used.

Selecting the seed								
Frequency	Conditions for Interaction effect	MNI coordinates (cm)			Deep Source	Source max. power value	Distance from thalamus (cm)	Number of seeds selected from source max.
		x	y	z				
Delta band (1-3 Hz)	During-pre	1.5	1.5	-0.75	Yes	59.4675	3.0923	2
	During-post	0.75	-0.75	6.75	No	35.7757	6.0467	
Theta band (4-7 Hz)	-	-	-	-	-	-	-	-
Alpha band (8-12 Hz)	During-pre	-5.25	3	-0.75	No	5.4374	6.6238	1
	During-post	-5.25	3	-0.75	No	5.2433	6.6238	
Beta band (13-30 Hz)	During-pre	1.5	7.5	0.75	No	3.1282	8.3853	1
	During-post	1.5	7.5	0.75	No	3.1722	8.3853	

**Table 8.1 Selection of the seed from the source maximum.**

*For all frequency bands and their interaction effect conditions, the MNI coordinates have been given alongside the source maximum power values and the information if the source is deep. This table also includes information on the distance between the source maximum and thalamus in centimetres and the number of seeds selected for each frequency band. Theta band was excluded due to no significant interaction effect.*

### 8.1.2 Calculation of the imaginary part of coherency (iCOH)

For the calculation of the iCoh the METH toolbox (<https://www.nitrc.org/projects/meth/>) was used. Firstly, the 1-dimensional filter obtained from the function *getdipdir*, used previously for source localization in chapter 7, was used to calculate the cross-spectra at source level. This was obtained using the following formula:

$$A1^T \times \text{cross-spectrum} \times A1$$

Where, A1 is the 1 dimensional filter and the cross spectrum here comes from sensor level.

Secondly, the function *cs2coh* was used to calculate the coherence from the cross-spectrum at source level. The output of this function is a coherency matrix (MxM) consisting of the real and imaginary part of the coherency at source level. Following this the matrix is used to

extract the coherency value corresponding to the selected seed. From this the absolute value of iCoh is taken.

### **8.1.3 Statistics**

The Fieldtrip toolbox (Oostenveld et al. 2011) was used for statistical analysis. Similar to source localization statistical analysis mentioned in chapter 7, for connectivity analysis also the two repeated measure ANOVA was used. Details regarding this test have been mentioned in chapter 6. The function *ft\_sourcestatistics* was used for this, and the configurations used for this function were similar to those mentioned in chapter 7. Also, for this function a statistic parameter (*cfg.statistic = depAnova2way*) was used to implement a two way ANOVA into the code. For significant ANOVA results post hoc test were done further.

### **8.1.4 Visualization**

The Fieldtrip toolbox was again used for visualizing the results. The procedure was similar to that mentioned in chapter 6. The function *ft\_sourceplot* was used to visualize these results. Using this function the iCOH results were visualized in 2D axial slices of the brain and also in orthogonal slices of the brain containing three directions (axial, sagittal and coronal). Further, the Automated Anatomical Labeling (AAL) atlas (Tzourio-Mazoyer et al. 2002) was used for anatomical labeling.

## **8.2 Results**

FC based on iCOH was applied to two scenarios at source level. Firstly, when the seed or point of interest was the source maximum and secondly when the seed was the thalamus. For further statistical analysis a two way repeated measure ANOVA was used for analyses. Results regarding both these cases have been further described.

### **8.2.1 Seed as source maximum**

#### **a) Delta band**

Delta band revealed two source maximums. For the first source maximum, which was a deep source, a two way repeated measure ANOVA (group x time) depicted a significant effect of time and significant effect of group. But, there was no significant interaction effect revealed.

Post-hoc test for main effect of time revealed that during-ictal/non-ictal interval had stronger coherence compared to pre- and post-ictal/non-ictal intervals. The maximum coherence difference for pre- to during-ictal/non-ictal time interval was observed in the occipital middle R region, while for the time intervals during- to post-ictal/non-ictal also, it was seen in the cingulum posterior R, and precuneus region (Figure 8.1).



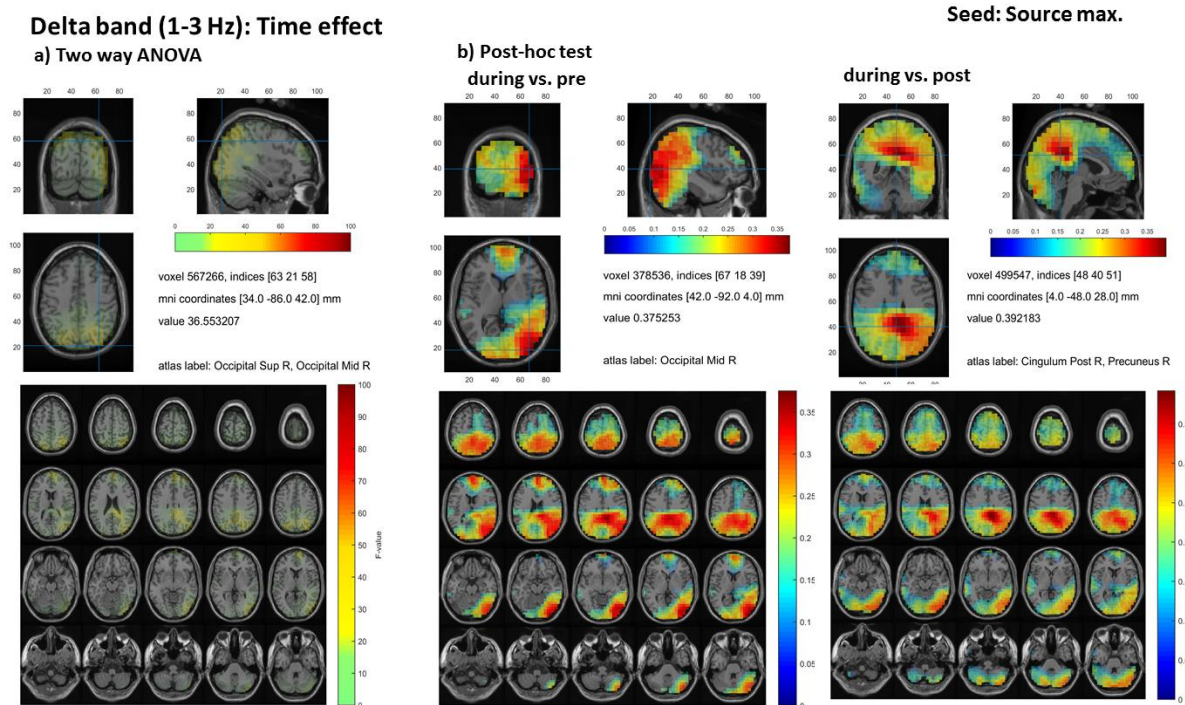


**Figure 8.1 Functional connectivity for source maximum-delta band time effect.**  
*a) two way ANOVA results demonstrating the F-value distribution. b) post-hoc test results for time effect conditions, depicting the coherent brain regions in correlation to the source maximum.*

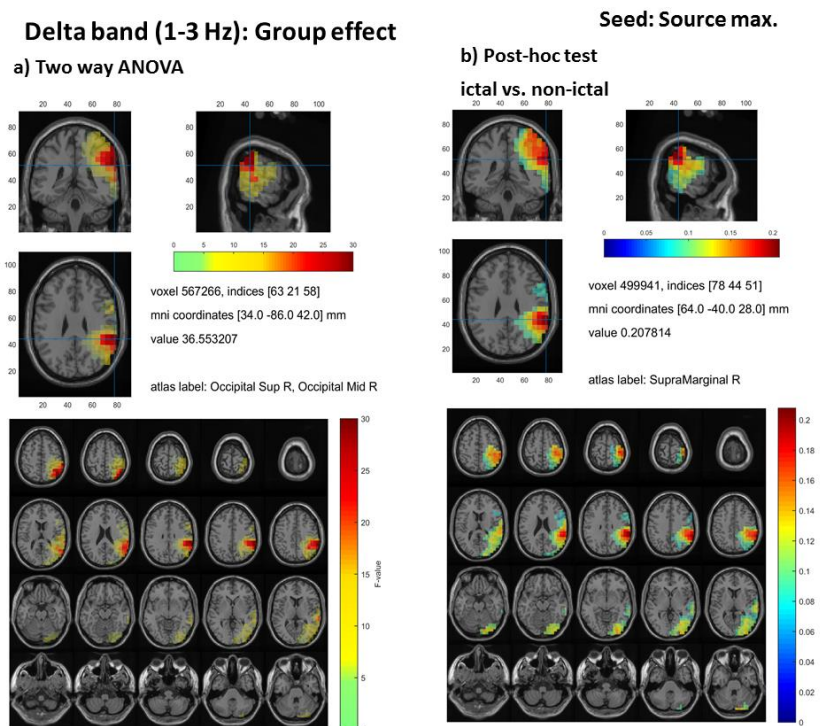


**Figure 8.2 Functional connectivity for source maximum-delta band group effect.**  
*a) two way ANOVA results depicting the regions of significance and F-value distribution. b) post-hoc test results depicting the coherence difference for ictal vs. non-ictal GSWDs.*

Post hoc test for the effect of group revealed that ictal GSWDs had a stronger coherence compared to non-ictal GSWDs. The maximum coherence difference was observed in the supramarginal R region (Figure 8.2).

For the second source maximum which was a surface source, two-way ANOVA only revealed a significant effect of time. Further, post hoc test revealed similar to before, that during-ictal/non-ictal interval had stronger coherence compared to pre- and post-ictal/non-ictal intervals. The maximum coherence difference for pre- to during-ictal/non-ictal interval and during- to post-ictal/non-ictal interval were observed in the temporal middle L region. (Figure 8.3).

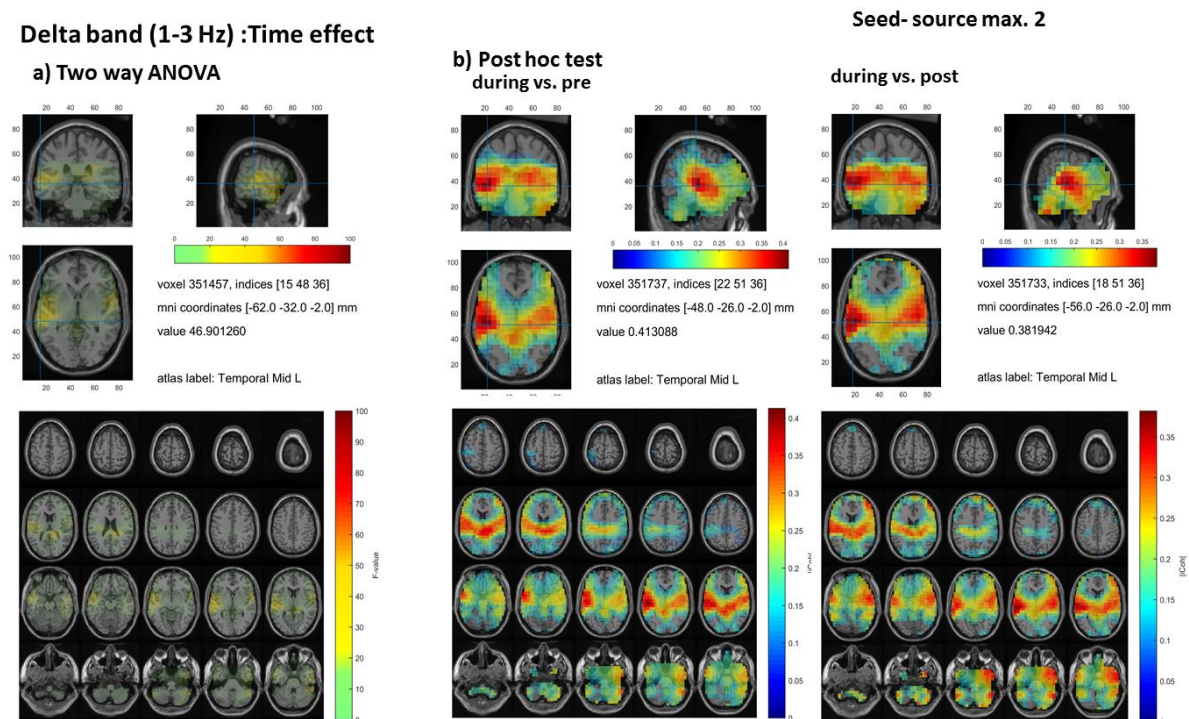


**Figure 8.3 Functional connectivity for second source maximum-delta band time effect**  
*a) two way ANOVA results demonstrating the F-value distribution. b) post-hoc test results for time effect conditions, during vs. pre interval and during vs. post interval, depicting the coherent brain regions in correlation to the source maximum.*

### b) Theta band

For theta band FC analysis for source maximum was not done since, there was no significant interaction effect revealed as previously mentioned in chapter 7. Therefore, the seed for coherence analysis could not be taken.

### c) Alpha band

For alpha band one source maximum was revealed. A two way ANOVA test revealed a significant effect of time but no significant effect of group. Moreover, a significant interaction effect was seen.

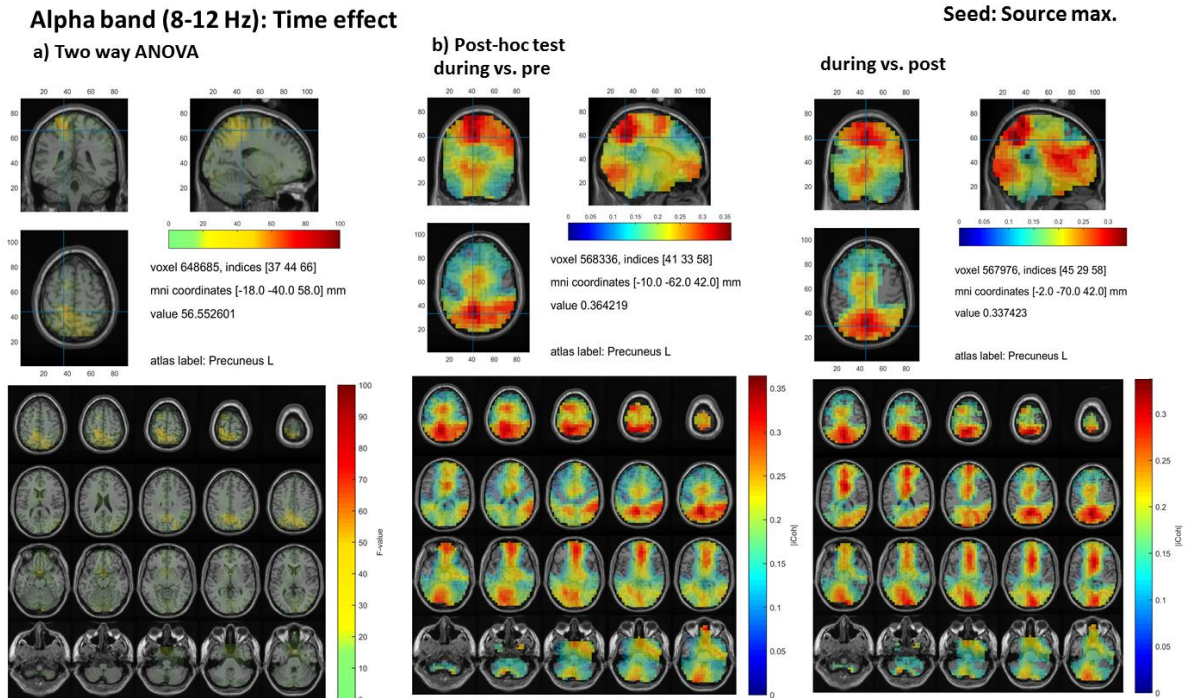


**Figure 8.4** Functional connectivity for source maximum-alpha band time effect  
*a) Two way ANOVA test results b) post-hoc test results for conditions during vs. pre time interval and during vs. post time interval.*

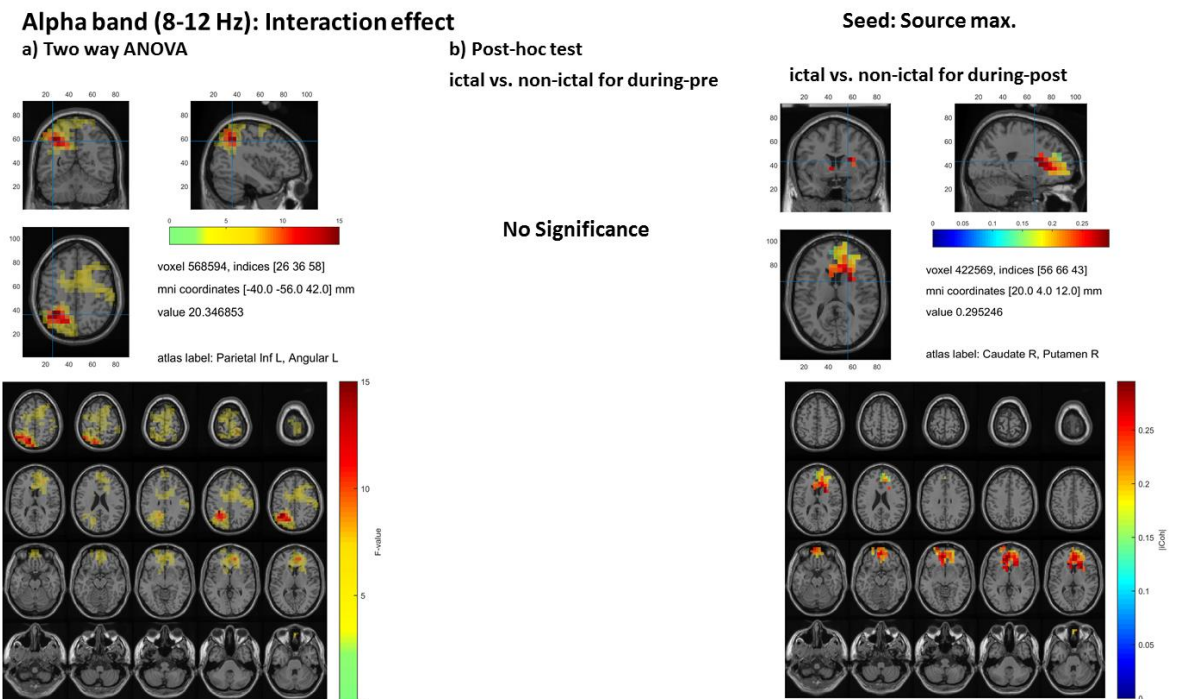


**Figure 8.5** Functional connectivity for source maximum-alpha band interaction effect.  
*a) Two way ANOVA results depicting regions of significance in the brain based on F-value distribution. b) post-hoc test results depicting coherent regions in the brain for the condition ictal vs. non-ictal (during-post).*

Post hoc test for the main effect of time demonstrated stronger and widespread coherence for during-ictal/non-ictal interval. The pre- and post-ictal/non-ictal intervals had a weaker coherence in comparison. These significant differences were seen to be widespread in all brain regions. The maximum coherence difference for the time interval pre- to during-ictal/non-ictal and during- to post-ictal/non-ictal was seen in precuneus L region (Figure 8.4).

For interaction effect it was seen that there was no significance for the condition ictal/non-ictal (during-pre). However for the condition ictal/non-ictal (during-post) it was seen that the coherence was stronger for ictal transition periods from during interval to post interval, compared to the transition periods of non-ictal discharges. The maximum coherence difference for this condition was observed in the caudate R and putamen R region (Figure 8.5).

#### d) Beta band

Beta band also revealed a significant effect of time for a two way ANOVA test. But there was no significant effect of group or interaction effect found.

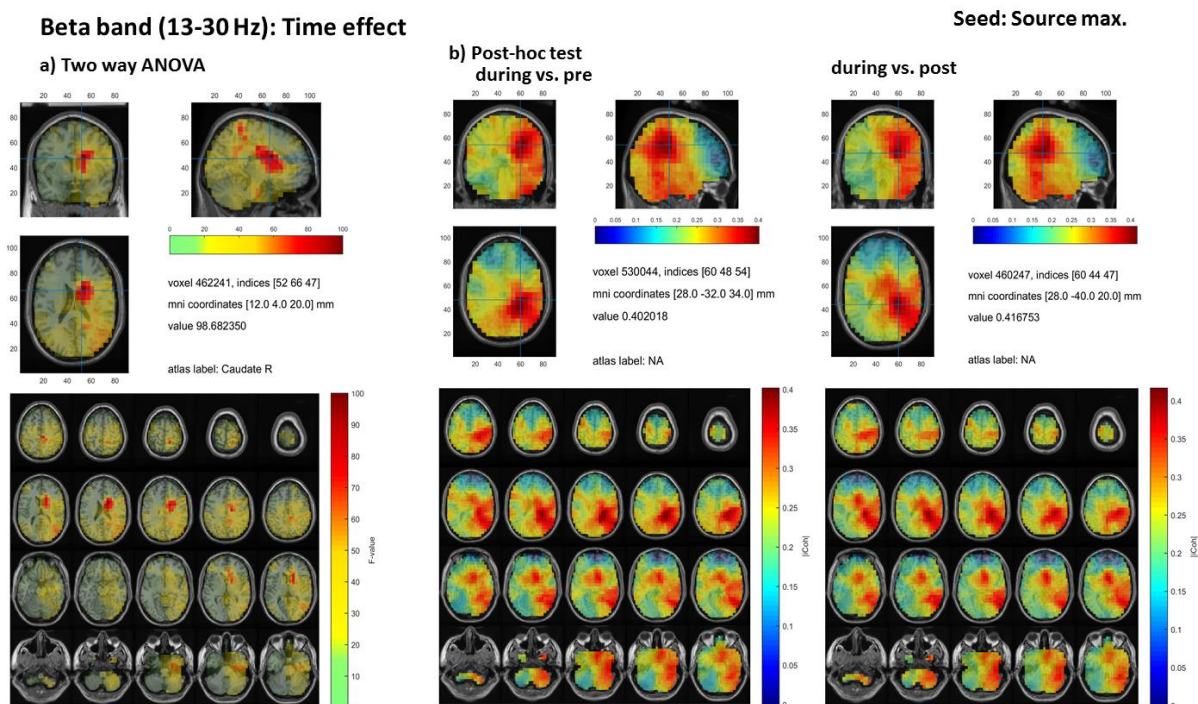


**Figure 8.6 Functional connectivity for source maximum-beta band time effect**

a) Two way ANOVA test results b) post-hoc test results for conditions during vs. pre time interval and during vs. post time interval, demonstrating coherent regions in the brain, in correlation to the source maximum.

Post hoc test for the main effect of time revealed that coherence was stronger for during-ictal/non-ictal interval compared to pre- and post-ictal/non-ictal GSWDs. The coherence was seen to be widespread, in all brain regions except the prefrontal cortex region. The maximum

coherence difference for the time interval pre- to during-ictal/non-ictal was seen in precuneus R, cingulum posterior R region. While for the time interval during- to post-ictal/non-ictal it was seen in the cuneus R and precuneus R region (Figure 8.6).

<b>Seed-Source maximum</b>					
<b>Conditions</b>	<b>Frequency Bands</b>				
	<b>Delta</b>		<b>Theta</b>	<b>Alpha</b>	<b>Beta</b>
	<b>Source max.1</b>	<b>Source max.2</b>	<b>Source max.1</b>	<b>Source max.1</b>	<b>Source max.1</b>
<b>Effect of time</b>					
during vs. pre	0.001	0.001	-	0.001	0.001
during vs. post	0.001	0.001	-	0.001	0.001
<b>Effect of group</b>					
ictal vs. non-ictal	0.03	-	-	No Significance	No Significance
<b>Interaction effect</b>					
ictal vs. non-ictal (during-pre)	No Significance	No Significance	-	No Significance	No Significance
ictal vs. non-ictal (during-post)	No Significance	No Significance	-	No Significance	No Significance

**Table 8.2 Functional connectivity p-values for source maximum as the seed.**

## 8.2.2 Seed as Thalamus

### a) Delta band

Two way ANOVA test demonstrated that there was a significant main effect of time and group when the seed was as the thalamus. For delta band there was a significant interaction effect was found.

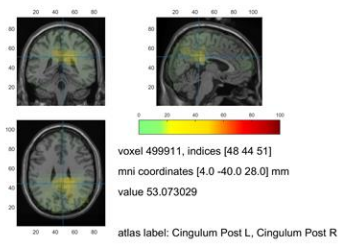
Post hoc tests revealed for the main effect of time that during-ictal/non-ictal time interval had a stronger coherence compared to the pre- and post-ictal/non-ictal time intervals. The significant difference in coherence was seen in the pre-frontal cortex, parietal R, L, and occipital R, L brain regions. The maximum coherence difference for the time effect was seen in the cingulum posterior R, precuneus R for pre- to during-ictal/non-ictal interval and for during- to post-ictal/non-ictal interval (Figure8.7).

The main effect of group revealed ictal GSWDs had stronger coherence compared to non-ictal GSWDs. The significant difference in coherence could be observed in parietal R, region of the brain. The maximum coherence difference was seen in the supramarginal R, and angular R region (Figure 8.8).

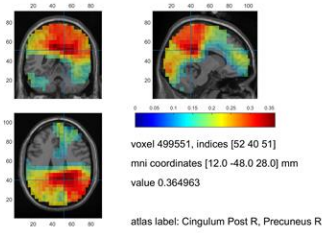
### Delta band (1-3 Hz): Time effect

Seed: Thalamus

#### a) Two way ANOVA



#### b) Post-hoc test during vs. pre



#### during vs. post

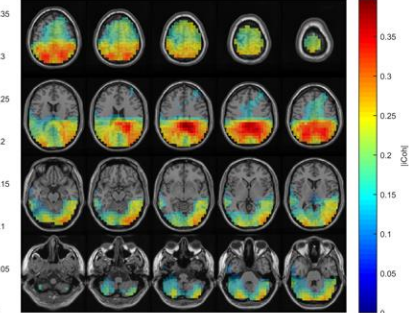
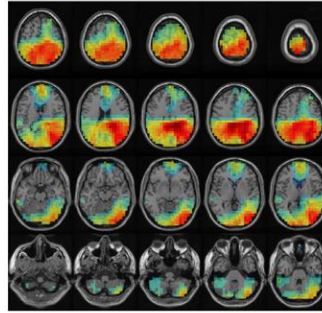
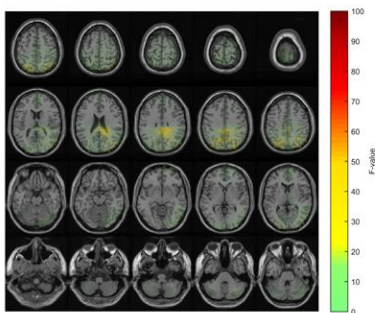
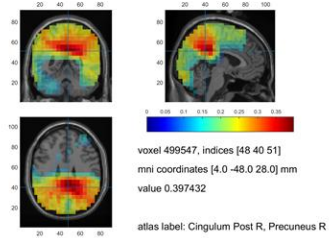


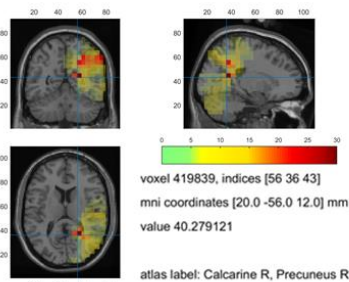
**Figure 8.7 Functional connectivity for thalamus-delta band time effect**

*a) Two way ANOVA test results b) post-hoc test results for conditions during vs. pre time interval and during vs. post time interval, demonstrating coherent regions in the brain, in correlation to the thalamus as the seed.*

### Delta band (1-3 Hz): Group effect

Seed: Thalamus

#### a) Two way ANOVA



#### b) Post-hoc test ictal vs. non-ictal

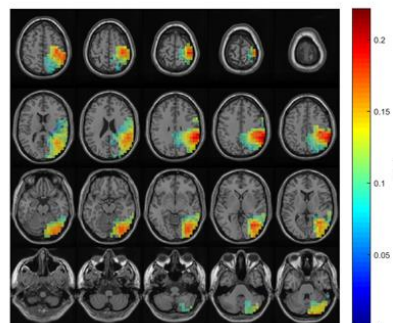
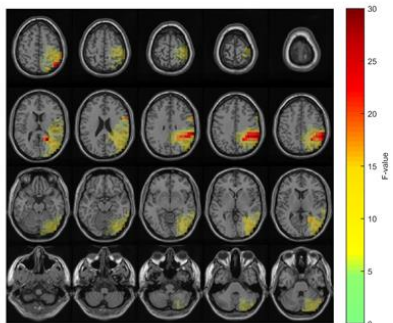
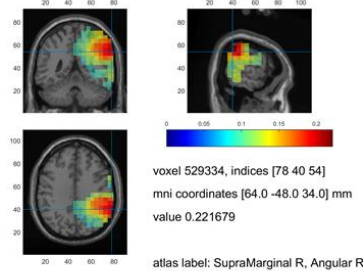


**Figure 8.8 Functional connectivity for thalamus-delta band group effect.**

*a) two way ANOVA results depicting the regions of significance and F-value distribution. b) post-hoc test results depicting the coherence difference for ictal vs. non-ictal GSWDs.*

Interaction effect demonstrated that the ictal transition periods from pre- to during- and from during- to post- intervals the coherence was stronger compared to the transition periods of non-ictal GSWDs. These significant differences were observed in the parietal R,L and occipital mid L, region. The maximum coherence difference for ictal/non-ictal (during-pre) and ictal/non-ictal (during-post) transition periods was seen in the occipital middle L, region (Figure 8.9).

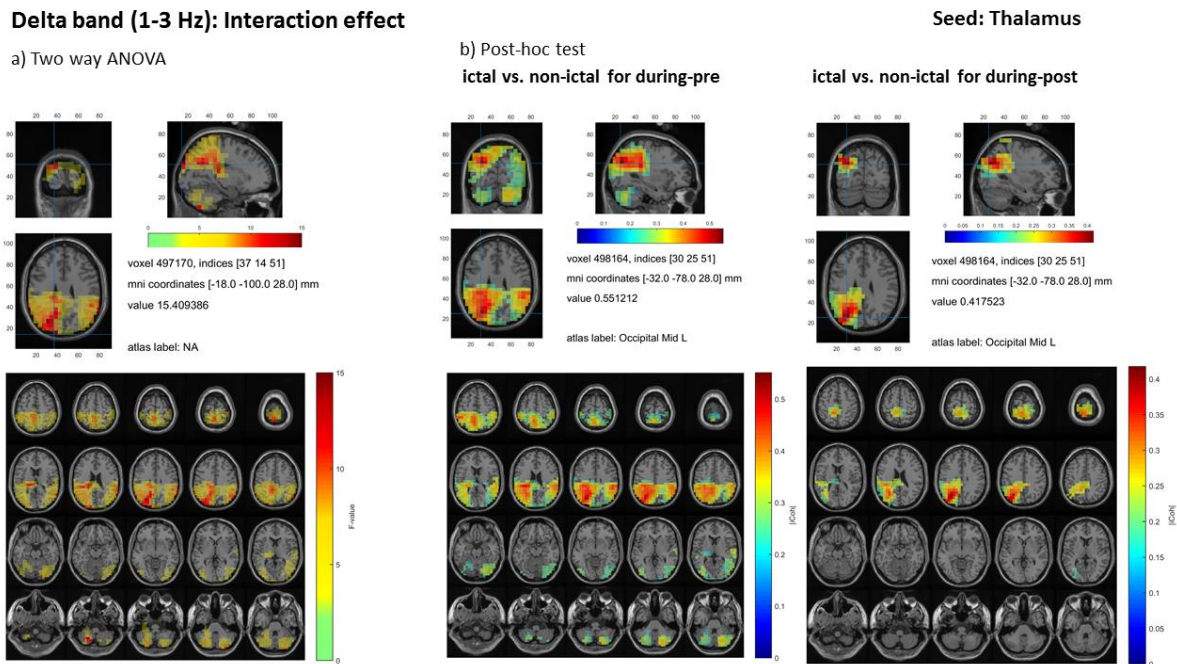


**Figure 8.9 Functional connectivity for thalamus-delta band interaction effect**

*a) two way ANOVA results depicting F-value distribution. b) post-hoc test results depicting coherent regions in the brain for the conditions ictal vs. non-ictal (during-pre) and ictal vs. non-ictal (during-post).*

## b) Theta band

Two way ANOVA test for theta band, depicted a significant effect of time and no significant effect of group or interaction effect.

Post hoc tests for theta band further demonstrated for the effect of time that, the during-ictal/non-ictal interval had stronger coherence compared to the time intervals pre- and post-ictal/non-ictal. These differences were widespread in the frontal-central, parietal R,L, occipital R,L region and the maximum coherence difference could be observed in the precuneus R region for the interval of pre- to during- ictal/non-ictal and in the cingulum middle L, cingulum posterior L, precuneus L regions for during- to post-ictal/non-ictal interval (Figure 8.10).

### Theta band (4-7 Hz): Time effect

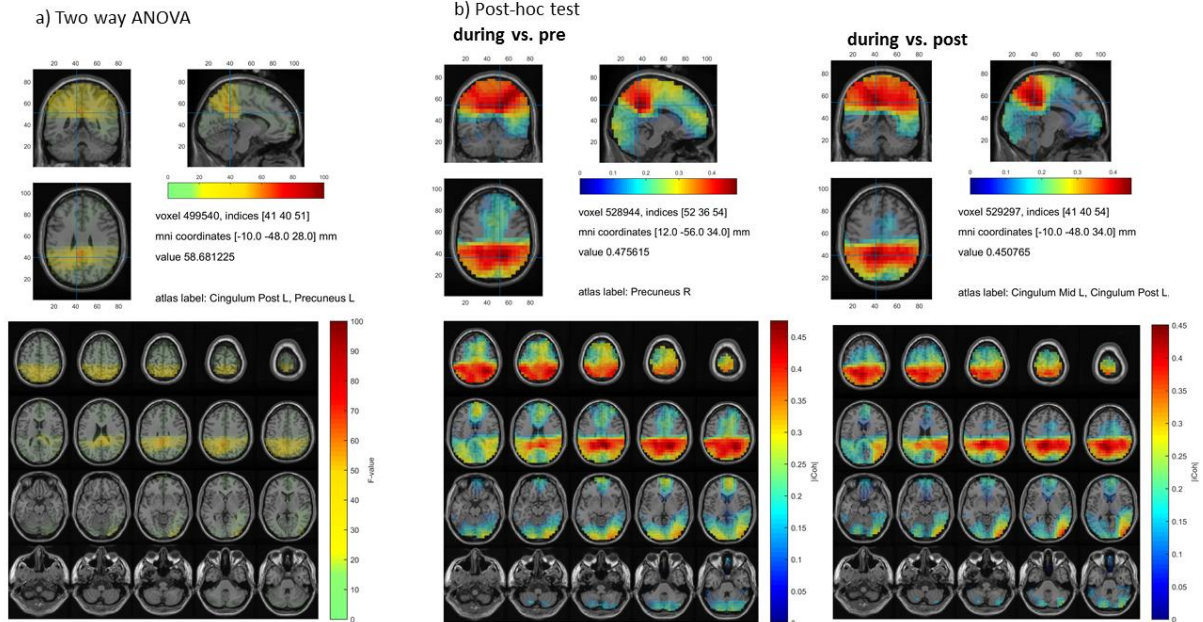


**Figure 8.10 Functional connectivity for thalamus-theta band time effect.**

a) Two way ANOVA test results b) post-hoc test results for conditions during vs. pre time interval and during vs. post time interval, for the thalamus as the seed.

### c) Alpha band

For alpha band two way ANOVA showed a significant effect of time but there was no significant group effect seen. Further, there was a significant interaction effect seen.

Post hoc test for the main effect of time showed that the during ictal/non-ictal interval had a stronger coherence compared to pre- and post- ictal/non-ictal time intervals. The coherence was seen to be widespread in the brain regions except for the mid central region. The maximum coherence difference could be observed in angular R region for time interval pre- to during-ictal/non-ictal and for the time intervals during- to post-ictal/non-ictal it could be observed in the parietal inferior R, angular R, supramarginal R regions (Figure 8.11).

For the interaction effect post hoc test revealed that the coherence for ictal transition periods from pre- to during- and from during- to post- intervals was stronger compared to the transition periods of non-ictal GSWDs. The maximum coherence difference for the condition ictal/non-ictal (during-pre) was seen in the postcentral R, parietal inferior R region. While for the condition ictal/non-ictal (during-post) the maximum coherence was seen in the parietal inferior R, and parietal superior R region (Figure 8.12).



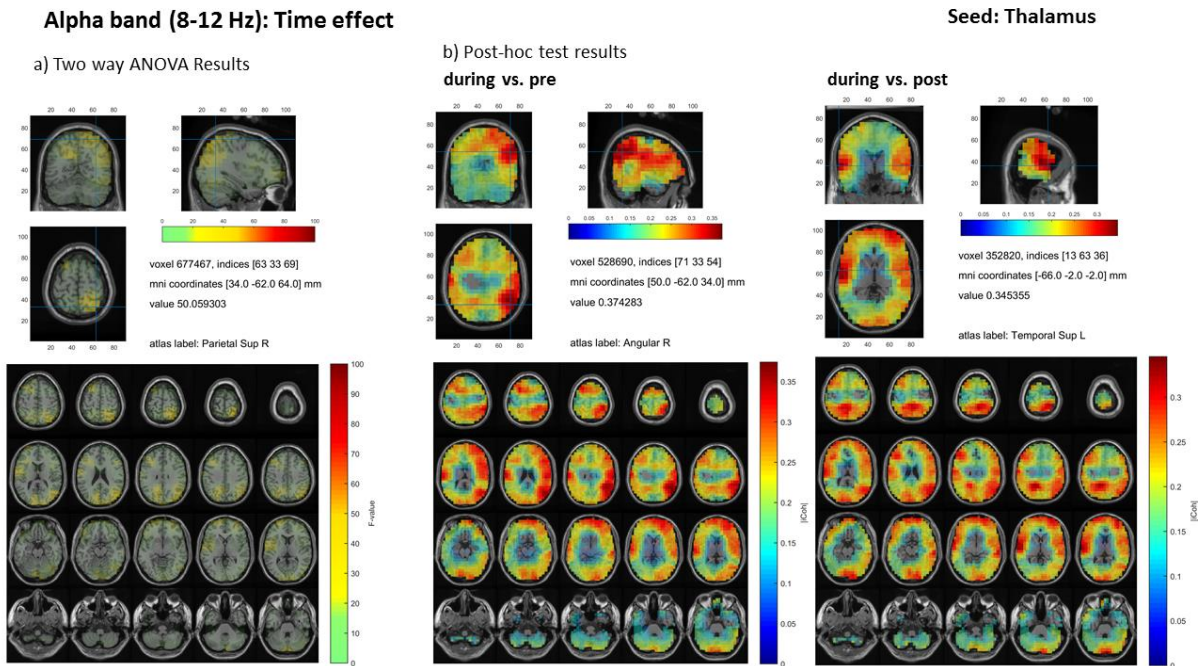


**Figure 8.11 Functional connectivity for thalamus-alpha band time effect.**  
a) Two way ANOVA test results b) post-hoc test results for conditions during vs. pre time interval and during vs. post time interval, for the thalamus as the seed.

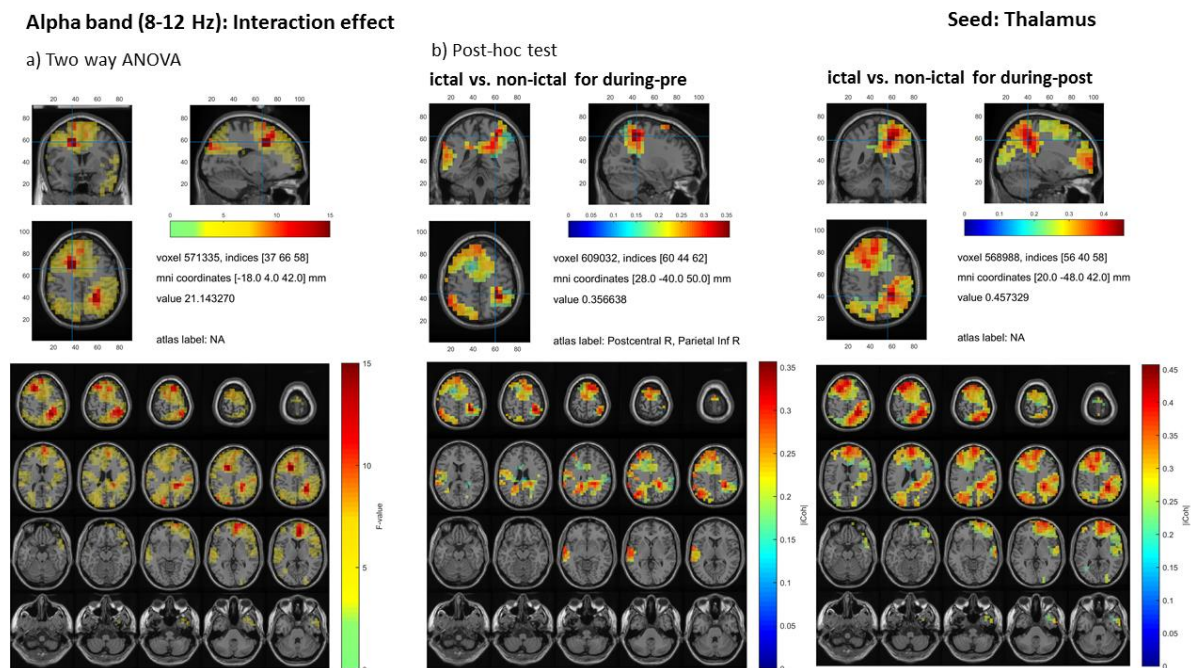


**Figure 8.12 Functional connectivity for thalamus-alpha band interaction effect.**  
a) two way ANOVA results depicting regions of significance in the brain based on F-value distribution. b) post-hoc test results depicting coherent regions in the brain for the conditions ictal vs. non-ictal (during-pre) and ictal vs. non-ictal (during-post).

#### d) Beta band

Two way ANOVA test for beta band frequency revealed a significant effect of time and no significant effect of group. There was also no significant interaction effect seen. Post hoc test for the main effect of time demonstrated similar results to other frequency bands. The during-ictal/non-ictal time interval had stronger coherence compared to pre- and post-ictal/non-ictal time intervals. The maximum coherence difference for the time interval pre- to during-ictal/non-ictal was observed in the angular R region. For the during- to post-ictal/non-ictal interval the maximum coherence difference was observed in the parietal inferior R, angular R, supramarginal R regions (Figure 8.13).

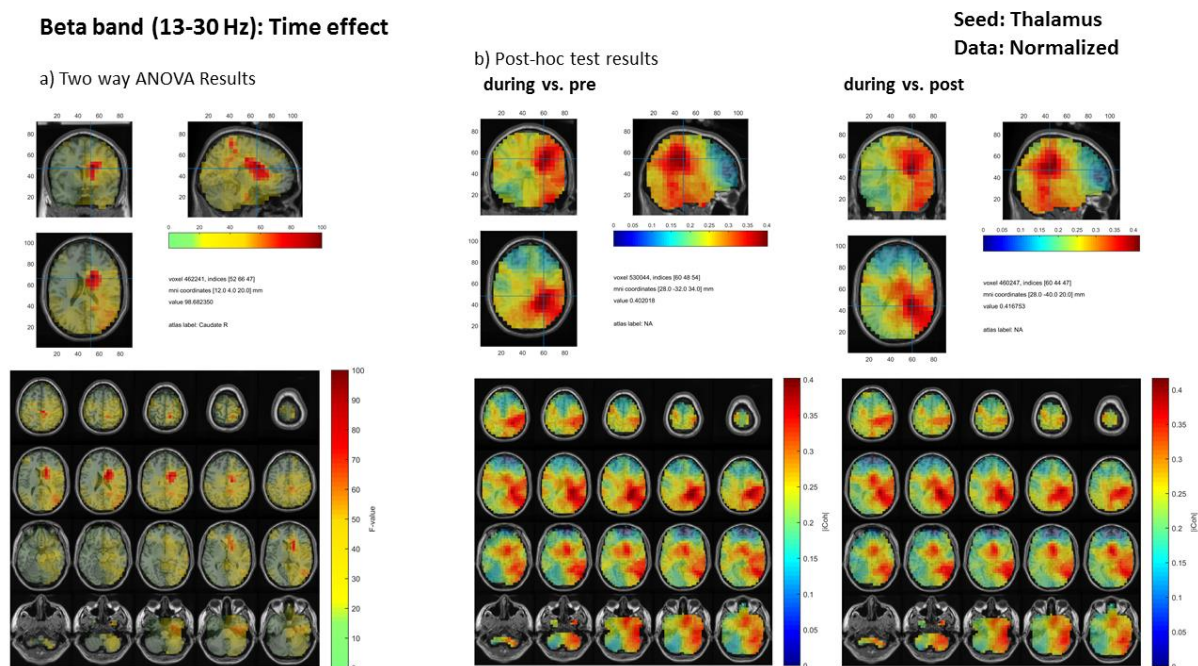


**Figure 8.13 Functional connectivity for thalamus-beta band time effect.**

a) Two way ANOVA test results b) post-hoc test results for conditions during vs. pre time interval and during vs. post time interval, demonstrating coherent regions in the brain.

Seed-Thalamus				
Conditions	Frequency Bands			
	Delta	Theta	Alpha	Beta
<b>Effect of time</b>				
during vs. pre	0.001	0.001	0.001	0.001
during vs. post	0.001	0.001	0.001	0.001
<b>Effect of group</b>				
ictal vs. non-ictal	0.02	-	-	-
<b>Interaction effect</b>				
ictal vs. non-ictal (during-pre)	0.006	-	0.01	-
ictal vs. non-ictal (during-post)	0.04	-	0.003	-

**Table 8.3 Functional connectivity p-values for the seed as thalamus.**

### 8.2.3 Comparison of coherence

For all frequency bands the significant coherence maximum was compared based on the seed of interest, to better understand the presumed shift of the source maximum.

#### a) Delta band

On comparing the coherence maximum difference with the seed being the source maximum or the thalamus, it was seen that there were differences in interaction effect. With the seed as source maximum interaction effect did not show any significant difference.

Time effect and group effect for both seeds of interest showed similar results. The group effect results were similar for all cases. The regions having maximum coherence difference have been mentioned below in table 8.7, for all statistical conditions.

Frequency band	Effect of time	Seed-source maximum	Seed-Thalamus
Delta Band	during vs. pre	S.m.1-Occipital Mid R S.m.2-Temporal Mid L	Cingulum Post R, Precuneus R
	during vs. post	S.m.1-Cingulum Post R, Precuneus R S.m.2-Temporal Mid L	Cingulum Post R, Precuneus R
	<b>Effect of group</b>		
	ictal vs. non-ictal	S.m.1- SupraMarginal R S.m.2- No Significance	SupraMarginal R, Angular R
	<b>Interaction effect</b>		
	ictal vs. non-ictal (during-pre)	S.m.1, S.m.2-No significance	Occipital Mid L
	ictal vs. non-ictal (during-post)	S.m.1, S.m.2-No significance	Occipital Mid L

**Table 8.4 Delta band-Comparison of brain regions showing maximum coherence.**

#### b) Theta band

For theta band, there was no coherence analysis done for source maximum. There was no significant effect of group or interaction effect seen in both cases. Only a significant time effect was seen for both seeds of interest.

Frequency band	Conditions	Seed-Thalamus
<b>Theta Band</b>	<b>Effect of time</b>	
	during vs. pre	Precuneus R
	during vs. post	Cingulum Mid L, Cingulum Post L, Precuneus L
	<b>Effect of group</b>	No significance
	<b>Interaction effect</b>	No significance

**Table 8.5 Theta band-Comparison of brain regions showing maximum coherence.**

### c) Alpha Band

For alpha band, time effect and interaction effect depicted different coherence maximum brain regions. With the seed of interest being the source maximum and the thalamus there was no significant group effect seen in both cases.

Frequency band	Conditions	Seed-source maximum	Seed-Thalamus
<b>Alpha Band</b>	<b>Effect of time</b>		
	during vs. pre	Precuneus L	Angular R
	during vs. post	Precuneus L	Temporal Sup L
	<b>Effect of group</b>		
	ictal vs. non-ictal	No Significance	No significance
	<b>Interaction effect</b>		
	ictal vs. non-ictal (during-pre)	No Significance	Postcentral R, Parietal Inf R
	ictal vs. non-ictal (during-post)	Caudate R, Putamen R	Parietal Inf R, Parietal Sup R

**Table 8.6 Alpha band-Comparison of brain regions showing maximum coherence.**

### d) Beta band

On comparing the coherence maximum for both seeds of interest, it was observed that only a significant time effect was present. The brain regions showing maximum coherence difference were different from each other for both seeds of interest. Furthermore, there was no significant group or interaction effect seen.

<b>Frequency band</b>	<b>Conditions</b>	<b>Seed-source maximum</b>	<b>Seed-Thalamus</b>
<b>Beta Band</b>	<b>Effect of time</b>		
	during vs. pre	Precuneus R, Cingulum post R	Angular R
	during vs. post	Cuneus R, Precuneus R	Parietal Inf R, Angular R, Supra Marginal R
	<b>Effect of group</b>		
	ictal vs. non-ictal	No significance	No significance
	<b>Interaction effect</b>		
	ictal vs. non-ictal (during-pre)	No significance	No significance
	ictal vs. non-ictal (during-post)	No significance	No significance

**Table 8.7 Beta band-Comparison of brain regions showing maximum coherence.**

## Discussion for experimental results

---

In the current study, spectral analysis and functional connectivity were used to differentiate ictal and non-ictal GSWDs at sensor and source level. This study was based on using surface EEG and analysing three time windows of pre-, during- and post- ictal and non-ictal GSWDs respectively. This multi-frequency study was done with an application to assist clinicians on a daily basis for EEG monitoring.

### 9.1 Sensor level

Initially in this study, non-ictal discharges longer than 3 seconds were selected for analysis. But since not all patients had these discharges, ictal and non-ictal GSWDs were assessed separately. Time frequency analysis alongside statistical testing of ictal and non-ictal discharges (with duration longer than 3 seconds) revealed significant spectral power differences for frequency bands delta, theta, alpha, beta and gamma (1-35 Hz). These significant differences were observed independently for both groups of interest. However since the dataset was not fit for comparing ictal and non-ictal discharges, for all further analysis non-ictal discharges less than 3 seconds were included in the dataset. On doing so the dataset was complete for comparing ictal and non-ictal discharges, which was used in all further analysis at sensor and source level.

Ictal and non-ictal GSWDs in CAE have a similar EEG appearance of synchronous, symmetrical GSWDs. In previous studies it has been well established that the GSWDs are of 3 Hz [6, 103]. Using power spectral analysis on surface-EEG data, this study revealed statistically significant differences between ictal and non-ictal GSWDs at frequencies 1-3 Hz (Delta), 8-13 Hz (Alpha) and 14-30 Hz (Beta). However, no significant interaction effect was found for frequencies 4-7 Hz (theta band). The implication of this finding is unclear. But it is well known that theta oscillations are associated with memory and emotional regulation in humans. Also, theta frequency is dominant in the EEGs of lower mammals, while for humans alpha frequency dominates [104].

It has been reported in previous EEG, EEG-fMRI and MEG studies that the frontal cortex plays an important role in the propagation of ictal GSWDs [10, 105–107]. In a study done by Kim et al (2011) [15], spectral power of 1-4 Hz frequency was analysed during absences in CAE using computational EEG. Their findings strongly suggest that absences may have focal features, even though ictal discharges on visual review by epileptologists appear to be broadly distributed. For delta band our study revealed significant activity of electrodes

localized in the frontal-central region, while for alpha and beta bands frontal, frontal-central, central-parietal, and temporal clusters of activity were observed. These findings seem to be in line with the above mentioned studies. Based on this we can presume that these electrode localizations may correlate with the cortical and subcortical regions involved in the pathogenesis of ictal and non-ictal GSWDs.

Also, we observed that the transition of spectral power from pre-ictal to during-ictal and from during-ictal to post-ictal was higher, compared to the transition periods of non-ictal GSWDs. This was seen for all the significant frequency bands: delta, alpha, and beta. These transition period differences between pre-during-post-ictal/non-ictal could play an important role in the development of seizure detection algorithms. Further, statistically significant spectral analysis results in this study show that this technique itself could be implemented as a way to differentiate between ictal and non-ictal GSWDs.

To get a deeper understanding of the brain regions that are in synchrony with each other, network analysis is essential. In our study, FC based on imaginary part of coherency revealed significant differences for delta, theta, alpha and beta bands over all time points, with an increase in channel synchronization in the following order: 1-3 Hz < 4-7 Hz < 8-12 Hz < 13-30 Hz.

Previous studies show that the cortico-thalamic network plays an important part in the generation and propagation 3Hz GSWDs present in absences [9, 10, 106, 108]. In a study done by Miao et al. (2019) [9] regarding the cortico-thalamic connectivity in CAE using MEG, it was seen that at 1-7 Hz inhibitory connections were seen in patients with the thalamo-parietal/occipital (F-T-P/O) network. In another resting state fMRI study, CAE patients had marked differences compared to controls in whole brain FC and had decreased connectivity in the thalamus and basal ganglia alongside increased connectivity in the medial occipital cortex [12]. Various studies have reported a decrease in activity in certain brain regions during absences, several of which coincide with the DMN [11, 109]. Also, thalamo-cortical activation and suspension of the default state have been shown in generalized epileptic discharges in an EEG-fMRI study [24]. Furthermore, resting state functional network analysis studies have shown abnormalities in the dorsal attention network (DAN), salience network (SN) and default mode network (DMN), suggesting that it might contribute to impairment of consciousness and cognitive deficits in CAE patients [110, 111].

In this study it was observed that ictal transition periods, from pre-ictal to during-ictal and from during-ictal to post-ictal had a significantly weaker connectivity compared to non-ictal transition periods for all significant frequency bands. FC showed a desynchronization of channels taking place during ictal GSWDs in frontal-temporal, frontal-central, central-parietal regions, involving areas of the default mode network (DMN) for delta band (1-3 Hz). It is presumed that this desynchronization leading to a weaker connectivity between regions may be a cause for severe impairment of consciousness during ictal GSWDs. While, in non-ictal GSWDs the connectivity between regions is slightly more pronounced, therefore there is

no impairment of consciousness. For differences in connectivity in theta, alpha and beta band, long range connections were observed linking the right and left hemispheres of the brain, which may relate to widespread network propagation.

## 9.2 Source level

In this study the inverse problem regarding source localization was solved using the eLORETA method. This method has been widely used for EEG source reconstruction in various fields of study [112–116]. For instance in the study done by Adebimpe et al. (2016) [116] on EEG resting state data of patients with benign epilepsy with centro-temporal spikes, source reconstruction was done using eLORETA method. In patients with schizophrenia-like psychosis of epilepsy (SLPE), Canuet et al. (2011) [114] analysed resting state EEG data using eLORETA, for source localization and functional connectivity. In a study done on Alzheimer's disease, Hata et al. (2016) [113] assessed functional connectivity using EEG data of patients. Using eLORETA the current source density and lagged phase synchronization was analysed.

Source reconstruction of ictal and non-ictal discharges using eLORETA method in this study revealed that ictal and non-ictal discharges had the same source in the brain for all frequency bands, but non-ictal discharges had a weaker source power compared to ictal discharges. Delta band (1-3 Hz) was the only frequency band where two sources were localized for interaction effect, a subcortical source and a surface source. The source maximum was localized in the subcortical regions of caudate R and putamen R alongside a surface source in the supplementary motor region of the brain. The spread of source power was seen in thalamus, dorsolateral prefrontal cortex, parietal and temporal regions. For group and time effect the significant source maximum was seen in the orbitofrontal cortex of the brain. For alpha (8-12 Hz) and beta band (13-30 Hz) the source maximum was seen in the frontal inferior orbital R, L and Frontal superior medial R, L and orbitofrontal regions. Similar to sensor level results theta band (4-7 Hz) again did not show any significant interaction effect.

In a previous study absence seizures in 5 patients were analysed using EEG data, and source analysis revealed mesial frontal and orbital frontal cortex sources for spike and wave activity [108]. Furthermore, in a study done by Wu et al. (2017) on 14 patients with CAE using MEG data, source analysis revealed localizations in frontal cortex and parieto-occipito-temporal junction (POT) in frequency bands 1–4 Hz, 4–8 Hz, 8–12 Hz, 12–30 Hz and 30–80 Hz. Similarly, Miao et al. (2019) [9] showed significant ictal sources obtained from MEG data, in the frontal and parietal cortex at 1-7 Hz and 8-30 Hz frequency bands, in CAE patients. In another MEG study, Tenny et al (2013) [117] observed that focal cortico-thalamic sources in the brain are involved during ictal generalized absence seizures. Based on these studies we can see that results from this study depicted similar results but we presume that the source was shifted due to the accuracy of the method for localizing deep sources and low number of channels.



In a study done by Moeller et al. (2008) [11] on drug naive children with absence epilepsy, using EEG-fMRI it was seen that BOLD signal decreases in the thalamus were present alongside decreases in the parietal region, frontal cortex, precuneus and the caudate nucleus. Absence seizure studies using EEG-fMRI have previously shown negative blood oxygen level dependent (BOLD) changes in parietal source localization [10, 12, 118]. Various other studies have also depicted thalamic activation in absence seizures [119]. Therefore for FC analysis using iCOH, the source maximum and the thalamus was used as a seed of interest.

FC at source level was done to better understand the neuronal networks during ictal and non-ictal GSWDs. The iCOH was mapped based on the source maximum and the thalamus being the nodes of interest and their correlation to the whole brain. FC results depicted that in ictal GSWDs, the coherence between the source maximum and whole brain was stronger compared to the coherence of non-ictal GSWDs. However, for source maximum as the node of interest there was no significant interaction effect seen for delta, theta and beta band. Only alpha band depicted a significant interaction effect for the transition period from during-ictal/non-ictal to post-ictal/non-ictal interval.

The coherence between thalamus and the whole brain done for ictal and non-ictal GSWDs also showed that ictal GSWDs have a stronger coherence to brain regions compared to non-ictal GSWDs. Though absence seizures are classified as generalized seizures, recent studies have suggested a more selective bilateral cortical and subcortical network to be involved [38, 119]. Tenny et al. (2018) investigated the pre-treatment ictal connectivity in CAE patients in an EEG-fMRI and MEG study, and observed strong connections in the thalamus and posterior brain regions including the parietal, posterior cingulate, angular gyrus, precuneus and occipital regions for delta frequency. With thalamus as the node of interest delta frequency band showed the significant coherence maximum with the Occipital mid L region in the brain, with a spread of coherence in the Parietal, Temporal and Occipital region. These regions were mainly the Parietal inferior and superior L, Angular L, Precuneus L, Cingulum posterior L and supramarginal L regions, associated with functions such as language processing, consciousness, visualization. FC results in this study at source level can be seen to be in line with the above mentioned studies assessing networks in CAE.

Based on the results of this study, it can be presumed that the thalamus is the node of interest in absence seizure propagation and it forms a network involving regions of the brain important to the consciousness system and the DMN network. Although thalamus has a strong coherence to these particular brain regions at source level, a weaker connectivity was observed at the sensor level between the channels, suggesting a disconnection between these regions between each other for ictal discharges. In non-ictal discharges the coherence at source level between the thalamus and other brain regions was weaker, while at sensor level the connectivity was stronger between channels. This leads to the understanding that for non-ictal discharges the complex neuronal network involved during absence seizures does not get

activated strongly, therefore the patients do not lose consciousness during these events and are able to respond unlike ictal discharges. The connectivity between coherent regions needs to be further investigated to corroborate these presumptions.

The entire analysis was based on normalized data. Though, there is still a debate whether the data should be normalized or not, source analysis and FC were done for non-normalized data too, for which the results can be found in Appendix A and B.

Several limitations of the present study should be considered. First, due to the relatively low spatial resolution of EEG, localizations of significant electrodes might show the activity of multiple sources. Second, in this study the number of subjects as well as the number ictal and non-ictal GSWDs analysed were small. In order to validate our findings it would be important that the sample size be larger. Third, deep source localization can be difficult to mark the exact seizure onset zone, therefore other methods could be used to validate whether the source is shifted. Also, the time periods of interest before and after the ictal/non-ictal GSWDs could be increased to better understand the transition period. Lastly, it is important to note that other techniques such as directionality analysis are required in order to improve FC at sensor, and source space level.

These findings suggest that using spectral analysis and FC at sensor level, EEG data alone could provide useful information regarding differences between ictal and non-ictal GSWDs in CAE. Further source analysis and FC gave insight regarding seizure onset zone and brain regions involved during ictal and non-ictal discharges. As a result, this quick methodology could be implemented for assistance in diagnostics of CAE patients as well as to develop machine learning algorithms for facilitating EEG monitoring.

## Conclusion

---

The current study was done on Childhood absence epilepsy in order to differentiate ictal and non-ictal GSWDs using surface EEG data. It demonstrated significant differences at sensor and source level for delta, alpha and beta frequency bands.

### 10.1 Sensor Level

At sensor level, it was revealed that delta, alpha, and beta band had significant spectral power differences between ictal and non-ictal GSWDs. In these frequency bands ictal GSWDs had significantly higher power compared to non-ictal GSWDs. Secondly, regarding time intervals, it was seen that the during-ictal/non-ictal interval had significantly higher power compared to pre- and post- intervals of these discharges. The transition of ictal discharges from pre-to during and from during to post interval had significantly stronger spectral power compared to non-ictal discharges.

Functional connectivity at sensor level using imaginary part of coherence as a measure showed that all frequency bands (delta, theta, alpha, and beta) showed significant time and interaction effect. For transition periods of ictal discharges it was seen that all frequency bands revealed a weaker connectivity compared to non-ictal transition periods (pre to during and during to post). For delta band a desynchronization of channels during ictal GSWDs involving areas of the default mode network (DMN) was seen. The functional hubs with connections were seen in channels Fp1, FC5, T3, Cz, and P3. Channel Cz showed maximum connections to other channels. Further, differences in connectivity in theta, alpha and beta band were long range, linking the right and left hemispheres of the brain

### 10.2 Source Level

Firstly we have given a detailed mathematical foundation for the EEG forward and inverse problem. We have also addressed the mathematical issues concerning the eLORETA algorithm. Accordingly we have formulated the correct solutions regarding the algorithm which further requires testing in an experimental setting.

Source analysis using the eLORETA method demonstrated that ictal and non-ictal GSWDs have the same source. Secondly, ictal discharges have a stronger source power compared to non-ictal discharges. Delta, alpha and beta bands showed significant differences. For delta band transition periods (pre to during and during to post) source localization revealed two

sources in the subcortical and the cortical region of the brain, while for the significant group effect the localization was found in frontal basal region (gyrus rectus). The spread of source power was seen in the thalamus, parietal and temporal regions. For alpha and beta band the frontal basal and frontal superior and inferior regions were localized.

The source was presumed to be shifted since the accuracy of interpolating surface EEG data to its particular source with less number of channels is difficult.

Further, functional connectivity after source analysis revealed that the coherence between the source maximum and various regions of the brain was stronger in ictal discharges compared to non-ictal discharges. All frequency bands showed a significant time effect, and only delta band showed a significant group effect. For interaction effect significant functional connectivity results were only seen in alpha frequency band.

Functional connectivity done between the thalamus and various regions of the brain gave more promising results. It was seen that the functional connectivity was stronger for ictal GSWDs compared to non-ictal GSWDs. For delta band, the coherence of thalamus was seen with brain regions important for consciousness, language processing, number processing, spatial cognition, memory retrieval and visualization. These regions were occipital mid (left), parietal inferior and superior (right and left), angular gyrus (left), posterior cingulum (left) and precuneus (left). Also, some of these regions were similar to those found in the DMN.

This study shows clearly that EEG is a powerful tool to assess ictal and non-ictal discharges. There are clear differences at sensor and source level between ictal and non-ictal GSWDs even though they have the same pattern on an EEG. Seeing the coherence patterns, it can be inferred that the complex neuronal network involved in ictal discharges gets more strongly activated compared to non-ictal discharges.

Based on FC results it can be presumed that even though various brain regions were seen to be strongly coherent with the thalamus, these regions may be disconnected with each other for ictal discharges, and therefore at sensor level a weaker connectivity between channels was seen i.e. a desynchronization between channels was seen. This presumptions needs to be further investigated.

Differentiating ictal and non-ictal discharges at sensor and source level could potentially be the foundation for future clinical research which would help facilitate clinicians in diagnosis and better management of CAE patients. This methodology has to be evaluated concerning sensitivity and specificity. Future work regarding this study will be based on building an automated classifier to distinguish between ictal and non-ictal GSWDs using various differences found in this study, to aid in EEG monitoring.

# References

---

1. Fisher RS, Acevedo C, Arzimanoglou A et al. (2014) ILAE official report: a practical clinical definition of epilepsy. *Epilepsia* 55: 475–482.
2. Epilepsy: a public health imperative. Summary. Geneva: World Health Organization; (2019) (WHO/MSD/MER/19.2). Licence: CC BY-NC-SA 3.0 IGO.
3. Engel Jr J (2001) A Proposed Diagnostic Scheme for People with Epileptic Seizures and with Epilepsy: Report of the ILAE Task Force on Classification and Terminology. *Epilepsia* 42(6):796-803.
4. Fisher RS, Cross JH, French JA et al. (2017) Operational classification of seizure types by the International League Against Epilepsy: Position Paper of the ILAE Commission for Classification and Terminology. *Epilepsia* 58: 522–530.
5. Panayiotopoulos CP (2005) *The epilepsies: seizures, syndromes and management*. Bladon Medical Publishing, Oxfordshire (UK).
6. Matricardi S, Verrotti A, Chiarelli F et al. (2014) Current advances in childhood absence epilepsy. *Pediatric Neurology* 50: 205–212.
7. Engel Jr J (2013) *Seizures and epilepsy*., (Vol. 83). Oxford University Press
8. Wu C, Xiang J, Jiang W et al. (2017) Altered Effective Connectivity Network in Childhood Absence Epilepsy: A Multi-frequency MEG Study. *Brain Topography* 30: 673–684.
9. Miao A, Wang Y, Xiang J et al. (2019) Ictal Source Locations and Cortico-Thalamic Connectivity in Childhood Absence Epilepsy: Associations with Treatment Response. *Brain Topography* 32: 178–191.
10. Bai X, Vestal M, Berman R et al. (2010) Dynamic time course of typical childhood absence seizures: EEG, behavior, and functional magnetic resonance imaging. *J Neuroscience* 30: 5884–5893.
11. Moeller F, Siebner HR, Wolff S et al. (2008) Changes in activity of striato-thalamo-cortical network precede generalized spike wave discharges. *Neuroimage* 39: 1839–1849.
12. Masterton RAJ, Carney PW, Abbott DF et al. (2013) Absence epilepsy subnetworks revealed by event-related independent components analysis of functional magnetic resonance imaging. *Epilepsia* 54: 801–808.
13. Danielson NB, Guo JN, Blumenfeld H (2011) The default mode network and altered consciousness in epilepsy. *Behavioural Neurology* 24: 55–65.
14. Sanchez Bornot JM, Wong-Lin K, Ahmad AL et al. (2018) Robust EEG/MEG Based Functional Connectivity with the Envelope of the Imaginary Coherence: Sensor Space Analysis. *Brain Topography* 31: 895–916.

15. Kim D-S, Nordli DR, JR, Zelko F (2011) Spectral Power of 1–4 Hz Frequency in the Ictal Phase of Childhood Absence Epilepsy. *Journal of Clinical Neurophysiology* 28: 463–468.
16. Pascual-Marqui RD, Lehmann D, Koukkou M et al. (2011) Assessing interactions in the brain with exact low-resolution electromagnetic tomography. *Philosophical Transactions of the Royal Society A: Mathematical, Physical and Engineering Sciences* 369: 3768–3784.
17. Pascual-Marqui RD (2007) Discrete, 3D distributed, linear imaging methods of electric neuronal activity. Part 1: exact, zero error localization. arXiv preprint arXiv:0710.3341.
18. Pascual-Marqui RD, Esslen M, Kochi K, Lehmann D (2002). Functional imaging with low-resolution brain electromagnetic tomography (LORETA): a review. *Methods and findings in experimental and clinical pharmacology* 24(Suppl C):91-5.
19. Pascual-Marqui RD (2002) Standardized low-resolution brain electromagnetic tomography (sLORETA): technical details. *Methods and findings in experimental and clinical pharmacology*. 24(Suppl D):5-12.
20. Bowyer SM (2016) Coherence a measure of the brain networks: past and present. *Neuropsychiatric Electrophysiology* 2: 1051.
21. Uhlhaas PJ, Roux F, Rodriguez E et al. (2010) Neural synchrony and the development of cortical networks. *Trends in Cognitive Science (Regul Ed)* 14: 72–80.
22. Yeragani VK, Cashmere D, Miewald J, et al. (2006) Decreased coherence in higher frequency ranges (beta and gamma) between central and frontal EEG in patients with schizophrenia: a preliminary report. *Psychiatry research* 141(1):53-60.
23. Brazier MA (1972) Spread of seizure discharges in epilepsy: anatomical and electrophysiological considerations. *Experimental neurology* 36(2):263-72.
24. Gotman J (1981) Interhemispheric relations during bilateral spike-and-wave activity. *Epilepsia* 22(4):453-66.
25. Song J, Tucker DM, Gilbert T et al. (2013) Methods for examining electrophysiological coherence in epileptic networks. *Frontiers in Neurology* 4: 55.
26. Nolte G, Bai O, Wheaton L et al. (2004) Identifying true brain interaction from EEG data using the imaginary part of coherency. *Clinical Neurophysiology* 115: 2292–2307.
27. Pascual-Marqui RD (1999) Review of methods for solving the EEG inverse problem. *International journal of bioelectromagnetism* 1: 75–86
28. Brigo F, Trinka E, Lattanzi S et al. (2018) A brief history of typical absence seizures - Petit mal revisited. *Epilepsy Behavior* 80: 346–353.
29. Gibbs FA, Davis H, Lennox WG (1935). The electro-encephalogram in epilepsy and in conditions of impaired consciousness. *Archives of Neurology & Psychiatry*, 34(6), 1133-1148.

30. Weir B (1965). The morphology of the spike-wave complex. *Electroencephalography and clinical neurophysiology*, 19(3), 284-290.
31. Commission on Classification and Terminology of the International League Against Epilepsy, 1981. Proposal for revised clinical and electroencephalographic classification of epileptic seizures. *Epilepsia* 22, 489–501.
32. Commission on Classification and Terminology of the International League Against Epilepsy, 1989. Proposal for revised classification of epilepsies and epileptic syndromes. *Epilepsia* 30, 389–399
33. Crunelli V, Leresche N (2002) Childhood absence epilepsy: genes, channels, neurons and networks. *Nature Reviews Neuroscience* 3: 371–382.
34. Rocca WA, Sharbrough FW, Hauser WA et al. (1987) Risk factors for absence seizures. A population-based case-control study in Rochester, Minnesota 37: 1309.
35. Callenbach PM, Geerts AT, Arts WF et al. (1998). Familial occurrence of epilepsy in children with newly diagnosed multiple seizures: Dutch Study of Epilepsy in Childhood. *Epilepsia*, 39(3), 331-336.
36. Berg AT, Shinnar S, Levy SR, et al.(2000). How well can epilepsy syndromes be identified at diagnosis? A reassessment 2 years after initial diagnosis. *Epilepsia*, 41(10), 1269-1275.
37. Loiseau J, Loiseau P, Guyot M et al. (1990). Survey of seizure disorders in the French southwest. I. Incidence of epileptic syndromes. *Epilepsia*, 31(4), 391-396.
38. Blumenfeld H (2012) Impaired consciousness in epilepsy. *The Lancet Neurology* 11: 814–826.
39. Panayiotopoulos CP, Obeid T, Waheed G. (1989). Differentiation of typical absence seizures in epileptic syndromes: a video EEG study of 224 seizures in 20 patients. *Brain*, 112(4), 1039-1056.
40. Panayiotopoulos C P (2006). Childhood absence epilepsy. *MedLink Neurology*.
41. Sadleir LG, Farrell K, Smith S, et al. (2006). Electroclinical features of absence seizures in childhood absence epilepsy. *Neurology*, 67(3), 413-418.
42. Eeg-Olofsson KE (Ed.) (2006) *Pediatric Clinical Neurophysiology*. Mac Keith Press for the International Child Neurology Association.
43. Jasper H, Penfield W, & Droogleever-Fortuyn J (1946). Origin of bilaterally synchronous epileptic discharges. *Proc. Research Nerv. Ment. Dis.*
44. Williams DE (1953). A study of thalamic and cortical rhythms in petit mal. *Brain*, 76(1), 50-69.
45. Avoli M, Gloor P (1982). Interaction of cortex and thalamus in spike and wave discharges of feline generalized penicillin epilepsy. *Experimental neurology*, 76(1), 196-217.
46. Danober L, Deransart C, Depaulis A., Vergnes M, & Marescaux C (1998). Pathophysiological mechanisms of genetic absence epilepsy in the rat. *Progress in neurobiology*, 55(1), 27-57.

47. Li Q, Luo C, Yang T et al. (2009) EEG-fMRI study on the interictal and ictal generalized spike-wave discharges in patients with childhood absence epilepsy. *Epilepsy Research* 87: 160–168.
48. Yeni SN, Kabasakal L, Yalçinkaya C et al. (2000) Ictal and interictal SPECT findings in childhood absence epilepsy. *Seizure* 9: 265–269.
49. Hirsch E, Panayiotopoulos CP (2005) Childhood absence epilepsy and related syndromes. In: Roger J, Bureau M, Dravet C, Genton P, Tassinari CA, Wolf P, eds. *Epileptic Syndromes in Infancy, Childhood and Adolescence*. 4th ed. Montrouge, France: John Libbey Eurotext.
50. Michelle B, Pierre G, Charlotte D (2012). *Epileptic syndromes in infancy, childhood and adolescence*. John Libbey Eurotext.
51. Yalçın, Ö. (2012). Genes and molecular mechanisms involved in the epileptogenesis of idiopathic absence epilepsies. *Seizure*, 21(2), 79-86.
52. Reid, C. A., Berkovic, S. F., & Petrou, S. (2009). Mechanisms of human inherited epilepsies. *Progress in neurobiology*, 87(1), 41-57.
53. Hughes JR (2009). Absence seizures: a review of recent reports with new concepts. *Epilepsy & behavior*, 15(4), 404-412.
54. Everett K, Chioza B, Aicardi J et al. (2007). Linkage and mutational analysis of CLCN2 in childhood absence epilepsy. *Epilepsy Research*, 75(2-3), 145-153.
55. Striano P, Weber YG, Toliat MR et al. (2012). GLUT1 mutations are a rare cause of familial idiopathic generalized epilepsy. *Neurology*, 78(8), 557-562.
56. Suls A, Mullen SA, Weber YG et al. (2009). Early-onset absence epilepsy caused by mutations in the glucose transporter GLUT1. *Annals of Neurology: Official Journal of the American Neurological Association and the Child Neurology Society*, 66(3), 415-419.
57. D'Agati E, Cerminara C, Casarelli L, et al. (2012). Attention and executive functions profile in childhood absence epilepsy. *Brain and Development*, 34(10), 812-817.
58. Killory BD, Bai X, Negishi M et al. (2011) Impaired attention and network connectivity in childhood absence epilepsy. *Neuroimage* 56: 2209–2217.
59. Rogawski MA, Löscher W (2004). The neurobiology of antiepileptic drugs. *Nature Reviews Neuroscience*, 5(7), 553-564.
60. Manning J-PA, Richards DA, Bowery NG (2003) Pharmacology of absence epilepsy. *Trends in Pharmacological Sciences* 24: 542–549.
61. Blomquist HKS, Zetterlund, B (1985). Evaluation of treatment in typical absence seizures: the roles of long-term EEG monitoring and ethosuximide. *Acta Pædiatrica*, 74(3), 409-415.
62. Covanis, A, Gupta AK, Jeavons PM (1982). Sodium valproate: monotherapy and polytherapy. *Epilepsia*, 23(6), 693-720.



63. Glauser TA, Cnaan A, Shinnar S, et al. (2010). Ethosuximide, valproic acid, and lamotrigine in childhood absence epilepsy. *New England Journal of Medicine*, 362(9), 790-799.
64. Cohen MX (2014) *Analyzing neural time series data: Theory and practice*. Issues in clinical and cognitive neuropsychology. The MIT Press, Cambridge Massachusetts
65. Oostenveld R, Fries P, Maris E et al. (2011) FieldTrip: Open source software for advanced analysis of MEG, EEG, and invasive electrophysiological data. *Comput Intell Neurosci* 2011: 156869.
66. Cuspidada-Bravo E R, Martínez-Montes E, Farach-Fumero M, Machado-Curbelo C (2015). Improving Electroencephalographic Source Localization of Epileptogenic Zones With Time-Frequency Analysis. *Clinical EEG and neuroscience*, 46(2), 153-168.
67. Tzallas AT, Tsipouras MG, Fotiadis DI (2007). Automatic seizure detection based on time-frequency analysis and artificial neural networks. *Computational Intelligence and Neuroscience*, 2007.
68. Sitnikova E, Hramov AE, Grubov V, Koronovsky AA (2014). Time-frequency characteristics and dynamics of sleep spindles in WAG/Rij rats with absence epilepsy. *Brain research*, 1543, 290-299.
69. Colominas MA, Jomaa ME, Jrad N et al. (2017). Time-varying time–frequency complexity measures for epileptic eeg data analysis. *IEEE transactions on biomedical engineering*, 65(8), 1681-1688.
70. Sun Y, Zhang G, Zhang X et al. (2016). Time-frequency analysis of intracranial EEG in patients with myoclonic seizures. *Brain research*, 1652, 119-126.
71. Tenney JR, Fujiwara H, Horn PS et al. (2014). Low-and high-frequency oscillations reveal distinct absence seizure networks. *Annals of neurology*, 76(4), 558-567.
72. Celka, P., Boashash, B., & Colditz, P. (2001). Preprocessing and time-frequency analysis of newborn EEG seizures. *IEEE Engineering in Medicine and Biology Magazine*, 20(5), 30-39.
73. Williams WJ, Zaveri HP, & Sackellares JC (1995). Time-frequency analysis of electrophysiology signals in epilepsy. *IEEE Engineering in Medicine and Biology Magazine*, 14(2), 133-143.
74. Blanco S, Kochen S, Rosso, OA, Salgado P (1997). Applying time-frequency analysis to seizure EEG activity. *IEEE Engineering in medicine and biology magazine*, 16(1), 64-71.
75. Drinkenburg WH, Van Luijtelaa EL, Van Schaijk WJ, Coenen A. (1993). Aberrant transients in the EEG of epileptic rats: a spectral analytical approach. *Physiology & behavior*, 54(4), 779-783.
76. Numer MR (1988). Frequency analysis and topographic mapping of EEG and evoked potentials in epilepsy. *Electroencephalography and clinical neurophysiology*, 69(2), 118-126.

77. Sitnikova E, van Luijtelaar G (2009) Electroencephalographic precursors of spike-wave discharges in a genetic rat model of absence epilepsy: Power spectrum and coherence EEG analyses. *Epilepsy Research* 84: 159–171.
78. Mitra PP, Pesaran B (1999) Analysis of Dynamic Brain Imaging Data. *Biophysical Journal* 76: 691–708.
79. Podder P, Khan TZ, Khan MH et al. (2014) Comparative performance analysis of hamming, hanning and blackman window. *International Journal of Computer Applications* 96.
80. Grech R, Cassar T, Muscat J et al. (2008) Review on solving the inverse problem in EEG source analysis. *Journal of neuroengineering and rehabilitation* 5: 25.
81. Sander TH, Bock A, Leistner S et al. (2010) Coherence and imaginary part of coherency identifies cortico-muscular and cortico-thalamic coupling. In: 2010 Annual International Conference of the IEEE Engineering in Medicine and Biology, pp 1714–1717
82. García Domínguez L, Stieben J, Pérez Velázquez JL et al. (2013) The Imaginary Part of Coherency in Autism: Differences in Cortical Functional Connectivity in Preschool Children. *PLOS ONE* 8: e75941.
83. Elshahabi A, Klamer S, Sahib AK et al. (2015) Magnetoencephalography Reveals a Widespread Increase in Network Connectivity in Idiopathic/Genetic Generalized Epilepsy. *PLOS ONE* 10: e0138119-e0138119.
84. Wolters CH, Grasedyck L, Hackbusch W (2004) Efficient computation of lead field bases and influence matrix for the FEM-based EEG and MEG inverse problem. *Inverse Problems* 20: 1099–1116.
85. Wolters CH, Köstler H, Möller C et al. (2008) Numerical Mathematics of the Subtraction Method for the Modeling of a Current Dipole in EEG Source Reconstruction Using Finite Element Head Models. *SIAM J Sci Comput* 30: 24–45.
86. Munck JC de, van Dijk BW, Spekreijse H (1988) Mathematical dipoles are adequate to describe realistic generators of human brain activity. *IEEE Transactions on Biomedical Engineering* 35: 960–966
87. Wolters CH (2003) Influence of tissue conductivity inhomogeneity and anisotropy on EEG/MEG based source localization in the human brain, Doctoral dissertation, Max Planck Institute of Cognitive Neuroscience Leipzig.
88. Plonsey R, Heppner DB (1967) Considerations of quasi-stationarity in electrophysiological systems. *The Bulletin of mathematical biophysics* 29: 657–664
89. Gulrajani RM (1998) *Bioelectricity and biomagnetism*. J. Wiley.
90. Yao D, Qin Y, Hu S et al. (2019) Which Reference Should We Use for EEG and ERP practice? *Brain Topography* 32: 530–549.

91. Magnus J R. and NEUDECKER, H.(1988). *Matrix Differential Calculus with Applications in Statistics and Econometrics*. John Wiley& Sons
92. James M (1978) The generalised inverse. *The Mathematical Gazette* 62: 109–114.
93. Chaumon M, Bishop DVM, Busch NA (2015) A practical guide to the selection of independent components of the electroencephalogram for artifact correction. *J Neurosci Methods* 250: 47–63.
94. DeCoster J, Claypool H (2004) *Data analysis in SPSS*. Retrieved October 2: 2015
95. Kim H-Y (2015) Statistical notes for clinical researchers: A one-way repeated measures ANOVA for data with repeated observations. *Restor Dent Endod* 40: 91–95
96. Kumar A, Lyzhko E, Hamid L et al. (2020) Differentiating ictal and non-ictal EEG generalized spikes and waves in childhood absence epilepsy using spectral and network analyses. (Submitted to *Epilepsy Research*)
97. Chaumon M, Bishop DVM, Busch NA (2015) A practical guide to the selection of independent components of the electroencephalogram for artifact correction. *J Neuroscience Methods* 250: 47–63
98. Syam SH-F, Lakany H, Ahmad RB et al. (2017) Comparing Common Average Referencing to Laplacian Referencing in Detecting Imagination and Intention of Movement for Brain Computer Interface. *MATEC Web Conferences* 140: 1028.
99. Anderson M, Braak C (2003) Permutation tests for multi-factorial analysis of variance. *Journal of statistical computation and simulation* 73(2):85-113.
100. Suckling J, Bullmore E (2004) Permutation tests for factorially designed neuroimaging experiments. *Human Brain Mapping* 22: 193–205.
101. Hallez H, Vanrumste B, Grech R et al. (2007) Review on solving the forward problem in EEG source analysis. *Journal of neuroengineering and rehabilitation* 4: 46.
102. Tzourio-Mazoyer N, Landeau B, Papathanassiou D et al. (2002) Automated anatomical labeling of activations in SPM using a macroscopic anatomical parcellation of the MNI MRI single-subject brain. *Neuroimage* 15: 273–289
103. Sadleir LG, Farrell K, Smith S et al. (2006) Electroclinical features of absence seizures in childhood absence epilepsy. *Neurology* 67(3):413-8.
104. Sainsbury RS (1998) Hippocampal theta: a sensory-inhibition theory of function. *Neuroscience & Biobehavioral Reviews* 22(2):237-41.
105. Gupta D, Ossenblok P, van Luijtelaar G (2011) Space-time network connectivity and cortical activations preceding spike wave discharges in human absence epilepsy: a MEG study. *Med Biol Eng Comput* 49: 555–565.
106. Amor F, Baillet S, Navarro V et al. (2009) Cortical local and long-range synchronization interplay in human absence seizure initiation. *Neuroimage* 45: 950–962.

107. Szaflarski JP, DiFrancesco M, Hirschauer T et al. (2010) Cortical and subcortical contributions to absence seizure onset examined with EEG/fMRI. *Epilepsy & Behavior* 18(4):404-13.
108. Holmes MD, Brown M, Tucker DM (2004) Are “Generalized” Seizures Truly Generalized? Evidence of Localized Mesial Frontal and Frontopolar Discharges in Absence. *Epilepsia* 45: 1568–1579.
109. Berman R, Negishi M, Vestal M et al. (2010) Simultaneous EEG, fMRI, and behavior in typical childhood absence seizures. *Epilepsia* 51: 2011–2022.
110. Li Q, Cao W, Liao X et al. (2015) Altered resting state functional network connectivity in children absence epilepsy. *J Neurol Sci* 354: 79–85.
111. Luo C, Yang T, Tu S et al. (2014) Altered intrinsic functional connectivity of the salience network in childhood absence epilepsy. *J Neurol Sci* 339: 189–195.
112. Aoki Y, Ishii R, Iwase M et al. (2013) Normalized power variance change between pre-ictal and ictal phase of an epilepsy patient using NAT analysis: A case study. In: 2013 35th Annual International Conference of the IEEE Engineering in Medicine and Biology Society (EMBC), pp 437–440
113. Hata M, Kazui H, Tanaka T et al. (2016) Functional connectivity assessed by resting state EEG correlates with cognitive decline of Alzheimer’s disease – An eLORETA study. *Clinical Neurophysiology* 127: 1269–1278.
114. Canuet L, Ishii R, Pascual-Marqui RD et al. (2011) Resting-state EEG source localization and functional connectivity in schizophrenia-like psychosis of epilepsy. *PLOS ONE* 6: e27863-e27863.
115. Ikeda S, Ishii R, Canuet L et al. (2017) Source estimation of epileptic activity using eLORETA kurtosis analysis. *Case Reports* 2017.
116. Adebimpe A, Aarabi A, Bourel-Ponchel E et al. (2016) EEG Resting State Functional Connectivity Analysis in Children with Benign Epilepsy with Centrotemporal Spikes. *Frontiers in Neuroscience* 10: 143.
117. Tenney JR, Fujiwara H, Horn PS et al. (2013) Focal corticothalamic sources during generalized absence seizures: a MEG study. *Epilepsy Research* 106: 113–122.
118. Carney PW, Jackson GD (2014) Insights into the mechanisms of absence seizure generation provided by EEG with functional MRI. *Frontiers in Neurology* 5: 162.
119. Blumenfeld H (2005) Consciousness and epilepsy: why are patients with absence seizures absent? In: *The Boundaries of Consciousness: Neurobiology and Neuropathology*, vol 150. Elsevier, pp 271–603

# List of Figures

---

## Chapter 1

Figure 1.1 ILAE classification of seizures.....	15
---	----

## Chapter 2

Figure 2.1 Time and frequency smoothening. ....	31
---	----

## Chapter 3

Figure 3.1 Geometric illustration of an electric dipole.....	35
--	----

## Chapter 4

Figure 4. 1 Electrode layout.....	64
Figure 4. 2 Time intervals of interest.....	65
Figure 4. 3 EEG ictal GSWDs. ....	67
Figure 4. 4 EEG Non-ictal GSWDs.....	67

## Chapter 5

Figure 5.1 Time intervals.....	70
Figure 5.2 ICA topographical plots. ....	71
Figure 5.3 ICA plot properties.....	72
Figure 5.4 Time frequency analysis.....	73
Figure 5.5 Estimated marginal means for during-ictal interval. ....	77
Figure 5.6 Estimated marginal means for pre-ictal interval. ....	79
Figure 5.7 Estimated marginal means for post-ictal interval.....	81
Figure 5.8 Estimated marginal means for during-non-ictal interval.....	83
Figure 5.9 Estimated marginal means for pre-non-ictal interval.....	85
Figure 5.10 Estimated marginal means of post-non-ictal interval.....	87

## Chapter 6

Figure 6.1 Spectral analysis-time effect.....	93
Figure 6.2 Spectral analysis-group effect .....	94
Figure 6.3 Spectral analysis- interaction effect.....	95
Figure 6.4 Functional connectivity-time effect.....	96
Figure 6.5 Functional connectivity-interaction effect.....	97

## Chapter 7

Figure 7.1 Delta band time effect. ....	102
Figure 7.2 Delta band group effect. ....	103
Figure 7. 3 Delta band interaction effect. ....	103
Figure 7.4 Theta band time effect. ....	104
Figure 7.5 Alpha band time effect. ....	105
Figure 7.6 Alpha band group effect. ....	106
Figure 7.7 Alpha band interaction effect. ....	106
Figure 7.8 Beta band time effect.....	107
Figure 7.9 Beta band group effect.....	108

Figure 7.10 Beta band interaction effect.....108

**Chapter 8**

Figure 8.1 Functional connectivity for source maximum-delta band time effect.....113  
Figure 8.2 Functional connectivity for source maximum-delta band group effect.....113  
Figure 8.3 Functional connectivity for second source maximum-delta band time effect.....114  
Figure 8.4 Functional connectivity for source maximum- alpha band time effect.....115  
Figure 8.5 Functional connectivity for source maximum- alpha band interaction effect.....115  
Figure 8.6 Functional connectivity for source maximum- beta band time effect.....116  
Figure 8.7 Functional connectivity for thalamus-delta band time effect .....118  
Figure 8.8 Functional connectivity for thalamus-delta band group effect .....118  
Figure 8.9 Functional connectivity for thalamus-delta band interaction effect.....119  
Figure 8.10 Functional connectivity for thalamus-theta band time effect. ....120  
Figure 8.11 Functional connectivity for thalamus-alpha band time effect. ....121  
Figure 8.12 Functional connectivity for thalamus-alpha band interaction effect. ....121  
Figure 8.13 Functional connectivity for thalamus-beta band interaction effect time effect..122

# List of Tables

---

## Chapter 2

Table 2.1 Exclusion and inclusion criteria for CAE. ....	23
Table 2.2 Drugs used for CAE patients. ....	26

## Chapter 4

Table 4.1 Demographic data of all subjects. ....	63
Table 4.2 The duration of ictal and non-ictal. ....	68

## Chapter 5

Table 5.1 Depiction of number of ictal and non-ictal GSWDs > 3 seconds. ....	69
Table 5.2 Descriptive statistics for during-ictal GSWDs interval. ....	75
Table 5.3 Mauchly's test of sphericity for during-ictal interval. ....	75
Table 5.4 Tests for within subject effects for during-ictal interval. ....	76
Table 5.5 Descriptive statistics for pre-ictal interval. ....	77
Table 5.6 Mauchly's test of sphericity for pre-ictal interval. ....	78
Table 5.7 Tests of within subject effects for pre-ictal interval. ....	78
Table 5.8 Descriptive statistics for post-ictal interval. ....	79
Table 5.9 Mauchly's test of sphericity for post-ictal interval. ....	80
Table 5.10 Tests of within subject effects for post-ictal interval. ....	80
Table 5.11 Descriptive statistics for during-non-ictal GSWDs > 3 seconds. ....	81
Table 5.12 Mauchly's test of sphericity for durin-non-ictal GSWDs > 3 seconds. ....	82
Table 5.13 Tests for within subject effects for during-non-ictal GSWDs > 3 seconds. ....	82
Table 5.14 Descriptive statistics for pre-non-ictal GSWDs > 3 seconds. ....	84
Table 5.15 Mauchly's test of sphericity for pre-non-ictal GSWDs > 3 seconds. ....	84
Table 5.16 Tests of within-subject effects for pre-non-ictal GSWDs > 3 seconds. ....	84
Table 5.17 Descriptive statistics for post-non-ictal GSWDs > 3 seconds. ....	86
Table 5.18 Mauchly's test of sphericity for post-non-ictal GSWDs > 3 seconds. ....	86
Table 5.19 Tests of within-subject effects for post-non-ictal GSWDs > 3 seconds. ....	86

## Chapter 6

Table 6.1 Time effect. ....	90
Table 6.2 Group effect. ....	90
Table 6.3 Interaction effect (group x time). ....	90
Table 6.4 Spectral analysis p-values for two way ANOVA test. ....	92
Table 6.5 Spectral analysis p-values for Post hoc comparisons. ....	92
Table 6.6 Functional hubs and there significant connections for all channels. ....	98
Table 6.7 Functional connectivity p-values for two way ANOVA test. ....	98
Table 6.8 Functional connectivity p-values for post-hoc comparisons. ....	99

## Chapter 7

Table 7.1 Source analysis p-values for all frequency bands and conditions. ....	109
Table 7.2 Brain regions showing the source maximum. ....	109

## **Chapter 8**

Table 8.1 Selection of the seed from the source maximum.....	111
Table 8.2 Functional connectivity p-values for source maximum as the seed. ....	117
Table 8.3 Functional connectivity p-values for the seed as thalamus.....	122
Table 8.4 Delta band-Comparison of brain regions showing maximum coherence.....	123
Table 8. 5 Theta band-Comparison of brain regions showing maximum coherence. ....	124
Table 8.6 Alpha band-Comparison of brain regions showing maximum coherence.....	124
Table 8.7 Beta band-Comparison of brain regions showing maximum coherence. ....	125



# Appendix A

## A.1 Source analysis for non-normalized data

### A.1.1 Seed selection

Non-Normalized data								
Frequency	Conditions for Interaction effect	MNI coordinates (cm)			Deep Source	Source max. power value	Distance from thalamus (cm)	Number of seeds selected from source max.
		x	y	z				
Delta band (1-3 Hz)	During-pre	0	2.25	-3.75	Yes	3.5756e+04	5.4083	1
	During-post	0	2.25	-3.75	Yes	3.5296e+04	5.4083	
Theta band (4-7 Hz)	-	-	-	-	-	-	-	-
Alpha band (8-12 Hz)	During-pre	0	0.75	-3	Yes	2605.7	4.0389	1
	During-post	0	0.75	-3	Yes	2536	4.0839	
Beta band (13-30 Hz)	During-pre	0	3.75	-0.75	Yes	1110.6	4.7434	1
	During-post	0	3.75	-0.75	Yes	1126.3	5.4601	

*Table A.1: Non-Normalized data. For all frequency bands, information regarding the MNI coordinates, the source maximum power value, the distance between thalamus and source maximum, source depth, and the number of seeds selected based on source maximum has been given. This information has been given for each interaction effect condition. Theta band was excluded due to no significant interaction effect.*

### A.1.2 Source localization results

#### a) Delta band

For delta band two-way repeated measure ANOVA (group x time) depicted a significant effect of time, significant effect of group as well as a significant interaction effect. Post-hoc test for main effect of time revealed that during-ictal/non-ictal interval had a stronger source power compared to pre- and post-ictal/non-ictal intervals. The significant source maximum for during vs. pre interval and during vs. post interval was observed in the Rectus R,L region. For the effect of group it was seen that the source power for ictal GSWDs was stronger compared to non-ictal GSWDs. The source maximum, for the significant difference between ictal vs. non-ictal group was also seen in the Rectus R. Further, post hoc tests for interaction effect depicted, that the source power transition from pre interval to during interval and from during interval to post interval is stronger for ictal GSWDs is stronger compared to the transition periods of non-ictal GSWDs. The source maximum for the significant difference of

during-pre (ictal/non-ictal) and post-during (ictal/non-ictal) was observed in the Rectus region again. Neighbouring sources were seen in the regions of Frontal superior R, Frontal Inferior orb R, Para-hippocampal R,L, Olfactory L, and Frontal medial orb R.

### Delta band (1-3 Hz):Time effect

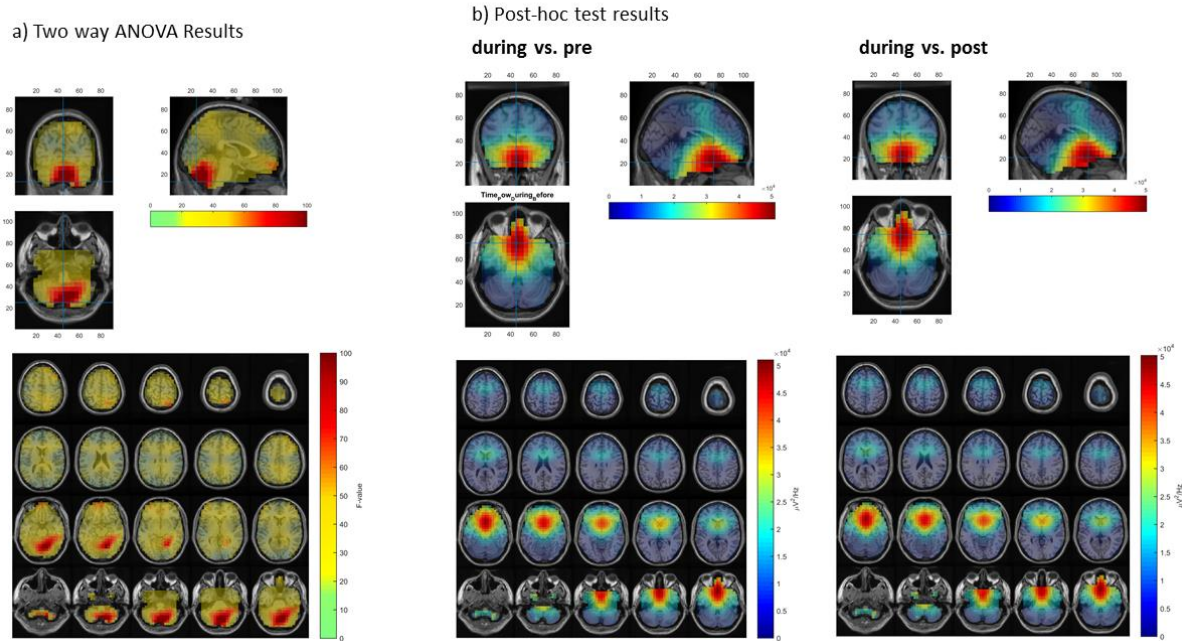


Figure A.1: Delta band time effect for non-normalized data. a) Two way ANOVA results depicting the F-value b) Post-hoc test results for conditions during vs. pre interval and during vs. post interval, indicating the source maximum.

### Delta band (1-3 Hz):Group effect

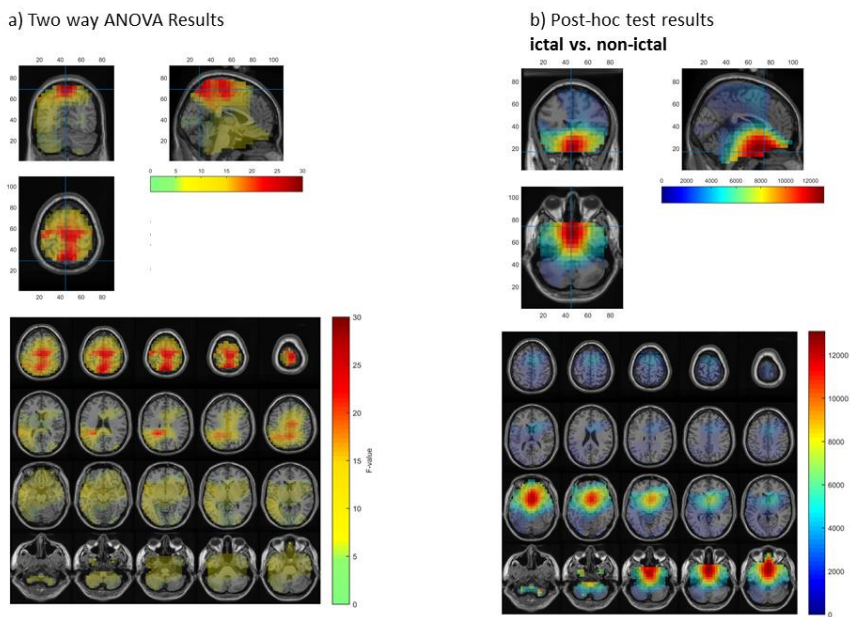


Figure A.2: Delta band group effect. a) Two way ANOVA results depicting the F-value b) Post-hoc test results for the condition ictal vs. non-ictal, indicating the source maximum

## Delta band (1-3 Hz):Interaction effect

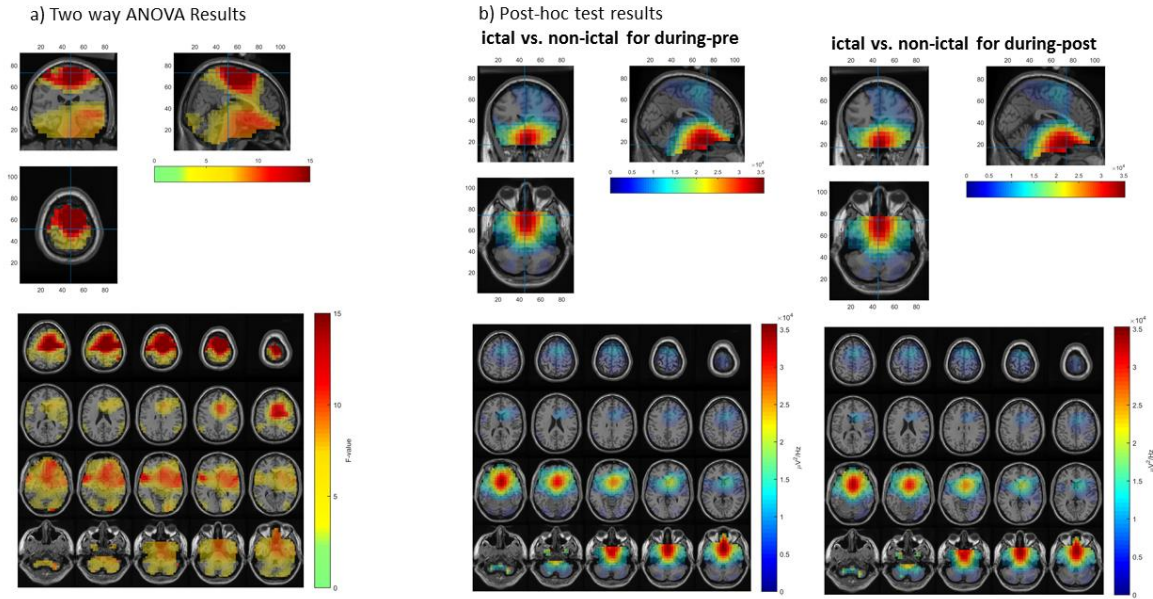


Figure A.3: Delta band interaction effect for non-normalized data. a) Two way ANOVA results depicting the F-value b) Post-hoc test results for the conditions ictal vs. non-ictal (during-pre) and ictal vs. non-ictal (during-post), indicating the source maximum.

## b) Theta Band

For theta band two-way repeated measure ANOVA, only demonstrated a significant effect of time. A significant group effect and interaction effect was not found.

## Theta band (4-7 Hz):Time effect

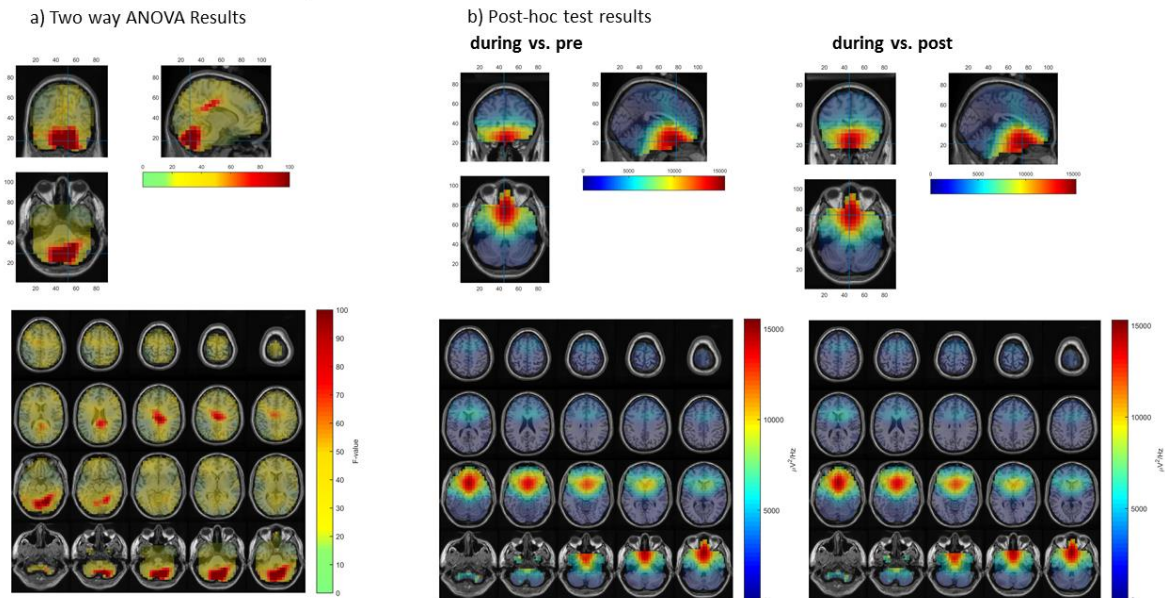


Figure A.4: Theta band time effect for non-normalized data. a) Two way ANOVA results depicting the F-value b) Post-hoc test results for conditions during vs. pre interval and during vs. post interval, indicating the source maximum.

Post hoc tests for the main effect of time depicted that during-ictal/non-ictal interval had a stronger source power compared to pre- and post-ictal/non-ictal intervals. The significant source maximum for during vs. pre interval and for during vs. post interval was observed in the Rectus R,L region. Whereas, neighbouring sources were found in the Frontal superior orb R, Frontal Inferior orb R, region.

### c) Alpha band

Two-way repeated measure ANOVA, depicted a significant effect of time, significant effect of group and a significant interaction effect.

Post-hoc test for main effect of time revealed that during-ictal/non-ictal interval for alpha band frequency had a stronger source power compared to pre- and post-ictal/non-ictal intervals. The significant source maximum for during vs. pre interval and during vs. post interval was observed in the Rectus R,L region. The neighbouring sources were found in the regions of Frontal mid orb R, Frontal Inferior tri R, and Frontal Inferior orb R, L. For the effect of group it was seen that the source power for ictal GSWDs was stronger compared to non-ictal GSWDs. The source maximum, for the significant difference between ictal vs. non-ictal group was seen in the Rectus, with neighbouring source maximum points being in Frontal inferior orb L, Temporal pole superior L, Amygdala L, R, Caudate R, region.

#### Alpha band (8 -12 Hz) :Time effect

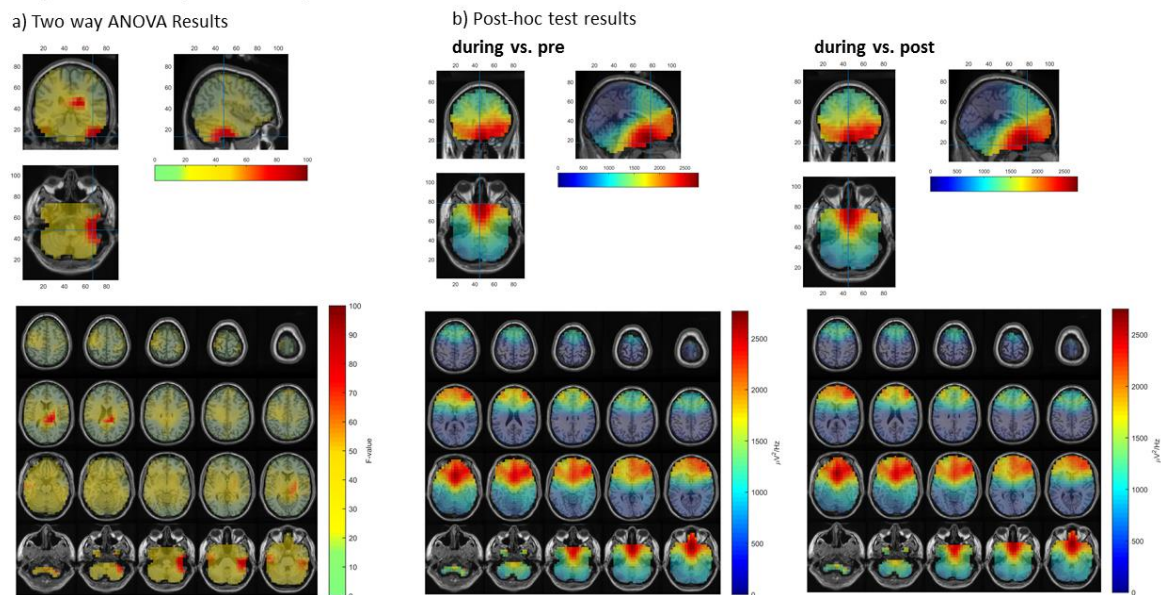


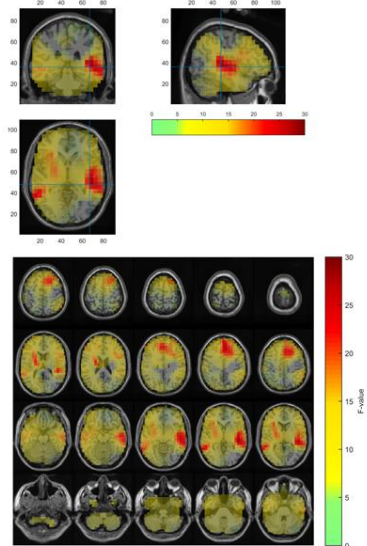
Figure A.5: Alpha band time effect for non-normalized data. a) Two way ANOVA results depicting the F-value b) Post-hoc test results for conditions during vs. pre interval and during vs. post interval, indicating the source maximum.

Post hoc tests for interaction effect revealed that the source power transition from pre interval to during interval, and from during interval to post interval was stronger for ictal GSWDs is stronger, compared to the transition periods of non-ictal GSWDs. The source maximum for the significant difference of during-pre (ictal/non-ictal) and post-during (ictal/non-ictal) was

observed in the Rectus R,L, followed by neighbouring sources in the Frontal inferior orb L, Insula L, Temporal pole superior L, Hippocampus L, Amygdala L, Para-hippocampal L region.

### Alpha band (8 -12 Hz):Group effect

a) Two way ANOVA Results



b) Post-hoc test results  
ictal vs. non-ictal

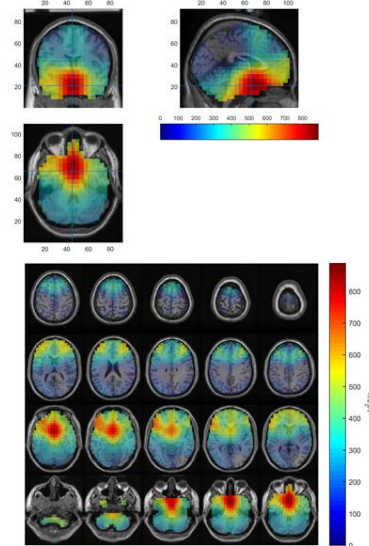
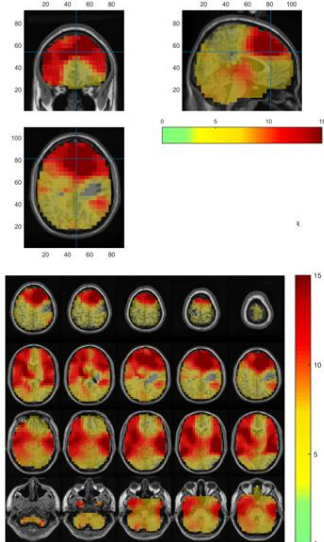


Figure A1.6: Alpha band group effect for non-normalized data. a) Two way ANOVA results depicting the F-value b) Post-hoc test results for the condition ictal vs. non-ictal, indicating the source maximum.

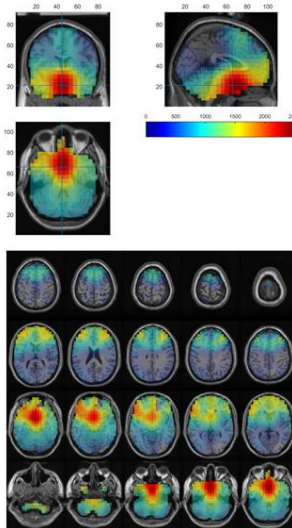
### Alpha band (8 -12 Hz) : Interaction effect

a) Two way ANOVA Results



b) Post-hoc test results

ictal vs. non-ictal for during-pre



ictal vs. non-ictal for during-post

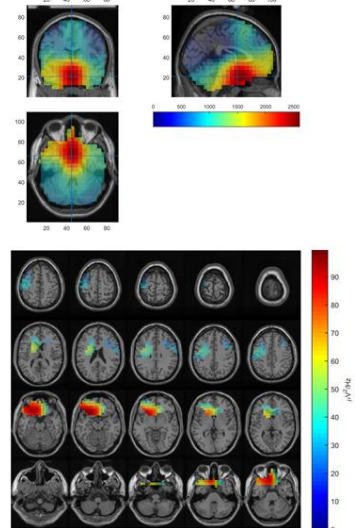


Figure A.7: Alpha band interaction effect for non-normalized data. a) Two way ANOVA results depicting the F-value b) Post-hoc test results for the conditions ictal vs. non-ictal (during-pre) and ictal vs. non-ictal (during-post), indicating the source maximum.

#### d) Beta band

Two-way repeated measure ANOVA for beta band depicted a significant effect of time, significant effect of group and a significant interaction effect.

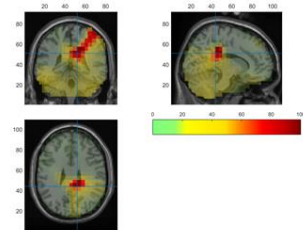
Post-hoc test for main effect of time revealed that during-ictal/non-ictal interval for beta band frequency had a stronger source power compared to pre- and post-ictal/non-ictal intervals. The significant source maximum for during vs. pre interval and during vs. post interval was observed in the Frontal superior medial R, region.

For the effect of group it was seen that the source power for ictal GSWDs was stronger compared to non-ictal GSWDs. The source maximum, for the significant difference between ictal vs. non-ictal group was seen in Frontal superior medial R, and Cingulum anterior R, region.

Post hoc tests for interaction effect revealed, that the source power transition from pre interval to during interval and from during interval to post interval was stronger for ictal GSWDs is stronger compared to the transition periods of non-ictal GSWDs. The source maximum for the significant difference of during-pre (ictal/non-ictal) was in the Frontal medial orb L, R, and Cingulum anterior region. For post-during (ictal/non-ictal), the source maximum was seen in Frontal medial orb L, R region.

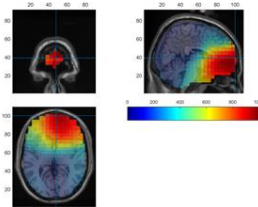
#### Beta band (13-30Hz) :Time effect

a) Two way ANOVA Results



b) Post-hoc test results

during vs. pre



during vs. post

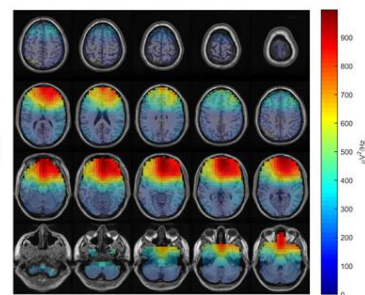
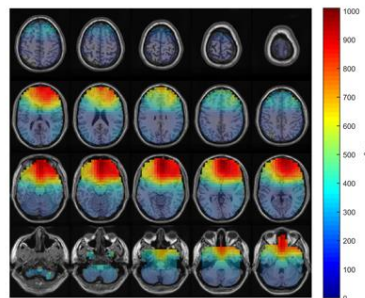
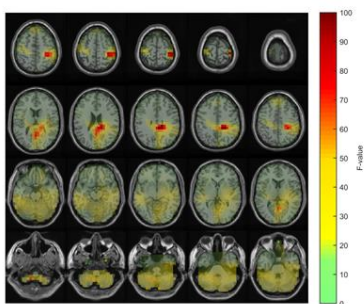
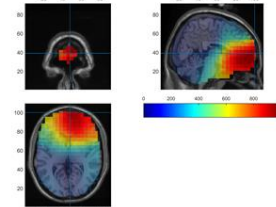


Figure A.8: Beta band time effect for non-normalized data. a) Two way ANOVA results depicting the F-value b) Post-hoc test results for conditions during vs. pre interval and during vs. post interval, indicating the source maximum.

## Beta band (13-30Hz) : Group effect

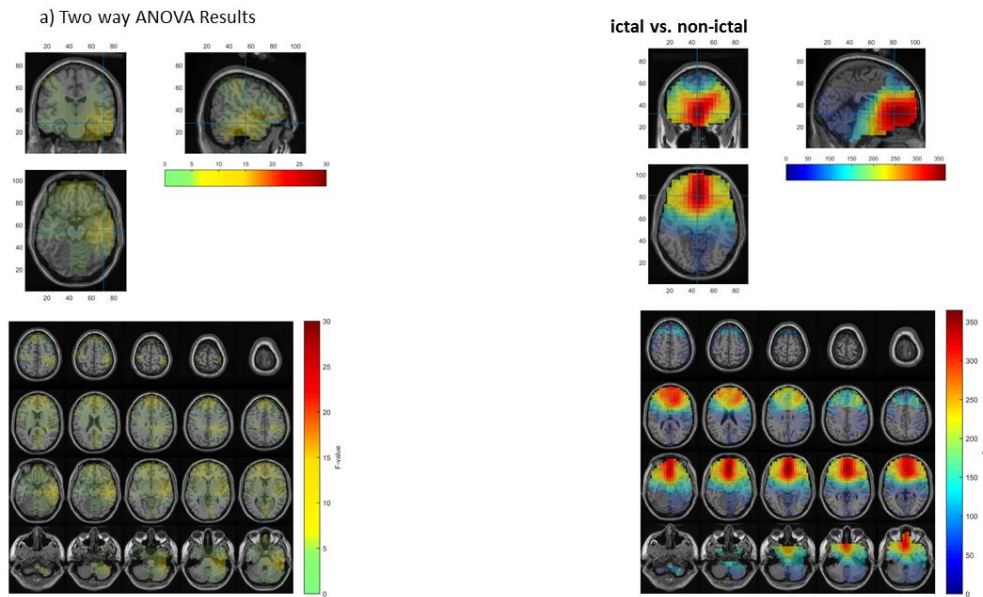


Figure A.9: Beta band group effect for non-normalized data. a) Two way ANOVA results depicting the  $F$ -value b) Post-hoc test results for the condition ictal vs. non-ictal, indicating the source maximum.

## Beta band (13-30Hz) : Interaction effect

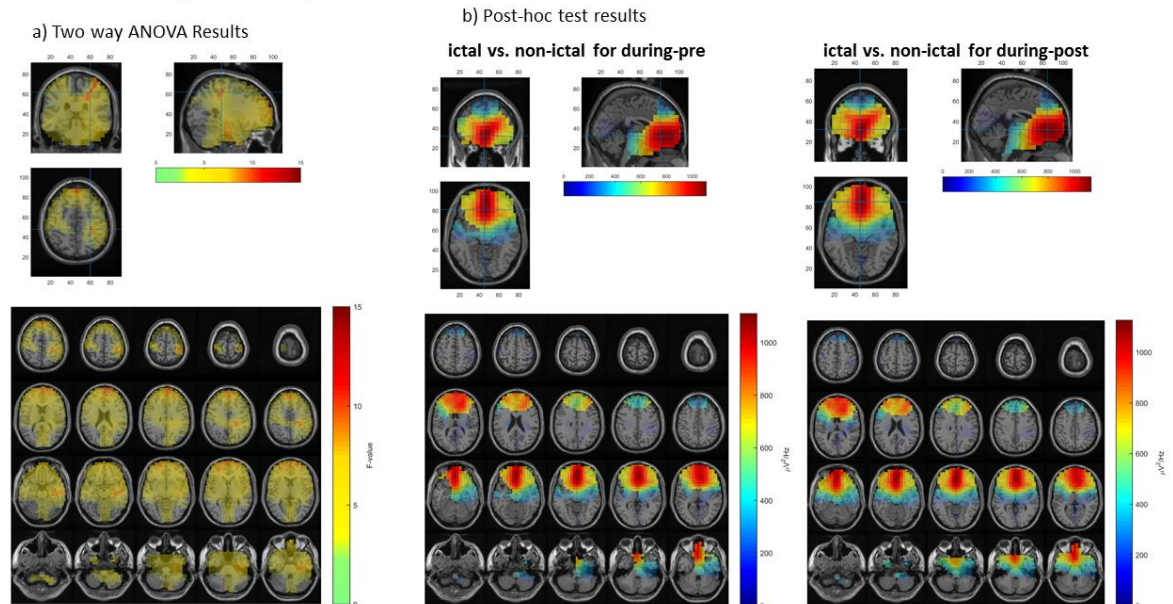


Figure A.10: Beta band interaction effect for non-normalized data. a) Two way ANOVA results depicting the  $F$ -value b) Post-hoc test results for the conditions ictal vs. non-ictal (during-pre) and ictal vs. non-ictal (during-post), indicating the source maximum.

Conditions	Frequency Bands			
	Delta	Theta	Alpha	Beta
<b>Effect of time</b>				
during vs. pre	0.001	0.001	0.001	0.001
during vs. post	0.001	0.001	0.001	0.001
<b>Effect of group</b>				
ictal vs. non-ictal	0.002	No significance	0.001	0.01
<b>Interaction effect</b>				
ictal vs. non-ictal (during-pre)	0.002	No significance	0.002	0.01
ictal vs. non-ictal (during-post)	0.006	No significance	0.001	0.005

Table A.2: Depiction of p-values for all frequency bands and for each condition, done for non-normalized data.

### A.1.3 Comparison of source analysis for normalized data vs. non-normalized data

On comparing the source maximum obtained from normalized data and non-normalized data it was seen that the results were similar. For both cases, delta, alpha and beta band showed a significant time, group, and interaction effect. While theta band only showed the effect of time for normalized and non-normalized data.

Delta band source maximums differed in both cases. For normalized data delta band had two source maximums, a deep source and a surface source. The comparison of source maximum has been given below.

Frequency bands	Conditions	Normalized data source maximum	Non-normalized data source maximum
<b>Delta Band</b>	<b>Effect of time</b>		
	during vs. pre	Rectus R,L	Rectus R,L
	during vs. post	Rectus R,L, Caudate L	Rectus R,L
	<b>Effect of group</b>		
	ictal vs. non-ictal	Rectus R	Rectus R
	<b>Interaction effect</b>		
	ictal vs. non-ictal (during-pre)	Caudate R, Putamen R	Rectus R,L
ictal vs. non-ictal (during-post)	Supplementary Motor area R	Rectus R,L	
<b>Theta Band</b>	<b>Effect of time</b>		
	during vs. pre	Rectus R,L	Rectus R,L
	during vs. post	Rectus R,L	Rectus R,L
	<b>Effect of group</b>	No significance	No significance



	<b>Interaction effect</b>	No significance	No significance
<b>Alpha Band</b>	<b>Effect of time</b>		
	during vs. pre	Rectus R,L	Rectus R,L
	during vs. post	Rectus R,L	Rectus R,L
	<b>Effect of group</b>		
	ictal vs. non-ictal	Frontal inferior orb L	Rectus R,L
	<b>Interaction effect</b>		
	ictal vs. non-ictal (during-pre)	Frontal inferior orb L	Rectus R,L
	ictal vs. non-ictal (during-post)	Frontal inferior orb L	Rectus R,L
<b>Beta Band</b>	<b>Effect of time</b>		
	during vs. pre	Frontal orb R	Frontal superior medial R
	during vs. post	Frontal orb R	Frontal superior medial R
	<b>Effect of group</b>		
	ictal vs. non-ictal	Frontal superior medial R	Frontal superior medial R, Cingulum anterior R
	<b>Interaction effect</b>		
	ictal vs. non-ictal (during-pre)	Frontal superior medial R	Frontal medial orb L, R, and Cingulum anterior
	ictal vs. non-ictal (during-post)	Frontal superior medial R	Frontal medial orb L, R

*Table A.3: Comparison of the source maximum region for normalized data vs. non-normalized data. For all frequency bands and conditions the source maximum has been given.*

# Appendix B

## B.1 Functional connectivity for non-normalized data

### B.1.1 Seed as source maximum

#### a) Delta band

For non-normalized data, delta band revealed one source maximum. A two way repeated measure ANOVA (group x time) depicted a significant effect of time and significant interaction effect. But, there was no significant effect of group.

Post-hoc test for main effect of time revealed that during-ictal/non-ictal interval had stronger coherence compared to pre- and post-ictal/non-ictal intervals. The maximum coherence difference for pre- to during-ictal/non-ictal time interval was observed in the Occipital Mid R region, while for the time intervals during- to post-ictal/non-ictal also, it was seen in the Cingulum Mid L, Cingulum Post L, Precuneus L region. Post hoc test for the interaction effect revealed that the ictal transition periods had a stronger coherence compared to non-ictal transition periods. The maximum coherence difference for the condition ictal/non-ictal (during-pre) was seen in the Temporal Sup L, Temporal Mid L region. While for the condition ictal/non-ictal (during-post) it was seen in the Rolandic Oper L, Temporal Sup L region.

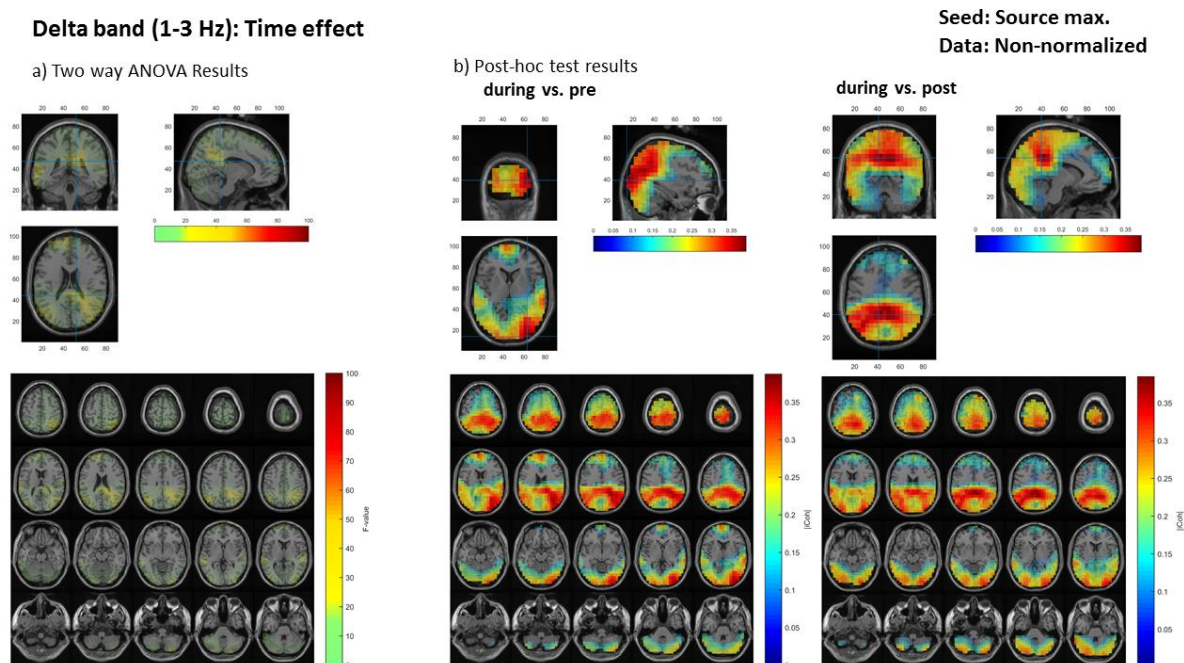
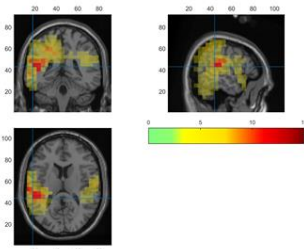


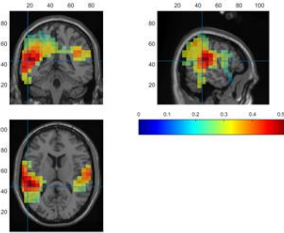
Figure B.1: Delta band time effect for non-normalized data and for the seed as source maximum. a) Two way ANOVA test results b) post-hoc test results for conditions during vs. pre time interval and during vs. post time interval.

### Delta band (1-3 Hz): Interaction effect

a) Two way ANOVA Results



b) Post-hoc test results  
ictal vs. non-ictal for during-pre



Seed: Source max.  
Data: Non-normalized  
ictal vs. non-ictal for during-post

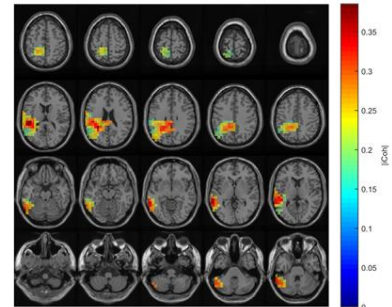
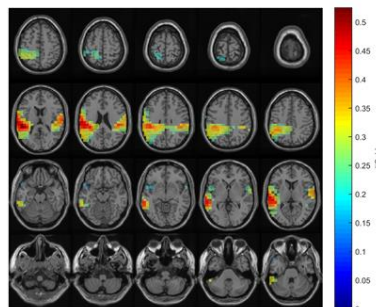
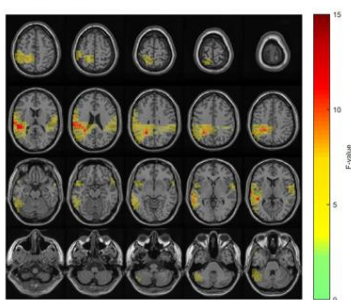
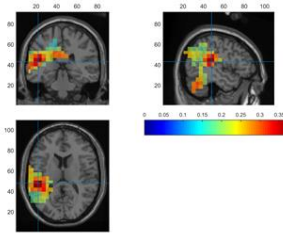


Figure B.2: Delta band interaction effect for non-normalized data and for the seed as source maximum. a) two way ANOVA results depicting regions of significance in the brain based on F-value distribution. b) post-hoc test results depicting coherent regions in the brain for the conditions ictal vs. non-ictal (during-pre) and ictal vs. non-ictal (during-post).

### b) Theta band

For theta band as before, FC was not done considering the fact there was no significant source maximum found for the interaction effect as previously mentioned in chapter 6. Therefore, the seed for coherence analysis could not be taken.

### c) Alpha band

A two way ANOVA test revealed a significant effect of time, significant effect of group and a significant interaction effect for alpha band.

Post hoc test for the main effect of time revealed stronger coherence for during-ictal/non-ictal interval. The pre- and post-ictal/non-ictal intervals had a weaker coherence in comparison. These significant differences were seen to be widespread in all brain regions except the central region. The maximum coherence difference for the time interval pre- to during-ictal/non-ictal was seen in the Frontal Sup Medial L region and for the during- to post-ictal/non-ictal interval it was seen in the Cerebellum Crus2 R region. For the main effect of group, the maximum coherence was seen in the Precuneus L region for alpha band. It was seen that ictal GSWDs had a stronger coherence compared to non-ictal GSWDs. In addition, interaction effect demonstrated that the ictal transition periods from pre to during and during to post had a stronger coherence compared to non-ictal transition periods. For the condition ictal/non-ictal (during-pre) the maximum coherence was observed in the Cuneus R, Precuneus R region. While for the condition ictal/non-ictal (during-post) it was seen in the Frontal Sup L, Frontal Sup Medial L region.

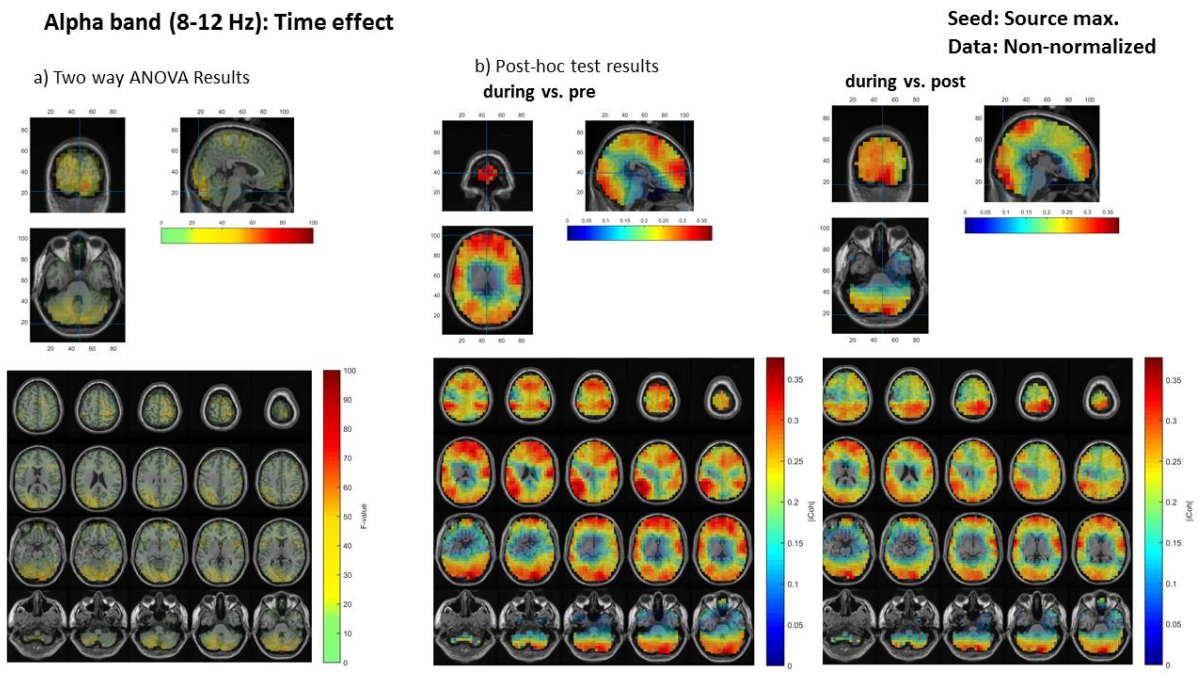


Figure B.3: Alpha band time effect for non-normalized data and seed as source maximum. a) Two way ANOVA test results b) post-hoc test results for conditions during vs. pre time interval and during vs. post time interval.

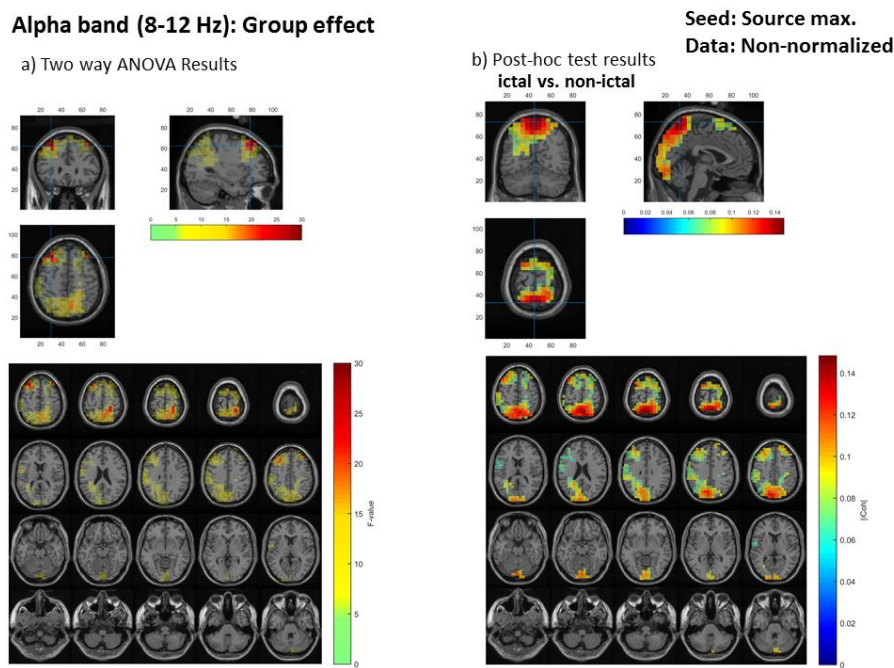
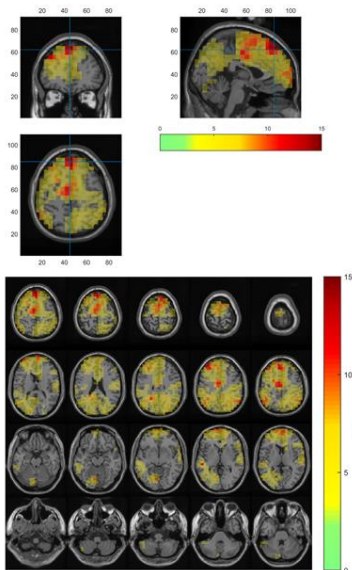


Figure B.4: Alpha band group effect for non-normalized data and seed as source maximum. a) two way ANOVA results depicting the regions of significance based on the  $F$ -value distribution. b) post-hoc test results depicting the coherence difference for ictal vs. non-ictal GSWDs.

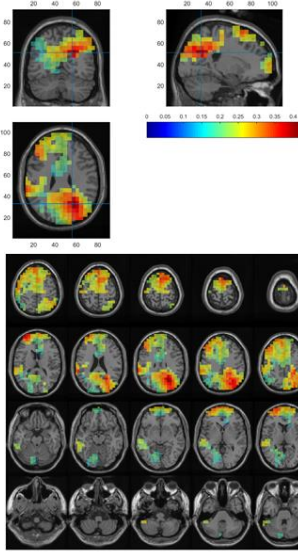
**Alpha band (8-12 Hz): Interaction effect**

a) Two way ANOVA Results



b) Post-hoc test results

ictal vs. non-ictal for during-pre



Seed: Source max.

Data: Non-normalized

ictal vs. non-ictal for during-post

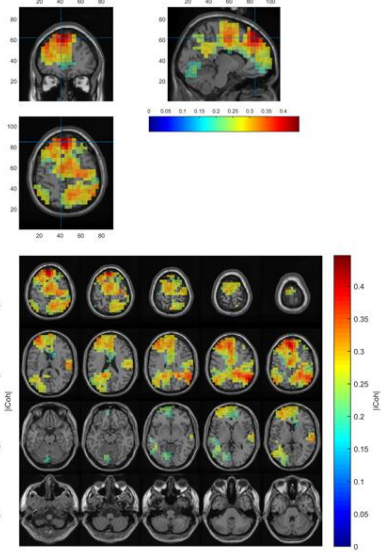


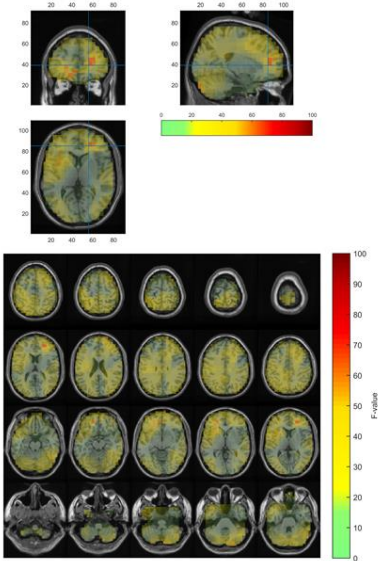
Figure 1.5: a) two way ANOVA results b) post-hoc test results depicting coherent regions in the brain for the conditions ictal vs. non-ictal (during-pre) and ictal vs. non-ictal (during-post).

**d) Beta band**

A two way ANOVA test revealed a significant effect of time but no significant effect of group or interaction effect for beta band.

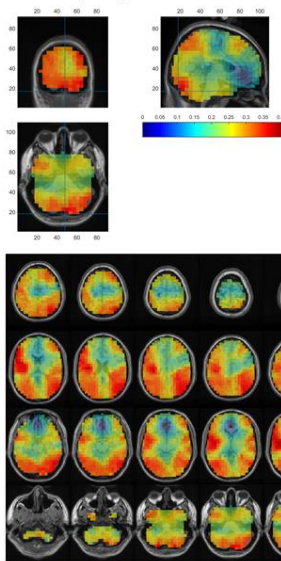
**Beta band (13-30 Hz): Time effect**

a) Two way ANOVA Results



b) Post-hoc test results

during vs. pre



during vs. post

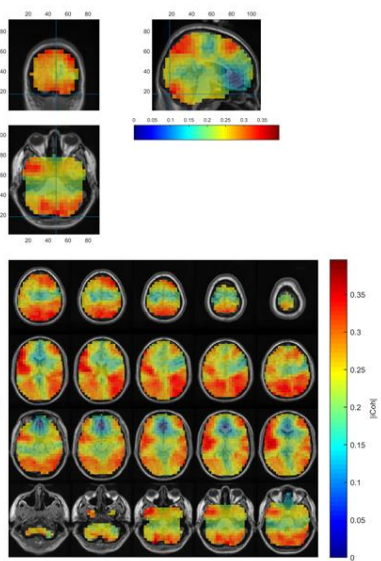


Figure B.6: Beta band time effect for non-normalized data and seed as source maximum. a) Two way ANOVA test results b) post-hoc test results for conditions during vs. pre time interval and during vs. post time interval.

Post hoc test for the main effect of time revealed that coherence was stronger for during-ictal/non-ictal interval compared to pre- and post-ictal/non-ictal GSWDs. The maximum coherence difference for the time interval pre- to during-ictal/non-ictal and the interval during- to post-ictal/non-ictal it was seen in the Cerebellum Crus2 R region.

<b>Non-normalized data</b>				
<b>Seed- Source maximum</b>				
<b>Conditions</b>	<b>Frequency Bands</b>			
	<b>Delta</b>	<b>Theta</b>	<b>Alpha</b>	<b>Beta</b>
	<b>Source max.1</b>	<b>Source max.1</b>	<b>Source max.1</b>	<b>Source max.1</b>
<b>Effect of time</b>				
during vs. pre	0.001	-	0.001	0.001
during vs. post	0.001	-	0.001	0.001
<b>Effect of group</b>				
ictal vs. non-ictal	No significance	-	0.3	No significance
<b>Interaction effect</b>				
ictal vs. non-ictal (during-pre)	0.03	-	0.005	No significance
ictal vs. non-ictal (during-post)	0.01	-	0.003	No significance

*Table B.1: P-values for all frequency bands and for all statistical conditions. Delta, alpha and beta band showed a significant effect of time. Only alpha band depicted a significant group effect. For interaction effect delta and alpha band both demonstrated significance.*

## **B.1.2 Seed as Thalamus**

### **a) Delta band**

For delta band a two way ANOVA test revealed a significant main effect of time and group as well as a significant interaction effect.

Post hoc tests revealed for the main effect of time that during-ictal/non-ictal time interval had a stronger coherence compared to the pre- and post-ictal/non-ictal time intervals. The significant difference in coherence was seen in the pre-frontal cortex, mid central and parietal R, L, brain regions. The maximum coherence difference for the time effect was seen in the Postcentral L, Parietal Sup L for pre- to during-ictal/non-ictal interval and for during- to post-ictal/non-ictal interval it was seen in the Precuneus R, Cingulum Mid R,L, Parietal Inferior L, Occipital mid L, Angular L regions. The main effect of group revealed ictal GSWDs had stronger coherence compared to non-ictal GSWDs. The maximum coherence difference was seen in the supramarginal R region. For interaction effect it was seen that the ictal transition periods from pre- to during- and from during- to post- intervals had stronger coherence compared to the transition periods of non-ictal GSWDs. The maximum coherence difference for the condition ictal/non-ictal (during-pre), was observed in the supramarginal R, Rolandic

Oper R regions. While for the condition ictal/non-ictal (post-during) it was seen in the Temporal Inferior L, Cerebellum Crus1 L region.

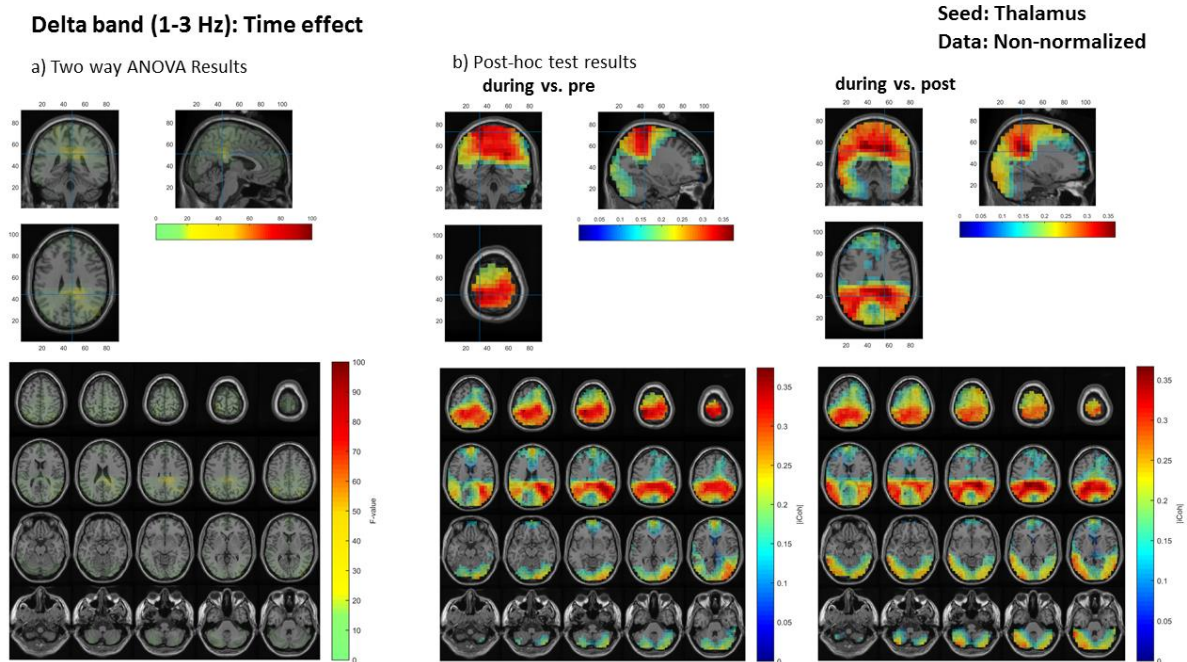


Figure B.7: Delta band time effect for non-normalized data and seed as thalamus. a) Two way ANOVA test results b) post-hoc test results for conditions during vs. pre time interval and during vs. post time interval.

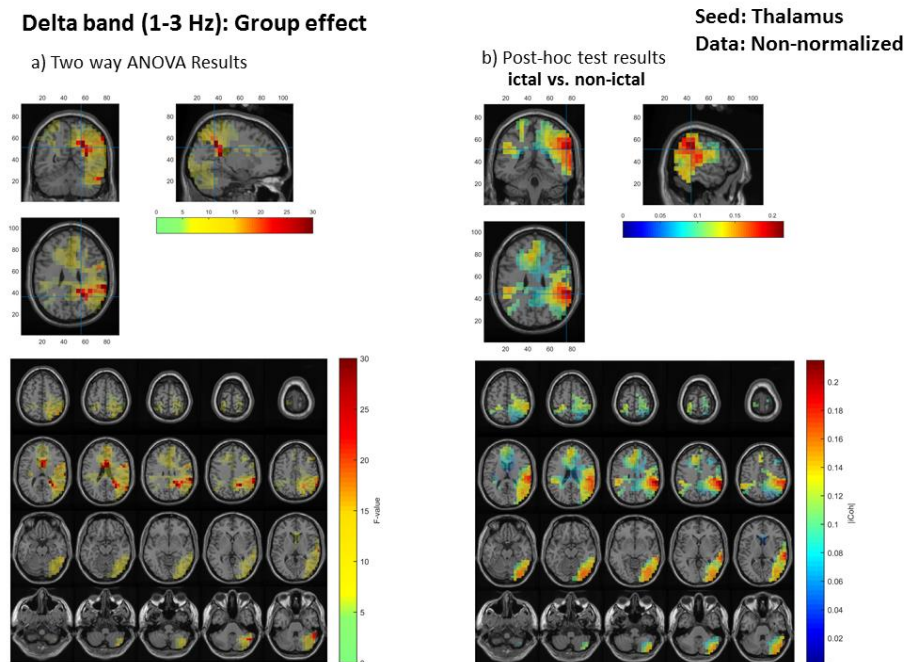
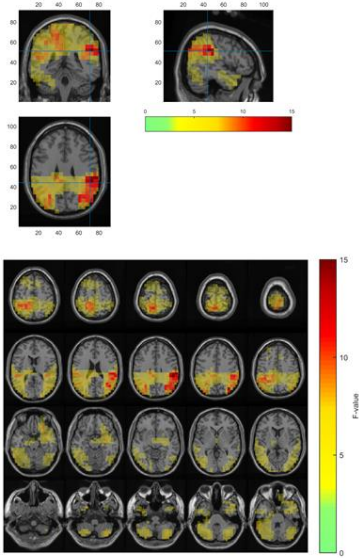


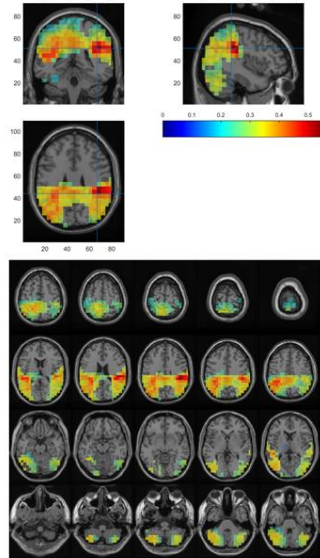
Figure B.8: Delta band group effect for non-normalized and seed as the thalamus. a) two way ANOVA results depicting the regions of significance based on the F-value distribution. b) post-hoc test results depicting the coherence difference for ictal vs. non-ictal GSWDs.

**Delta band (1-3 Hz): Interaction effect**

a) Two way ANOVA Results



b) Post-hoc test results  
ictal vs. non-ictal for during-pre



Seed: Thalamus  
Data: Non-normalized

ictal vs. non-ictal for during-post

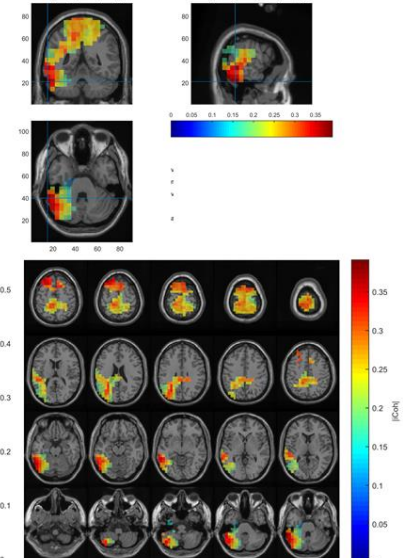
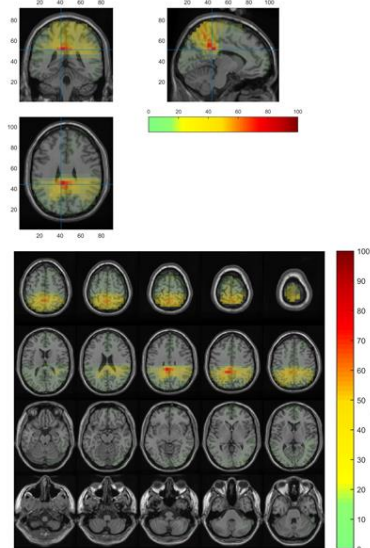


Figure B.9: Delta band interaction effect for non-normalized data and for the seed as thalamus. a) two way ANOVA results depicting regions of significance in the brain based on F-value distribution. b) post-hoc test results depicting coherent regions in the brain for the conditions ictal vs. non-ictal (during-pre) and ictal vs. non-ictal (during-post).

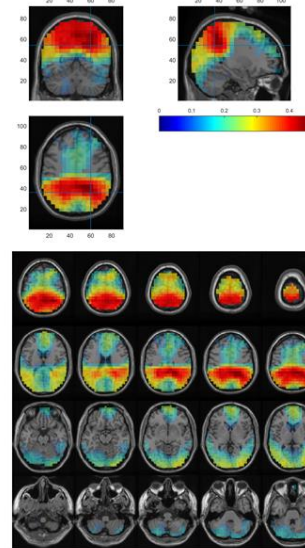
**b) Theta band:** For theta band a two way ANOVA test showed a significant effect of time however no significant effect of group or significant interaction effect.

**Theta band (4-7 Hz): Time effect**

a) Two way ANOVA Results



b) Post-hoc test results  
during vs. pre



Seed: Thalamus  
Data: Non-normalized

during vs. post

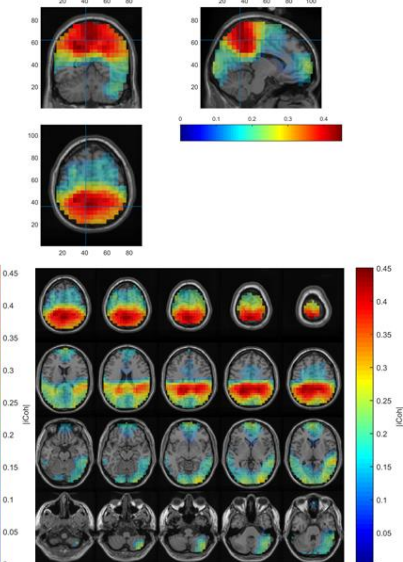


Figure B.10: Theta band group effect for non-normalized and seed as the thalamus. a) two way ANOVA results depicting the regions of significance based on the F-value distribution. b) post-hoc test results depicting the coherence difference for ictal vs. non-ictal GSWDs.



Post hoc tests for theta band further demonstrated for the effect of time that, the during-ictal/non-ictal interval had stronger coherence compared to the time intervals pre- and post-ictal/non-ictal. These differences were widespread in the frontal-central, parietal R,L, occipital R,L region and the maximum coherence difference could be observed in the Angular R, Parietal Inf R, Precuneus R, L regions for the interval of pre- to during- ictal/non-ictal and in the Precuneus L region for during- to post-ictal/non-ictal interval.

### c) Alpha band

For alpha band two way ANOVA showed a significant effect of time but there was no significant group effect seen. Further, there was a significant interaction effect seen.

Post hoc test for the main effect of time showed that the during ictal/non-ictal interval had a stronger coherence compared to pre- and post- ictal/non-ictal time intervals. The maximum coherence difference could be observed in rolandic operculum R, supramarginal R, and Temporal Sup R regions for time interval pre- to during-ictal/non-ictal and for the time intervals during- to post-ictal/non-ictal it could be observed in the postcentral R, Parietal Sup R regions. For the interaction effect post hoc test revealed that the coherence for ictal transition periods from pre- to during- and from during- to post- intervals was stronger compared to the transition periods of non-ictal GSWDs. The maximum coherence difference for the condition ictal/non-ictal (during-pre) was seen in the Sup Motor Area L, region. While for the condition ictal/non-ictal (during-post) the maximum coherence was seen in the Frontal Sup Medial L region.

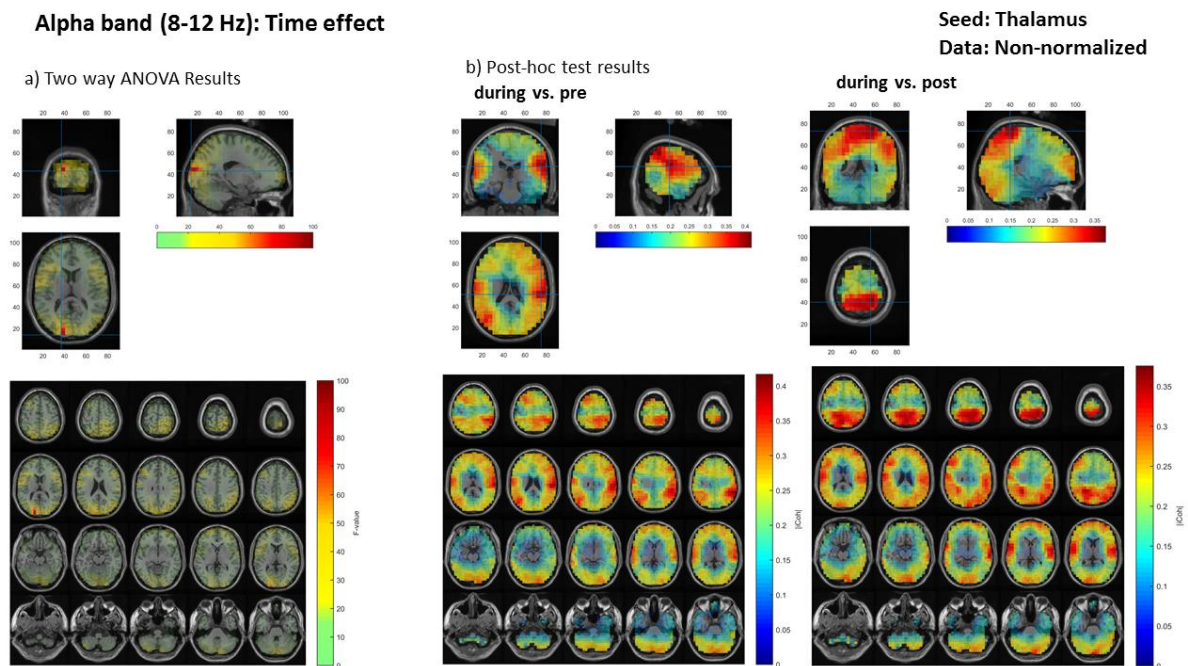
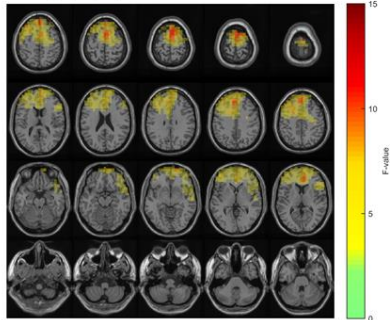
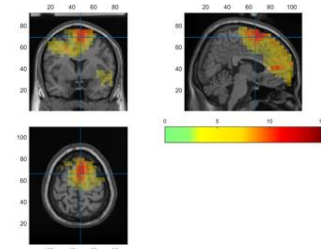


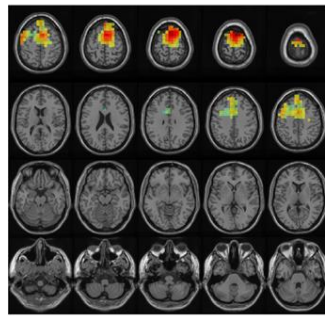
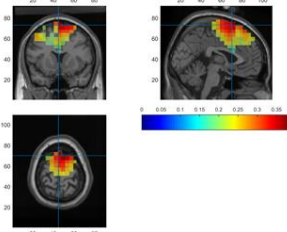
Figure B.11: Alpha band group effect for non-normalized and seed as the thalamus. a) two way ANOVA results depicting the regions of significance based on the F-value distribution. b) post-hoc test results depicting the coherence difference for ictal vs. non-ictal GSWDs.

**Alpha band (8-12 Hz): Interaction effect**

a) Two way ANOVA Results



b) Post-hoc test results  
ictal vs. non-ictal for during-pre



Seed: Thalamus  
Data: Non-normalized

ictal vs. non-ictal for during-post

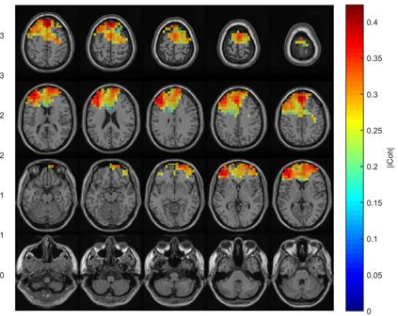
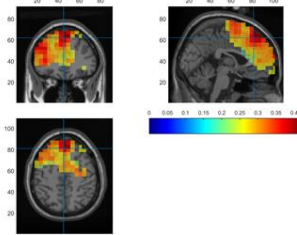
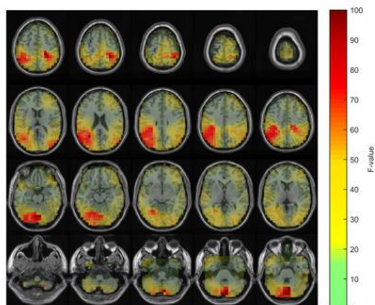
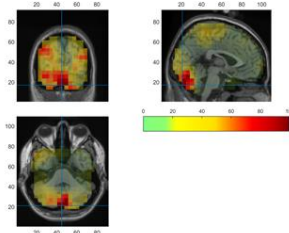


Figure B.12: Alpha band interaction effect for non-normalized data and for the seed as thalamus. a) two way ANOVA results depicting regions of significance in the brain based on  $F$ -value distribution. b) post-hoc test results depicting coherent regions in the brain for the conditions ictal vs. non-ictal (during-pre) and ictal vs. non-ictal (during-post).

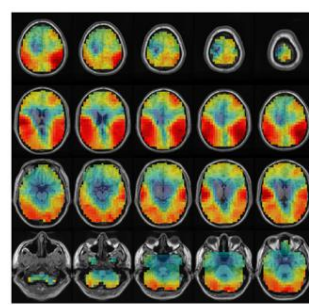
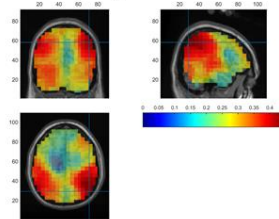
**d) Beta band:** Two way ANOVA test for beta band frequency revealed a significant effect of time. However, no significant effect of group or significant interaction effect was seen.

**Beta band (13-30 Hz): Time effect**

a) Two way ANOVA Results



b) Post-hoc test results  
during vs. pre



Seed: Thalamus  
Data: Non-normalized

during vs. post

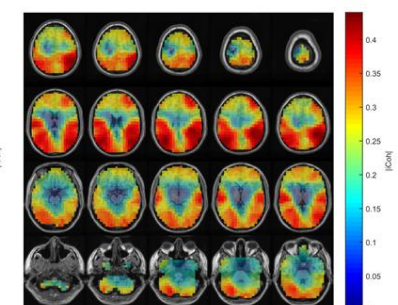
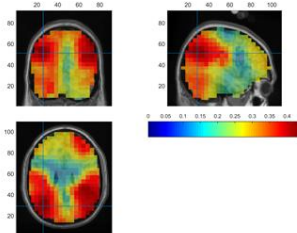


Figure B.13: Beta band group effect for non-normalized and seed as the thalamus. a) two way ANOVA results depicting the regions of significance based on the  $F$ -value distribution. b) post-hoc test results depicting the coherence difference for ictal vs. non-ictal GSWDs.

Post hoc test for the main effect of time demonstrated that during-ictal/non-ictal time interval had stronger coherence compared to pre- and post-ictal/non-ictal time intervals. The maximum coherence difference for the time interval pre- to during-ictal/non-ictal was observed in the Angular R region. For the during- to post-ictal/non-ictal interval the maximum coherence difference was observed in the Occipital Mid L, Angular L regions.

<b>Non-normalized data</b>				
<b>Seed- Thalamus</b>				
<b>Conditions</b>	<b>Frequency Bands</b>			
	<b>Delta</b>	<b>Theta</b>	<b>Alpha</b>	<b>Beta</b>
<b>Effect of time</b>				
during vs. pre	0.001	0.001	0.001	0.001
during vs. post	0.001	0.001	0.001	0.001
<b>Effect of group</b>				
ictal vs. non-ictal	0.02	-	-	-
<b>Interaction effect</b>				
ictal vs. non-ictal (during-pre)	0.01	-	0.02	-
ictal vs. non-ictal (during-post)	0.01	-	0.01	-

Table B.2: P-values for all frequency bands and for all statistical conditions. All frequency bands showed a significant effect of time. Only delta band depicted a significant group effect. For interaction effect delta and alpha band both demonstrated significance.

### B.1.3 Comparison of normalized and non-normalized datasets

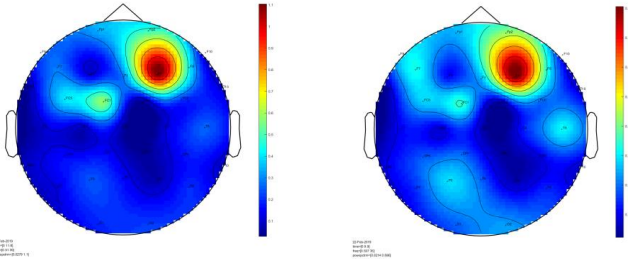
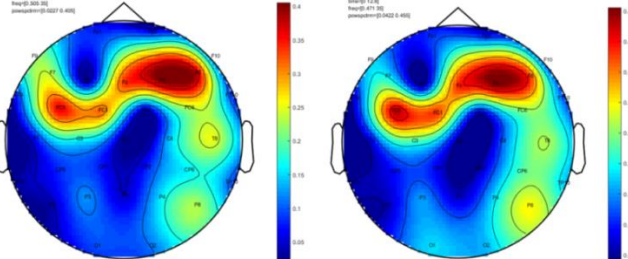
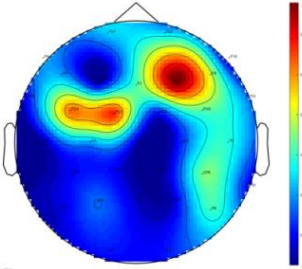
<b>Frequency band</b>	<b>Conditions</b>	<b>Non-Normalized data</b>	
		<b>Seed-source maximum</b>	<b>Seed-Thalamus</b>
<b>Delta Band</b>	<b>Effect of time</b>		
	during vs. pre	Occipital Mid R	Postcentral L, Parietal Sup L
	during vs. post	Cingulum Mid L, Cingulum Post L, Precuneus L	Precuneus R, Cingulum Mid R,L, Pareital Inf L, Occipital mid L, Angular L
	<b>Effect of group</b>		
	ictal vs. non-ictal	No Significance	Supramarginal R
	<b>Interaction effect</b>		
	ictal vs. non-ictal (during-pre)	Temporal Sup L, Temporal Mid L	Supramarginal R, Rolandic Oper R
	ictal vs. non-ictal (during-post)	Rolandic Oper L, Temporal Sup L	Temporal Inf L, Cerebellum Crus1 L

		<b>Normalized data</b>	<b>Non-normalized data</b>
		<b>Seed-Thalamus</b>	<b>Seed- Thalamus</b>
<b>Theta Band</b>	<b>Effect of time</b>		
	during vs. pre	Precuneus R	Angular R, Parietal Inf R, Precuneus R, L
	during vs. post	Cingulum Mid L, Cingulum Post L, Precuneus L	Precuneus L
	<b>Effect of group</b>	No significance	No significance
	<b>Interaction effect</b>	No significance	No significance
		<b>Non-normalized data</b>	<b>Non-normalized data</b>
		<b>Seed-source maximum</b>	<b>Seed- Thalamus</b>
<b>Alpha Band</b>	<b>Effect of time</b>		
	during vs. pre	Frontal Sup Medial L	Rolandic Oper R, SupraMarginal R, Temporal Sup R
	during vs. post	Cerebellum Crus2 R	Postcentral R, Parietal Sup R
	<b>Effect of group</b>		
	ictal vs. non-ictal	Precuneus L	No significance
	<b>Interaction effect</b>		
	ictal vs. non-ictal (during-pre)	Cuneus R, Precuneus R	Sup Motor Area L,
	ictal vs. non-ictal (during-post)	Frontal Sup L, Frontal Sup Medial L	Frontal Sup Medial L
		<b>Non-normalized data</b>	<b>Non-normalized data</b>
		<b>Seed-source maximum</b>	<b>Seed- Thalamus</b>
<b>Beta Band</b>	<b>Effect of time</b>		
	during vs. pre	Cerebellum Crus2 R	Angular R
	during vs. post	Cerebellum Crus2 R	Occipital Mid L, Angular L
	<b>Effect of group</b>		
	ictal vs. non-ictal	No significance	No significance
	<b>Interaction effect</b>		
	ictal vs. non-ictal (during-pre)	No significance	No significance
	ictal vs. non-ictal (during-post)	No significance	No significance

# Appendix C

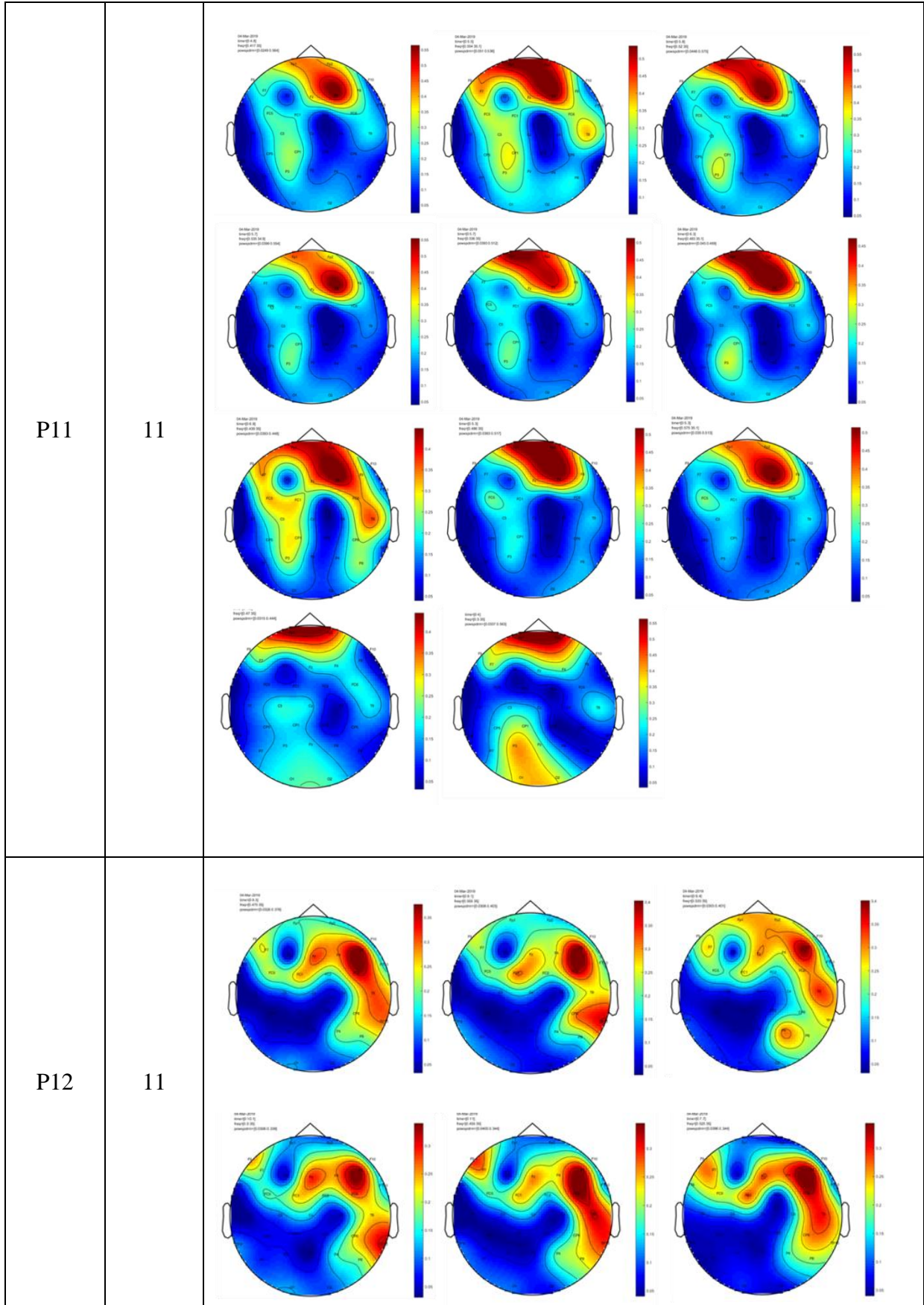
Time frequency analysis for ictal and non-ictal discharges longer than 3 seconds, allows us to see the power distribution in the form of topographical plots. Here, the time frequency power distributions for ictal and non-ictal discharges have been depicted along with the plots for pre- and post- intervals. Red distribution marks higher power while blue colour marks weaker power distribution.

## C.1 Time frequency topographical plots for ictal GSWDs

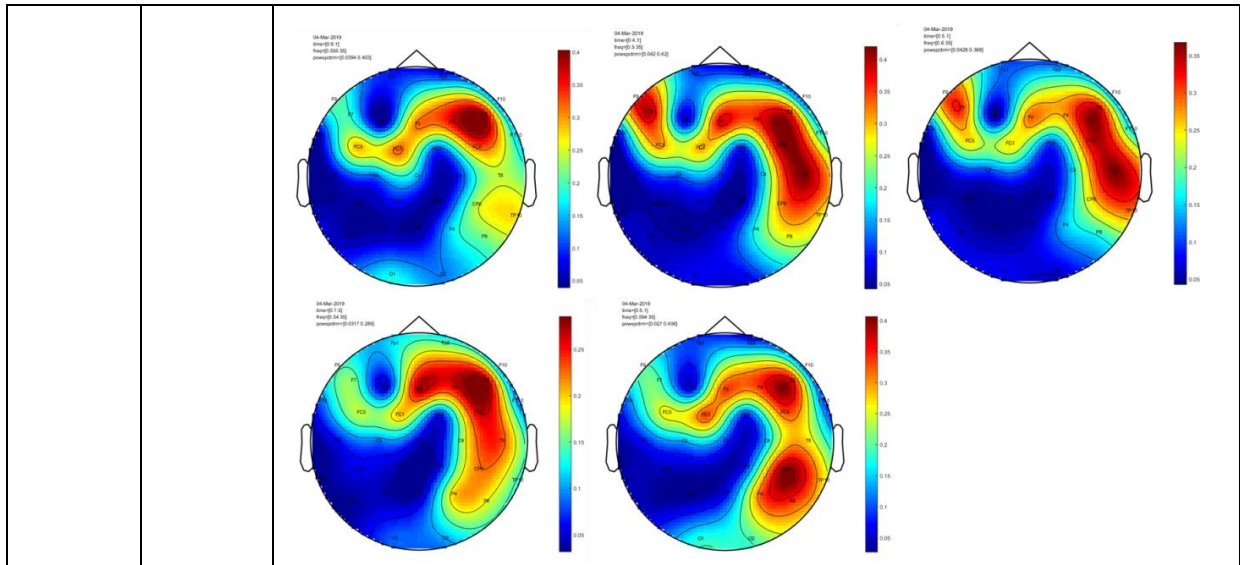
Patients	Number of ictal GSWDs	Topographical plots for ictal GSWDs
P1	2	
P2	2	
P3	1	

P4	2	
P5	3	
P6	1	
P7	1	

<p>P8</p>	<p>5</p>	
<p>P9</p>	<p>1</p>	
<p>P10</p>	<p>4</p>	

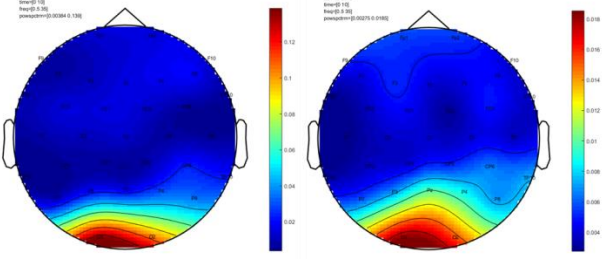
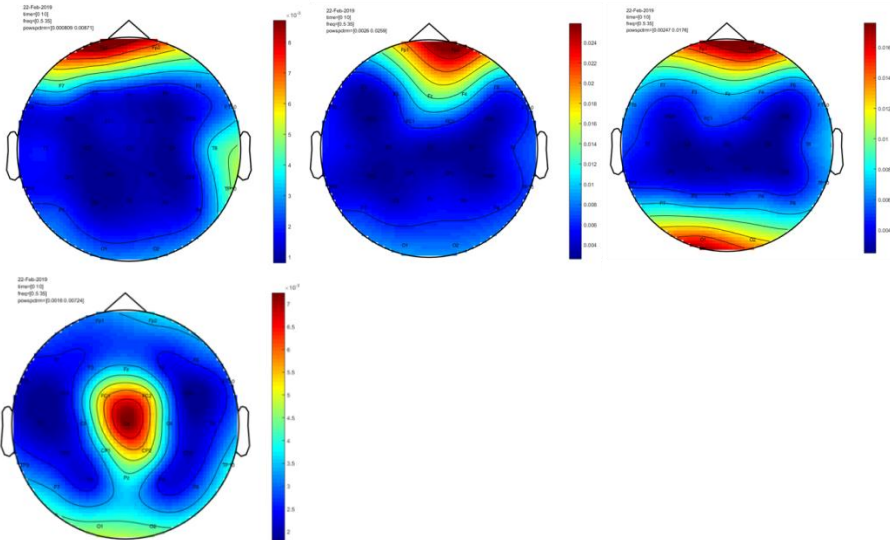
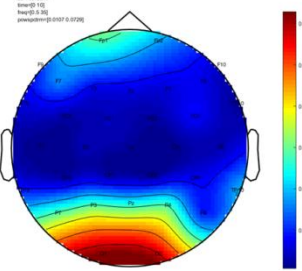
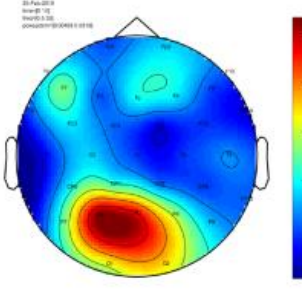






### C.2 Time frequency topographical plots for pre-ictal GSWDs

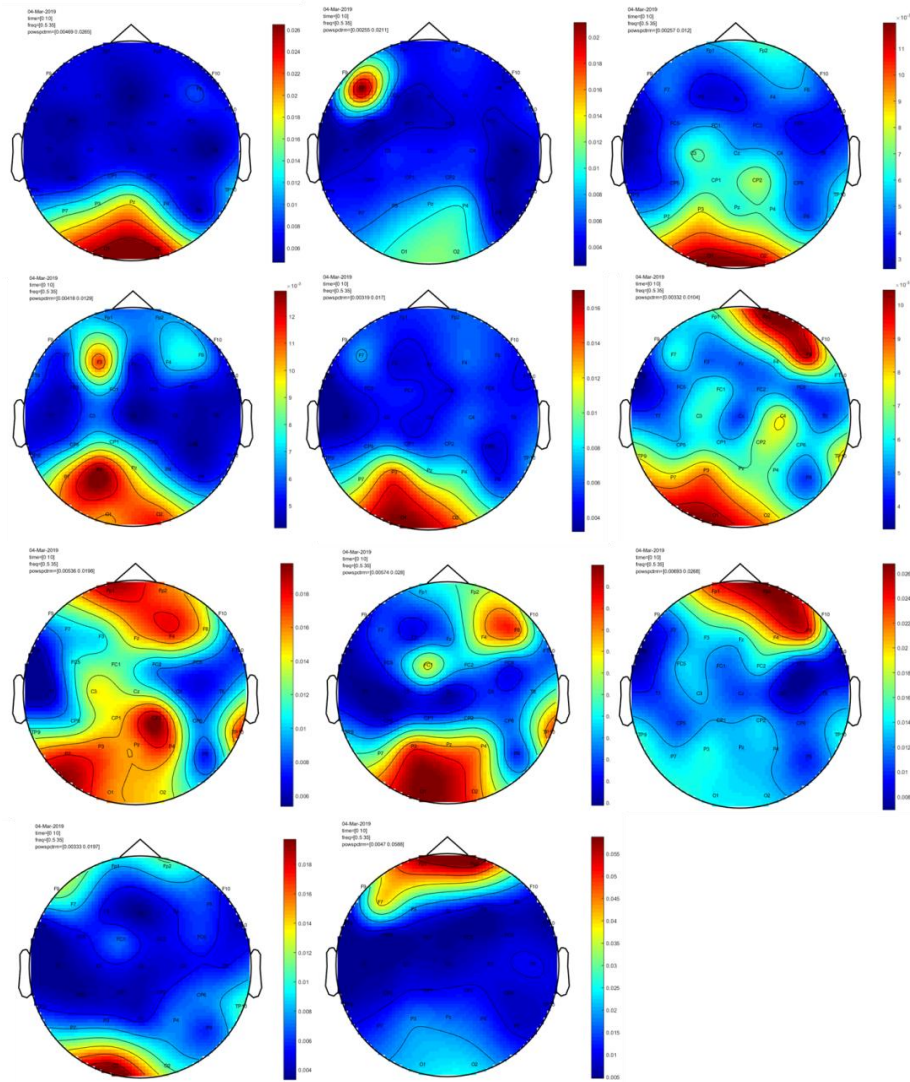
Patients	No. of pre-ictal GSWDs	Topographical plots for pre-ictal GSWDs
P1	2	
P2	1	
P3	1	

P4	2	
P5	4	
P6	1	
P7	1	

<p>P8</p>	<p>5</p>	<p>Five circular maps showing spatial distributions of variables for P8. Each map includes a color scale and technical parameters like date (25-Feb-2019), time (10), and frequency (3.35).</p>
<p>P9</p>	<p>1</p>	<p>One circular map showing a spatial distribution for P9 with a color scale and technical parameters.</p>
<p>P10</p>	<p>4</p>	<p>Four circular maps showing spatial distributions for P10 with color scales and technical parameters.</p>

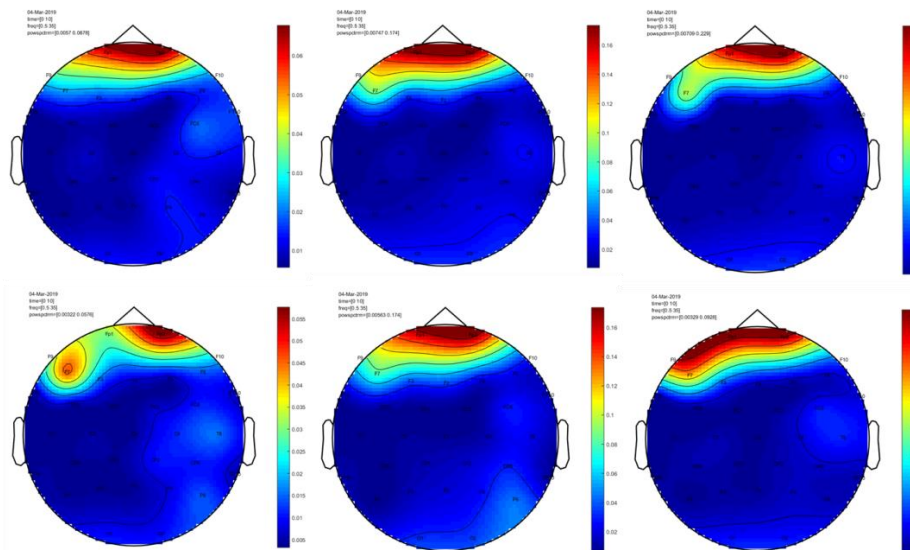
P11

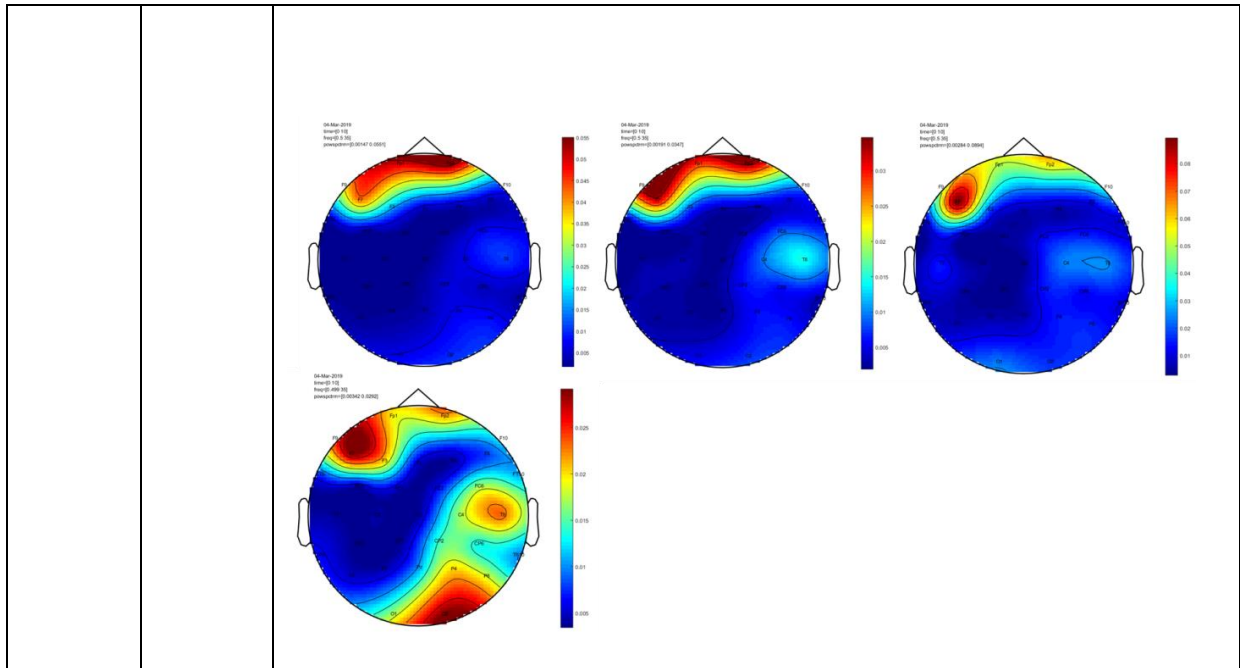
11



P12

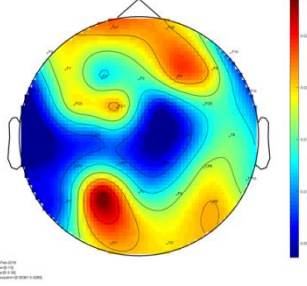
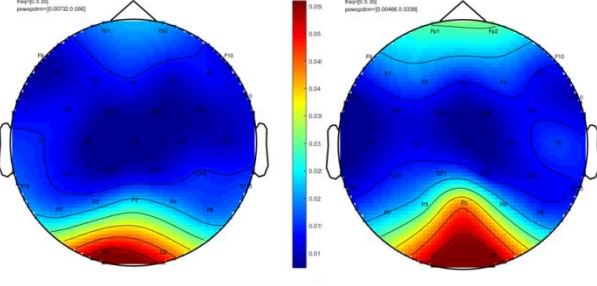
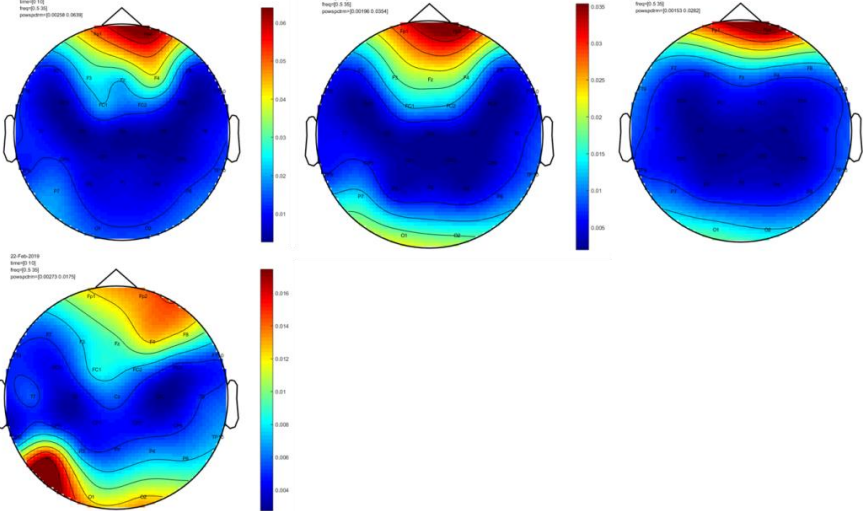
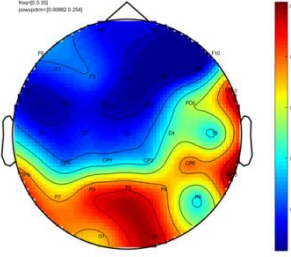
10

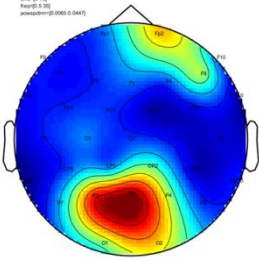
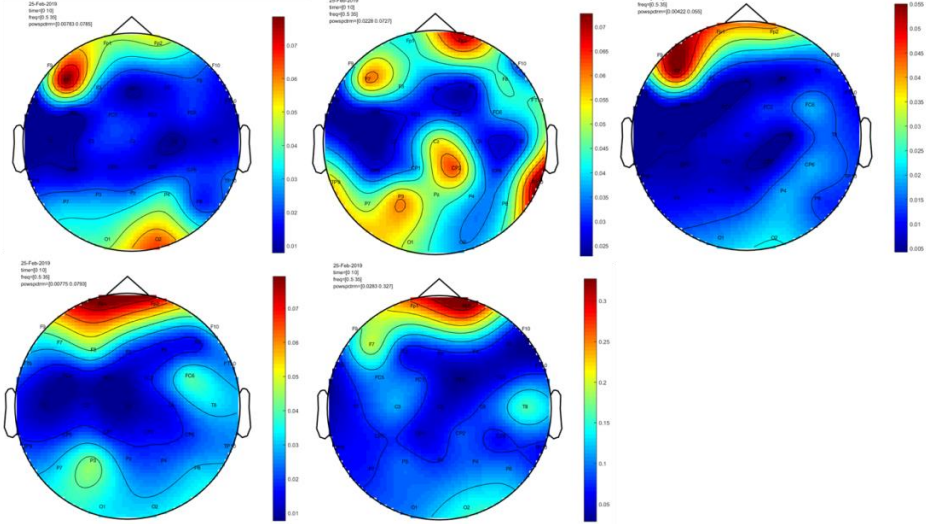
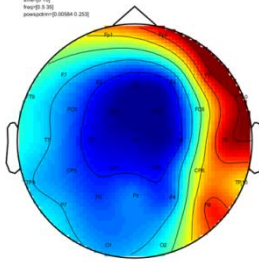
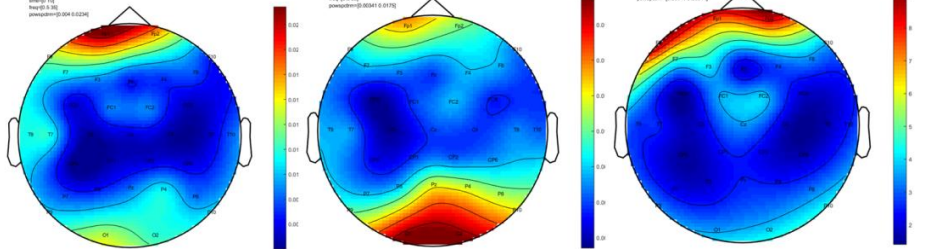




### C.3 Time frequency topographical plots for post-ictal GSWDs

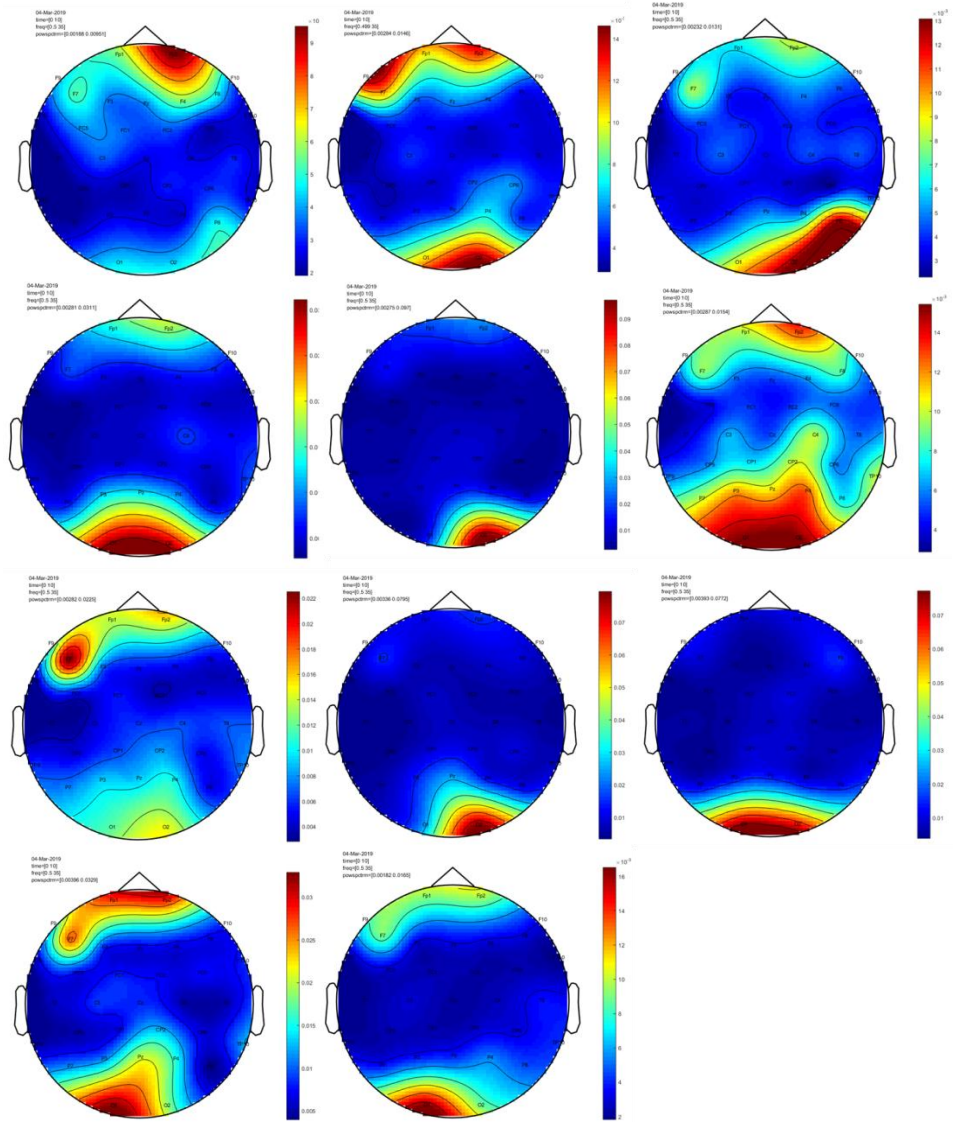
Patients	Number of post-ictal GSWDs	Topographical plots for post-ictal GSWDs
P1	2	
P2	2	

P3	1	 <p>22 Feb 2019 Inseriti: 102 Inseriti: 305 parametri: (2) (0.0072) (0.0082)</p>
P4	2	 <p>22 Feb 2019 Inseriti: 102 Inseriti: 305 parametri: (2) (0.0072) (0.0082)</p> <p>22 Feb 2019 Inseriti: 102 Inseriti: 305 parametri: (2) (0.0072) (0.0082)</p>
P5	4	 <p>22 Feb 2019 Inseriti: 102 Inseriti: 305 parametri: (2) (0.0072) (0.0082)</p> <p>22 Feb 2019 Inseriti: 102 Inseriti: 305 parametri: (2) (0.0072) (0.0082)</p> <p>22 Feb 2019 Inseriti: 102 Inseriti: 305 parametri: (2) (0.0072) (0.0082)</p> <p>22 Feb 2019 Inseriti: 102 Inseriti: 305 parametri: (2) (0.0072) (0.0082)</p>
P6	1	 <p>22 Feb 2019 Inseriti: 102 Inseriti: 305 parametri: (2) (0.0072) (0.0082)</p>

P7	1	<p>25-Feb-2019        ItemID: 135        ItemID: 3 (2)        pmmaker@03045 (0.0447)</p> 
P8	5	<p>25-Feb-2019        ItemID: 135        ItemID: 3 (2)        pmmaker@03078 (0.078)</p> <p>25-Feb-2019        ItemID: 135        ItemID: 3 (2)        pmmaker@03229 (0.072)</p> <p>25-Feb-2019        ItemID: 135        ItemID: 3 (2)        pmmaker@03042 (0.042)</p> <p>25-Feb-2019        ItemID: 135        ItemID: 3 (2)        pmmaker@03075 (0.075)</p> <p>25-Feb-2019        ItemID: 135        ItemID: 3 (2)        pmmaker@03281 (0.32)</p> 
P9	1	<p>25-Feb-2019        ItemID: 135        ItemID: 3 (2)        pmmaker@03284 (0.28)</p> 
P10	3	<p>25-Feb-2019        ItemID: 135        ItemID: 3 (2)        pmmaker@03041 (0.041)</p> <p>25-Feb-2019        ItemID: 135        ItemID: 3 (2)        pmmaker@03041 (0.072)</p> <p>25-Feb-2019        ItemID: 135        ItemID: 3 (2)        pmmaker@03041 (0.041)</p> 

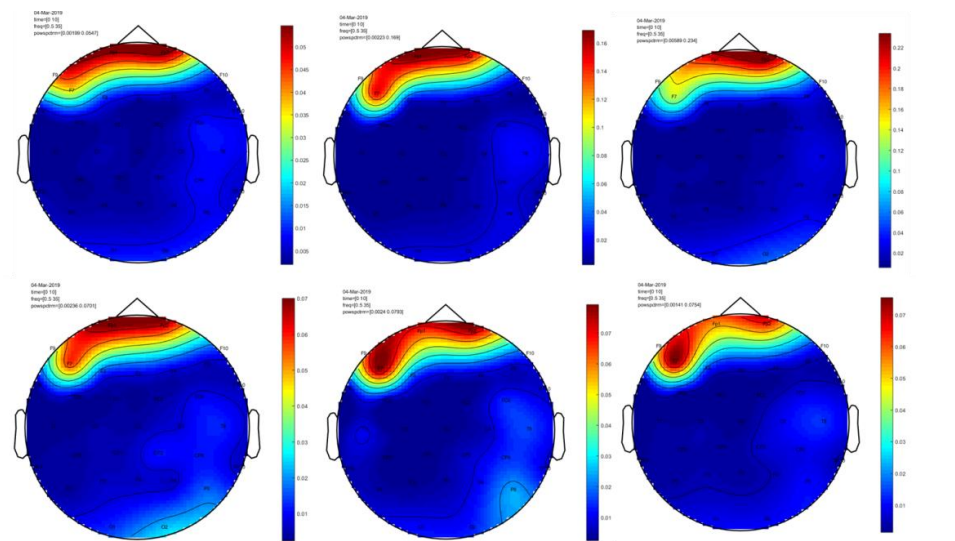
P11

11

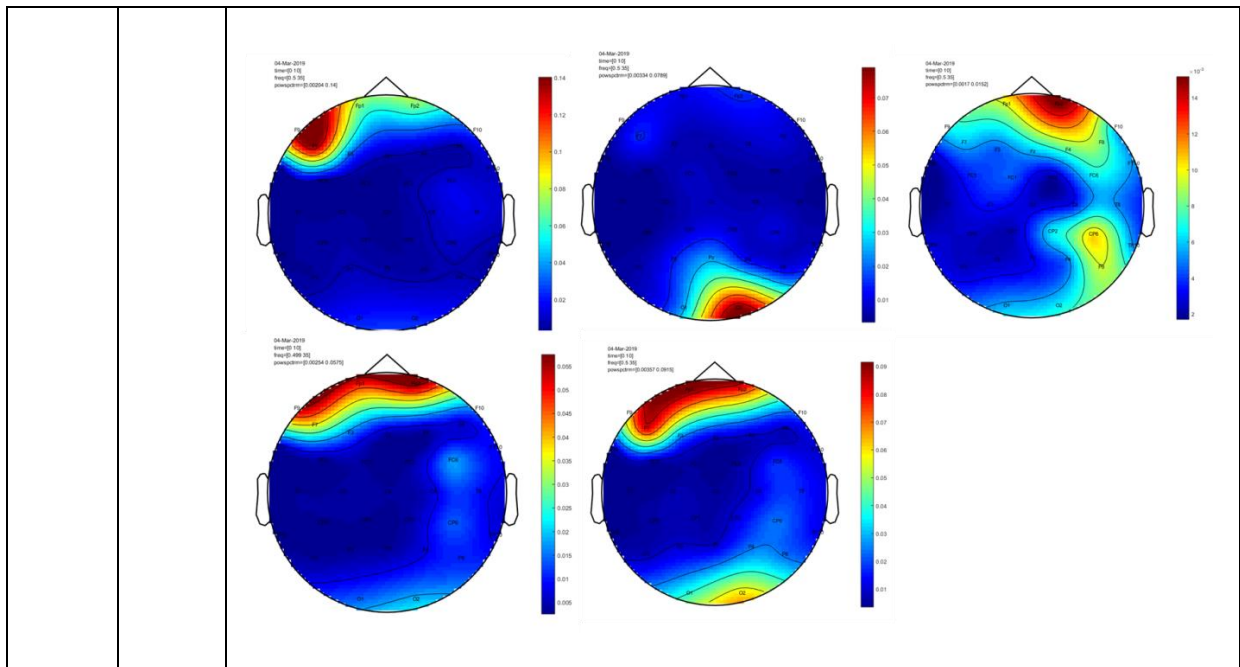


P12

11







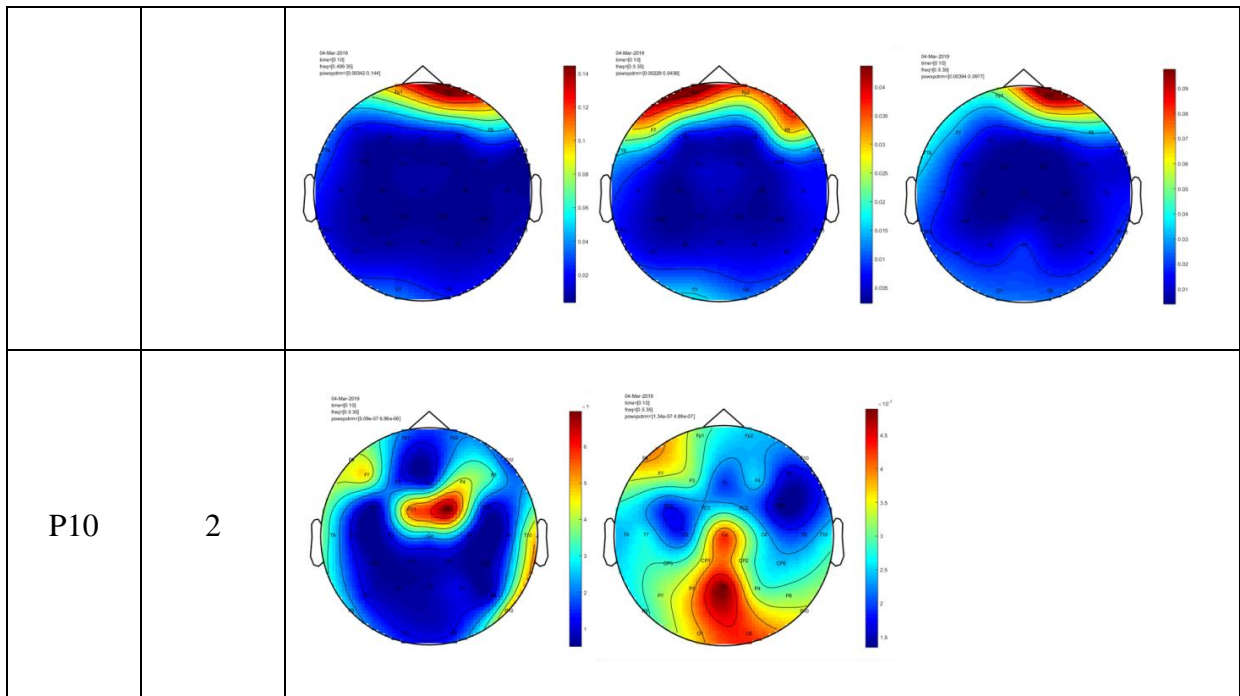
**C.4 Time frequency topographical plots for non-ictal GSWDs.**

Patients	No. of non-ictal GSWDs	Topographical plots for non-ictal GSWDs
P6	3	
P7	3	

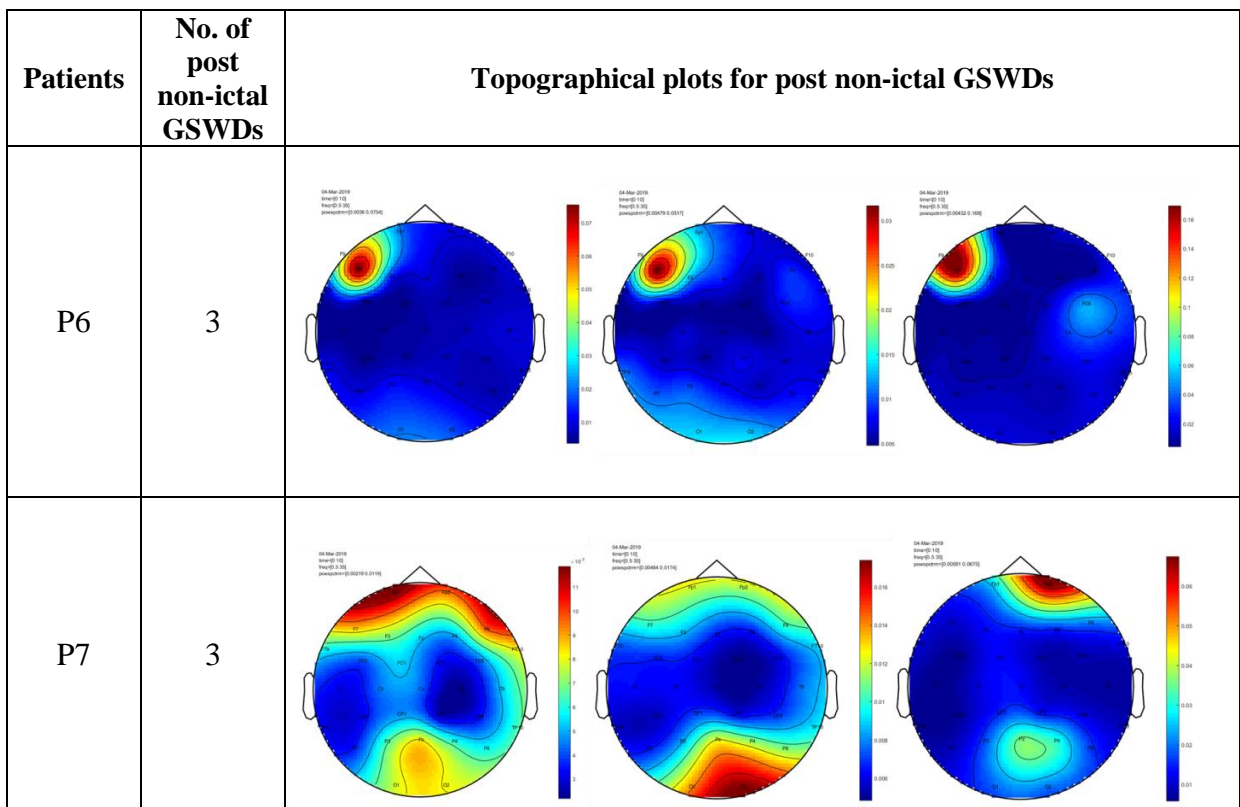


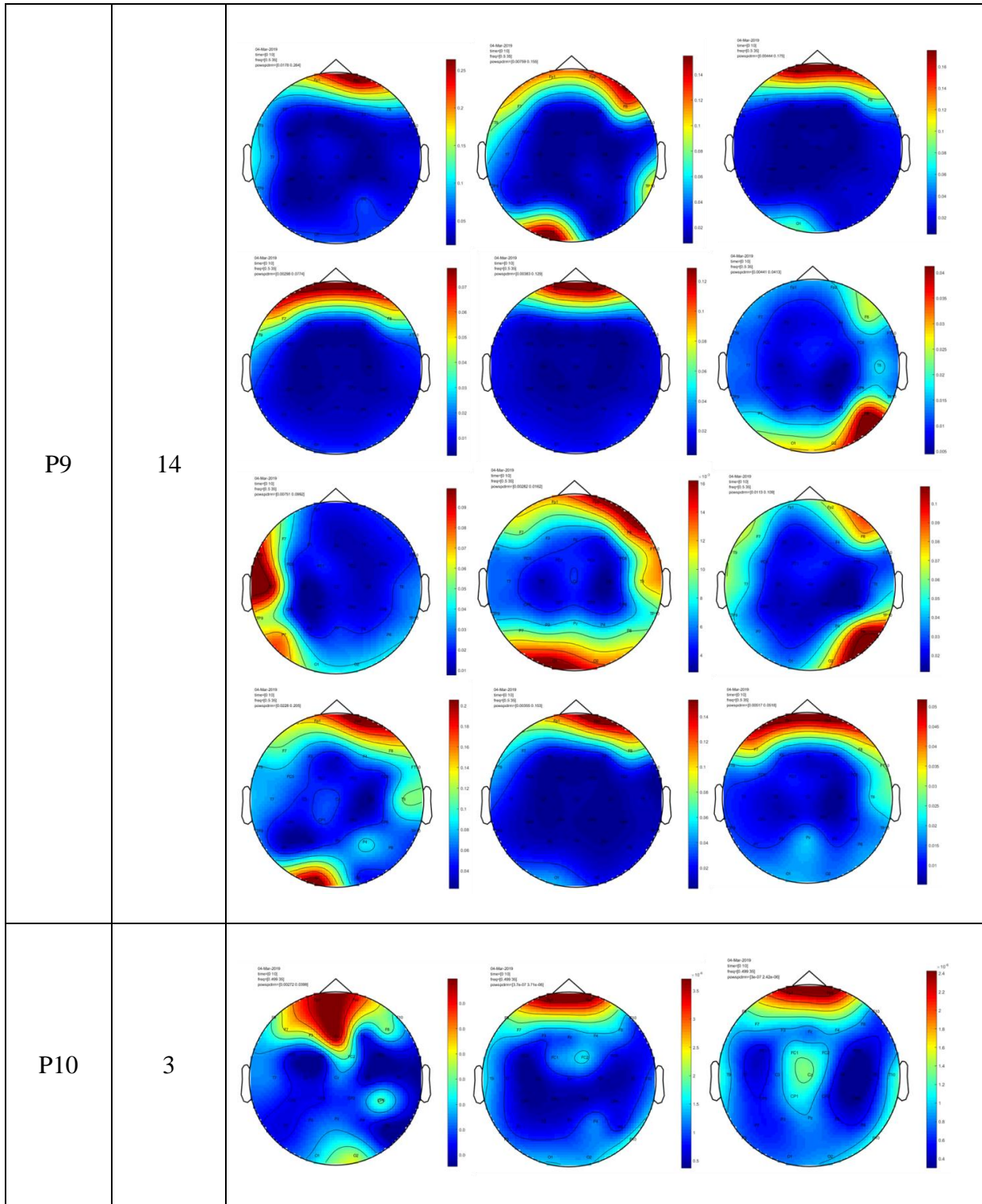
## C.5 Time frequency topographical plots for pre-non-ictal GSWDs

Patients	No. of pre-non-ictal GSWDs	Topographical plots for pre-non-ictal GSWDs
P6	3	
P7	2	
P9	14	



### C.6 Time frequency topographical plots for post non-ictal GSWDs





# Declaration

---

I declare that:

- Apart from my supervisor's guidance - the content and design of the thesis is all my own work and only using the sources listed in the thesis.
- I have not submitted the thesis either partially or wholly as part of a doctoral examination procedure to another examining body and neither it has been published or submitted for publication.
- The thesis has been prepared subject to the Rules of Good Scientific Practice of the German Research Foundation.
- No academic degree has ever been withdrawn for me.

Ami Kumar

(Kiel, 2020)